

'MainzTPC'

Design and commissioning of a dual-phase xenon
time-projection-chamber for studies of the scintillation pulse shape

Dissertation
Zur Erlangung des Grades
Doktor der Naturwissenschaften

Am Fachbereich Physik
Der Johannes Gutenberg-Universität Mainz

Bastian Beskers
geb. am 16.07.1983 in Karlsruhe

Mainz, 2017

Dekanin: Prof. Dr. Concettina Sfienti

1. Berichterstatter: Prof. Dr. Uwe Oberlack

2. Berichterstatter: Prof. Dr. Ferdinand Schmidt-Kaler

Tag der mündlichen Prüfung: -

D77: Dissertation Johannes Gutenberg-Universität Mainz

Hiermit versichere ich gemäß § 12 Abs. 3e der Promotionsordnung des Fachbereichs 08, Physik, Mathematik und Informatik der Johannes Gutenberg-Universität Mainz vom 02.12.2013:

Ich habe diese als Dissertation vorgelegte Arbeit selbständig verfasst. Es wurden ausschließlich die angegebenen Quellen und Hilfsmittel verwendet. Von der Ordnung zur Sicherung guter wissenschaftlicher Praxis in Forschung und Lehre und vom Verfahren zum Umgang mit wissenschaftlichem Fehlverhalten habe ich Kenntnis genommen.

Bastian Beskers (Mainz, April 10, 2017)

Summary

In 1933 Fritz Zwicky first claimed the existence of Dark Matter in the universe. Since that time, astronomy, particle and astro-particle physics have made some effort to understand the effect. Yet Dark Matter remains an unsolved puzzle. Especially in the last three decades direct detection experiments have been built and conducted, restricting the parameter space for Dark Matter particles, but none of the experiments could detect Dark Matter interactions with baryonic matter yet. Some of the leading experiments in the last decade have been based on liquid xenon as detector material and upcoming experiments based on the same principle are still most promising. To improve background discrimination and analysis techniques, a refined knowledge on the properties of xenon as detector material and the microscopic processes in liquid xenon that lead to scintillation and ionization are necessary.

The MainzTPC, a detector dedicated to study the scintillation and ionization process of liquid xenon systematically has been built in the course of this thesis. Like the Dark Matter experiments (XENON100, XENON1T, LUX) the MainzTPC is built as a dual-phase time projection chamber. Hence, it provides charge readout, which yields 3D position resolution and the possibility to study the influence of the strength of an applied drift field on the scintillation process.

Pulse shape discrimination (PSD) could be used as a background discrimination technique complementary to the established method using charge-over-light ratio. For the liquid xenon scintillation pulse shape it was shown in earlier measurements that two excimer states, singlet and triplet, contribute to the scintillation. But their short decay time constants of 2 ns and 27 ns poses a challenge to the measurement of the pulse shape. Although pulse shape discrimination might be possible without measuring the signal with high time resolution, a detailed study of the ratio of singlet to triplet excimers and the influence of electron-ion recombination (and its suppression by the drift field) on the pulse shape requires fast photo detectors and electronics with high bandwidth.

This thesis describes the MainzTPC and the measurement setup, including electronics and photo-sensors. The abilities for pulse shape measurements with the MainzTPC are investigated and some issues that require improvement for the future are pointed out. Finally, the thesis shows various measurements of nuclear and electronic recoils taken at the neutron source nELBE at the Helmholtz-Center Dresden-Rossendorf. First analysis approaches to model the scintillation signal pulse shape are described. With a signal shape averaged over many interactions, the results clearly show a difference in the shape of electronic and nuclear recoils without drift field, and hence qualitatively confirm older results from [KHR78] and [HTF⁺83]. The attempt to determine the pulse shape on an event-by-event basis by fitting individual scintillation signals with a model function is hampered by low photon statistics. The reason for this difficulty is the shape of the individual signal, which does not have one single rise followed by a decay as the averaged signal shape, but shows fluctuations of the signal especially in the decaying part. A Monte Carlo simulation, in which the signal shape of individual events was simulated based on the knowledge of the average scintillation shape from the previous measurements and the single photo-electron response of our photo-multiplier tubes showed that the fluctuations seen on individual measured signals originate indeed from the statistical fluctuations in photon generation times. Prospects for future improvements are discussed.

Zusammenfassung

Seit Fritz Zwicky 1933 erstmals die Existenz von Dunkler Materie postulierte, wurden von Astronomen, Teilchen- und Astroteilchenphysikern Anstrengungen unternommen, mehr darüber zu lernen. Insbesondere in den letzten drei Jahrzehnten wurden Experimente entworfen und durchgeführt, um Dunkle Materie direkt nachzuweisen. Jedoch konnte bisher nur der Parameterraum für mögliche Dunkle Materie Teilchen eingeschränkt werden, ein Nachweis ist bisher nicht gelungen. Einige der bisher führenden Experimente, und auch vielversprechende geplante Dunkle Materie Experimente, nutzen verflüssigtes Xenon als Detektionsmedium. Um für zukünftige Experimente die Untergrund-Diskriminierung und Analysen zu verbessern, ist ein umfassenderes Verständnis von flüssigem Xenon und der mikroskopischen Prozesse, die zur Freisetzung von Ladung und Szintillationslicht führen, notwendig.

Die MainzTPC wurde zur Untersuchung dieser Detektionsprozesse entworfen und gebaut. Die MainzTPC funktioniert, genau wie die Dunkle Materie Experimente XENON100, XENON1T und LUX nach dem Prinzip einer Zwei-Phasen-Zeitprojektionskammer. Damit ist eine Auslese der bei Wechselwirkungen erzeugten Ladung (Elektronen-Ionen-Paaren) möglich und damit eine 3D Positionsrekonstruktion des Wechselwirkungspunktes. Außerdem ist es durch eine Variation des Driftfeldes möglich, den Einfluss verschiedener Feldstärken auf den Szintillationsprozess zu untersuchen.

Der zeitliche Verlauf des Szintillationslichts könnte eine weitere, zur bisher etablierten Methode des Ladungs-Licht-Verhältnisses komplementäre Technik zur Untergrunddiskriminierung sein, welche die Sensitivität von Dunkle Materie Experimenten, insbesondere im Bereich kleiner Energiedepositionen, erhöhen könnte. Frühere Messungen zeigen, dass zwei Exzimer-Zustände (Singlet und Triplet) zum Szintillationsprozess beitragen, aber die sehr kurzen Lebensdauern der beiden Exzimer (2 ns und 27 ns) stellen hohe Anforderungen an die Bandbreite und Samplingrate von Elektronik und die Zeitauflösung von Lichtdetektoren. Auch wenn Signalform-Diskriminierung (pulse-shape discrimination, PSD) auch ohne zeitlich hochaufgelöste Messung der Signale möglich sein kann, ist dies für eine Messung, die zu erweitertem Verständnis des Szintillationsprozesses führen soll, unabdingbar.

In dieser Arbeit wird der Entwurf und der Aufbau der MainzTPC sowie der Messaufbau und die verwendete Elektronik und Lichtsensoren beschrieben. Diese Arbeit zeigt das Potential der MainzTPC, die Szintillationslichtform zu messen, und stellt ein paar Punkte die in Zukunft verbessert werden müssen heraus. Außerdem werden erste Ergebnisse für Hüllen- und Kernrückstöße aus Messungen an der Neutronenquelle nELBE am Helmholtz-Zentrum Dresden-Rossendorf vorgestellt. Es werden Analysewege für eine Bestimmung der Szintillationslichtform gezeigt. Mit einem über viele Streueignisse gemittelten Signal ohne anliegendes Driftfeld ist ein deutlicher Unterschied zwischen den Formen von Hüllen- und Kernrückstoß-Szintillationslicht erkennbar. Damit werden die Ergebnisse von [KHR78] und [HTF⁺83] qualitativ bestätigt. Es stellte sich als schwierig heraus, die Signalform für einzelne Ereignisse mittels Anpassung der Modellfunktion an die Signale zu bestimmen. Der Grund dafür ist, dass die Signalform eines einzelnen Ereignisses nicht wie das gemittelte Signal einen Anstieg mit darauf folgendem Abfall hat, sondern dass insbesondere im abklingenden Teil viele Fluktuationen zu sehen sind. Mittels einer einfachen Simulation von zu erwartenden Signalen konnte gezeigt werden, dass diese Fluktuationen durch die statistisch verteilten Erzeugungszeitpunkte der Photonen im Szintillationsprozess begründet sind. Zukünftige Verbesserungsmöglichkeiten werden diskutiert.

Contents

List of Abbreviations	VII
1. Introduction	1
2. Dark Matter and Detection	3
2.1. Dark Matter	3
2.1.1. Evidences	3
2.1.2. Particle candidates	6
2.1.3. Detection Methods	7
2.1.4. Direct Detection	8
2.2. Liquid Xenon TPC principle	9
3. Noble Gas Scintillation and Ionization	13
3.1. Scintillation mechanism	13
3.1.1. Typical time constants	14
3.2. Pulse Shape discrimination	19
4. Experimental Setup	21
4.1. The MainzTPC	22
4.1.1. Design Goals	22
4.1.2. Simulations – uniformity of drift field	25
4.1.3. Technical Design	28
4.1.4. Leveling solutions and levelmeters	30
4.1.4.1. Leveling Solution 1: Bellow	30
4.1.4.2. Leveling Solution 2: Clearance Fit	32
4.1.4.3. Levelmeters	35
4.2. Liquid Level issues	37
4.3. Infrastructure	41
4.3.1. Gas System	41
4.3.2. Cooling System	43
4.4. Slow Control System (SCS)	47

7.4.2. Waveform overlaying and averaging	134
7.4.2.1. Pulse shapes	137
7.4.3. Fitting individual waveforms	141
7.5. Simulating the scintillation signal shape	146
7.5.1. Simulation approach	146
7.5.2. Simulated signals	147
8. Summary and perspectives	151
8.1. Summary	151
8.2. Future perspectives	152
A. Datasheets and Schematics	155
B. Trigger Setup: Tables	161
C. Example xml configuration file	165
D. Raised Cosine	171
E. PMT calibration: Additional figures and tables	173
F. Pulse Shape: Model Function	183
G. S1 vs. energy deposits: additional figures	185
H. Pulse shape: additional figures	191

4.5. Signal Readout	48
4.5.1. Light detectors used for the MainzTPC	48
4.5.1.1. Photo Multiplier Tubes: Hamamatsu R6041	48
4.5.1.2. Large-Area Avalanche Photo-Diodes: RMD S1315	49
4.5.2. Detectors for scattered particles	50
4.5.2.1. Germanium detector	50
4.5.2.2. Plastic scintillators	51
4.5.3. Data-Acquisition System	51
4.5.3.1. Flash ADCs	51
4.5.3.2. Amplifiers	53
4.5.3.3. Constant Fraction Discriminators	54
4.5.3.4. TDC: CAEN VX1290	55
4.5.3.5. Trigger Unit	55
4.5.4. High Voltage Modules	56
4.6. The Compton setup	56
4.7. The neutron scattering experiment	57
4.7.1. The neutron Source nELBE	58
4.7.2. Neutron interactions in xenon	60
4.7.3. The measurement setup at nELBE	61
4.7.4. Measurement of the energy deposits in the MainzTPC	63
4.7.5. Uncertainties	65
4.7.5.1. Double Time-of-flight measurement	65
4.7.5.2. Scattering angle	65
4.7.6. Trigger Setup	68
5. Raw Data Analysis - Framework and Algorithms	75
5.1. Data Format and Analysis Framework	75
5.1.1. Raw Data Format	75
5.1.2. Analysis Framework	75
5.1.2.1. Visitor pattern: Analyzer	77
5.2. Class: MainzWaveform and inheriting classes	79
5.2.1. MovingWindowFilteredWaveform	80
5.2.1.1. Raised cosine filter	81
5.2.2. MedianFilteredWaveform	84
5.2.3. LinearFilteredWaveform	84
5.2.4. FFTFilteredWaveform	84
5.2.5. PatternFilteredWaveform	85
5.3. Waveform Features	86
5.3.1. XeRawPeak	86

5.3.2.	Step	87
5.3.3.	Format of the ROOT file: WaveformFeaturesToRoot	87
5.3.4.	FWIntegral	88
5.3.5.	Format of the ROOT file: FWIntegralToRoot	89
5.4.	TDCFeatures	90
5.4.1.	CoincidenceHit	90
5.4.2.	Format of the ROOT file: TDCToRoot	91
5.5.	PeakFinder	92
5.5.1.	Algorithm	92
5.6.	StepFinding and StepFitting	92
5.6.1.	StepFinding algorithm	95
5.6.2.	StepFitting algorithm	96
5.7.	Coincidence Hit Finder	97
5.7.1.	CoincidenceHit finding algorithm	97
5.7.2.	Interaction time	98
5.7.3.	z-position and path-of-flight-2	99
6.	Photomultiplier Calibration	101
6.1.	Measurement of the absolute gain	101
6.2.	Measurement of the relative gain	104
6.3.	Single photo-electron response	108
6.3.1.	Model of the shape	108
6.3.2.	Investigation of the second bump	113
7.	Data Analysis	115
7.1.	Selections	115
7.1.1.	Event Selection	115
7.1.2.	CoincidenceHit Selections	116
7.1.2.1.	CoincidenceHit selection: TPC	116
7.1.2.2.	CoincidenceHit selection: Plastics	119
7.2.	Event Classification and Identification	121
7.2.1.	TOF1 vs TOF2	121
7.2.2.	Event Classification	121
7.3.	S1 vs. Energy Deposit	124
7.4.	Pulse shape analysis	127
7.4.1.	Fit functions	128
7.4.1.1.	Fermi-Dirac Threshold with Exponential Decays	129
7.4.1.2.	Model-based fit function	131

List of Abbreviations

ADC analog-to-digital-converter

APD avalanche photo diode

CERN European Organization for Nuclear Research

CFD constant-fraction discriminator

CSP charge-sensitive preamplifier

CTD coincidence time difference

DAQ data acquisition system

DM Dark Matter

ELBE Electron Linac for beams with high Brilliance and low Emittance

FADC flash analog-to-digital-converter

FEM finite-element method

HV high-voltage

HZDR Helmholtz-Zentrum Dresden-Rossendorf

IC integrated circuit

JGU Johannes Gutenberg-University Mainz

LCE light collection efficiency

LHC Large Hadron Collider

LN2 liquid nitrogen

LVDS low voltage differential signal

MAW moving average window

nELBE Neutron TOF experiments at ELBE

NIM Nuclear Instrumentation Module

OFC	oxygen-free copper
PCB	printed circuit board
PEEK	polyether ether ketone
PID	proportional-integral-differential
PMT	photo multiplier tube
PSD	pulse-shape discrimination
PTFE	Polytetrafluoroethylene
PTR	pulse-tube refrigerator
QCE	charge collection efficiency
QE	quantum efficiency
SCS	slow-control system
SiPM	silicon photo-multiplier
SMD	surface-mounted device
SPE	single photo-electron
TDC	time-to-digital-converter
TOF	time-of-flight
TPC	time-projection-chamber
UHV	ultra-high vacuum
UML	unified markup language
UTI	universal transducer interface
VUV	vacuum ultra violet
WIMP	Weakly Interacting Massive Particle
XML	extended markup language

1. Introduction

Many different observations show, that only a small fraction of our universe is made from baryonic matter. The major part of the universe consists of dark energy and dark matter. No standard model particle has the properties to be the dark matter particle. Generally accepted is a yet unknown non-standard-model particle, the so-called Weakly Interacting Massive Particle (WIMP). Among the many different experiments trying to detect WIMPs by their interaction with baryonic matter, the most stringent limits on mass – cross-section have been set by experiments based on dual-phase liquid xenon time-projection-chambers (TPCs): XENON10, XENON100 and LUX. Future experiments based on the same technique are in the commissioning phase (XENON1T). Despite their well-accepted technology, there is still room for improvement for future detectors, besides increasing their size for improved sensitivity.

As the interaction rates with WIMPs are extremely low, background suppression is one of the important points for all experiments trying to detect dark matter. Besides background suppression, discrimination of remaining background is crucial. Therefore, a complementary background suppression to the commonly used charge-over-light ratio will improve the experiments' sensitivity. A promising complementary method is the use of pulse-shape discrimination, which is already successfully used for TPCs based on liquid argon. For liquid xenon this is not yet the case, for the reason that knowledge on the scintillation pulse shape is limited. It is known, that the scintillation time constants involved are relatively fast (2 ns and 30 ns), which also sets challenging requirements to the light detectors and electronics to allow measuring the pulse-shape and using pulse-shape discrimination.

Additional improvement of the experiments would come from increased sensitivity for low-mass WIMPs ($\lesssim 10 \text{ GeV}/c^2$). This requires improved knowledge on the scintillation efficiency and the charge yield of nuclear and electronic recoils for low energy deposits. Large uncertainties dominate current knowledge of those quantities below 10 keV.

As liquid xenon is not only used in dark matter detectors, but also for neutrinoless double beta decay experiments (EXO), in particle physics (MEG) and even for medical imaging (pet PET-scanner) improved knowledge of the scintillation process, the pulse shape, charge yield and light yield and their dependency on an applied electrical drift field is of broader interest.

To study the scintillation process systematically and reduce the uncertainties of the measurements of scintillation efficiency and charge yield for both, nuclear recoils and electronic recoils,

we designed a small dual-phase xenon TPC, the MainzTPC. This thesis describes the design of the MainzTPC with its components and the required infrastructure. It shows the experimental setups used to carry out first measurements of nuclear and electronic recoils. The framework that was developed for data-analysis is described. First new insights on the scintillation pulse shape are given and compared with previous results. Improvements required for further systematic studies are also discussed reaching from changes in the detector design and experimental setup over improvements in the analysis routines to required changes to the electronics and readout.

2. Dark Matter and Detection

2.1. Dark Matter

About 100 years ago, some physicists believed, that most of the fundamental physics is known and mainly understood. In the last century, more and more hints occurred, that this assumption was wrong. Examples for this are the existence of neutrinos and discovery of CP-violation. The gravitational observations of large amounts of invisible matter in the universe, and the accelerated expansion of the universe are two further observations, showing that fundamental physics are far from being completely understood. The COBE, WMAP and Planck satellite missions showed, that in fact only 4.99% [O⁺14] of the universes energy density are made up from baryonic matter, 26.5% [O⁺14] consists of Dark Matter and the majority is made up from so-called Dark Energy. We don't know very much about Dark Matter yet, except the fact, that it interacts gravitationally. This is, how it is observed on different scales in the universe. About dark energy we know even less.

2.1.1. Evidences

The observations, that show the existence of dark matter, exist in very different scales in the universe. It is visible in the relatively small scale of single galaxies and up to the scale of the complete universe, when looking at structure formation and the cosmic microwave background.

Rotational curves in galaxies

Maybe the clearest evidence, is the observation of rotation velocities of stars and gas-clouds in spiral galaxies. For the distribution of (visible) mass in the galaxy, one can used Newtonian laws to calculate the radial velocity of the galaxy as a function of r:

$$v(r) = \sqrt{\frac{G \cdot M(r)}{r}}$$

In this equation $M(r)$ is the mass of the galaxy inside the radius r. This equation also states, that outside of the stellar disc, where almost all mass is inside r and therefore $M(r) \approx \text{const.}$, the rotational velocity should follow $v(r) \propto r^{-1/2}$. Observations of stars in the stellar disc, and

gas-clouds further out, do not show the expected behavior [BBS91]. The stars in the inner regions follow the expected velocity curve for the distribution of stars and interstellar gas, but further out, the rotational velocity stays rather constant. This behavior can be explained, by assuming, that the galaxies are embedded in a halo of (invisible) matter. Another way of explaining the discrepancy between expectation and observation, is to modify Newtonian dynamics for large scales. This approach however, can not explain the different observations on the different size-scales.

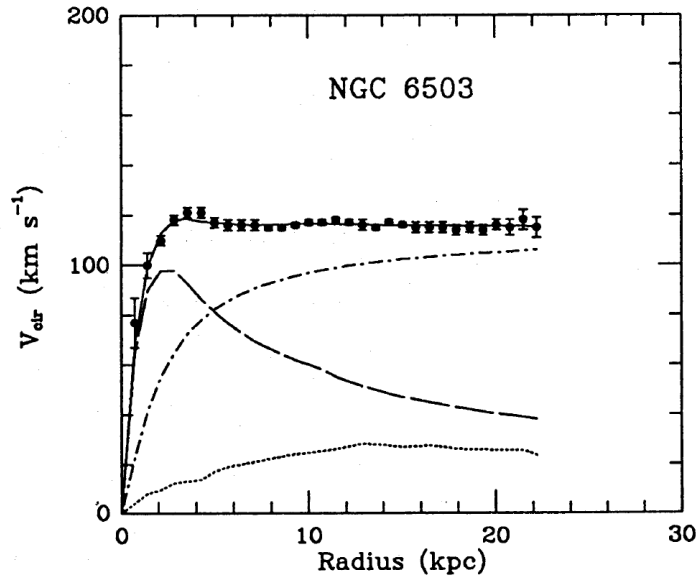


Figure 2.1. Rotational Curve of spiral galaxy NGC6503. The measured curve is shown, together with the density profiles of visible mass (stars/disk), the interstellar gas and the dark matter halo required to explain the rotational velocities. [BBS91]

Movement of galaxies in galaxy clusters

The first observed evidence for the existence of additional, invisible matter in the universe was the observation of the velocities of galaxies in galaxies in the coma cluster. From the observed velocities Zwicky derived the total mass of the cluster using the virial theorem and compared it with the mass derived from optical observations using the luminosity of the single galaxies [Zwi33]. He found a discrepancy between the two values, the mass inferred using virial theorem was larger. Therefore he claimed that additional invisible matter had to exist in the coma cluster. Later observations of the Virgo cluster [Smi36] and the local group [HW55] showed the same behavior.

Gravitational lensing

Gravitational lensing is the bending of light by a massive object, as described by the theory of general relativity. Very massive objects in the foreground of a bright object in the background lead to a distorted image of the bright object similar to the effect of an optical lens, therefore the term gravitational lensing. The effect can also lead to multiple images of the object. The effect of course, depends on the distances between observer, massive object and bright background object and the alignment of their positions. This effect has been observed by several optical telescopes, like the Hubble space telescope.

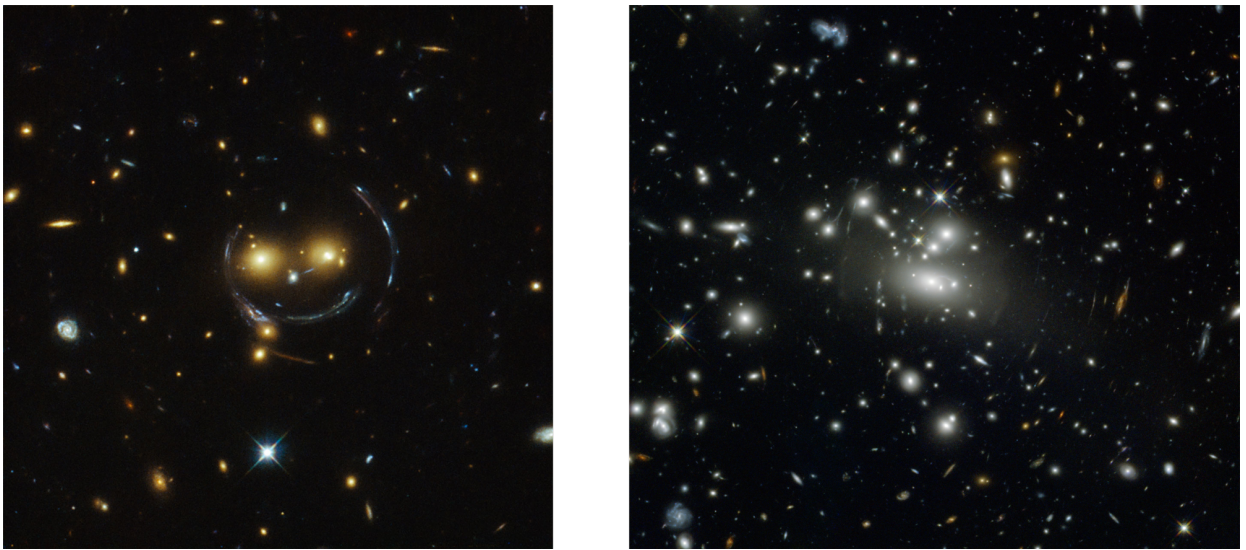


Figure 2.2. Two images taken by Hubble space telescope. [ESA17]

Left: The image of a distant light source occurs here as an Einstein ring surrounding the two galaxies SDSSCGB 8842.3 and SDSSCGB 8842.4 which serve as gravitational lens. Einstein rings occur if observer, gravitational lens and distant source are aligned.

Right: Light from distant galaxies occurs as arcs, due to the gravitational lensing of galaxy cluster Abell S1077.

Cosmic microwave background

The cosmic microwave background, the “echo” of the big bang, shows the best ever measured black-body spectrum at a temperature of 2.726 ± 0.010 K[M⁺94]. The local fluctuations in temperature (the anisotropy), reveal the seeds for structure formation in the later universe. The shape of the angular power spectrum of the cosmic microwave background strongly depends on the amount of dark matter and baryonic matter in the early universe. Therefore, the measurement of those anisotropies by the Planck satellite [Ade14] and its predecessor WMAP set the strongest constraints on the composition of the universe.

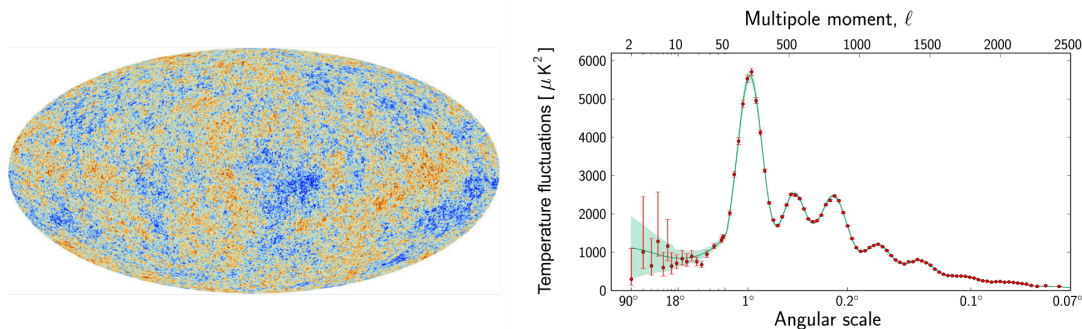


Figure 2.3. Anisotropy map of the cosmic microwave background (left), as recorded by the Planck satellite. The according angular power spectrum is shown on the right. [ESA17]

2.1.2. Particle candidates

As there is evidence for dark matter, the question remains, what this ominous dark matter is made of. To answer this question, it is helpful to summarize the properties that dark matter particle candidates must fulfill. They must interact gravitationally. They may not interact with photons (or at least, the cross-section has to be extremely small), because otherwise, dark matter would have been detected by absorption or emission of light. It can also not have a high cross-section for baryonic interactions, as otherwise, it would have been detected by laboratory experiments and it would not form halos around the galaxies, but rather reflect the mass distribution of the baryons. Checking the list of standard model particles, the neutrino is the only possible candidate. But, as the neutrinos rest mass is small (<2.2 eV [BBB⁺01]), neutrinos would be so-called hot dark matter. Simulations on structure formations exclude that dark matter is consisting of hot dark matter primarily, as this would wash out early small structures. Structure formation would have to proceed by fragmentation of large structures (“top-down”) rather than building up from smaller ones (“bottom-up”) in contradiction to deep field galaxy surveys. Self-evident, but worth mentioning, is the fact that the particle has to be stable (or long-lived on the timescale of the Hubble time), as otherwise it could not be observed throughout the whole history of the universe, beginning with the cosmic microwave background, in structure formation and also in the current universe (movement of spiral galaxies). As dark matter cannot consist of standard model particles, theorists introduced different hypothetical particles that could be the dark matter particles. Besides the axion, a particle introduced to solve the strong CP problem by Peccei and Quinn [PQ77], the so-called WIMP is the particle that is generally seen as the best motivated candidate.

WIMP

The term WIMP is an acronym and stands for **W**eakly **I**nteracting **M**assive **P**article. The name therefore reflects the properties of the particle, as it has to be massive and its interaction cross-section with photons, baryons and for self-interactions has to be at most on the scale of weak interactions. If one assumes WIMPs were in thermal equilibrium in the early universe, i.e. the production rate and annihilation rate were equal and then calculates the effect of the expansion of the universe one comes to the following conclusion: With the expansion the temperature of the universe drops together with the baryon and WIMP densities and at some point, the temperature is too low to produce WIMPs any more. After this time, the WIMP density decreases faster, as there is still WIMP annihilation but little WIMP production. At some point, the WIMP density becomes so low, that WIMP annihilations become unlikely, and the amount of WIMPs in the universe stays constant, the so-called “freeze out”. The WIMP density therefore decreases only by the expansion of the universe. The interesting fact is, that the required relic density of WIMPs, that matches the requirement for dark matter, if the cross-section is on the order of weak interactions [JKG96]. The WIMP could for example be the lightest supersymmetric particle, and its detection would therefore be of great interest for this theory and particle physics in general.

2.1.3. Detection Methods

As dark matter is so abundant in our universe and the underlying physics are of huge interest not only for astroparticle physics, huge efforts are undertaken to find the dark matter particles. The experiments searching for the particles are based on three complementary approaches: direct detection of the particles, indirect detection of the particles and production of the particles. Production could possibly be observed at particle colliders, particularly at the highest energies achieved by the Large Hadron Collider (LHC) at CERN. Indirect detection means the search for products of annihilating or decaying dark matter particles. The signature of annihilating dark matter is searched for in data taken by neutrino- and gamma-telescopes or with the search for anti-matter (positrons, light anti-nuclei) in cosmic rays. The expected annihilation product would possibly be two mono-energetic neutrinos or gammas and the signature would therefore be a mono-energetic line at the dark matter particle’s mass, that should be especially prominent in regions of high dark matter density, such as the galactic center. Direct detection means, to search for interactions of dark matter particles with baryonic matter. Despite the huge efforts, and the different complementary experiments, neither WIMP-like nor axion-like particles have been detected so far.

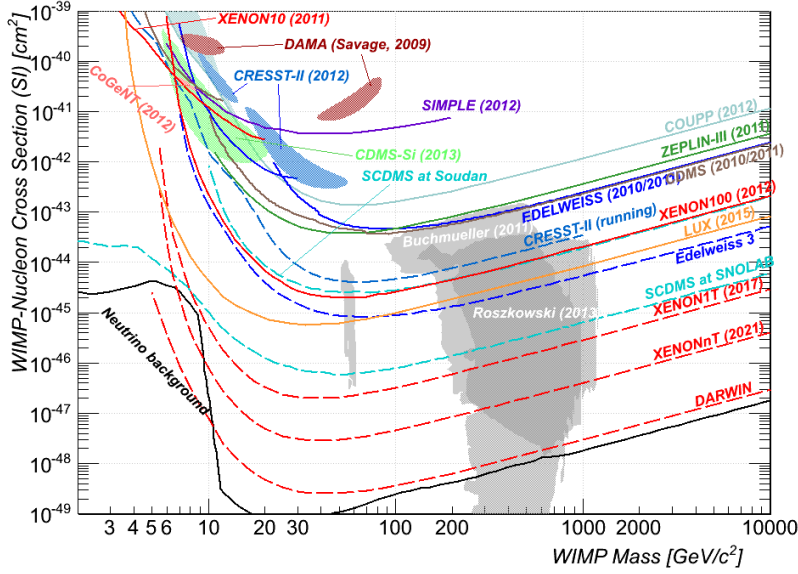


Figure 2.4. Mass-cross-section limits set by different direct detection experiments. Currently the best limit is set by the LUX experiment, which is based on a dual-phase xenon TPCs. The dashed lines show projected limits for experiments currently running or in construction phase (CRESST-II, XENON1T, EDELWEISS-3, SCDMS) and for planned future experiments (XENONnT, DARWIN). The background from atmospheric neutrinos (black), will for the planned experiments start to be important part of the background. Data from [Bro16].

2.1.4. Direct Detection

Direct detection experiments search for nuclear recoils due to the elastic interaction of a dark matter particle with a nucleus of the detector target atoms. They in general face the problem of very small signal rates (due to the small interaction cross-section). Background suppression is therefore one of the main difficulties. For this reason, these experiments are undertaken in underground laboratories, well shielded from cosmic rays and air showers, and often use active vetoes in addition. For further background discrimination, many experiments are based on detectors that allow reading two complementary channels (charge+light, charge+heat, heat+light) to distinguish nuclear recoils from electronic recoils. Experiments reading charge and heat are CDMS and EDELWEISS, based on germanium detectors operated at cryogenic temperatures, allowing to read charge and heat generated by a particle interaction in the crystal. An experiment using scintillation light and heat readout is CRESST. Experiments using scintillation light and ionization readout are mostly based on liquid noble gas as detector material (xenon and argon). Especially the experiments based on dual-phase xenon TPCs have been setting the most stringent limits in mass - cross-section in the past decade.

2.2. Liquid Xenon TPC principle

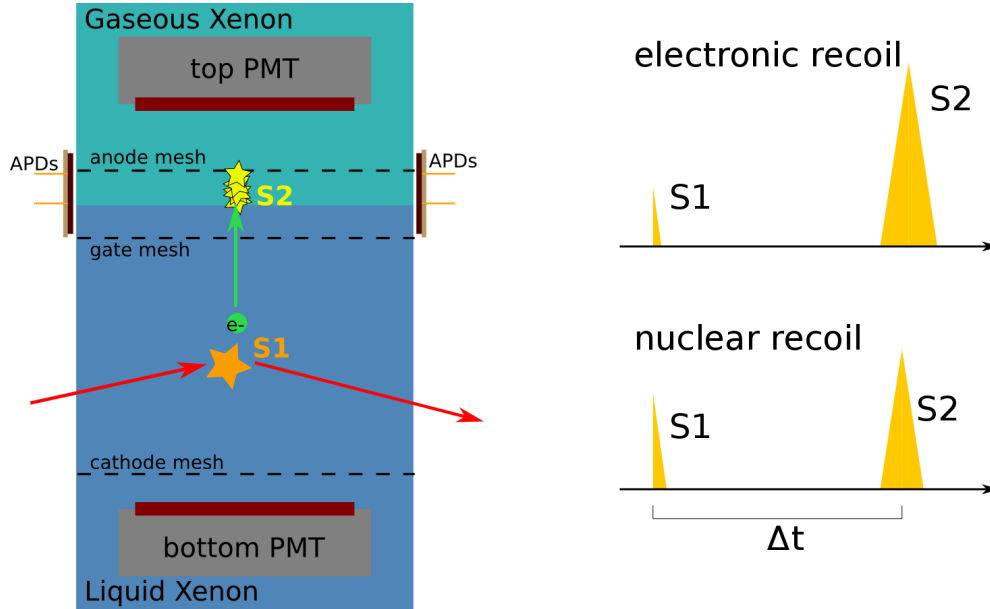


Figure 2.5. Principle of a dual-phase TPC: An interaction in the liquid leads to prompt scintillation light (S1) and ionization. The electrons are drifted upwards by a field applied by the cathode and gate mesh and extracted into the gas-phase by a stronger field between gate-mesh and anode. In the gas-phase, the electrons produce secondary scintillation light (S2), proportional to the number of electrons. Recording the two signals (S1 and S2) allows 3D position reconstruction and identification of recoil type (nuclear or electronic recoil).

As already mentioned, XENON100 and LUX are based on dual-phase xenon TPCs. The principle of these TPCs is relatively simple, though there are of course technical challenges in construction and design. Those dual-phase TPCs use liquid xenon as detection medium. A particle (WIMP, but also standard model particles) can scatter off the nuclei of liquid xenon, depositing small amounts of energy in the liquid. This energy deposit is partially used to excite and partially to ionize xenon atoms. The excited atoms form so-called excimers together with neutral xenon atoms, and emit scintillation light (S1), when de-exciting to their ground states. The electrons freed by the ionization process can be drifted upwards in the liquid by an applied electric field. On top of the active volume the electrons can be extracted into the gas-phase by a stronger electric field. Due to the lower density, the mean free path of the electrons in the gas phase is much larger than in liquid. Therefore the electrons gain enough energy to excite atoms in the xenon gas phase, which leads to secondary scintillation light (S2). The amount of secondary scintillation photons is proportional to the number of electrons. The absolute number depends on pressure (density), field strength and drift path of electrons in gaseous xenon and can be several hundred photons per electron. Thus detecting those photons provides a good resolution and low threshold for the charge measurement.

Although S1 and S2 can independently be used to measure the energy deposit, the combination provides two big advantages:

- 3D-position resolution
- identification of interaction type (nuclear recoil vs. electronic recoil)

3D-position resolution in such dual-phase TPCs is a combination of measuring the depth of the interaction, using the drift-time of the electrons (= time difference between S1 signal and S2 signal) and x/y-position. The x/y-position can be determined by detecting the S2 photons with an array of photo-detectors, and making use of the different amount of photons seen by each of the light-detectors, depending on the position of the S2 signal. The big dark matter detectors XENON100, XENON1T and LUX use an array of photo multiplier tubes (PMTs) above the liquid-gas interface for this purpose. The MainzTPC is using eight avalanche photo diodes (APDs), surrounding the liquid-gas interface, to provide the x/y-position resolution. The 3D-position resolution allows to fiducialize the volume, i.e. using the outer layer as active veto and to correct the measured amount of photons and charge and therefore compensating anisotropies of the detector. Identification of the interaction type can be done, by using the ratio of charge to light

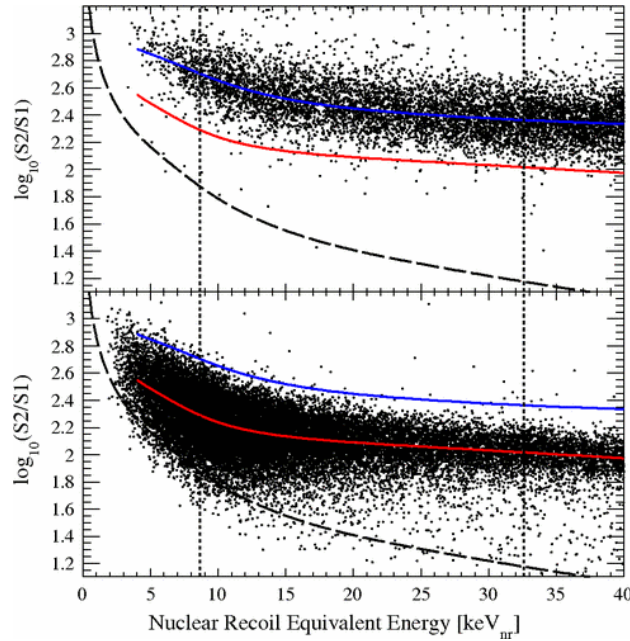


Figure 2.6. The recoils bands in $\log(S2/S1)$ space as measured by XENON100 [Ae10]. The upper part shows the electronic recoil band from ^{60}Co and the lower the nuclear recoil band from $^{241}\text{AmBe}$. The red and blue lines mark the medians of electronic and nuclear recoils $\log(S2/S1)$.

(S2 to S1). Particles interacting with the xenon nuclei (neutrons, WIMPs) will create a different S2/S1 ratio than particles interacting with electron shell of the xenon atoms (gammas, electrons). This provides a powerful way for the dark matter experiments to discriminate background from

2.2. LIQUID XENON TPC PRINCIPLE

intrinsic radioactivity of impurities in the liquid xenon, the materials used to build the TPC and from surrounding materials.

Background discrimination works well for higher energy deposits, but for very small energy deposits, the discrimination power is lower, as the nuclear and electronic recoil band in $\log(S2/S1)$ -vs- $S1$ space are overlapping. Especially WIMPs of lower masses ($\leq 10 \text{ GeV}/c^2$) generally deposit less energy. Improving background suppression at low energy deposits will therefore help increase the sensitivity of the detectors for low-mass WIMPs.

3. Noble Gas Scintillation and Ionization

3.1. Scintillation mechanism

To understand the scintillation process in liquid noble gases basically, first efforts have been undertaken already in the late 70's ([KHR78], [KNT⁺78], [KHN78], [KHSR79], [KGS79]) and early 80's ([KSR80], [KHSzR82], [HTH⁺82], [HTF⁺83]). Later more work has been done, mainly with the focus on liquid noble gases as Dark Matter and particle detector material ([DMS90], [DDL⁺94], [Aki02], [DHA⁺05], [Hit05], [KBS⁺10]). A review of previous work covering many aspects of xenon as detector medium extensively has been published too [Ae10]. It also contains descriptions and applications of liquid xenon detectors. This review treats the pulse shape only short, therefore this section will summarize the measurements and findings of above mentioned references, which mainly focus on pulse shape. As this thesis is about liquid xenon, results of other noble gases mentioned in references above are mainly neglected in the summary here, as long as they are not of general interest.

Any process, which finally leads to scintillation, is based on the movement and stopping of a fast (= non-thermal), charged particle in the scintillator material. This particle (electron, alpha particle or fission fragment) can come from a radioactive source immersed in the liquid noble gas, which is useful for experiments to understand the scintillation process. Alternatively, like it happens when the noble gas is used as detector, it can be created by a particle (gamma, neutron, WIMP) from an outside source which interacts with one of the noble gas atoms.

Gamma radiation from an outside source can Coulomb scatter off one of the shell-electrons of a noble gas atom. The electron will be knocked off the noble gas atom and then move through the liquid noble gas. During its movement it will do many interactions with the electron-shells of the atoms and transfer some energy in each interaction, until it is finally thermalized.

Neutrons coming from outside sources can scatter off the noble gas nuclei, transferring energy to the noble gas atom. This atom, which might also get ionized by the initial process, will then move through the liquid and its kinetic energy will be distributed along its path. WIMPs are supposed to scatter off nuclei, as neutrons. Therefore the general description is as for neutrons.

Independent of the type of the particle coming from the outside, typically the mean free path of those is much larger than the stopping path of the generated electron or noble gas atom. This means, for the following, we can restrict the considerations to only one interaction of the primary

particle and therefore only the processes occurring in the stopping process of electrons or noble gas atoms/ions have to be discussed.

When a charged particle moves through liquid xenon it can undergo two different types of interaction: Inelastic Coulomb interaction or elastic atomic recoils. The term “inelastic Coulomb interactions” means interactions with shell electrons of the noble gas atoms. They are inelastic, because those interactions lead to excited and ionized atoms. In the case of ionization, the knocked-off electron is a so-called δ -ray, secondary electron radiation. Those δ -rays also move through the liquid and will eventually be stopped. Inelastic Coulomb interactions are dominant for electrons, but occur for fast ions too [Hit05].

With the term “elastic atomic recoils” interactions with complete noble gas atoms is meant here. In this case kinetic energy from the moving charged particle (typical for alpha particles and heavier ions) is transferred to atomic motion of the scatter-target atom.

With a combination of those two interaction types ultimately the complete kinetic energy of the primary charged particle will be transferred into excitation, ionization and thermal atomic movement. The part of energy going into excitation E_{ex} and ionization E_{ion} can be observed, whereas the thermal atomic movement E_{thermal} is lost for observation.

As primary heavy particles (alphas, heavier ions) transfer significant amounts of energy via elastic atomic recoils, the observable fraction of their original energy E_{tot} is considerably smaller compared to that of primary electrons, which are dominantly interacting by inelastic Coulomb scattering. This effect is called “nuclear quenching” and can be stated as:

$$q_{\text{nc}} = (E_{\text{ex}} + E_{\text{ion}}) / E_{\text{tot}}$$

In addition to this difference in total observable energy for different primary particles, the ratio of ionization to excitation is different too, due to the different probabilities of elastic atomic scattering and inelastic Coulomb interactions. This effect is used by dual-phase xenon TPCs for particle identification, as electronic recoils from external gammas lead to primary moving electrons, whereas nuclear recoils from external neutrons (and WIMPs) lead to primary moving xenon ions. This is shown in the previous chapter 2.2.

3.1.1. Typical time constants

Here, a more detailed description of the atomic and nuclear states that lead to scintillation will be given, as these processes and the involved time scales define the scintillation light shape. We may start the description at the point, where the primary moving charged particle and all secondaries are thermalized, as this happens within picoseconds. That means, we have a track of excited atoms Xe^* (called excitons), ionized atoms Xe^+ and a cloud of free electrons.

3.1. SCINTILLATION MECHANISM

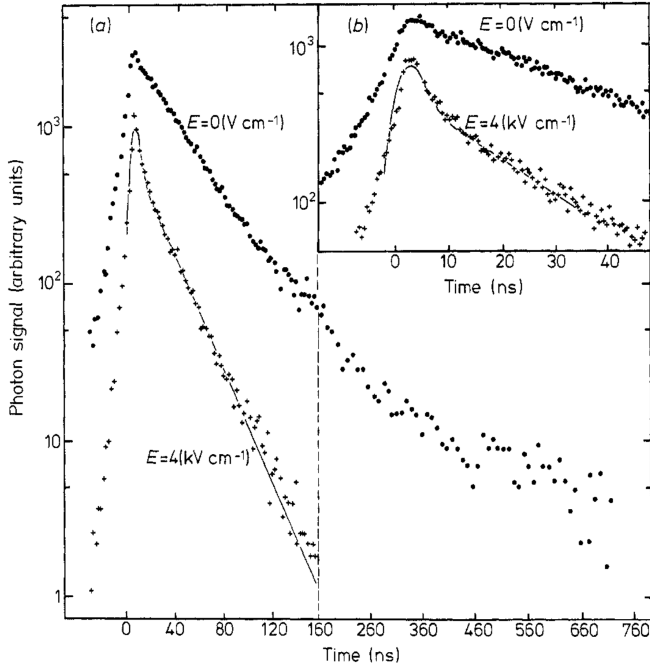


Figure 3.1. Time dependence of the luminescence intensity for liquid xenon with and without an applied electric field. The long time range (a) and the short time range (b) are indicated. Note the change of the time scale at 160 ns in (a). The solid lines represent fitted lifetime curves. (Taken from [KHR78])

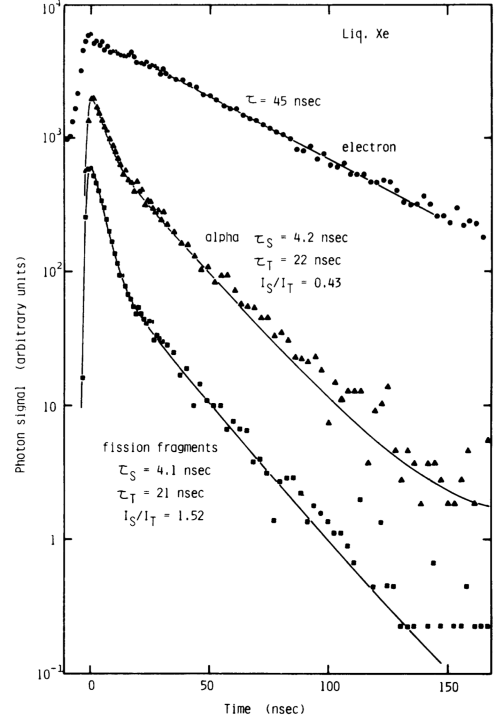


Figure 3.2. Decay curves obtained for the luminescence from liquid xenon excited by electrons (●), α particles (▲), and fission fragments (■). (Taken from [HTF⁺83])

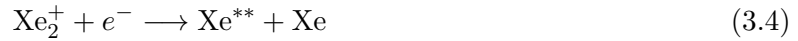
Let's first discuss what happens with excitons: They will combine with a neighboring neutral xenon atom and form a so-called excimer, an excited xenon molecule Xe_2^* . The two lowest state excimers are the singlet $^1\Sigma^+$ and triplet $^3\Sigma^+$. Both excimer states scintillate in the vacuum ultra violet (VUV) region and go to the repulsive ground state excimer $^1\Sigma_g^+$. This process can be written as:



Although, in liquid xenon the transitions of singlet and triplet excimer scintillation light cannot be distinguished by their spectrum, the typical lifetimes of the two states $\tau_{\text{singlet}} = 2.2 \pm 0.3$ ns and $\tau_{\text{triplet}} = 27 \pm 1$ ns are different as shown in figure 3.1 from [KHR78] using an electron source and confirmed by later measurements.

Now we need to discuss what happens with the xenon ions and free electrons, in the stopping path of the primary charged particle. The xenon ions can, together with neutral xenon atoms, form ionized xenon molecules Xe_2^+ . Those can, in the absence of an externally applied drift field

(unlike in dual-phase TPCs) recombine with free electrons. This recombination will lead to excited xenon atoms (excitons) and if those combine with neutral xenon atoms to excimers in singlet and triplet state too. This recombination process can be written as:



Of course, in dual-phase TPCs and in any other detector where an external field is applied, the recombination process is suppressed. It was shown [KHSR79] that for a field strength of 2 kV/cm and higher charge collection is complete for electronic recoils, i.e. no recombination occurs. If recombination is not completely suppressed, the scintillation signal shape will include another characteristic time, the recombination time τ_r . As the overall scintillation yield is suppressed by more than factor 2 in the case of complete charge readout (70% for electrons in xenon [KHR78]), the time-scale of recombination plays an important role for the overall scintillation shape in the case of a weak or no field. Without field, they find a scintillation signal shape which can be well described with only one time constant of 34 ns (figure 3.1). The above mentioned decay time constants τ_{singlet} and τ_{triplet} have been measured at a field of 4 kV/cm (i.e. complete charge collection and fully suppressed recombination). This assures that the time constants are really the life times of the excimers and not influenced by the recombination time scale.

The Kubota group later tried to find a description for the recombination process [KHSR79] and measured the time constant at zero field using the difference of the shape between measurements with field and without field. They find $\tau_r = 15$ ns for xenon. They also derive a recombination cross-section $\sigma_r = 10 \pm 2 \cdot 10^{-16}$ cm² from the recombination time constant.

As recombination depends also on the density of noble gas ions and electrons, studies using alpha particles instead of electrons to generate the scintillation were done by the same group. In [KSR80] they find that alpha particles even without field show two time constants of $\tau_{\text{singlet}} = 4$ ns and $\tau_{\text{triplet}} = 27$ ns. Due to the fact that these results are similar to the results for electrons with applied field, they conclude that the recombination time is significantly shorter than τ_{singlet} , which is expected due to the high ionization density the initial alpha particle generates. In an later investigation [KHSzR82] with solid and liquid noble gases, they find a temperature dependency of the decay constants, and for electrons a very slow decay that extends up to 2 μ s, which was not observed for alpha particles or for electrons with an applied field.

3.1. SCINTILLATION MECHANISM

The results on the decay time constants τ_{singlet} and τ_{triplet} found by the Kubota group could be confirmed by Hitachi in a measurement with alpha particles and fission fragments without drift field [HTF⁺83]. However, they find a longer time constant to describe the scintillation signal produced by electrons of $\tau = 45$ ns as compared to $\tau_{\text{Kubota1978}} = 34$ ns, as shown in figure 3.2.

The experiments from Kubota and Hitachi used radioactive sources immersed in the liquid noble gases. For Kubotas experiments a ^{207}Bi source provided conversion electrons with energies between 0.48 MeV and 1.05 MeV and the alpha particles used in their measurements were generated by a ^{210}Po source, which means the alphas had an energy of 5.305 MeV. Hitachi used a ^{207}Bi source for the electrons, and a ^{210}Po source for alphas too. Additionally they used $^{212}\text{Bi}(\text{ThC})$, ^{252}Cf and $^{212}\text{Po}(\text{ThC})$ as alpha sources with energies of 6.051 MeV, 6.12 MeV and 8.785 MeV. The fission fragments also originated from the ^{252}Cf source and have energies of 80.3 MeV and 106.2 MeV. Overall, this means that the measurements have been done with rather high total energy deposits, compared to what one obtains from gammas, neutrons or WIMPs scattering off xenon nuclei, where only some keV are transferred.

In 2002 a measurement of low energy recoils (below 100 keV) was published [Aki02]. They used neutrons of 2.85 MeV and had them scatter in a liquid xenon detector without applied drift field, depositing energies between 40 and 70 keV. Due to the nuclear quenching this corresponds to 6 to 30 keV equivalent energies of electronic recoils from gammas. As a comparison they used electronic recoils in this equivalent energy range from a ^{57}Co source. They find, that electronic recoil events as well as neutron recoil events can be well described using a single exponential decay, although they state that for nuclear recoils a double exponential fit is slightly better. They also state that for electronic recoils the decay time is energy dependent, while this is not the case for nuclear recoils. The values obtained are stated together with previous results in table 3.1.

Another newer measurement, which also includes measurements at higher fields up to 3.7 kV/cm is shown in [DHA⁺05]. They use energy deposits between 100 keV and 1 MeV for electronic recoils from ^{60}Co and 50 to 400 keV for alpha particles, which is the lower tail of a ^{241}Am source. To measure the characteristic time, they do not fit the signals, but instead measure the charge and the amplitude of each pulse and calculate the characteristic time as $\tau = Q/U_{\text{max}}$. This corresponds to a single exponential decay with decay constant τ , if the signal rise is infinitely fast and any shaping from PMT and electronics is neglected. Their results are shown in figure 3.3. For alpha particles, $\tau_{\alpha} = 15$ ns does not change with increasing drift field. As only one decay constant is used to describe the shape here, it cannot easily be compared with the previous results. Nevertheless it is not unreasonable to assume it might agree with the Kubota and Hitachi measurements as the stated 15 ns are between the short τ_{singlet} values in the order of some ns and the long τ_{triplet} in the range of 22 ns. For electronic recoils, the value of the decay time constant changes from $\tau_{\text{ER}}(0 \text{ kV/cm}) = 46.1 \pm 0.1$ ns without field over $\tau_{\text{ER}}(0.5 \text{ kV/cm}) = 25.2 \pm 0.1$ ns at 0.5 kV/cm to $\tau_{\text{ER}}(3.7 \text{ kV/cm}) = 22.6 \pm 0.1$ ns for the strongest drift field. For zero field it is in good agreement

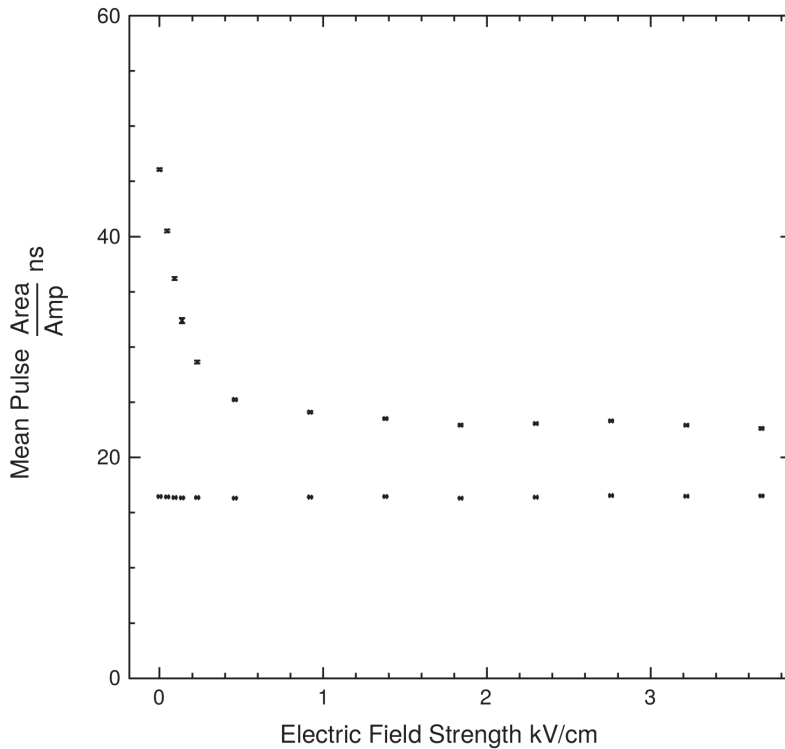


Figure 3.3. Variation of pulse area to amplitude ratio with applied electric field for source alphas and gammas from an external ^{60}Co source. The alphas (lower points) show no change with increasing electric field. The gamma rays (upper points) decrease rapidly with increasing electric field from $46.1 \pm 0.1\text{ns}$ with no electric field to $22.6 \pm 0.1\text{ns}$ at 3.7 kV/cm . (Taken from [DHA⁺05])

with the result obtained by Hitachi. For the strong field, the result is significantly shorter than the result from Kubota (27 ns), but agrees with the results for τ_{triplet} of alpha particles and fission fragments as obtained by Hitachi and Kubota.

Summarizing the current state of knowledge on the time constants involved in liquid xenon scintillation, one can state that the measurements by Kubota and Hitachi had a focus on understanding the underlying principles of the scintillation process and have been exploring different particle types [KSR80], [KHSzR82], [HTF⁺83], the influence of a drift field [KHR78],[KHSR79] and even the state (solid, liquid) and different temperatures [KHSzR82] in a systematic way for xenon, argon and krypton. As a result they provide singlet and triplet decay constants and a description of the recombination process for the track of relativistic electrons in the absence of a drift field [KHSR79]. For their investigations they relied on high energy deposits in the range of MeV and the lower performance of electronics and especially PMTs at that time, that required the use of a wavelength shifter (POPOP), which, although relatively fast ($\tau_{\text{POPOP}}(\text{FWHM}) = 1.8\text{ ns}$), introduces another time constant.

The newer measurement [Aki02] explores the low energy range (40-70 keV), but only investigates the pulse shape at zero field. The latest measurement [DHA⁺05] suffers from not separating multiple

3.2. PULSE SHAPE DISCRIMINATION

particle	E [kV/cm]	τ_{singlet} [ns]	τ_{triplet} [ns]	Reference
e^- (^{207}Bi)	0		34 ± 2	[KHR78]
e^- (^{207}Bi)	4.0	2.2 ± 0.3	27 ± 1	[KHR78]
α (^{210}Po)	3.0	4	27	[KSR80]
e^- (^{207}Bi)	0		33 ± 1	[KHSzR82]
α (^{210}Po)	0	3	22	[KHSzR82]
e^- (^{207}Bi)	0		45	[HTF ⁺ 83]
α (^{210}Po , ^{252}Cf)	0	4.3 ± 0.6	22 ± 1.5 ¹	[HTF ⁺ 83]
fission fragments (^{252}Cf)	0	4.3 ± 0.5	22 ± 2	[HTF ⁺ 83]
electronic recoils (13.5 keV)	0		29.1 ± 0.6 ²	[Aki02]
electronic recoils (37.5 keV)	0		34.0 ± 0.6 ²	[Aki02]
nuclear recoils (6 – 30 keV _{ee})	0	11.3 ± 4.1	28.9 ± 5.3 ³	[Aki02]
α (50-500 keV)	0 - 3.7		15 ⁴	[DHA ⁺ 05]
e^- (0.1-1 MeV)	0		46.1 ± 0.1 ⁴	[DHA ⁺ 05]
e^- (0.1-1 MeV)	0.5		25.2 ± 0.1 ⁴	[DHA ⁺ 05]
e^- (0.1-1 MeV)	3.7		22.6 ± 0.1 ⁴	[DHA ⁺ 05]

¹ non exponential decay

² only one exponential decay used

³ $\chi^2/\text{dof} = 1.117$; using one decay $\tau = 21.5 \pm 0.76$ ns ($\chi^2/\text{dof} = 1.386$)

⁴ only one time constant $\tau = \text{area}/\text{amplitude}$ used

Table 3.1. Summary of previous measurements of the scintillation decay times of liquid xenon.

decay time constants and is therefore to be seen as an approach to investigate a technique for pulse shape discrimination for practical application, rather than a more fundamental attempt to improve the knowledge of the scintillation and recombination mechanisms.

3.2. Pulse Shape discrimination

The measurements [HTF⁺83], [KHR78], [KHSzR82] show, that the pulse shape of the scintillation light is different for different incident particles and depends on the applied field. This could provide an additional way for background discrimination in dark matter detectors. Here we will have to distinguish nuclear recoils from electronic recoils.

Electronic recoils, like a gamma scattering off a shell electron of an xenon atom, will ionize the atom and transfer additional energy to the electron. The electron will than be stopped in the liquid. The pulse shape therefore should be the same as measured for electrons.

WIMPs and neutrons will interact with the nucleus of a xenon atom. It will transfer energy to the nucleus, which is ionized, as it is kicked away from its weakly bound electron(s) from the outer shell(s). That said, it is clear, that the stopping process of the xenon ion in the surrounding liquid is similar to that of alpha particles or fission fragments and the pulse shape equivalently.

Therefore, pulse shape discrimination is a promising complementary method for background

discrimination in liquid xenon TPCs. However, due to the fast time constants and the resulting requirements to electronics and light detectors, no extensive and systematic measurements of the scintillation pulse shape and its dependency on the energy deposit, the interaction type and the applied drift field have been done. The MainzTPC, which will be described in chapter 4, is build with the purpose to do this.

As the scintillation time constants involved are rather short, light detectors and flash analog-to-digital-converters (FADCs) have to be fast to allow the use of pulse shape discrimination. An additional difficulty in the rather big dark matter detectors (Xenon1T: 1 m, successors will be larger), is the time that photons need to reach the PMTs and especially the time-spread between the photons. The larger the detector, the larger the time-spread might be, due to reflections on the liquid gas interface and the Polytetrafluoroethylene (PTFE) walls. Assuming that the average difference of the length of the path a photon has to cover is in the order of the size of the detector, and using the dielectric constant of liquid xenon $\epsilon_{\text{LXe}} = 1.96$. One obtains a time-spread of

$$\overline{\Delta t} = \frac{l \cdot \epsilon_{\text{LXe}}}{c} = \frac{1 \text{ m} \cdot 1.96}{2.99 \cdot 10^8 \text{ m/s}} = 6.55 \text{ ns}$$

This is already larger than the decay time of singlet excimers. Therefore, the usability of pulse-shape discrimination in large scale detectors will have to be studied by detailed simulations for different geometries and read-out systems.

4. Experimental Setup

The design and construction of the experiment, especially the detector itself, constitutes the main part of this thesis. The design of the TPC was the principal focus, but also the design of the cryogenic infrastructure – cooling chamber with the pulse-tube refrigerator (PTR) and cryostats. In parallel to the doctoral thesis, several diploma and bachelor theses delivered input for the design or provided required infrastructure. The gas-system was designed and built in [Hil14], the collimator and the rotation-table for the Germanium detector originate from [Sch13]. Input for the design of the TPC was provided from simulations done in [Sis12]. Input from [Mor12] and [Jen12] helped to understand the APDs and PMTs respectively. The slow-control system (SCS) programmed in [Kja12] was used extensively to monitor the thermodynamics of the system and delivered useful input in understanding some difficulties with the liquid level.

This chapter gives an overview of the detector design, including simulations on the drift field and descriptions of two methods to set the liquid level in section 4.1. The following section 4.2 describes the issues that occurred with the liquid level in various setups, the attempts to stabilize the level and describes the state, that could finally be reached and reproduced. An idea for future improvement is given too. In section 4.3 the required cryogenic and gas-handling infrastructure is described, and the SCS we used to monitor the system is discussed in 4.4. After the description of the photo-sensors and electronics used for the data acquisition system (DAQ) in section 4.5, the experimental setup for a Compton scattering setup in the laboratory in Mainz is shown (section 4.6). An description of the neutron scattering setup, including the neutron source Neutron TOF experiments at ELBE (nELBE), the energy deposits of neutrons in liquid xenon and the measurement methods can be found in section 4.7. The trigger setup including a discussion of possible background triggers can be found in the same section.

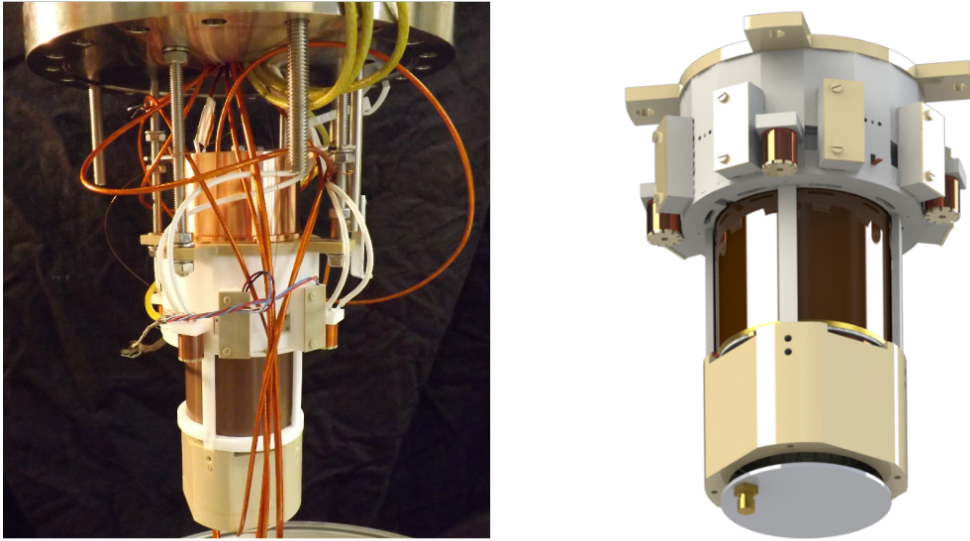


Figure 4.1. On the left a picture of the MainzTPC taken during the mounting process. On the right a rendered view from the CAD drawings.

4.1. The MainzTPC

4.1.1. Design Goals

While designing the MainzTPC, it was important to optimize it for the physics requirements and goals, while keeping mechanical and technical limitations in mind. From the physics side, the MainzTPC is optimized for a Compton scattering experiment to measure recoil energies in liquid xenon down to 1 keV. That means:

- small size
- little passive material
- high light collection efficiency (LCE)
- uniform drift and extraction fields

Small Size

The size has to be small, to minimize multiple scattering of single incoming γ 's. The plan was to use ^{137}Cs for the Compton scattering experiment and use ^{60}Co to crosscheck the results. The reason for the use of ^{137}Cs is, that the energy of the γ 's is with 662 keV small enough, to provide larger scattering angles, even when depositing only small amounts of energy in liquid xenon (compare

table 4.1). Still the energy is high enough to penetrate the walls of the cryostat and TPC vessel and the passive xenon surrounding the TPC. Due to the good energy resolution of germanium detectors, it is also possible to measure energy deposits of 1 keV accurately for those source energies.

energy deposit in TPC [keV]	source isotope		
	^{22}Na	^{137}Cs	^{60}Co
2	5.08°	3.92°	2.21°
10	11.47°	8.83°	4.96°
20	16.41°	12.60°	7.05°
50	26.93°	20.47°	11.30°

Table 4.1. Relation between energy deposits for Compton scatters in liquid xenon and the scatter angles. The lower the energy deposit, the lower the scattering angle. The lower the source energy, the higher is the scattering angle, for a given energy deposit. This illustrates, why smaller source energies are preferred, when interested in low-energy recoils. Higher scattering angles are an advantage, because the germanium detector does not have to be in the beam, to measure the scattered γ s and therefore chance coincidences are significantly reduced. The table is taken and modified from [Sis12].

Little Passive Material

The main reason for keeping the amounts of passive material small is to keep data samples clean, i.e. to avoid scattering of γ 's in passive materials. First, the probability of γ 's scattering in passive materials before entering the TPC should be kept small, that is, why the walls of the cryostat and of the TPC-vessel are kept as thin as possible. Also the thickness of the liquid xenon surrounding the active volume of the TPC and the thickness of the PTFE-cylinder around the active volume were kept small. This way, the probability for 662 keV- γ -rays to enter the active volume without losing energy before is kept as high as possible.

For the same reason, it is unlikely, that γ 's that scattered inside the active volume will lose additional energy before being detected by the Germanium detector. Also much less important, but still not negligible are passive materials that are neither on the direct path from γ -source to active volume of the TPC, nor in the path from TPC to the germanium detector. Having large amounts of passive materials close to the TPC could lead to registering events, that first scatter in the TPC and afterwards scatter on some surrounding material into the direction of the germanium crystal.

Light Collection Efficiency

The LCE is defining energy threshold and energy resolution of a scintillation detector. In case of a dual-phase TPC, the energy resolution is given by a combination of charge collection efficiency (QCE) and LCE. Regarding the threshold it depends on the trigger setup. When triggering on S1, the threshold is still given by LCE only. When triggering on S2, QCE is defining the threshold. In our

case, we decided to trigger on S1, as this allowed to record the scintillation pulse shape on the fast digitizer.

Uniformity of Fields

The uniformity of the drift field is important for the reconstruction of the z-position and the x/y-position of a recoil. As described in chapter 2.2, the depth of an interaction is reconstructed from the time difference between S1 and S2. The time difference is given by the drift path of the electrons, whereas the drift velocity is given by the field strength. Therefore it is obvious that non-uniformities in the field can lead to (x/y/z)-position dependency of the electron drift time. This effect can be compensated partly by measuring it, but it is simpler and more effective to just avoid it.

Technical and Mechanical Aspects

From the technical side, the following aspects generally had to be considered for the design:

- ultra-high vacuum (UHV) compatibility of materials
- usability at liquid xenon temperature
- different thermal expansion coefficients
- mechanical stability
- feasibility
- high-voltage (HV) suitable design

To match all these technical requirements, without compromising the physics properties of the detector was overall challenging and lead to a long design phase of the detector. The restriction of using UHV suitable materials only required special cables and the use of metals, wherever possible. Metals automatically bring the advantage of being mechanically relatively strong, on the other hand, they are electrically conductive and do not reflect the VUV scintillation light. The conductivity disfavors metals to be used close to the components providing the drift field, because the high-voltage applied, might lead to unwanted sparking to metallic structures. Therefore the structures surrounding the meshes, field-shaping printed circuit board (PCB), the APDs and PMTs have to be made from plastics. The poor reflection properties for VUV light also forbid the use of metal for the inner surfaces of the detector, as this would lead to a worse LCE. PTFE is here the material of choice, due to the very good reflection properties also for liquid xenon scintillation light. PTFE on the other hand is a very soft material, and shrinks significantly when cooled to liquid xenon temperatures ($\approx 1 - 2\%$). This must be kept in mind when combining different materials.

As a last important constraint, the feasibility had to be kept in mind. The softness of PTFE makes it difficult to produce fine structures and to produce complex parts with high accuracy.

4.1.2. Simulations – uniformity of drift field

The drift and extraction field of a dual-phase TPC is generated by a set of meshes and formed by a field cage, as described in chapter 2.2. To optimize the drift and extraction field for the MainzTPC, finite-element method (FEM) simulations have been done, using COMSOL [COM17]. Generally, FEM simulations are computationally expensive, especially when simulating small structures (wire-diameter of mesh: $14\ \mu\text{m}$) in large geometries (TPC diameter: 50mm). To keep computing efforts acceptable only a simplified version of the TPC has been simulated. The field cage of the MainzTPC, for the same reason, has not been simulated in 3D, but in a 2D-axisymmetrical geometry as shown in figure 4.2. For the field shaping rings (PCB) this is the truth, except at the line where the resistor chain is soldered, but for the mesh, which has a square-shaped lattice in reality, it is just an approximation.

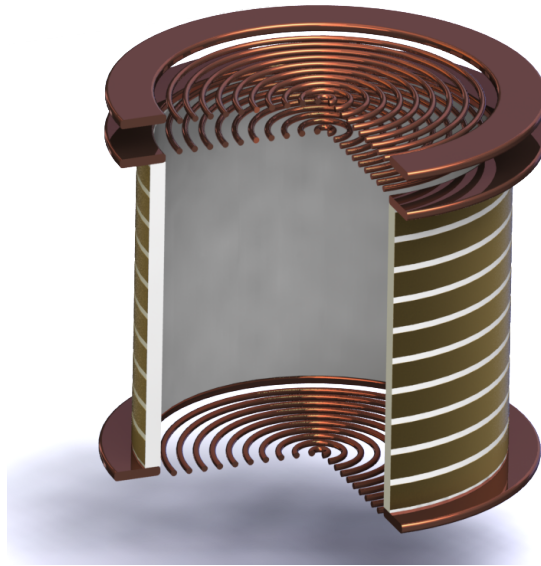


Figure 4.2. Illustration of the 2D-axisymmetrical geometry simulated with COMSOL Multiphysics. For better visualization, shield meshes have been left out in this picture. Pitch and wire diameter of the meshes (copper) and pitch and width of the field shaping rings (gold) are much larger in this graphic than the final design.

The simulations helped comparing various designs of the meshes and the field cage and compare them at different values of the drift field. Additionally the simulations allowed to study different configurations for the field, either with the gate mesh or the anode mesh on ground potential. In case of having the anode mesh on ground potential, it is also possible to get rid of the top-shield

mesh, as the anode already screens the upper PMT from the extraction field. This option was also investigated.

The drift field is generated by two meshes, the cathode mesh at the bottom of the active volume and the gate mesh just below the liquid gas interface on top of the active volume. To keep the field cylindric, i.e. avoid barrel-shaped distortion, the active volume has to be surrounded by field shaping rings. This way, the active volume is fully enclosed in the field cage. For the large Dark Matter detectors (XENON100 [Ae12], XENON1T [Ae17] [Ae16], LUX [Ake13]) it is easily possible to implement the field-shaping rings as full copper rings. As we wanted to keep passive materials as little as possible, we decided to use a flexible PCB for the field shaping. The FEM simulations helped to understand the influence of using different pitch and width of the field-shaping rings on the PCB and visualize the remaining distortion of the field.

In addition to different PCB geometries, meshes of different pitch and wire diameter have been simulated too, to find a good trade-off between high transparency and little field leakage. The larger the pitch of the meshes, the stronger is the field leakage through the mesh, which means, that the uniformity of the field is compromised. Field leakage can lead to a position dependent strength of the drift field ($|E|$) as well as a non-zero radial component of the field. Both are effects that are undesired, as it will make position reconstruction more difficult and less accurate.

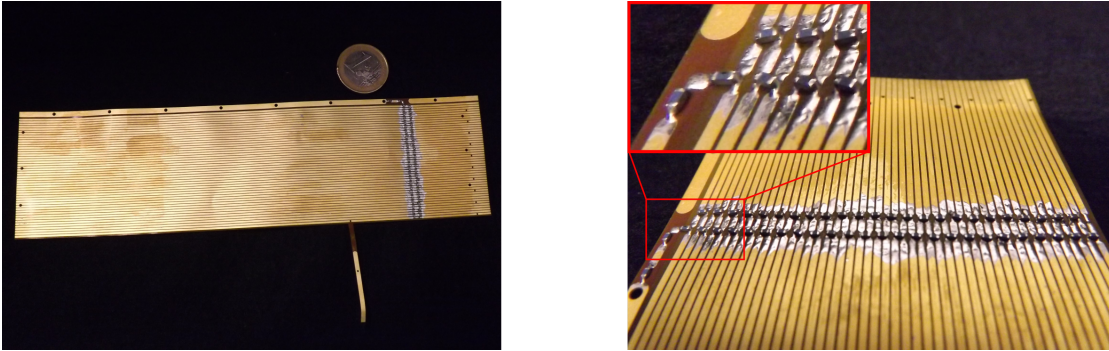


Figure 4.3. The flexible printed circuit board serving as field cage. The pitch of two neighboring strips is 1 mm, the width of one strip is 0.8 mm. The SMD resistors ($100\text{ M}\Omega$) are soldered and can be seen in the close-up. For mounting the PCB it is wrapped around a PTFE cylinder surrounding the active volume of the TPC. [Gro17]

The final decision was, to use meshes provided by PRECISION EFORMING LLC [Pre17]. The meshes are of type MC-20, made of nickel and have a pitch of $268\text{ }\mu\text{m}$ and wire diameter of $14\text{ }\mu\text{m}$, which results in a transparency of 88 %. The field shaping PCB (figure 4.3), provides 50 field-shaping rings, each 0.8 mm wide with a pitch of 1 mm. To provide the proper potential to each of the rings, they are connected via an SMD-resistor chain. The resistance value separating two neighboring rings is $100\text{ M}\Omega$. The lowest ring is also separated via $100\text{ M}\Omega$ from the cathode and the uppermost ring is separated by $200\text{ M}\Omega$ from the gate. The higher separation between uppermost ring and gate mesh was induced as a result of the simulations.

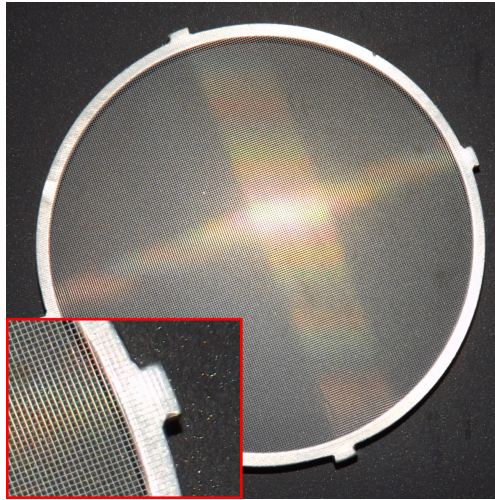


Figure 4.4. A mesh produced and bonded by PRECISION EFORMING LLC. with a transparency of 88%, wire diameter of $14\ \mu\text{m}$ and pitch of $268\ \mu\text{m}$. Here bonded to the frame for the cathode. The frames for anode mesh, gate mesh and bottom-shield mesh are shaped differently, the type of mesh (MC-20) is the same.[Gro17]

In figure 4.5 the different simulated configurations for the potential distribution are illustrated. **Configuration 1** uses five meshes in total, in addition to the meshes generating drift and extraction field (cathode, gate and anode), both PMTs are screened by an additional screening mesh (top and bottom shield mesh). In this configuration the gate mesh is kept on ground potential. To reach the design drift and extraction field, the cathode mesh has to be at $-15\ \text{kV}$ and the gate mesh at $+5\ \text{kV}$. This configuration has several advantages: the highest voltage used is $-15\ \text{kV}$, which is only 75% of what is required for configurations 2-4, and therefore is a bit easier to achieve. Additionally, as the two power-supplies generating drift and extraction field are not cascaded in this configuration, both operate independently and the current has the direction intended by the manufacturer. The major concern for this configuration is, that the anode is on positive HV ($+5\ \text{kV}$). Although much lower than the cathode potential, it could have lead to more difficulties, as the anode mesh is not immersed in liquid but in gaseous xenon of lower dielectric strength, compared to the liquid. Additionally, it is surrounded by the APDs and therefore the edge of the mesh can't be enclosed in PTFE or polyether ether ketone (PEEK) to prevent sparking without significantly reducing the field of view of the APDs. A minor disadvantage is the required additional shield mesh in front of the topPMT, which reduces the amount of light collected by the topPMT. This concern is minor, because the shield mesh could have a much higher pitch (and higher transparency), as field uniformity above the anode is not so much of a concern.

Configurations 2-4 are similar. In those configurations, the top-shield mesh is left out, cathode and gate are both on negative potential. The anode is only on a relatively weak ($500\ \text{V}$) or ground potential, and therefore HV break-throughs in the xenon-gas are no concern. The difference between the three configurations, is the field above the anode. **Configuration 2**, provides zero

field between anode and topPMT. **Configuration 3 and 4** provide a field with inverted direction (compared to drift and extraction field), to make sure, electrons passing the anode or being created above the anode do not accumulate there or reach the topPMT. In configuration 3 this is achieved by having positive voltage on the anode, in configuration 4 this is achieved by having the photo-cathode of the topPMT at negative voltage.

Mechanically, configurations 2-4 are identical. It is simple to switch between configuration 2 and 3 without any hardware modifications, just by connecting a power supply to the anode instead of grounding it. To switch to configuration 4, the voltage divider of the topPMT has to be adapted, which is foreseen in the design, but of course cannot be changed during detector operation.

	configuration 1	configuration 2	configuration 3	configuration 4
top shield mesh	$U = 0 \text{ V}$	$U = 0 \text{ V}$ PMT	$U = 0 \text{ V}$ PMT	$U = -1 \text{ kV}$ PMT
anode mesh	$U = +5 \text{ kV}$	$U = 0 \text{ V}$	$U = +500 \text{ V}$	$U = 0 \text{ V}$
liquid-gas-interface				
gate mesh	$U = 0 \text{ V}$	$U = -5 \text{ kV}$	$U = -4.5 \text{ kV}$	$U = -5 \text{ kV}$
cathode mesh	$U = -15 \text{ kV}$	$U = -20 \text{ kV}$	$U = -19.5 \text{ kV}$	$U = -20 \text{ kV}$
bottom shield mesh	$U = 0 \text{ V}$	$U = 0 \text{ V}$	$U = 0 \text{ V}$	$U = 0 \text{ V}$

Figure 4.5. The field has been simulated for the different potential distributions, schematically shown here. Configuration 1 is the classical configuration. Configurations 2-4 provide higher light collection efficiency as the top-shield mesh is left out. In configuration 4 the topPMT is biased with negative HV.

The configuration finally used was configuration 2. With this configuration and the meshes and PCB designed as described above, the drift field shows good uniformity, except in the outer corners. At $z=0 \text{ mm}$ is the cathode mesh and at $z=50 \text{ mm}$ the gate mesh. The color scale in figure 4.6 for the vertical component and absolute value of the field is chosen to be design value (3 kV/cm) $\pm 1\%$. For the radial component it is $0 \text{ kV} \pm 50 \text{ V/cm}$. It is clearly visible, that for the maximum design drift field, the field is uniform within 1% almost everywhere. Using fiducialization events close to the walls and in the corners will anyway be cut to avoid edge effects which occur for the scintillation light of those events.

4.1.3. Technical Design

The MainzTPC is mounted with 4 threaded rods on a plate made of PEEK. The plate closes off and therefore fixes the topPMT inside the upper APD holder, a structure made of PTFE. This has a relatively complex shape, with gaps for the APDs. It covers the outermost part of the front

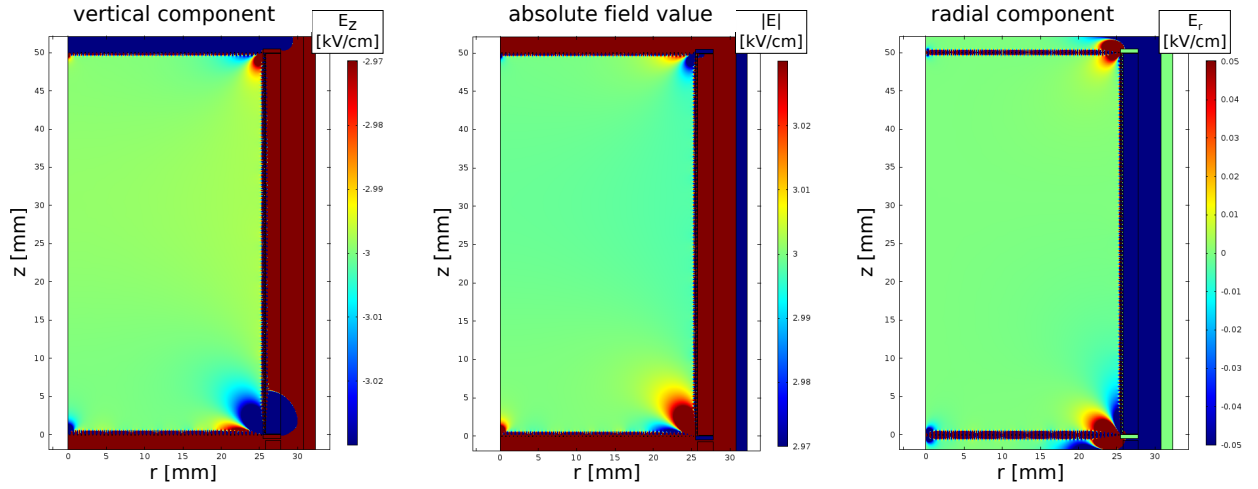


Figure 4.6. From left to right: vertical component, absolute value and radial component of the drift field for the maximum design value of 3 kV/cm. The cathode is at $z=0$ mm, the gate at $z=50$ mm. The field is very uniform with this configuration. Only in the outermost corners ($r \approx 25$ mm) uniformities are above 1%.

surface of the topPMT, just leaving the diameter of its photo-cathode open. It reaches down to the anode mesh. At the anode mesh, the lower APD ring starts. This ring supports the APDs on the backside and small blocks to prevent the APDs from moving inwards. Between the APDs, these two parts have triangles, holding the meshes and separating the view of the APDs. Figure 4.8 illustrates the complexity of these two parts. Here one can also see the frames of gate and anode. The frames of those two meshes are only 0.5 mm thick, and have an outer diameter of 63 mm and an inner diameter of 55 mm. They are kept thin to avoid covering too much of the APDs field of view for S2 signals.

Just below the lower APD ring, there is the gate mesh. The gate mesh is held in place by the column carrier. This part consists of a ring, which also holds the APDs from the bottom. The ring has four rectangular pillars (visible in figure 4.1), which connect the upper part of the TPC with the bottomPMT holder. The bottomPMT holder is made of PEEK. It has a cylindric shape, but is flattened on 4 sides, to allow liquid xenon to flow by.

Between the four pillars, the active volume is surrounded by a cylinder made of PTFE. The field-shaping PCB is wrapped around this cylinder, and connected to the cathode on the bottom via an M1 screw. Below the cathode there is a spacer ring, which separates cathode and bottom shield mesh by 1 mm of PTFE. This spacer covers the outer parts of the front surface of the bottomPMT too, reflecting photons that would otherwise be absorbed undetected. To prevent sparks from the cathode to the TPC vessel, another PTFE ring is installed surrounding the whole cathode. This ring's second function is to prevent liquid xenon from flowing past the active volume, instead of flowing through it. The holder of the bottomPMT has four openings just below the shield mesh, to allow the liquid xenon to enter the active volume (figure 4.9).

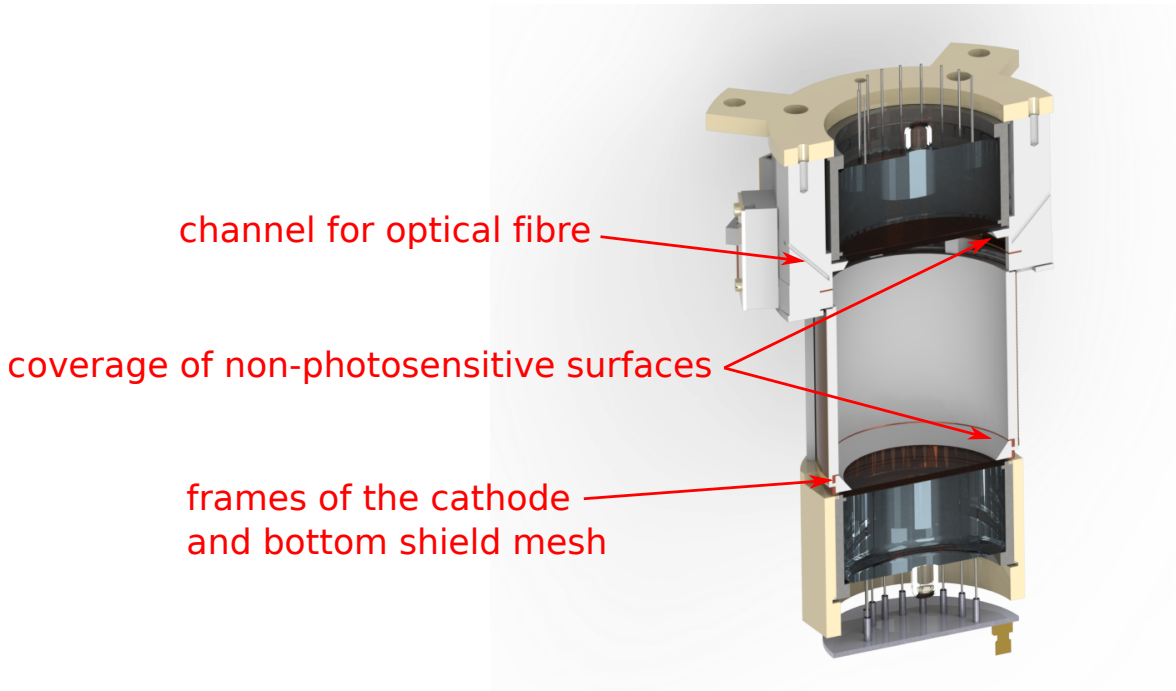


Figure 4.7. Cut view through the MainzTPC. This view shows clearly, that almost all surfaces are either photo-sensitive or reflective (PTFE, white).

4.1.4. Leveling solutions and levelmeters

Being able to set the liquid level accurately, keep it stable and monitor its stability is crucial for optimum charge readout of a dual-phase TPC. In this section the levelmeters are described and the technical details of the two leveling solutions that were used are introduced. Both solutions are based on a spillway, that can be moved up- and down using a precision linear feed-through. The difference between the two implementations of the spillway is the use of a flexible bellow (Leveling solution 1) or of tubes with a tight clearance fit (Leveling solution 2). We used a linear feed-through from accuglass-products (Model HTL-133-1, [Acc17]), which has a resolution of 0.001 inch and allows linear movement of up to 1 inch. Both solutions did not provide stable levels when first used. For reasons not yet understood the fluctuations of the levels were gone in the last measurement. The fluctuations are discussed in 4.2.

4.1.4.1. Leveling Solution 1: Bellow

The bellow version (figure 4.10) was first favored, because it does not have any leakage as opposed to the clearance fit. Its disadvantage is that it can't be moved upwards (except by it's own spring constant) and the free path of this bellow is limited. Still, the free path was designed to be

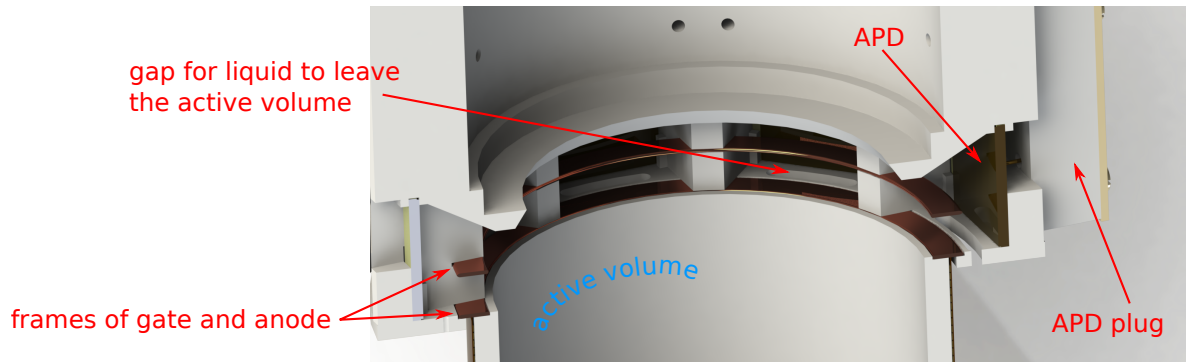


Figure 4.8. Detailed view of the upper region of the MainzTPC. The topPMT is hidden, to provide a better view on the frames of gate and anode. One can also see the complex structure of the PTFE parts, which hold the meshes in place and provide gaps for the APDs.

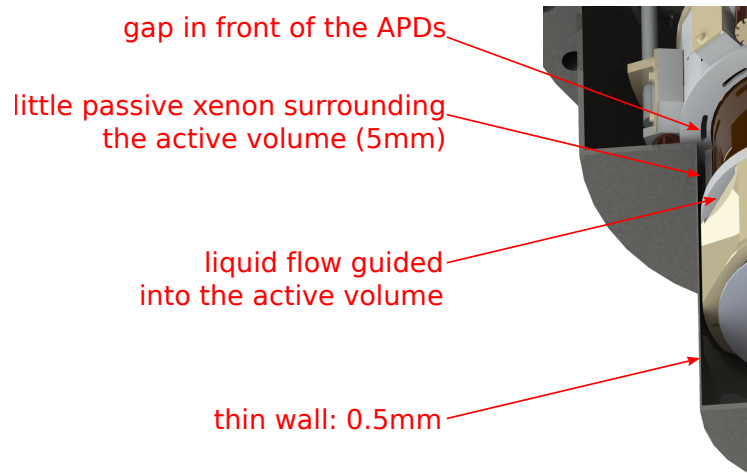


Figure 4.9. Thin walls of the vessel and narrow construction lead to a minimal amount of passive material surrounding the active volume.

5 mm without elongating the bellow from its normal length, i.e. just compressing it. A further disadvantage may be dead volumes around the bellow, which might contain impure liquid xenon.

This solution was not kept, mainly because we thought it was responsible for the oscillating and unstable liquid levels due to the relatively small gaps on the sides, which are only 2 mm wide. Surface tension preventing a continuous flow as well as too small cross-section of the gaps to allow the planned flow of liquid xenon were considered to be the reason for the liquid level issues. Modifications of this leveling solution without replacing it completely were not possible because of the fragile bellow.

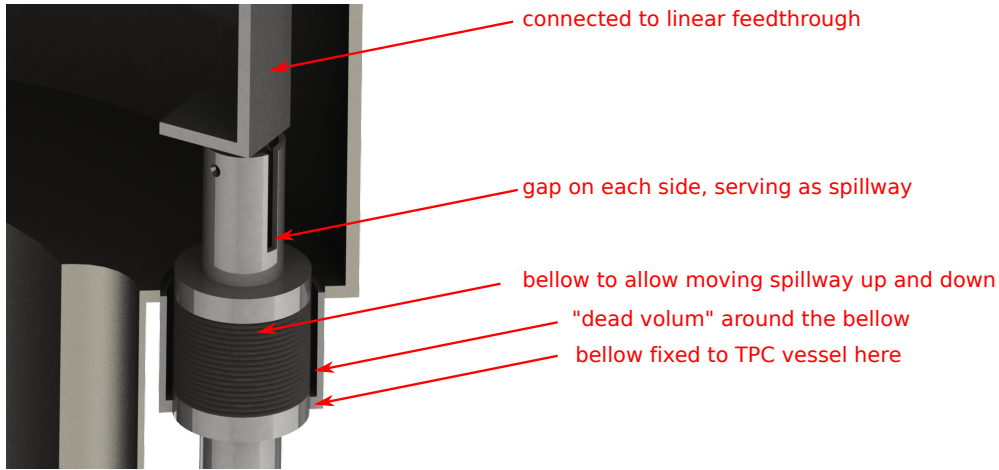


Figure 4.10. Illustration of the leveling system using a flexible bellow. Picture rendered from CAD.

4.1.4.2. Leveling Solution 2: Clearance Fit

As replacement for the bellow we introduced a system of two tubes with a tight clearance fit as a spillway with changeable height. This solution is much simpler and allows to change the liquid level by almost the full possible movement of the linear feed-through, i.e. from below the gate mesh to above the anode mesh. A small limitation in range is introduced for ease of mounting the TPC vessel.

Calculation of flux through clearance fit

Of course a clearance fit is never perfectly tight. Yet the flux through the gap of two axial tubes can be estimated using the formula for laminar flow of liquids between parallel plates, as found in [Ger04]. Starting with the velocity profile of the flow between two parallel plates of distance $2d$ in x -direction and length l in z -direction, as shown in figure 4.11:

$$v(x) = v_0 - \frac{1}{2\eta} \cdot \frac{dp}{dz} \cdot x^2$$

with η the viscosity of the liquid, $\frac{dp}{dz}$ the gradient of pressure in vertical direction and v_0 the velocity of the liquid in the center between the two plates ($x = d$). Making use of the fact that for laminar flows the velocity at the walls must be zero ($v(x = 0) = 0 \text{ ms}^{-1}$) we derive:

$$v_0 = \frac{d^2}{2\eta} \frac{dp}{dz}$$

Assuming $p = p(z)$ and independent of x , the average velocity \bar{v} can be calculated as:

$$\bar{v} = \frac{1}{2d} \int_{-d}^{+d} v(x) dx = \frac{2}{3} v_0 = \frac{d^2}{3\eta} \frac{dp}{dz}$$

The flux between a rod (outer radius r) and a coaxial tube (inner radius R) can approximately be treated as the flow between two parallel plates, if $\Delta r = R - r$ is small compared to the circumference of the inner rod $C = 2\pi r$. We rewrite the previous equation for this case as:

$$\bar{v} = \frac{(\Delta r)^2}{3\eta} \frac{dp}{dz}$$

The flux f through a gap with cross-section A is given by:

$$f = \bar{v} \cdot A$$

for the case of the axial rod and tube:

$$A = \pi \cdot (R^2 - r^2) = 2\pi \Delta r \cdot \left(R - \frac{\Delta r}{2}\right)$$

For the flux through the gap we therefore get:

$$f = \frac{(\Delta r)^2}{3\eta} \frac{dp}{dz} \cdot 2\pi \Delta r \cdot \left(R - \frac{\Delta r}{2}\right)$$

$$f = (\Delta r)^3 \cdot \left(R - \frac{\Delta r}{2}\right) \cdot \frac{2\pi}{3\eta} \cdot \frac{dp}{dz}$$

For a tight clearance fit it is $\Delta r \ll R$ and we find:

$$f \propto (\Delta r)^3$$

The pressure change per unit z is given by gravitation only, as the connecting tube between TPC vessel and buffer volume is wide enough to serve as liquid and gas connection in parallel and pressure is therefore identical everywhere along the clearance fit. The pressure gradient in z -direction is :

$$\frac{dp}{dz} = \rho_{LXe} \cdot g$$

Where g is the gravitational acceleration ($g = 9.80665 \text{ ms}^{-2}$).

With this formula, we can finally calculate the leakage flux of xenon through the clearance fit. In the design, the inner diameter of the outer tube is $R = 6 \text{ mm}$ and the outer diameter of the inner tube is $r = 5.99 \text{ mm}$. Using the density of liquid xenon $\rho_{LXe} = 2.966 \frac{\text{g}}{\text{cm}^3}$ [NIS16] at the triple point and the viscosity of liquid xenon $\eta_{LXe} = 5169 \cdot 10^{-6} \frac{\text{g}}{\text{cm}\cdot\text{s}}$ [NIS16]

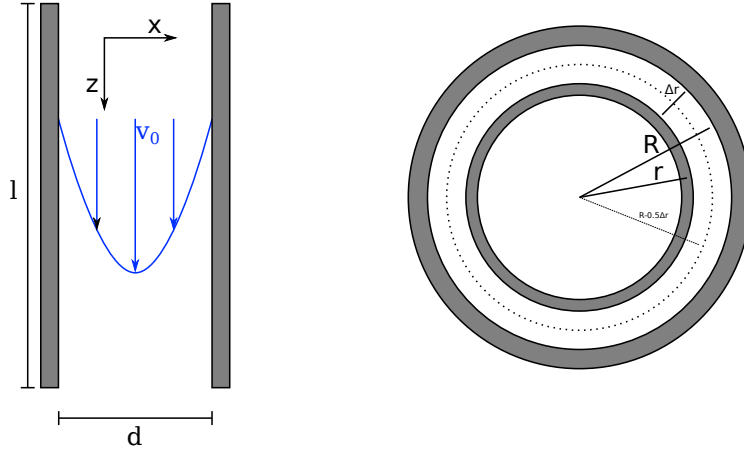


Figure 4.11. Flux between parallel plates (left) and flux between two coaxial tubes (right)

we can calculate the flux for the implementation:

$$f = (\Delta r)^3 \cdot \left(R - \frac{(\Delta r)^2}{2}\right) \cdot \frac{2\pi}{3\eta} \cdot \rho_{LXe} \cdot g$$

$$f = (0.01 \text{ mm})^3 \cdot \left(12 \text{ mm} - \frac{(0.01 \text{ mm})}{2}\right) \cdot \frac{2\pi}{3 \cdot 5169 \cdot 10^{-6} \frac{\text{g}}{\text{cm}\cdot\text{s}}} \cdot 2.966 \frac{\text{g}}{\text{cm}^3} \cdot 9.80665 \frac{\text{m}}{\text{s}^2}$$

$$f = 1.567 \cdot 10^{-9} \frac{\text{m}^3}{\text{s}} = 1.567 \cdot 10^{-3} \frac{\text{cm}^3}{\text{s}} = 1.567 \frac{\text{mm}^3}{\text{s}}$$

To compare this flow with the foreseen recirculation speed of 5 slpm gaseous xenon, we translate it into the mass flow f_{mass} using the liquid density:

$$f_{mass} = f \cdot \rho_{LXe} = 1.567 \cdot 10^{-3} \frac{\text{cm}^3}{\text{s}} \cdot 2.966 \frac{\text{g}}{\text{cm}^3} = 4.66 \cdot 10^{-3} \frac{\text{g}}{\text{s}}$$

The recirculation flow is

$$f_{mass}^{recirc} = f^{recirc} \cdot \rho_{GXe} = 5 \frac{\text{l}}{\text{min}} \cdot 5.858 \frac{\text{g}}{\text{l}} = 0.488 \frac{\text{g}}{\text{s}}$$

We realize, that the recirculation speed is about 104 times higher than the leakage through the clearance fit, which means the flow through the gap is negligible compared to the recirculation. Therefore the liquid level should be set by the spillway as intended.

Technical design

The calculation above showed, that the principle of a clearance fit as a spillway can work, if the clearance is tight enough. For the final design, we decided to use an inner diameter of 12 mm for the outer tube, and realized the spillway tube with an outer diameter of 11.98 mm. This clearance

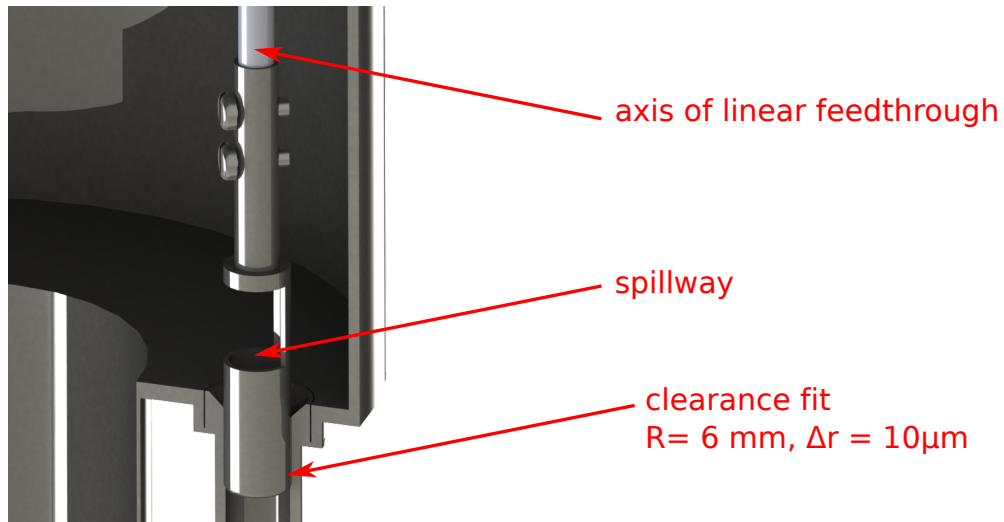


Figure 4.12. Illustration of the leveling using a clearance fit. Picture rendered from CAD.

is still large enough to move the spillway without force, but is tight enough, not to let large amounts of xenon flow through the gap (less than 1% of the planned recirculation flow of 5 slpm). To avoid issues with surface tension, the gap for the spillway has been increased significantly compared to the bellow solution. The spillway-gap spans three quarters of its circumference. The resulting length of the edge is about 28 mm and therefore about seven times larger than the two gaps in the bellow solution together.

For easier closing of the TPC vessel the spillway tube does not reach into the outer tube, at the uppermost position of the linear feed-through. At the lowest position of the linear feed-through the gap of the spillway is just on level with the wide floor of the TPC vessel. Therefore it is possible to set the level over almost the full range of the linear feed-through.

4.1.4.3. Levelmeters

To measure the liquid level, we took advantage of the experience of XENON100 using the same principle and electronics developed in the Oberlack group at Rice University [Ae12]. The measurement principle is based on a capacitive measurement, using the different dielectric constants of gaseous and liquid xenon: ($\epsilon_{GXe} = 1.00126$ and $\epsilon_{LXe} = 1.96$). For the readout of the capacitance we use the Universal Transducer Interface (UTI) chip developed by SmartTec [Sma17]. To keep it simple, we used the readily available evaluation board, which already includes a micro-controller and allows communication via RS-232. With the available demo software for the evaluation board, it could easily be integrated into the SCS.

We placed four small levelmeters around the TPC's liquid-gas interface to measure tilt of the TPC and monitor the stability of the liquid level during operation. Those levelmeters consist of an outer hollow cylinder made of oxygen-free copper (OFC) and an inner full cylinder. The gap

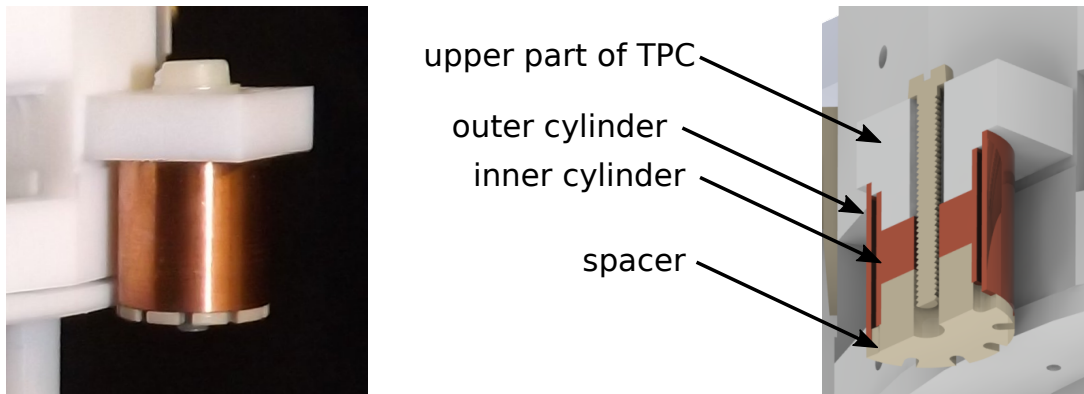


Figure 4.13. The TPC levelmeters. Left: Photo of the levelmeter connected to the upper part of the MainzTPC. Here, it is held together by a screw made of nylon. This screw was replaced by a screw made of PEEK, as shown in the picture rendered from the SolidWorks on the right. One can also see the spacer disc with the circle of $d = 1$ mm holes. The holes allow liquid to enter the gap between the cylinders. An identical circle of holes is drilled into the PTFE part where the levelmeter is fixed, so gaseous xenon can evade the gap. [Gro17]



Figure 4.14. The levelmeter of the buffer volume. On top the rendered CAD-version, on bottom a photograph. One can see the long holes for the liquid to enter and the PEEK-end caps.[Gro17]

between outer and inner cylinder is kept small to keep stray capacitance small and the capacity well defined. On the lower side, the inner and outer cylinder are kept in position by a spacer made of PEEK. This spacer has a circle of holes ($d = 1$ mm), to allow the liquid to enter. On the upper side, the two cylinders are fixed to the upper part of the TPC on a part made of PTFE which has holes too, to let gaseous xenon evade while the liquid level inside the levelmeter rises during the filling process.

For additional monitoring purposes, a further levelmeter, made of stainless steel has been installed inside the buffer-volume. The principle used here is the same but it is much longer ($l = 3.5$ inch = 8.89 cm), to allow measuring the amount of liquid inside the buffer. The outer cylinder of the buffer levelmeter has axial long-holes for the liquid to enter.

Design capacitance of the Levelmeters

The universal transducer interface (UTI) has two modes to measure capacitances. The first mode allows to measure one capacitance of up to 300 pF, the second mode allows measuring three capacitances up to 12 pF each. Therefore the levelmeters have been designed to match 12 pF when completely filled with liquid xenon. We use two evaluation boards, the first to measure the buffer levelmeter and one of the TPC levelmeters (levelmeter A), the second for the remaining three TPC levelmeters.

For the **TPC levelmeters** surrounding the liquid gas interface, the requirement is to cover the full range of the liquid level between gate and anode of 5 mm. We decided to use a length of 10 mm for the inner cylinder to start measuring already below the gate and also to measure a bit above the anode. For technical reasons, the inner and outer cylinders are not of identical length but the outer cylinder is 1 mm longer both on top and bottom. With the defined length of the cylinders, one can use the formula for cylindrical capacitances to find suitable radii for the two cylinders, which match the required capacitance. The formula for a long double cylinder (i.e. $l \gg R_1, R_2$) is:

$$C = 2\pi\epsilon_0\epsilon_r \frac{l}{\ln \frac{R_2}{R_1}}$$

Here, l is the length of the cylinders, R_2 the inner diameter of the outer cylinder and R_1 the outer diameter of the inner cylinder. We decided to use $R_1 = 5.0$ mm and $R_2 = 5.5$ mm. The resulting capacity when filled with liquid xenon ($\epsilon_r^{LXe} = 1.96$) is $C^{full} = 11.44$ pF and when empty ($\epsilon_r^{GXe} \approx 1.0$) we derive: $C^{empty} = 5.84$ pF. This results in a rise of 0.560 pF per mm liquid level, or a rise of the measured capacitance by 1 pF corresponding to a rise of the liquid level by 1.79 mm.

The **buffer levelmeter** has to be much longer, to be able to measure the liquid level all over the height of the buffer. To keep it simple and compatible with liquid xenon purity, it is made out of a stainless steel tube ($D_{in} = 6.35$ mm, $D_{out} = 8$ mm) as the outer cylinder and a stainless steel rod ($D = 3.175$ mm) as the inner cylinder. This geometry results in a total capacity of the empty buffer levelmeter of $C_{buffer}^{empty} = 7.14$ pF and correspondingly $C_{buffer}^{full} = 13.99$ pF. That means, the buffer levelmeter's capacity rises by 0.077 pF per mm rise of the liquid level, or 12.98 mm/pF.

4.2. Liquid Level issues

A well defined liquid level is important for dual-phase TPCs, as the secondary scintillation process depends on the field strength and the length of the electron path from liquid level to anode. Changes in the level lead to changes in the amount of photons produced per electron and the width of the S2-signal. As mentioned already in the previous chapter, stabilizing the liquid level was one major issue of the design. Despite different changes and attempts to understand the origin of the

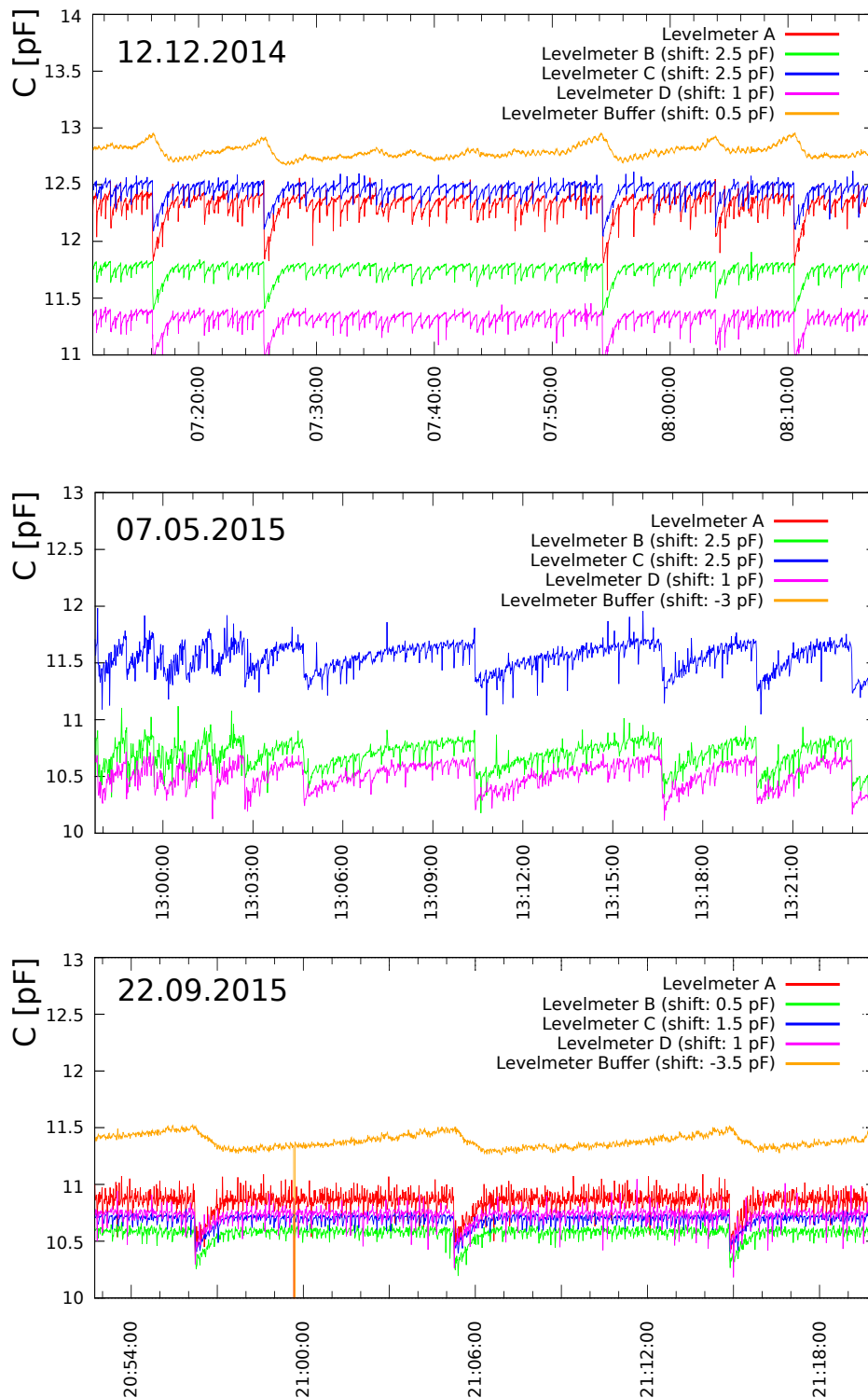


Figure 4.15. Fluctuations of the liquid level. Some of the measured values of the levelmeters have been shifted (as stated in the legends) to allow identical range of the y-axis. The uppermost plot (12.12.2014) is an example from using the bellow for the leveling. The second plot (07.05.2015) also uses the bellow, but has an additional gas-connection between buffer volume and TPC-volume was installed. The third plot (22.09.2015) is using the clearance-fit spillway, but the heat-exchanger is still mounted in the PTR cryostat.

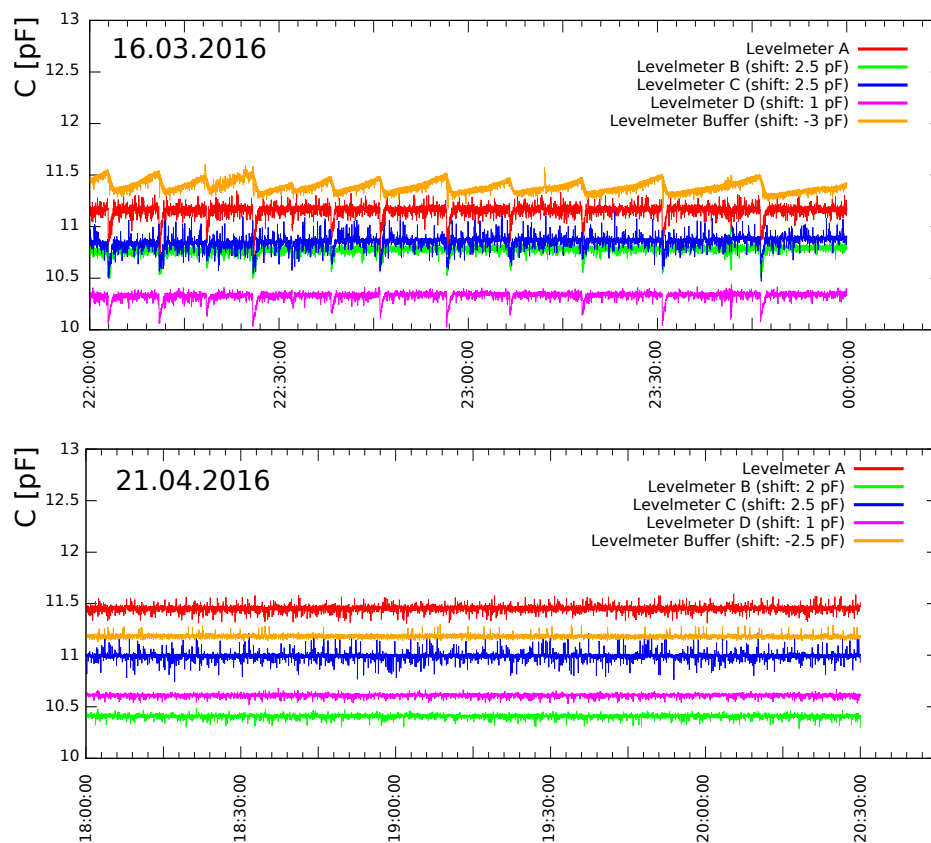


Figure 4.16. Fluctuations of the liquid level as during the beam time at nELBE (top) with the heat-exchanger mounted in the TPC-cryostat and all tubing with wider diameters. The lower plot shows the state of the levels during a Compton scattering run at HZDR (bottom), where the oscillations did not occur over one week, although no changes had been done to the system.

level fluctuations by adding additional temperature sensors the issues could not finally be solved. Although, for yet not understood reasons and without additional modifications, the level was stable in a final Compton measurement, unfortunately not for the neutron scattering experiment.

With the first leveling solution, the flexible bellow, the assumption was that the narrow gaps that should have defined the liquid level allowed to lift the level above the foreseen level due to surface tension effects. This could be confirmed by tests using water, which allowed to increase the level several millimeters above the foreseen level, which is shown in figure 4.17. Water of course is a polar molecule and its density is lower than that of liquid xenon, therefore the height of the effect cannot be assumed to be identical for xenon. Still it confirmed that surface tension played a role. The second effect that was considered was, that in the original design a quarter-inch tube served as only connection between the buffer volume and the TPC-volume. It should have allowed for liquid to run from the TPC to the buffer and in the same time allow to equalize the pressure in the two volumes by exchange of gas.

As a modification of the gaps in the bellow were not possible without destruction of the bellow, we decided to change the leveling system to the clearance fit version. This also allowed to exchange the quarter inch-tube to a half-inch tube to allow for gas-flow in opposite direction of the liquid flow. Unfortunately this still did not help. In a further attempt to solve the problem, the heat-exchanger, which was originally located about 1.5 m above the TPC close to the PTR was moved into the cryostat of the TPC. Although the temperature sensor mounted on the heat-exchanger showed that it was reached by the liquid sucked out of the buffer up to the heat-exchanger to evaporate there as foreseen, we assumed that by sucking the liquid up, the liquid in the tubes leading from buffer volume to heat-exchanger was boiling. Additionally we introduced the CF-16 cross to have an external volume to mix the liquid from PTR and heat-exchanger and equalize their temperatures. Furthermore, we exchanged the quarter-inch tubes leading liquid xenon with larger diameter tubing, to make sure, that, if gas-bubbles would form somewhere, they would not block the liquid flow but rather drift upwards in the inlet-tubing and not enter the TPC-volume from the bottom.

The changes in the end allowed to operate the MainzTPC in a state, where the liquid level dropped from time to time to recover relatively quickly to a steady state. This means one can use the measured level to discriminate events where the level was not in the flat and stable conditions. Still, there should be some effort undertaken to understand the origin of the level fluctuations and why they did not occur at the end, by further studying the temperatures and pressure in the system. Currently we think, that the main difficulty is to reach a thermodynamical state of equilibrium. The measured temperature in the TPC was always warmer than at the PTR and also in the buffer volume. This means, gas will condense at the colder places and the liquid will boil in the TPC, which is very undesirable. We also found, that while the system was warming up (for example after increasing the set-point temperature of the PTR) the liquid level was stable, and started with the fluctuations only, when the temperatures everywhere in the system stabilized again. This sometimes lasted for more than a day. Therefore changing the system to the bell-mode



Figure 4.17. Photo of the leveling bellow in the TPC-vessel. The vessel is filled with water to test the surface tension effect on the gaps.

as used in XENON100 and XENON1T might be anyway the better and more promising approach than further changes on the spillway-system.

4.3. Infrastructure

The operation of a dual-phase xenon TPC not only requires a clean detector (to be evacuated to UHV conditions for purity), but additional support systems too.

The gas system: The xenon gas has to be stored when the detector is not in operation. The xenon has also to be purified when filling the detector and continuously during detector operation. This is done using the so-called gas system, designed and built in the course of a diploma thesis ([Hil14]).

Cryogenics: To liquefy the xenon, a cooling system is required, and all the parts of the system that contain xenon at cryogenic temperatures must be properly thermally insulated in vacuum-cryostats.

To monitor and control the proper thermodynamic operation of the detector, one needs a slow-control system, which has to regulate the temperature and pressure, log the thermodynamic parameters and gas flow and alert the user if any parameter moves out of a pre-defined range.

4.3.1. Gas System

The gas system (figure 4.18 and figure 4.19) has mainly two tasks: storage of the xenon when the detector is not operated and purification and circulation of the xenon during detector operation.

Storage of the gas is done in two commercially available gas cylinders, with a volume of 20 l each. Those gas cylinders are made from aluminum, which is preferred over stainless steel because of the cryogenic cycles that the cylinders have to withstand while recuperating the xenon from the detector. Stainless steel might get brittle due to the thermal shocks and internal tension occurring when cooling the bottle to liquid nitrogen temperature (-196 °C). Both gas cylinders are hanging on mass sensors, which allow us to monitor the amount of xenon filled in the system. There is only one display contained for both mass-sensors. The sensor displayed (and monitored by the SCS) can be selected via a switch.



Figure 4.18. The gas-storage system (left) and the gas-recirculation system (right). [Hil14]

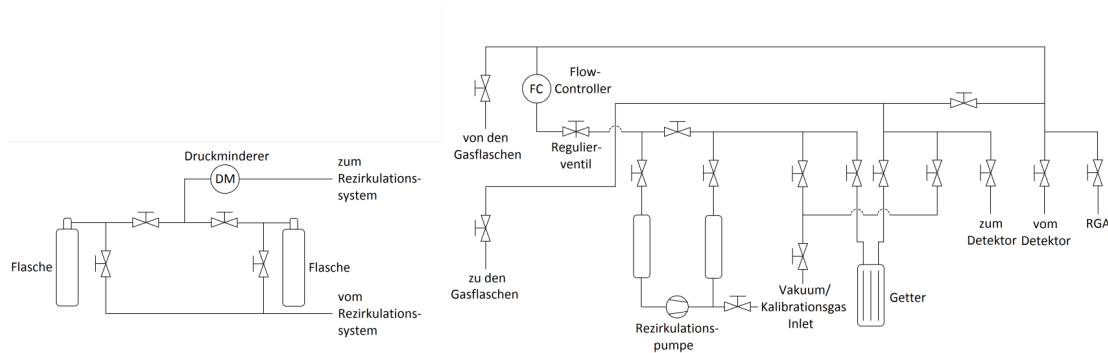


Figure 4.19. Schematic of the connections and valves of the gas storage system (left) and the gas recirculation system (right). [Hil14]

4.3. INFRASTRUCTURE

To recirculate and purify the xenon, the gas system contains a double-diaphragm pump (KNF N143 [KNF17]) which can provide gas flows of up to 30 slpm. The pump recirculates the xenon gas (at room temperature) through a gas purifier (SAES monotorr PS4-MT3 [SAE17]), which removes H_2O , O_2 , CO , CO_2 , N_2 , CH_4 and H_2 down to less than 1 ppm. Compared to the recirculation pump, the getter is only specified for 3 slpm xenon. Above this flow, the purity specifications won't be reached. The gas system also contains two pressure sensors to monitor inlet and outlet pressure of the recirculation pump. For each pressure sensor, there is a corresponding display mounted on the gas system. The analog-out of the display elements are fed into the SCS. A flow controller (Teledyne Hastings HFC-302 [Tel17b]) with the corresponding display and control unit (PowerPod THPS-100 [Tel17a]) allows setting the recirculation speed and, using its display's analog out, monitor and log the xenon flow with the SCS.

The gas system additionally provides a sub-system, which allows to mix a radioactive calibration gas into the xenon for detector calibration purposes. This system wasn't used for this thesis. It is described in more detail in [Hil14].

4.3.2. Cooling System

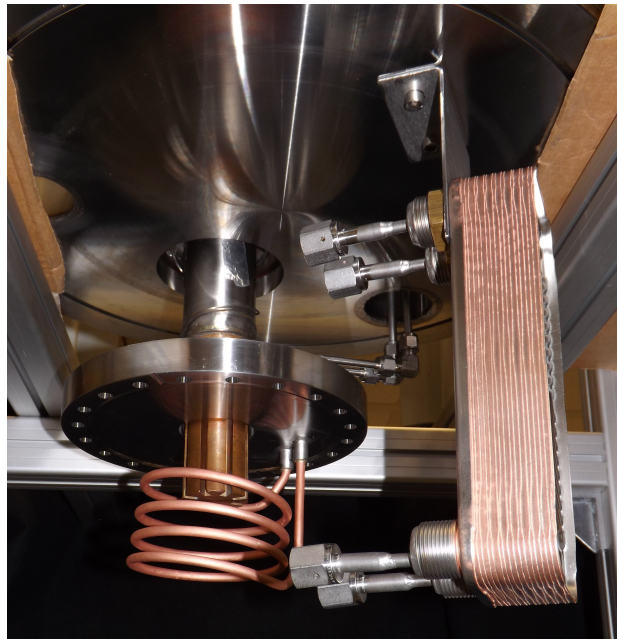


Figure 4.20. View into the cryostat of the cooling chamber. One can see the cold-finger of the PTR and the copper spiral for emergency and add-on cooling with liquid nitrogen. Copper spiral and cold finger are enclosed with a half-sphere from the bottom, serving as funnel for the liquefied xenon. On the right, one can see the heat exchanger we used. The heat exchanger was later mounted in the cryostat of the TPC. [Gro17]

The second important subsystem required to operate the MainzTPC is the cooling system. The system uses a pulse-tube refrigerator (QDrive 2S132W [Cha17]) as main cooling device. As

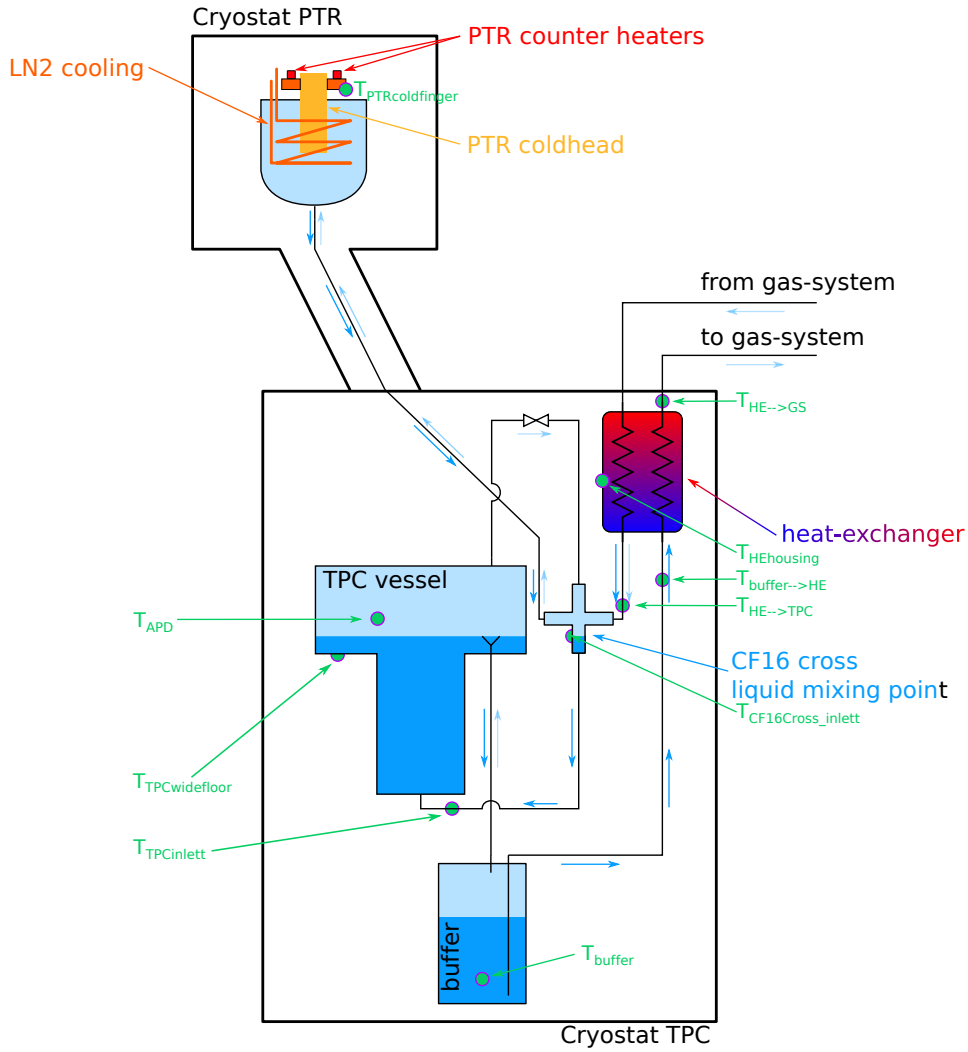


Figure 4.21. Schematic of xenon system: On top the cooling chamber is shown in its vacuum cryostat, including the PTR cold-head, the LN2 cooling spiral and the PTR counter heaters. On the bottom, the TPC cryostat is shown, including the heat exchanger, buffer volume and TPC vessel. The xenon flow during detector operation is visualized by arrows next to the tubes (light blue: gaseous xenon, dark blue: liquid xenon). The temperature sensors are shown using green circles.

a backup in case of emergencies or to provide additional cooling power while filling the detector, cooling with liquid nitrogen is foreseen too. The cold-head of the PTR and a copper-spiral flown through by liquid nitrogen are both cooling xenon gas in the so-called cooling chamber (figure 4.20). The cooling chamber is closed on the upper side by a CF200 flange and has a half-sphere on the lower side, serving as a funnel to guide condensed liquid into a half-inch tube connected at the lowest point of the half-sphere. The half-inch tube is assumed to transport liquid (driven by gravity) down to the TPC, while still being wide enough, to allow gaseous xenon to flow upwards to the cold-head of the PTR. The xenon connection pipes and the xenon flows in detector operation are schematically shown in 4.21. The schematic also shows, that xenon evaporated in the buffer volume or in the TPC vessel by heat-loads introduced by conduction, radiation or electrical power supplied to sensors can flow up through the half-inch tube to the PTR as well as xenon which is pushed through the heat exchanger without liquefying it.

Pulse-Tube Refrigerator (PTR)

The PTR has the advantage, that its cooling power can be controlled, by controlling the parameters of the motor drive. Using a thermocouple in the cold-head and a process controller, this allows regulating the cooling power to keep the temperature of the cold-head stable. This option was already supplied by the manufacturer. The system worked in principle, but didn't stabilize the temperature and pressure very well. Especially, if the required cooling power increased rapidly, the regulation didn't work properly.

An example is, that, when the detector is filled and in a stable state, and one decreases the temperature set-point by some degrees, the PTR first increases its cooling power to the maximum. After a short time (typically some minutes), the cold-head would reach the set-point, but of course, the rest of the system is still at the previous temperature. Then, after the cold-head reaches the set-point, the cooling power would be reduced to the lowest possible value. This leads to an increasing temperature of the cold-head again, due to the warmer gas surrounding it. The process controller tries to compensate this by increasing the cooling power again. When monitoring temperature and power settings of the PTR, one realizes, that the cooling power is not regulated continuously, but there is always a big jump, when the temperature of the thermocouple reaches the next digit. So the issue might be due to a lack of precision of the process controller. The display of the process controller only has 4 digits, one of those is used by the minus sign, therefore the precision of the display is only 1 °C. Maybe the precision of the regulation is the same as for the display, which would explain the non-continuous behavior.

The automatic power control did not only lead to problems when changing the settings, the temperature and pressure stability was not very good, even with stable operation settings (xenon flow, temperature). In any case, the automatic power control worked well enough for pre-cooling the system, which is typically started the evening before filling the detector. For the pre-cooling

the system obviously has to be filled with some gas, as pre-cooling the TPC vessel only works if liquid runs down the tubing. Heat transport through the walls of the tubes would not be enough to cool the TPC vessel down to liquid xenon temperatures. For pre-cooling a reasonable xenon pressure at room temperature is 2.5 bar.

To achieve better temperature and pressure stability and to circumvent the problems of the automatic power control of the PTR, we installed counter-heaters. The counter-heaters are two 25 W heating-resistors, each mounted on a copper plate. The copper plates are pressed to the cold-finger of the PTR on two opposing sides outside of the xenon volume but inside the insulation vacuum (compare figure 4.21). Operating the PTR on constant electrical power and controlling the power of the counter heaters to stabilize the temperature $T_{\text{PTRcoldfinger}}$ leads to the required stable operation conditions.

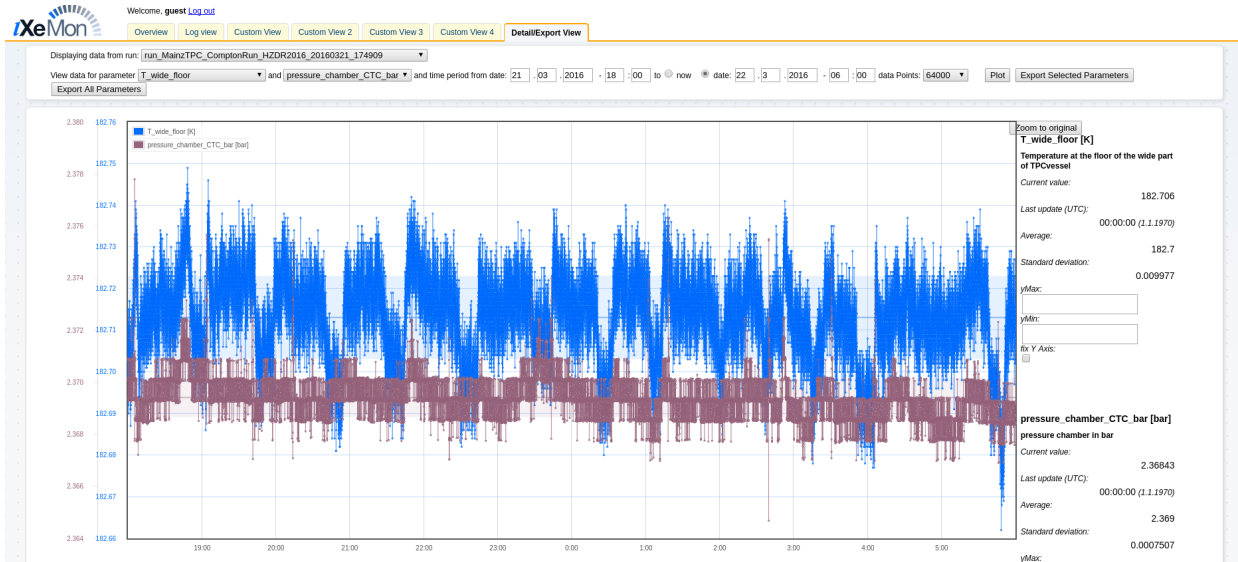


Figure 4.22. Screenshot from the web interface of the SCS. The final operation achieved using a fixed electrical power for the PTR and PID-controlled counter-heaters achieved a good stability of temperature and pressure in the TPC. The pressure was stable to ± 0.75 mbar and the temperature to 9.9 mK for twelve hours (and longer). For the pressure, the standard deviation is strongly influenced by the resolution of the ADC, as the steps can be seen in the data shown here.

Heat Exchanger

The power required to liquefy a mass flow f_{mass} of xenon is:

$$P = f_{\text{mass}} \cdot \frac{q_v}{M}$$

where M is the molar mass of xenon and q_v the enthalpy of vaporization. For xenon we get $P(1 \text{ slpm}) = 8.96 \text{ W}$. Therefore, a recirculation velocity of 5 slpm would require about 45 W of

cooling power, in addition to what is required to compensate the heat load to the system. The PTR we are using, can provide around 50-60 W of cooling power, depending on the temperature set point. To allow the recirculation flow of 5 slpm it is accordingly necessary to use a heat exchanger. We are using a plate heat exchanger (figure 4.20) model GBS-300 produced by GEA [GEA17]. This heat exchanger consists of 10 brazed parallel copper plates, and hence 5 channels per direction. As the heat exchanger is normally meant for use with water, the efficiency for our application is not clear. We chose it, as a similar heat exchanger has been used in a similar system in [GAC⁺11]. The connectors of the heat exchanger were not available as VCR, which we used for all our xenon-tubing. We therefore had the workshop weld VCR connectors into the holes. The connections going to and coming from the gas system were chosen to be ¼-inch Swagelok VCR connectors. The connection from the buffer volume into the heat exchanger is ½-inch to allow liquid and probably gas to flow through in parallel continuously. The connection from the heat exchanger leading to the TPC is ¼-inch. This might not be ideal, as here liquid and gas might coexist. It was kept at the small diameter, because otherwise the throttle-valve we installed directly after the heat exchanger would have been larger, and the available space above the TPC vessel was limited anyway.

4.4. Slow Control System (SCS)

The TPC and the gas system, together with the cryogenics, requires the use of an SCS. An SCS controls a system, as the name already suggests. It also allows monitoring and logging of important parameters of the system. In our case, the control is done by a commercially available system, a cryogenic temperature controller SRS CTC100 [Sta17], whereas the monitoring and logging is provided by the SCS-software developed in the course of a bachelor thesis ([Kja12]). The software got some minor improvements and bug fixes since its state after the bachelor thesis. As the hardware requirements developed during detector design, construction and commissioning, the software was extended with drivers for the added hardware. The hardware of the SCS now consists of:

CTC100 The Cryogenic Temperature Controller, manufactured by Stanford Research Instruments (SRS). This device provides the control of the SCS. It provides four inputs for temperature sensors, 4 analog inputs/outputs, two power outputs (100 W each). One analog input and one analog output are used to measure and control the flow of nitrogen gas through the nitrogen flow controller of the emergency cooling. This offers not only to set a fixed flow of the nitrogen, but allows to use the PID-control of the CTC100 to keep T_{LN_2} stable.

It is also used to stabilize the temperature of the PTR cold-finger ($T_{PTRcoldfinger}$), by controlling the counter-heaters (connected to one of the power-outs). Connecting the analog signal of the pressure in the TPC vessel, it is also possible to regulate on the pressure instead of the temperature.

USB-ADC The USB-ADC we are using is a MeasurementComputing (MCC) USB-1608G [Mea17a], providing 16 single-ended or 8 differential analog inputs and a sampling rate of 250 kS/s. It is used to monitor the mass of the gas cylinder(s) in the gas system, the inlet and outlet pressure of the xenon pump and the xenon flow provided by the flow controller.

USB-Temperature logger To be able to monitor more temperatures, the system was extended by a USB temperature logger. We use an USB-Temp [Mea17b] from MeasurementComputing, providing up to eight inputs for temperature sensors. This device is used to measure the remaining temperatures in the system, that are not used as input parameters for any PID controls.

UTI-Evaluation board The evaluation boards can be used to measure different quantities (including temperatures). Currently, we use the UTI evaluation boards to measure the capacities of the levelmeters. In the system we included two evaluation boards, the first one measuring the levelmeters B, C and D of the TPC, the second one measuring the capacity of TPC-levelmeter A and of the buffer levelmeter.

File Watcher The so-called file watcher device is not a hardware device, but an interface to read SCS data from another computer via Ethernet. The file watcher uses a file as buffer. The need to transfer data from the DAQ computer to the SCS, made implementation of such a device necessary. It is used to log and monitor the bias voltages of PMTs, APDs and cathode-HV, which are controlled by the DAQ computer. It also allows monitoring of DAQ parameters like trigger rates and lifetime-fraction.

4.5. Signal Readout

4.5.1. Light detectors used for the MainzTPC

4.5.1.1. Photo Multiplier Tubes: Hamamatsu R6041

We chose to use Hamamatsu R6041 PMTs because they fulfill the requirements for the measurement goals of the MainzTPC. First of all, they must be sensitive to VUV light, as xenon scintillates at 178 nm. Of course, they should not only be sensitive, but also have a high quantum efficiency (QE) for the scintillation light. The QE is a strong contributor to the energy threshold of the TPC. To achieve sensitivity and high QE, they have synthetic silica glass windows and a bi-alkali photocathode. We ordered the PMTs with quantum efficiency selected to be above 30 % at 178 nm. As one of the goals of the MainzTPC is, to measure and understand the pulse shape of the scintillation light, it is also necessary, that the PMTs have a quick response, ideally as fast or faster than the scintillation decay time constants of singlet excimers (2 ns, compare chapter 3). According to

4.5. SIGNAL READOUT

Hamamatsu, the PMTs have an anode pulse rise time of 2.3 ns and a transit time spread of 0.75 ns, which should allow to measure the pulse shape, without being dominated by the PMT response. According to the data sheet, the PMTs provide a gain of 10^6 at a bias voltage of 800V.

These PMTs are cylindrical, with a diameter of 2 inch, have a metal housing and can withstand pressure of up to 6 bar. The cylindrical shape is also very advantageous with respect to avoiding surfaces in the inner of the TPC that are neither reflective nor photo-sensitive. Using several squared PMTs, for example of type Hamamatsu R8052 (1 inch), would lead to photo-insensitive areas in between the PMTs. The 2-inch-diameter of the R6041s does also match very well the diameter that we wanted to have for the TPC to avoid too much multiple scattering in the active volume for 662 keV gammas from a cesium source. Of course, the R6041s are capable of working at low temperatures. In fact they were specifically developed for liquid xenon applications.

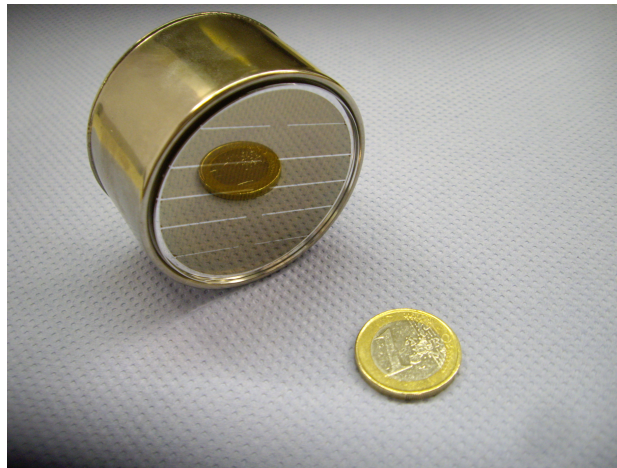


Figure 4.23. Hamamatsu PMT: R6041. One of those is used as top and bottom PMT in the MainzTPC.[Gro17]

4.5.1.2. Large-Area Avalanche Photo-Diodes: RMD S1315

To avoid having bulky PMTs on top of our relatively small MainzTPC, but still achieve 3D-position reconstruction, we included an array of eight large area APDs around the liquid gas interface. Of course the APDs can only be used, if they are sensitive to the secondary scintillation light and have a reasonable QE for those VUV-photons. Additionally, they need to provide sufficient internal gain to make sure that the signals are above noise level. We compared data sheets and previous use of different devices (Advanced Photonics, Hamamatsu and RMD Inc.), and finally decided for the square-shaped large-area APDs manufactured by RMD Inc. The main reason being existing experience [SGO⁺09] with this type of APD and the fact, that they come without housing, and therefore are easiest to include in the TPC without including photo-insensitive areas.

We use RMD's model S1315, which features an active area of $14 \times 14 \text{ mm}^2$, and provide gains of 300-2000, according to the data sheet. It was shown in [SGO⁺09] that even higher gains – up to 10000 – can be achieved when cooled. The quantum efficiency was also measured to be $34 \pm 5\%$. Making use of the high gain and the reduced noise when cooled, it should be possible to detect small amounts of photons with those APDs and therefore provide x/y-position resolution in our TPC even at low energy deposits.

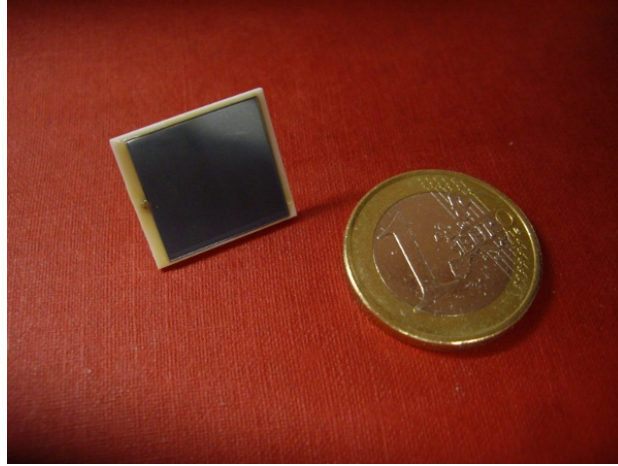


Figure 4.24. RMD Inc. S1315: An array of eight of those large-area avalanche photo diodes surrounding the liquid-gas interface provides position resolution to the MainzTPC. Their large active area of 196 mm^2 and the relatively high gain of about 1000, together with their compact design and their sensitivity to VUV-photons, makes them ideal for our application.[Gro17]

4.5.2. Detectors for scattered particles

4.5.2.1. Germanium detector

To measure the energy deposit in the TPC in a Compton-scattering setup a secondary detector is required. As the goal of the MainzTPC is to measure very low energy deposits in liquid xenon down to 1 keV, the secondary detector must be able to resolve that energy. For ^{137}Cs it is therefore necessary to have an energy resolution of

$$\frac{\Delta E}{E_0} = \frac{1 \text{ keV}}{662 \text{ keV}} < 0.5\%$$

Scintillating crystals like sodium-iodide do not provide the required energy resolution, as opposed to germanium detectors.

We bought a germanium detector (GEM-F5930-S [Ort17]) from Ortec for the Compton setup. It is a coaxial HPGe-detector with a crystal diameter of 58.8 mm and a length of 42.2 mm. Ortec states a measured energy resolution (FWHM) of 1.7 keV at 1.33 MeV and of 626 eV at 122 keV.

The crystal has an efficiency of 27% for 1.33 MeV gammas. Further information on the germanium detector can be found in the data sheet and in [Sch13].

4.5.2.2. Plastic scintillators

The plastic scintillators we used for the neutron scattering setup, were provided, tested and characterized [Bey07] by the group of Dr. Arnd Junghans (HZDR). The scintillators are panels made of EJ-200 with a length of 1 m, a width of 4.2 cm and a thickness of 1.1 cm. The plastic is wrapped into two layers of PTFE and then surrounded with reflective foil. To protect it from light from outside, it is then wrapped into black tape. After a PMT (Hamamatsu R2059-01) has been connected with optical grease on either side of the panel, it is covered with black shrinking tube.

4.5.3. Data-Acquisition System

The DAQ consists of a VME-crate containing two flash analog-to-digital-converter (FADC) boards, a VME controller, a time-to-digital-converter (TDC), a programmable logic board and three HV-modules. All those modules are described below. Additionally the PMTs have been amplified by home-made PMT-amplifiers. It also turned out that the signal produced by the internal charge-sensitive preamplifier (CSP) of the germanium detector was too weak to provide sufficient resolution, when digitizing the CSP signal without the use of a shaping amplifier. Therefore, an existing amplifier, originally designed for silicon photo-multipliers (SiPMs) was adapted to provide additional amplification to this CSP. For the neutron scattering experiment, the DAQ was extended by a TDC, which is also used, to measure the trigger efficiency of the TPC. The trigger generation is done by a set of constant-fraction discriminators (CFDs), designed and produced by Helmholtz-Zentrum Dresden-Rossendorf (HZDR), together with the VME-logic board. In figure 4.25, the connections of the different components of the DAQ are schematically shown.

4.5.3.1. Flash ADCs

High resolution Flash-ADC: Struck SIS3316

This FADC is the main digitizer in our DAQ system. It is used to digitize the signals of all the light sensors (PMTs, APDs) of the MainzTPC, as well as additional detectors (germanium, sodium-iodide, lanthanum-bromide) during the Compton measurement or trigger efficiency measurements. The traces of the PMTs of the plastic scintillators used for the neutron scattering experiment are never digitized. This digitizer is used to sample continuously over the complete drift-time in our TPC (30 μ s) plus an additional pre-trigger window. The settings used varied from 35 to 42 μ s. The SIS3316 provides 16 channels with 16 bit resolution and an adjustable input range of ± 1 V or

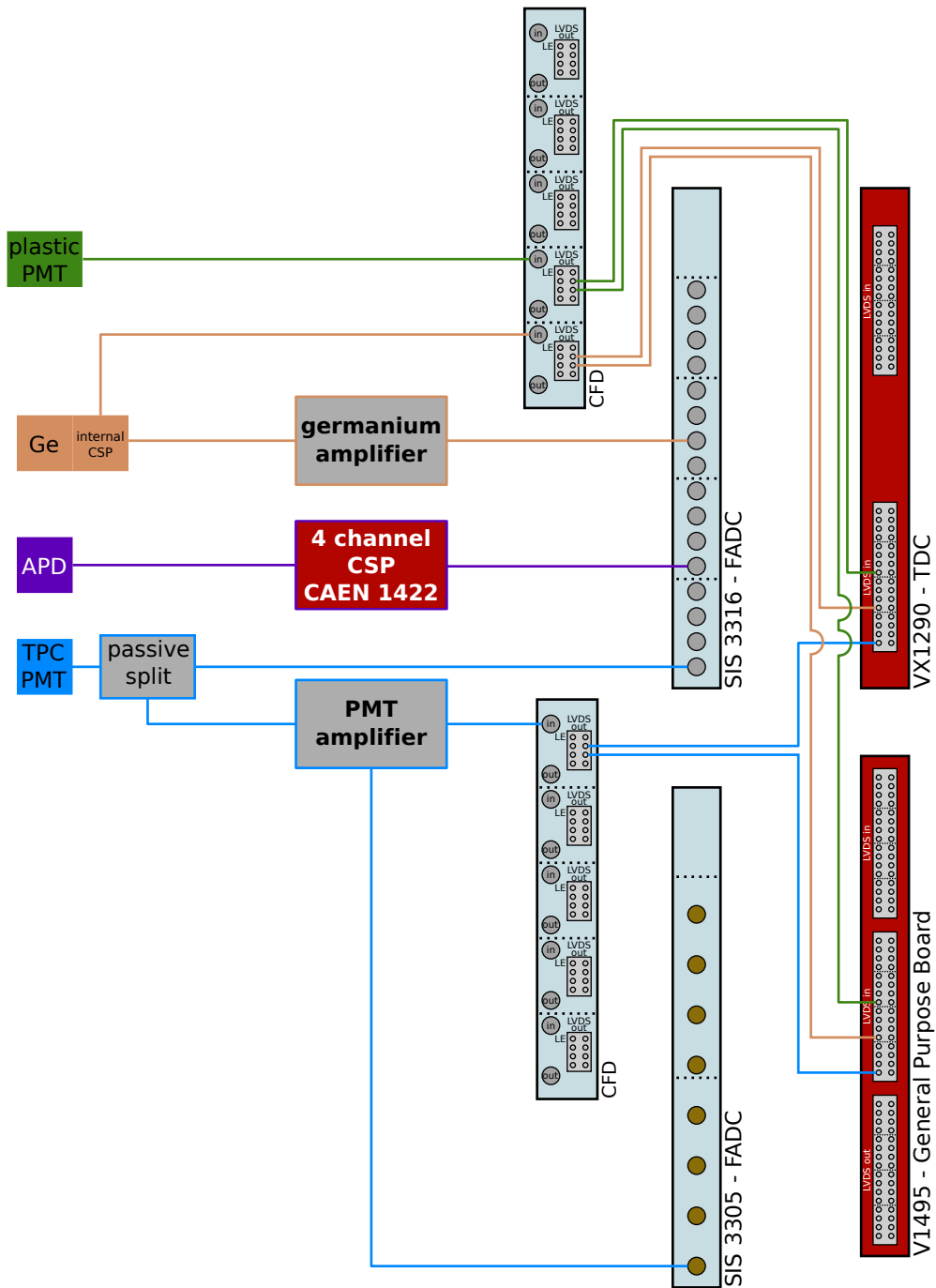


Figure 4.25. Connection Scheme of the different detectors’ sensors to ADCs, TDC and logic module, including amplifiers and signal splits. To keep the schematic clear, only one sensor of each type is shown. Not shown here are additional electronics required for trigger generation, like gate and delay modules. A complete and extensive description of the trigger setup and DAQ will be found in [Sis17].

4.5. SIGNAL READOUT

± 2.5 V with an adjustable offset over the full range. It samples with a frequency of 125 MS/s and has an analog bandwidth of 62.5 MHz.

Fast Flash-ADC: Struck SIS3305

To analyze the pulse shape of the primary scintillation light the sampling frequency of the SIS3316 is not sufficient as the 125 MS/s only correspond to one sample per 8 ns. Therefore the signal of the PMTs is split and not only fed into the SIS3316, but also in a second FADC, the SIS3305, which is much faster. The 3305 has eight inputs, and can be operated with all eight inputs active, providing a sampling frequency of 1.25 GS/s. It is also possible to multiplex some of the channels, allowing to digitize four channels at 2.5 GS/s or just two channels at 5 GS/s. As we're only interested in the pulse-shape detected with the top- and bottom-PMT of the TPC, we only need two channels and could make use of the highest sampling frequency. The SIS3305 provides an analog bandwidth of 2 GHz using SMA-connectors. It's resolution is 10 bit spanning from -1 V to +1V in the standard configuration. As the PMT signals are anyway negative only, we asked Struck to provide a modified input stage, allowing only negative signal inputs of -1 V to 0 V and therefore increasing the effective resolution for our application by a factor of two.

4.5.3.2. Amplifiers

Kernphysik-Amplifier

To amplify the PMT signal, we had two different amplifiers, both with advantages and disadvantages. One of the amplifiers was designed, built and provided by the institute of nuclear physics of the Johannes Gutenberg-University Mainz (JGU). It is a two-stage amplifier, based on THS3201 [Tex17] integrated circuits (ICs). Both amplification stages have identical layouts. The input is provided by a panel-mount SMA-connector with industrially connected cable, the cable is soldered to the input on the printed circuit board of the amplifier. The input signal is amplified by the first amplification stage by factor 2, than split and both lines are again amplified by a factor of 5, resulting in two outputs, with a total gain of 5 each. As output, it is foreseen to solder BNC connectors onto the PCB, which we did using BNC connectors specified up to a bandwidth of 2 GHz. This amplifier provides a rather high bandwidth but its drawback is that it is limited in its maximum output voltage to less than 1.5 V. This amplifier requires +7.5 V and -7.5 V for operation. We supply this via a 3-Pin-connector. The power supply used is built from two 230V(AC)-to-7.5V(DC)-converters.

Detector-Lab-Amplifier for the PMT

As a second amplifier, we made use of an amplifier designed by the PRISMA Detector Laboratory (JGU) [PRI17] to be used with SiPMs. This amplifier is a single stage amplifier, based on a AD8009 [Ana17] IC, without split of the signal. The PCB provides solder-spots for PCB-mount SMA-connectors. We used the solder spot for the signal input, but at the output we connected a passive signal split done by three $16\ \Omega$ resistors which lead to panel-mount SMA connectors delivering the output signals. We adapted the components on the PCB, to provide $50\ \Omega$ input termination and to provide a gain of 10.5. This amplifier is also limited in its output range to less than 2 V and its bandwidth is smaller than the bandwidth of the Kernphysik-Amplifier. This amplifier requires a power supply of +5 V and -5 V. We therefore included a DC-DC-converter together with the amplifier (including the passive split on the output) in a aluminum box. The DC-DC-converter requires a +12 V input. We chose to use a D-Sub-9 connector with the Pin-Layout as for CSPs to make use of commercially available cables and power supplies from Nuclear Instrumentation Module (NIM) modules.

Detector-Lab Amplifier for the germanium detector

As the output of the CSP integrated into the germanium detector is usually used with an external shaping amplifier, its signal is relatively small. For example a 662 keV gamma results in a signal amplitude of about 27 mV. We do not want to use analog signal shaping before recording the signal trace of the germanium to be able to recognize multiple scattering in the germanium. The dynamic range of our FADC is $2\ \text{V} - 75\times$ larger than a typical signal from a 662 keV gamma. Therefore we decided to amplify the output signal of the germanium CSP by another factor of 10. The amplifier we used for this, is the based on the Detector-Lab Amplifier, too. Its input impedance is adapted to be $93\ \Omega$, its gain is set to 10.5. As the CSP of the germanium already provides two outputs, additional signal splitting is not necessary for this amplifier. We used panel-mount BNC connectors soldered via coaxial cables to the amplifier PCB for the signal input and output in this case.

4.5.3.3. Constant Fraction Discriminators

To generate the trigger and to record the hits with the TDC the analog signals of the sensors (PMTs of the TPC and the plastic scintillators) have to be translated into logic signals, with a good time resolution. Therefore we used CFDs provided from HZDR. The CFDs are NIM modules with five channels per module. Each channel has an analog input (LEMO) and provides three differential LVDS outputs and an additional NIM output (LEMO). The LVDS output signals have a length of 30 ns and are fed into the logic module and the TDC. The NIM output was used with an oscilloscope for setting the thresholds.

4.5.3.4. TDC: CAEN VX1290

The TDC has been implemented in the system mainly to measure neutron time-of-flight (TOF) in the neutron scattering experiment, required to determine the energy deposits. It is also very useful when measuring the trigger efficiency. This TDC has 32 input channels (differentially supplied via ECL/LVDS). It provides a resolution of 21 bit with the least-significant bit corresponding to 25 ps. The absolute timing is only precise to 25 ns, but the 25 ps precision can be reached, by using relative timing, e.g. using the accelerator clock as a reference. The TDC records every single PMT of the plastics and of the MainzTPC on one channel. Additionally the accelerator clock is recorded on one channel, and the TPC trigger (AND or OR between top and bottomPMT) and the plastics trigger (AND between the top and bottomPMT of at least one of the plastic scintillators) are recorded.

4.5.3.5. Trigger Unit

To trigger the DAQ, we set up a trigger logic using a VME logic board, provided by CAEN. The general logic is relatively simple: The final trigger is generated by either the TPC alone for calibration measurements, or by a combination of the so-called TPC-trigger (T_{TPC}) and $T_{\text{secondary}}$, the trigger of the secondary detector system (germanium detector(s) or plastic scintillators). The trigger for Compton and neutron scattering therefore can generally be written as:

$$T_{\text{scatter}} = T_{\text{TPC}} \wedge T_{\text{secondary}}$$

The TPC-trigger can either be generated combining top and bottom PMT with AND or with OR. The former providing cleaner data, the latter providing lower threshold. The TPC trigger can be written as logic formulas like:

$$T_{\text{TPC}}^{\text{AND}} = \text{PMT}_{\text{TPC}}^{\text{top}} \wedge \text{PMT}_{\text{TPC}}^{\text{bottom}}$$

$$T_{\text{TPC}}^{\text{OR}} = \text{PMT}_{\text{TPC}}^{\text{top}} \vee \text{PMT}_{\text{TPC}}^{\text{bottom}}$$

For Compton Scattering measurements, the trigger is generated by:

$$T_{\text{Compton}} = T_{\text{TPC}} \wedge \left(\bigvee_i \text{Ge}_i \right)$$

when using i germanium detectors. In our case we used up to three Germanium detectors, but the logic is identical if using more or less. For neutron scattering measurements, with ten plastic

scintillators, each equipped with two photo multiplier tubes, the Trigger condition is:

$$T_{\text{Neutron}} = T_{\text{TPC}} \wedge \left[\bigvee_{i=0}^{i=10} \text{plastic}_i^{\text{top}} \wedge \text{plastic}_i^{\text{bottom}} \right]$$

The main part of the logic is done on the logic board (CAEN V1495), although it had to be expanded by external gate-and-delay generators to account for the different detector response times and the time of flight in case of the neutron measurement. To make use of the logic module, the analog signals had to be converted to digital signals. This conversion was done using CFD modules developed, built and provided by HZDR. The trigger logic, including the gates and delays and the modules used, will be described in more detail in [Sis17].

4.5.4. High Voltage Modules

CAEN V6533 This is a six channel VME HV supply module providing up to 4 kV and 3 mA per channel. The polarity has to be specified when ordered and cannot be changed by the user afterwards. We use two of these modules with positive output voltage. One board is used to deliver the bias voltage of six of the APDs, the second one provides the bias voltage for the remaining two APDs and the two PMTs.

ISEG VHQ 223M This VME module provides two channels, with user-changeable polarity. Each of the channels can provide voltage up to 3 kV and a maximum current of 2 mA. It has a ripple (Peak-to-Peak) of typically <1 mV and maximal 2 mV. We use this power-supply for the germanium detector, and used it to apply a small positive voltage (<100 V) to the anode of the TPC for some tests.

Bertan 225 Series This stand-alone power supply has one single channel, but can provide HV of up to -30 kV. It was used to apply the HV to the cathode to generate the drift field of the TPC.

ISEG NHQ 226L This module is a NIM power supply, which can be controlled via CAN Bus. It provides two channels, with user-changeable polarity. Each of the channels can provide up to 1 mA and 6 kV. This module is used for the gate.

4.6. The Compton setup

For the measurement of electronic recoils a Compton scattering measurement is done. The setup (figure 4.26) consists of the MainzTPC with its liquid xenon as scattering target and a germanium detector as secondary detector to measure the remaining energy of the scattered gammas. The setup

4.7. THE NEUTRON SCATTERING EXPERIMENT

for this has been designed in the course of a diploma thesis [Sch13] and is described in detail there. The germanium detector can be rotated around the MainzTPC, measuring different scattering angles of the gammas coming from a source (^{137}Cs or ^{60}Co) that is mounted in a collimator made of lead bricks.

To be able to do some electronic recoil measurements in exactly the same setup and detector configuration as the neutron scattering measurement, our collaborators from HZDR provided a solution to mount the germanium detector at the experimental site. The collimator used there was the one from [Sch13].



Figure 4.26. The Compton setup at HZDR. The germanium detector is mounted in front of the plastic scintillators. The collimator made from lead brick sits below the cooling chamber and in front of the neutron beam tube. Of course, for the neutron scattering experiment, germanium detector and collimator have been removed.[Gro17]

4.7. The neutron scattering experiment

For the measurement of the nuclear recoil response of liquid xenon, one needs a suitable neutron source. Other experiments measuring nuclear recoils in a small TPC have been using sealed-tube neutron generators [PAB⁺11]. The neutrons are produced by an $^2\text{H}(d, n)^3\text{He}$ reaction and have an average energy of 2.5 MeV at 90° with respect to the deuterons. For these measurements, the uncertainty of the energy of the incoming neutron is due to the kinematics of the neutron production (neutron energy is dependent on angle between deuteron and produced neutron as well as deuteron energy). Additionally the energy measurement of the scattered neutron is determined

by the angle under which it is scattered. As the detectors used do not have position resolution, the geometrical acceptance of TPC and neutron detector defines the uncertainties of the measurement of the scattering angle. Other measurements, done with the large-scale Dark Matter-detectors suffer from using non-mono-energetic neutron sources (AmBe) without the possibility to measure the energy of the incoming neutron [Ae13]. These measurements therefore rely on comparing simulated spectra with measured spectra. To overcome the uncertainties of the measurement of the energy deposit, i.e. incoming neutron energies and relying on the scattering angle for measuring the remaining energy of the scattered particle), we selected a neutron source, that allows to perform a double TOF measurement. The nELBE neutron source provides neutrons generated in short bunches, allowing to measure the incoming neutron energy with a precision of 1%, depending on the response time of the detector used.

4.7.1. The neutron Source nELBE

The nELBE neutron source is located at HZDR and part of the Electron Linac for beams with high Brilliance and low Emittance (ELBE) facility. ELBE itself is an electron accelerator. It has two ways of producing electrons: a thermal electron source and a laser electron source. Electrons produced by the thermal electron source are extracted in bunches and accelerated to about 50% of the speed of light. The accelerated electrons then get into the buncher, where the bunches are compressed. The buncher is followed by a two-stage super-conducting high-frequency accelerator, accelerating the electrons to up to 40 MeV and a pulse width of 5 ps(FWHM) [KAB⁺07], [HZD17]. Neutrons generated by these short pulses are ideal for TOF experiments. The achievable energy resolution is about 1 % at a flight path of only 4 m, of course, depending on the response time of the detector used.

Dumping the electron bunches in a high-Z material, such as lead, generates bremsstrahlung photons. These photons afterwards undergo (γ,n) -reactions producing neutrons. The electron beam dumps a power of up to 25 kW per cm³ in the neutron radiator, depending on the parameters of the electron beam. This is too much for any high density material to stay solid. Therefore, the neutron radiator at nELBE is realized as a liquid lead loop.

Of course, such a neutron source does not deliver mono-energetic neutrons. The generated neutrons span a range starting from about 50 keV reaching up to 10 MeV peaking at 1.5 MeV. Figure 4.27 shows the simulated spectrum of generated neutrons that enters the collimator. This collimators design allows 96 % of the neutrons to reach the experimental site without energy losses, therefore providing clean data samples. [KAB⁺07]

As the neutrons at nELBE are generated by bremsstrahlung photons, there is a huge amount of photons produced and reaching the experimental site per bunch of electrons. In fact, the integrated flux of photons entering the collimator is about 1000 times higher than the flux of neutrons. The

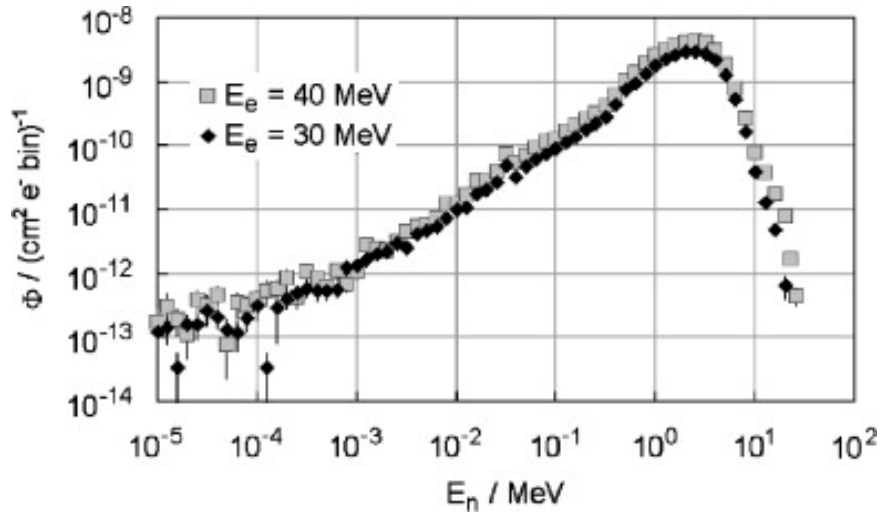


Figure 4.27. Simulated Spectrum of generated neutrons using MCNP. The y-axis shows the flux of neutrons entering the collimator per electron started.[KAB⁺07]

spectrum of the photons in figure 4.28 starts at the keV-range and reaches up to the electron energy, several tens of MeV. It peaks at 511 keV, showing that pair production and annihilation is a major process.

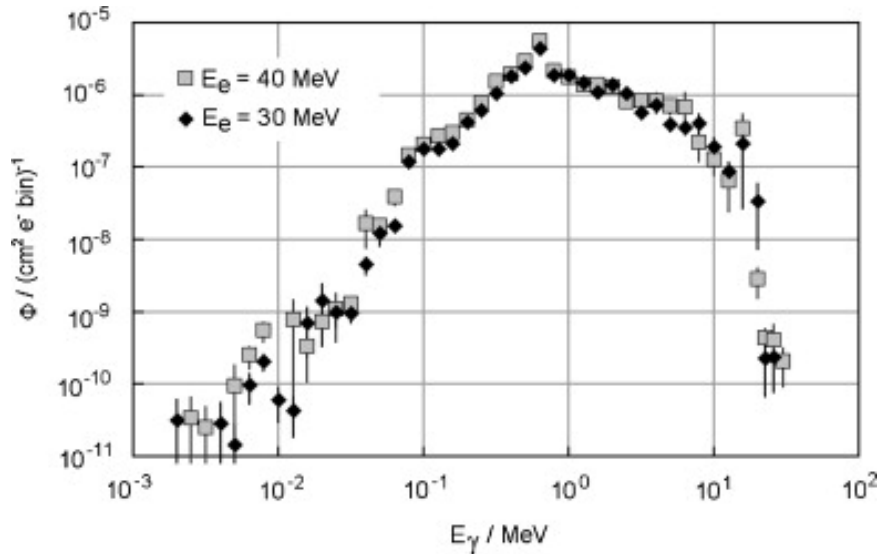


Figure 4.28. Simulated Spectrum of generated photons using MCNP. The y-axis shows the flux of photons entering the collimator per electron started.[KAB⁺07]

Due to the 5.9 m flight path, the photons reach a detector in the experiment hall about 100 ns before the fastest neutrons. Any detector with a timing response suitable for TOF measurements, will therefore be able to discriminate the photons. This is also true for the MainzTPC. Unfortunately, a dual-phase xenon TPC has a relatively long dead-time, after an event, due to the drift time of the electrons. In case of the MainzTPC the drift time is about 30 μ s – much longer than the time

between photons and neutrons from one electron bunch. If a photon and a neutron originating from one single bunch of accelerator electrons both interact in the MainzTPC, the two S1 signals can be distinguished by TOF. Together with the two S1 signals there will also be two S2 signals in this case, and without using a priori knowledge on the ratio S2/S1 it won't be possible to decide, which of the S2 signals belongs to the photon-S1 and which to the neutron-S1. Therefore it is necessary to make sure, that there is only one interaction of either photon or neutron per bunch of accelerator electrons.

Assuming equal average efficiencies for photons and neutrons of the generated spectra, this requirement means that one needs to suppress the photon flux by a factor of 1000 compared to the neutron flux. In fact, the average interaction probability for the photons is even higher than the one for neutrons. Thus, a suppression of more than a factor of 1000 is desired. Simulations using Geant4, carried out in the framework of another doctoral thesis [Sch18] showed that using a lead absorber of 15 to 18 cm thickness can achieve the required suppression. Of course a thick absorber also reduces the neutron flux at the experimental site but as the bunch-charge of the accelerator can be tuned up to $500 \cdot 10^6$ electrons per bunch and the bunch frequency is changeable from 25 kHz to 100 kHz, the remaining amount of neutrons is still high enough to get interaction rates in the MainzTPC of some kHz.

4.7.2. Neutron interactions in xenon

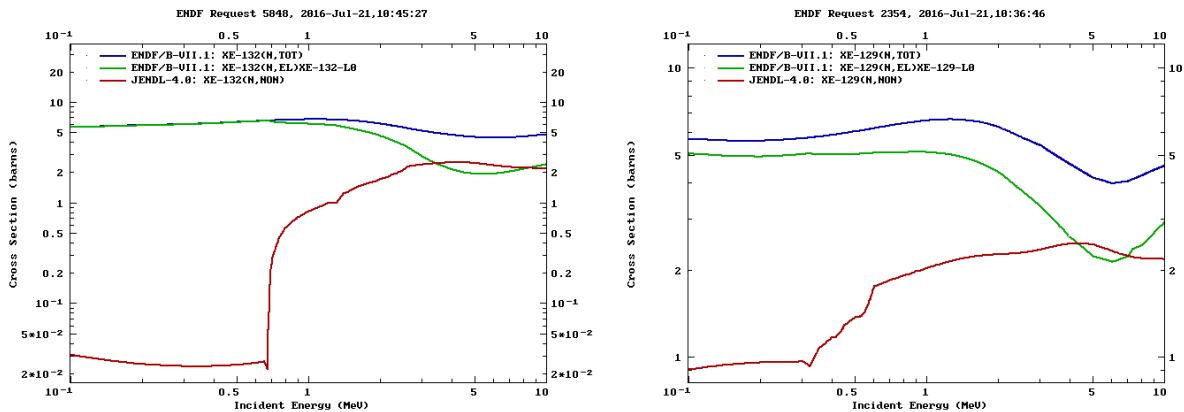


Figure 4.29. Elastic (green), inelastic (red) and total cross-section (blue) of neutrons with ^{132}Xe (left) and ^{129}Xe (right). For the even isotope the inelastic cross-section is negligible up to 0.7 MeV. For the odd isotopes inelastic scattering contributes with about 10% already at low neutron energies, increasing even more around 0.5 MeV. Plots generated using the tools of the International Atomic Energy Agency (IAEA) [IAE16].

Various types of neutron interactions with nuclei exist. Neutrons can scatter elastically off a nucleus – the kind of interaction we want to study – or they can scatter inelastically. Inelastic scattering results in many different final states. Often, the nucleus is excited and emits a gamma

4.7. THE NEUTRON SCATTERING EXPERIMENT

when de-exciting. The de-excitation can be spontaneous, within 1 ns or less, or the excited nucleus is meta-stable and decays only after a comparably long time in the order of days. The elastic and inelastic cross-sections vary with the energy of the primary neutron and with the isotope on which it scatters. In our case we use xenon in natural abundance, i.e. ^{132}Xe , ^{129}Xe and ^{131}Xe make up most of the xenon, some of ^{134}Xe , ^{136}Xe , ^{130}Xe and ^{128}Xe is also contained.

In figure 4.29 the elastic, inelastic and total cross-sections for neutrons with the most abundant even (^{132}Xe) and odd (^{129}Xe) xenon isotopes are shown. For even isotopes, the inelastic cross-section is negligible for neutrons with energies below 0.7 MeV, but starts contributing significantly above 1 MeV. In the range between 4 MeV and 8 MeV inelastic interactions dominate over elastic ones.

For odd isotopes, already at lower energies, the inelastic cross-section makes up for about 10% of the total cross-section. It rises at about 0.5 MeV by a factor of two and, as the elastic cross-section decreases, inelastic interactions dominate for neutrons with 4 MeV to 7 MeV. This is shown exemplary here for two of the isotopes, but is similar for the other even and odd isotopes contained.

Comparing this with the energy spectrum of neutrons at nELBE shown in figure 4.27 Neutrons produced at nELBE mainly are in the range of 1 MeV to 5 MeV. This is in a range, where inelastic interactions for all isotopes play an important role. Therefore we have to expect to see inelastic interactions in the MainzTPC too.

4.7.3. The measurement setup at nELBE

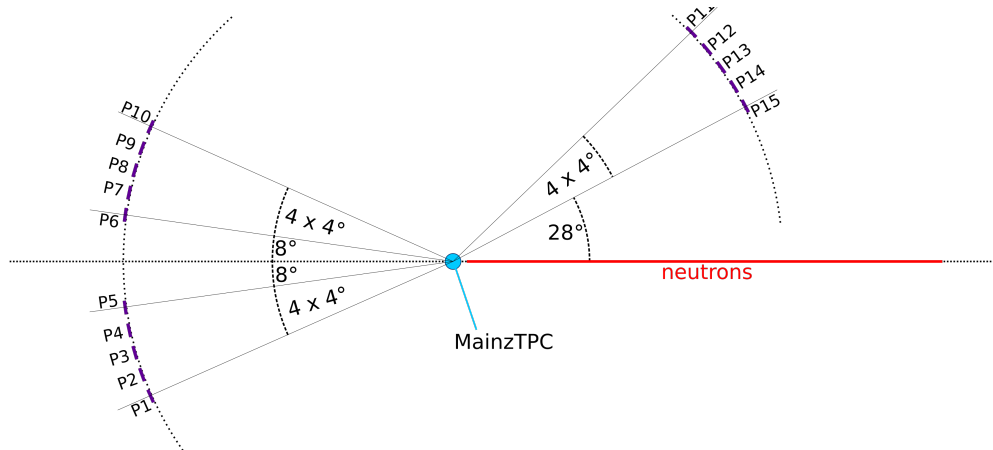


Figure 4.30. Schematic setup of the plastic scintillators around the MainzTPC (active volume). The IDs of the plastic scintillators are stated (P1-P5: forward left, P6-P10: forward right, P11-P15: backward). Scintillators, TPC active volume and distances are to scale. The nominal angles of the centers of the scintillators are given. The separation of two neighboring scintillator panels in one set of five is four degrees.

For the neutron scattering experiment, a set of neutron detectors to detect the scattered neutrons was required. 15 plastic scintillator panels, as described in 4.5 was provided by the group of Dr. A. Junghans (HZDR). Ten of the plastic scintillators have been mounted symmetrically in forward direction, five to the left, and five to the right of the beam axis. The panels were all installed at the same distance (1 m) to the MainzTPC, with their center at the same height as the centers of the neutron beam and the MainzTPC. The center points of the ten scintillator panels mounted in forward direction have been at angles of $\pm 8^\circ$, $\pm 12^\circ$, $\pm 16^\circ$, $\pm 20^\circ$ and $\pm 24^\circ$ with respect to the beam direction.

Five additional scintillator panels have been mounted in back-scattering direction at angles of 136° , 140° , 144° , 148° and 152° to the right of the beam. The backward-panels are also mounted in a distance of 1 m from the center of the TPC. Due to the lack of electronics, only ten of the panels could be operated simultaneously, but having the panels mounted allowed to change quickly from forward scattering only to a setup including backward scattering without losing much beam time. The use of forward and backward scattering, together with the broad energy spectrum of produced neutrons, allows to cover energy deposits in the MainzTPC ranging from below 1 keV up to around 140 keV (table 4.2).

plastic ID			$E_n^0 = 0.5 \text{ MeV}$		$E_n^0 = 1.5 \text{ MeV}$		$E_n^0 = 5.0 \text{ MeV}$	
	Θ_{nom} [$^\circ$]	Θ_{max} [$^\circ$]	$E_{\text{TPC}}^{\text{nom}}$ [keV]	$E_{\text{TPC}}^{\text{max}}$ [keV]	$E_{\text{TPC}}^{\text{nom}}$ [keV]	$E_{\text{TPC}}^{\text{max}}$ [keV]	$E_{\text{TPC}}^{\text{nom}}$ [keV]	$E_{\text{TPC}}^{\text{max}}$ [keV]
5 + 6	8.0	27.7	0.07	0.86	0.22	2.58	0.73	8.59
4 + 7	12.0	29.0	0.16	0.94	0.49	2.82	1.64	9.41
3 + 8	16.0	30.1	0.29	1.05	0.87	3.16	2.91	10.54
2 + 9	20.0	32.1	0.45	1.20	1.36	3.60	4.53	11.99
1 + 10	24.0	35.2	0.65	1.38	1.95	4.13	6.50	13.75

plastic ID			$E_n^0 = 0.5 \text{ MeV}$		$E_n^0 = 1.5 \text{ MeV}$		$E_n^0 = 5.0 \text{ MeV}$	
	Θ_{nom} [$^\circ$]	Θ_{min} [$^\circ$]	$E_{\text{TPC}}^{\text{nom}}$ [keV]	$E_{\text{TPC}}^{\text{min}}$ [keV]	$E_{\text{TPC}}^{\text{nom}}$ [keV]	$E_{\text{TPC}}^{\text{min}}$ [keV]	$E_{\text{TPC}}^{\text{nom}}$ [keV]	$E_{\text{TPC}}^{\text{min}}$ [keV]
11	136.0	130.1	12.93	12.36	38.78	37.07	129.27	123.56
12	140.0	133.3	13.28	12.67	39.83	38.01	132.78	126.70
13	144.0	136.4	13.60	12.96	40.80	38.88	136.01	129.59
14	148.0	139.3	13.89	13.22	41.68	39.66	138.94	132.21
15	152.0	142.2	14.16	13.46	42.47	40.37	141.57	134.56

Table 4.2. The two tables show the nominal positions of the plastic scintillators (Θ_{nom}) and the maximum scattering angle of neutrons their end cover (Θ_{max}). Energy deposits for neutrons with incoming energies of 500 keV, 1.5 MeV and 5 MeV are shown, for the nominal and the maximal scattering angle. In contrast to forward scattered neutrons the neutrons hitting the plastic scintillators at backward positions on their ends are scattered under smaller angles than the nominal angle. Energy deposits in the MainzTPC range from below 1 keV to 14 keV for the forward-scattering panels and 12 keV to 140 keV for the backward scattering panels.

4.7.4. Measurement of the energy deposits in the MainzTPC

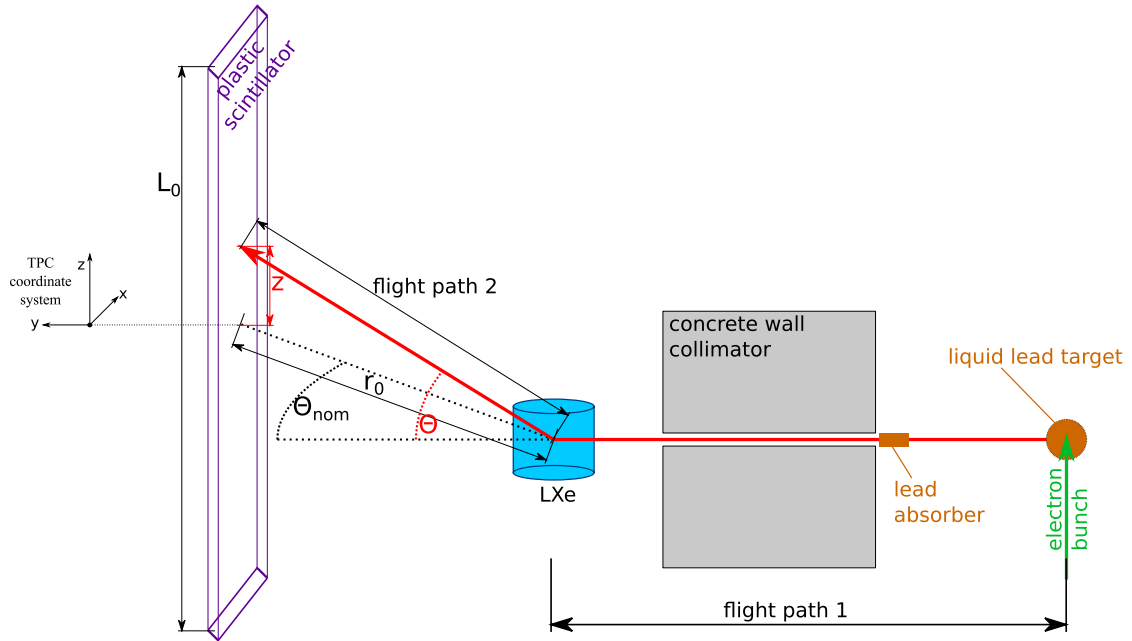


Figure 4.31. Illustration of the scattering geometry in a schematic, partly 3-dimensional view. On the right, the neutrons are generated by dumping a bunch of high-energetic neutrons on a liquid lead target, the neutrons are then guided by a collimator through a thick concrete wall. Gammas that are also produced are to large amounts absorbed by a lead-absorber (9-18 cm have been used) placed in front of the collimator. The flight path 1 (5.9 m) is shown, and the nominal angle of the scintillators (Θ_{nom}) and the real scattering angle (Θ) are shown. For our experiment we use the coordinate system typically used for liquid xenon TPCs, with the z-axis being the drift direction in the TPC. The center of the MainzTPC-active volume is at the coordinates (0/0/0) and the center of the plastic scintillators are in a plane at $z=0$.

The prerequisite to measure the response of liquid xenon, is to properly measure the energy deposit in liquid xenon. This measurement is done by measuring the energy of the incoming neutron (E_n^0) and of the scattered neutron (E_n^1). The energy deposit in the TPC is $E_{\text{TPC}} = E_n^0 - E_n^1$. Measurement of E_n^0 can only be done using TOF, which is what the nELBE is designed for. To measure E_n^1 one has two options: either measure the scattering angle to calculate the energy deposit or to measure the second TOF, from scattering target to the secondary detector. This is of course, only possible if the scattering target itself is a detector, like in our case the MainzTPC. Both methods can be combined, to improve the result and to discriminate chance coincidences and multiple scatters.

Measuring the neutron energy using TOF, the uncertainty is made up of uncertainties of the measurement of the length of the flight path and uncertainties of the measurement of the time-of-flight. In case of E_n^0 , the former has contributions of the uncertainty of the production position, the interaction position inside the MainzTPC and the positioning of the MainzTPC itself. The production position is known to < 1 cm, the positioning of the MainzTPC is accurate within

0.5 cm, and the interaction position is given by the resolution achieved with the APDs and the drift time. Without using the 3D-position resolution, the uncertainty of interaction position is defined by the thickness of the active volume (5 cm), and therefore the major contribution. Deviations perpendicular to the beam-direction are negligible, due to the long flight path of 5.985 m to the center of the MainzTPC. The uncertainties of the measurement of the TOF, are made up of the length of the electron bunch (25 ps) [HZD17] and the time resolution of the MainzTPC. The length of the electron bunch is negligible compared to the time resolution of the MainzTPC. For higher energy deposits, resulting in many scintillation photons, the time resolution of the MainzTPC is given by the response of the used PMTs ($t_{rise} = 2.3 \text{ ns}$). For low energy deposits, which generate just a few photons, the time resolution is dominated by the time scales of the scintillation process, typically several nanoseconds.

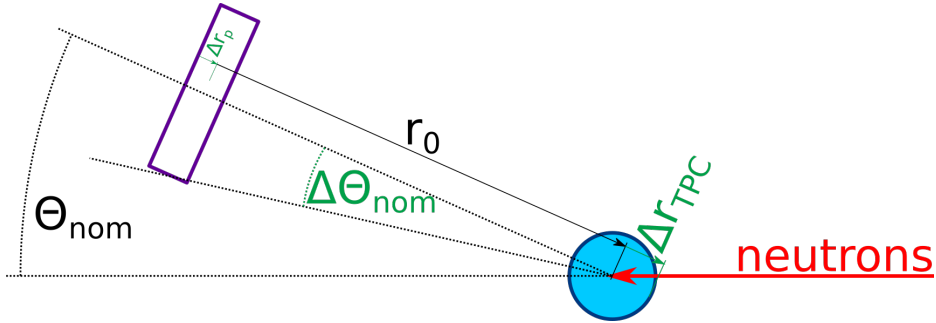


Figure 4.32. To estimate the uncertainties of the measurement of energy-deposits in liquid xenon, some assumptions on uncertainties in the measurements have to be done. The uncertainties used in the calculations are illustrated here.

Uncertainties for the measurement of E_n^1 using TOF again has contributions of the length of the flight path and the time response of the detectors (MainzTPC, plastic scintillators). For the time resolution the contribution of the MainzTPC is exactly the same as for the measurement of E_n^0 , the contribution of the plastic scintillators is comparably small, as their PMTs have higher gains. The measurement of the second flight path contributes strongly to the overall uncertainty, as it includes not only the uncertainty on the interaction position in the MainzTPC, which can be relatively well determined using the 3D position resolution, but the interaction position in the plastic scintillator is not known very well. Here the thickness of the panel (11 mm), the width of the panel (42 mm) and the position resolution in the plastic (5-5.5 cm) [BGH⁺07] are not negligible compared to the length of the second flight path, which is 1 m to 1.12 m, depending on z-position of the interaction on the plastic scintillator.

Measurement of E_n^1 can also be done using the scattering angle. This measurement suffers from the same uncertainties in measuring the interaction position in the plastic scintillators, as the pure TOF measurement does. Of course, both methods could be combined using, e.g. a maximum likelihood method, to achieve best results.

4.7.5. Uncertainties

4.7.5.1. Double Time-of-flight measurement

One approach to determine the energy deposit in the liquid xenon TPC consists of measuring the TOF before and after scattering. For such a double TOFTOF measurement the energy deposit in the TPC is calculated from:

$$E_{\text{TPC}} = E_n^0 - E_n^1$$

As the neutrons at nELBE have non-relativistic energies we can write this as:

$$E_{\text{TPC}} = \frac{1}{2} \cdot m_n \cdot (v_0^2 - v_1^2)$$

Using Gaussian error propagation one finds:

$$\left(\frac{\Delta E_{\text{TPC}}}{E_{\text{TPC}}} \right)^2 = \left[\frac{\left(\frac{\Delta t_0^2}{t_0^2} + \frac{\Delta d_0^2}{d_0^2} \right) \cdot (E_n^0)^2 + \left(\frac{\Delta t_1^2}{t_1^2} + \frac{\Delta d_1^2}{d_1^2} \right) \cdot (E_n^1)^2}{(E_n^0 - E_n^1)^2} \right] \cdot 4 \quad (4.1)$$

If we assume an uncertainty of the time measurements $\Delta t_0 = \Delta t_1 = 0.5$ ns and an uncertainty of the first flight path of $\Delta d_0 = 2$ mm given by the projected position resolution of the MainzTPC and of the second flight path of $\Delta d_1 = 1.2$ cm given by the thickness of the scintillator panels, we find for a 1.5 MeV neutron that deposits 10 keV in the TPC a relative uncertainty of the energy deposit of

$$\frac{\Delta E_{\text{TPC}}}{E_{\text{TPC}}} = 2.197 \approx 220\%$$

For energy deposits below 10 keV this is even worse. Therefore, double TOF will not provide the required energy resolution to directly measure E_{TPC} . Nevertheless, it is an important tool to discriminate elastic neutron scatters from inelastic ones and from pile-up of coincident γ and neutron interactions, as will be shown in section 7.2.

4.7.5.2. Scattering angle

If we want to use the scattering angle to measure the energy deposit in liquid xenon, we still need to use a TOF measurement to determine the energy of the primary neutron. The relative error is given by:

$$\frac{\Delta E_n^0}{E_n^0} = \frac{2}{d_0} \sqrt{\Delta d_0^2 + \Delta t_0^2 \frac{2 \cdot E_n^0}{m_n}} \quad (4.2)$$

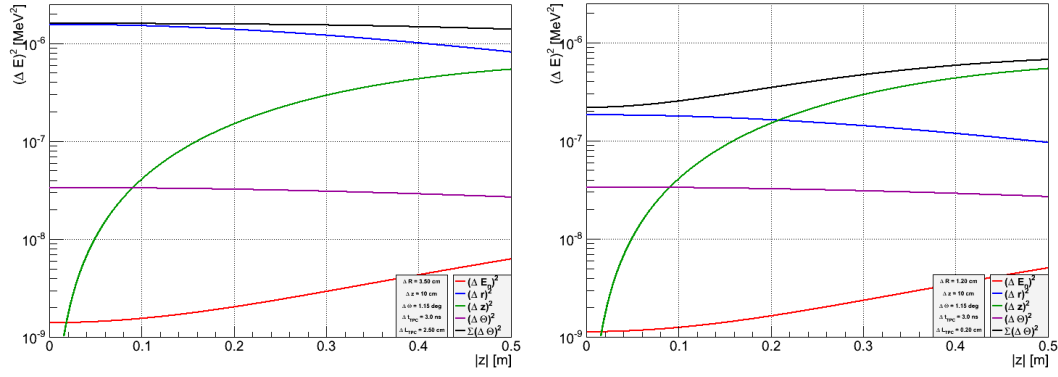


Figure 4.33. Squared contributions to the uncertainties for the plastic scintillator placed at 24 degrees for a neutron of 1.5 MeV primary energy. On the left, without applying position resolution in the TPC, on the right with x/y-position reconstruction with an uncertainty of 2 mm.

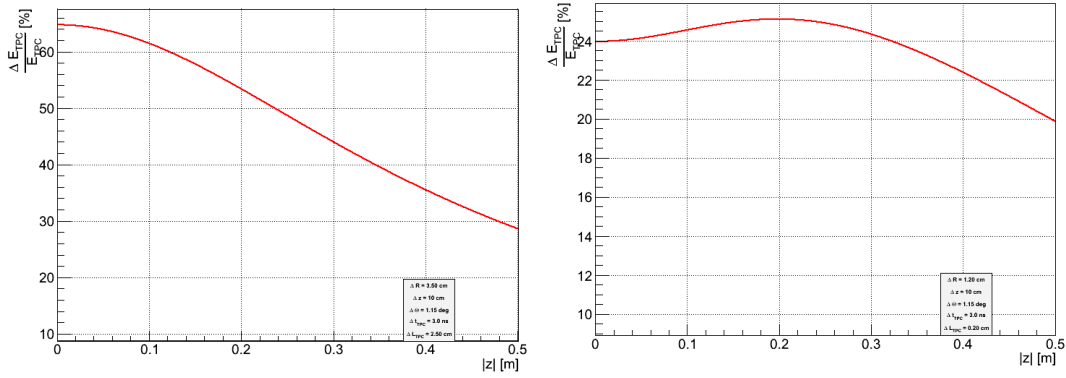


Figure 4.34. Relative uncertainty for the plastic scintillator placed at 24 degrees for a neutron of 1.5 MeV primary energy. Without position resolution applied, the energy resolution is far worse than with applied x/y-position reconstruction.

If no position resolution in the TPC is applied and the time measurement is assumed to be $\Delta t_0 = 3$ ns we get:

$$\frac{\Delta E_n^0}{E_n^0} = 2.45 \%$$

for $E_n^0 = 1.5$ MeV. The assumption if a time resolution of only 3 ns here is based on the width of the gamma-flash as measured later. This might be a very conservative assumption, but the main contribution of the error anyway comes from the uncertainty in the interaction position in the TPC.

The kinematics of an elastic neutron scattering process is given by:

$$E_{\text{TPC}} = E_n^0 \frac{2 \cdot m_n \cdot m_{Xe}}{(m_n + m_{Xe})^2} (1 - \cos \Theta) \quad (4.3)$$

4.7. THE NEUTRON SCATTERING EXPERIMENT

The maximum energy deposit is for $\Theta = 180^\circ$. If we use the atomic mass numbers for neutron ($m_n = 1$) and xenon ($m_{Xe} = 131$) we find:

$$E_{TPC}^{\max} = E_n^0 \frac{2 \cdot 1 \cdot 131}{(1 + 131)^2} (1 - (-1)) \approx \frac{E_n^0}{33} \approx 0.015 \cdot E_n^0 \quad (4.4)$$

That means, neutrons can transfer a maximum of about 1.5% of their original energy to when scattering elastically. Therefore, the velocity of the neutron is similar before and after scattering.

The scattering angle Θ in equation 4.3 can be written as a function of the nominal scattering angle Θ_{nom} , corresponding to the position of the plastic scintillator panel, and the z-position of the interaction on the plastic:

$$\Theta(z, \Theta_{nom}) = \arccos\left(\frac{r}{\sqrt{z^2 + r^2}} \cdot \cos(\Theta_{nom})\right) \quad (4.5)$$

where r: the distance between center of the TPC and the plastic as shown in figure 4.32. Using these formulas one can apply Gaussian error propagation and calculate the contributions to the overall uncertainty of the measurement of the energy deposit in the TPC:

- $\left(\frac{\partial E_{TPC}}{\partial E_n^0}\right)^2 \cdot (\Delta E_n^0)^2$: Contribution of the uncertainty on the primary neutron energy.
- $\left(\frac{\partial E_{TPC}}{\partial r}\right)^2 \cdot (\Delta r)^2$: Contribution of the uncertainty of the distance from the interaction position in the TPC and the interaction position in the plastic. $\Delta r = 3.5$ cm assumes no position resolution in the TPC (2.5 cm) and no knowledge of the radial position of the interaction in the scintillator (thickness of the panel = 1 cm).
- $\left(\frac{\partial E_{TPC}}{\partial z}\right)^2 \cdot (\Delta z^0)^2$: The contribution of the uncertainty on the z-position of the interaction in the plastic scintillator $\Delta z = 10$ cm.
- $\left(\frac{\partial E_{TPC}}{\partial \Theta_{nom}}\right)^2 \cdot (\Delta \Theta_{nom})^2$: The contribution due to the width of the plastic scintillator panel.
 $\Delta \Theta_{nom} = 1.15^\circ = 0.02$

With these assumptions and our geometry, one can plot the different contributions. For a primary neutron energy of 1.5 MeV and the plastic scintillator in forward direction, the squared contributions for a 1.5 MeV neutron are shown in figure 4.33. One can see that the main contribution comes from the uncertainty in r which can significantly be improved by applying x/y-position reconstruction. Even without position reconstruction, the relative uncertainty on E_{TPC} is much lower than for the double TOF method and gets even better if position reconstruction is applied (figure 4.34).

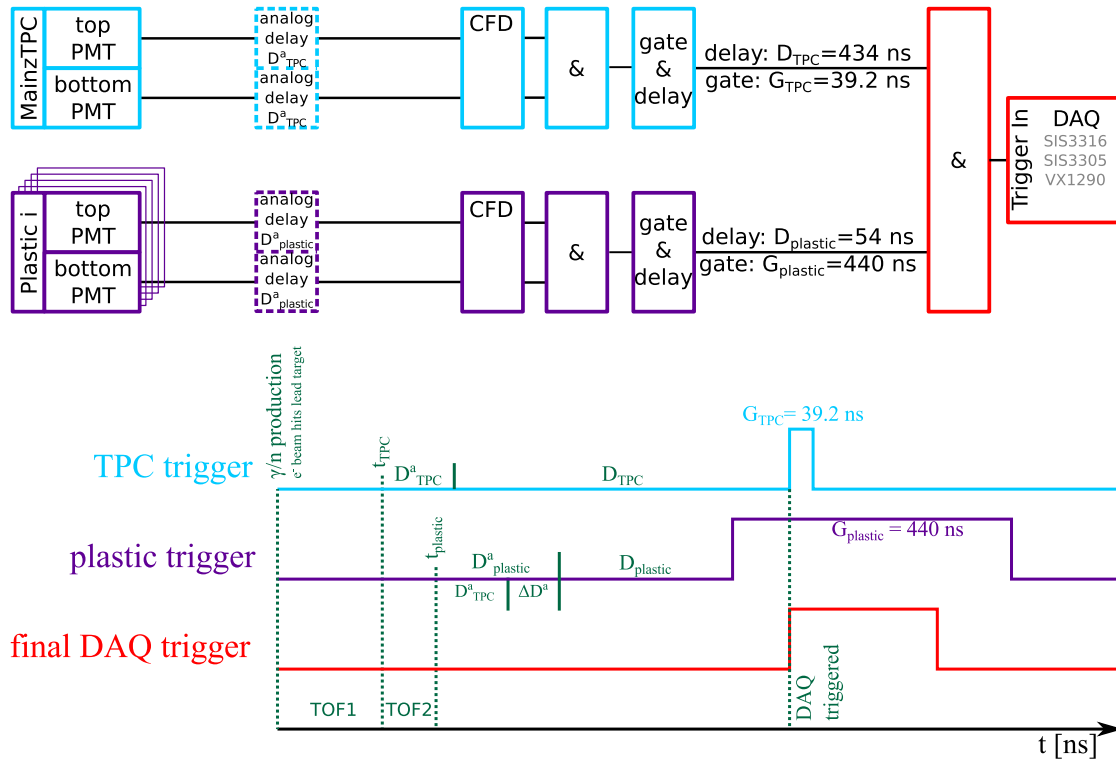


Figure 4.35. The schematic in the upper part illustrates the generation of the trigger. In addition to the delay artificially generated by the gate&delay module, there might be a delay in the generation of the analog signal due to the scintillation processes, the electron multiplication process in the PMTs and the cables and amplifiers between PMTs and CFD modules. The individual delays have not been measured, as they are not of interest. The important quantity is the difference between the analog delay of the MainzTPC and the analog delay of the plastic scintillators. From the measurement data taken, one can infer that the analog delay of the plastic scintillators is about 20 ns longer than for the MainzTPC.

In the lower part the three triggers, TPC trigger, plastic trigger and (final) DAQ trigger, are illustrated. The intention of the setup is to trigger the DAQ at the leading edge of the TPC trigger, as shown here. The different delays and gate widths are also shown.

4.7.6. Trigger Setup

The trigger for the DAQ is generated by delaying the so-called TPCtrigger relative to the plastic-Trigger by $(434 - 54) \text{ ns} = 380 \text{ ns}$. The plastic trigger opens a gate of 440 ns, whereas the gate of the TPC trigger has a length of 39.2 ns. As the TPC trigger is delayed, the leading edge of the TPC trigger should always generate the final trigger for the DAQ. In the schematic (figure 4.35) analog delays of the detector signals (D_{TPC}^a and D_{plastic}^a) before the CFDs are shown. These delays originate from the scintillation process, the transit time in the PMTs and the cables from PMT to CFD. These delays differ between TPC and plastic scintillators and were not measured in advance. However, as we recorded the TPC trigger and the plastic trigger with the TDC we could

4.7. THE NEUTRON SCATTERING EXPERIMENT

use events triggered by gammas (and therefore known TOF2) to infer the effective delay

$$\Delta D^a = D_{\text{plastic}}^a - D_{\text{TPC}}^a$$

of the analog signal being about 20 ns longer for the plastic scintillators compared to the MainzTPC.

Two conditions must be fulfilled to generate the trigger by the MainzTPC: the leading edge of the TPC trigger must be after the leading edge of the plastic trigger

$$t_{\text{TPC}} + D_{\text{TPC}}^a + D_{\text{TPC}} > t_{\text{plastic}} + D_{\text{plastic}}^a + D_{\text{plastic}} \quad (4.6)$$

and before the end of the gate opened by the plastic scintillators.

$$t_{\text{TPC}} + D_{\text{TPC}}^a + D_{\text{TPC}} < t_{\text{plastic}} + D_{\text{plastic}}^a + D_{\text{plastic}} + G_{\text{plastic}} \quad (4.7)$$

In both equations (4.6, 4.7) the symbols are defined as shown in figure 4.35: D_{plastic}^a and D_{TPC}^a are the analog delays of the cables connecting the PMTs with the CFDs, D_{plastic} and D_{TPC} the delays and G_{plastic} and G_{TPC} the gates introduced by the gate and delay generator. t_{TPC} and t_{plastic} are the times of interaction in the TPC and the plastic scintillators. The TOF from TPC to plastic scintillator TOF2 therefore is:

$$\text{TOF2} = t_{\text{plastic}} - t_{\text{TPC}}$$

Plugging the chosen values (which can be found in figure 4.35) into equation 4.6 we find:

$$\text{TOF2} < 360 \text{ ns} \quad (4.8)$$

As the flight path from TPC to plastic scintillators is 1 m, this condition is clearly fulfilled for photons ($\text{TOF2} = 3.3 \text{ ns}$). Neutrons need a kinetic energy of more than 10 keV to be faster than 360 ns for a flight path of 1 m. For the neutron spectrum of nELBE and the maximum energy loss for elastic scattering in xenon this is always the case.

In fact, even slower neutrons with

$$\text{TOF2} < 399.2 \text{ ns} = (360 + G_{\text{TPC}}) \text{ ns}$$

would generate a trigger, but the DAQ would in this case be triggered at the leading edge of the plastic gate instead of the TPC. This is illustrated for a 36 keV neutron in figure 4.36. Of course, this can be found in data afterwards, as TPC trigger, plastic trigger and final trigger are recorded with the TDC.

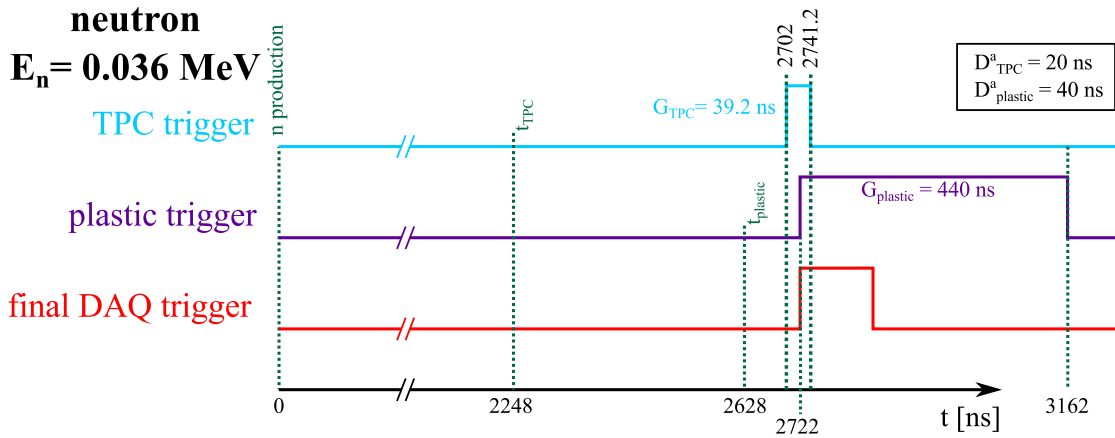


Figure 4.36. The trigger gates as they would occur for a very slow neutron (36 keV). In this case, the DAQ would be triggered at the leading edge of the plastic scintillator gate, and not as intended at the leading edge of the TPC trigger. This happens only for very slow neutrons, which are very rare at nELBE or for two independent particles. Such triggers can be found in the data afterwards, as the triggers are recorded with the TDC.

The second condition (equation 4.7) leads to:

$$\text{TOF2} > -80 \text{ ns} \quad (4.9)$$

This is of course always true as no particle is faster than the speed of light or could even travel backwards in time. Figure 4.37 shows the gates and trigger states for photons, typical nELBE neutrons with $E_n = 1.5 \text{ MeV}$ and slow nELBE neutrons with $E_n = 0.5 \text{ MeV}$, the time starting from the particle production (i.e. the ELBE electron beam hitting the liquid lead target) and reaching up to the time when the DAQ is triggered. It does not cover the drift time of electrons in the TPC, as this is more than one order of magnitude slower. Of course, there is a hold-off for the DAQ trigger during the drift time and while the DAQ is recording. Additionally there is a veto by the accelerator clock which is also not shown.

Although the trigger setup covers all particles scattering in the MainzTPC towards the plastic scintillators, i.e. the events we are interested in, it allows for background events to generate triggers, too. These background events are events where the trigger is generated by two independent particles in the TPC and the plastic scintillator. If both particles are gammas and therefore equally fast, this cannot be differentiated from a single gamma scattering in the TPC towards a plastic scintillator. It is in general clear, that two particles with similar velocities will generate a trigger. This holds for two independent gammas, as well as for two independent neutrons. Triggers can even be generated for events in the wrong time-order, i.e. the interaction in the plastic scintillator occurring before the interaction in the TPC. For example, a 1.5 MeV neutron interacting in the TPC, can generate a trigger together with neutrons interacting in the plastic scintillator in the energy range from 0.5 MeV up to 3.5 MeV. That means, two independent neutrons in the most

4.7. THE NEUTRON SCATTERING EXPERIMENT

commonly produced energy range at nELBE will generate triggers. More example calculations, based on equations 4.7 and 4.6 can be found in appendix B.

From these tables one can also see that triggers of a gamma in the TPC combined with a neutron interacting in the plastic scintillator ($E_n > 1.78$ MeV) can occur. Even if the neutron energy is only above 1.46 MeV a trigger is generated, although the by the leading edge of the plastic gate.

Gammas or neutrons that pass the TPC without interacting there, travel through the experimental hall and hit a so-called beam-dump consisting of lead, at the back wall. Gammas might be backscattered there and maybe additionally at the walls of the room and reach the plastic scintillators or the TPC then. As the length of the room is 8 m their minimal flight path from the production site is twice the room length plus the distance from production site to the experimental hall, but it might be longer, when scattering on the walls or anything else in the room. Their flight path can therefore be assumed to be longer than 20 meters, which corresponds to a TOF of more than 66 ns. These gammas can also contribute to trigger generation, either two of them (one in the TPC and one in the plastic scintillator) or only one of them scattering from the TPC towards the plastic scintillators (or vice versa). These backscattered gammas in combination with a direct particle can also lead to triggers, e.g. one direct gamma interacting in the TPC and a backscattered one in the plastic scintillator. A backscattered gamma in the TPC would even generate a trigger together with a neutron ($E_n \gtrsim 1.5$ MeV) interacting in one of the plastic scintillators only.

The following list summarizes the combination of particles that lead to triggers of **unwanted background** events:

neutron(TPC) - neutron(plastic): two independent neutrons with similar kinetic energies or with the neutron interacting in the TPC having a higher kinetic energy than the one in the plastic scintillator

gamma(TPC) - gamma(plastic): two independent gammas

gamma(TPC) - neutron(plastic): for neutron energies in the range $E_n > 1.78$ MeV (or $E_n > 1.46$ MeV, although the DAQ is triggered by leading edge of plastic trigger in this case)

neutron(TPC) - gamma(plastic): requires a neutron energy $E_n > 17.5$ MeV, which is unlikely at nELBE

backscattered gamma (TPC) - backscattered gamma (plastic): either by two backscattered gammas or by only one scattering in TPC and plastic scintillator

gamma - backscattered gamma: both triggers, the direct gamma in the TPC and the backscattered one in the plastic scintillator or vice versa

backscattered gamma (TPC) - neutron (plastic): requires $E_n > 1.5$ MeV

neutron (TPC)- backscattered gamma (plastic): requires $E_n > 10$ MeV

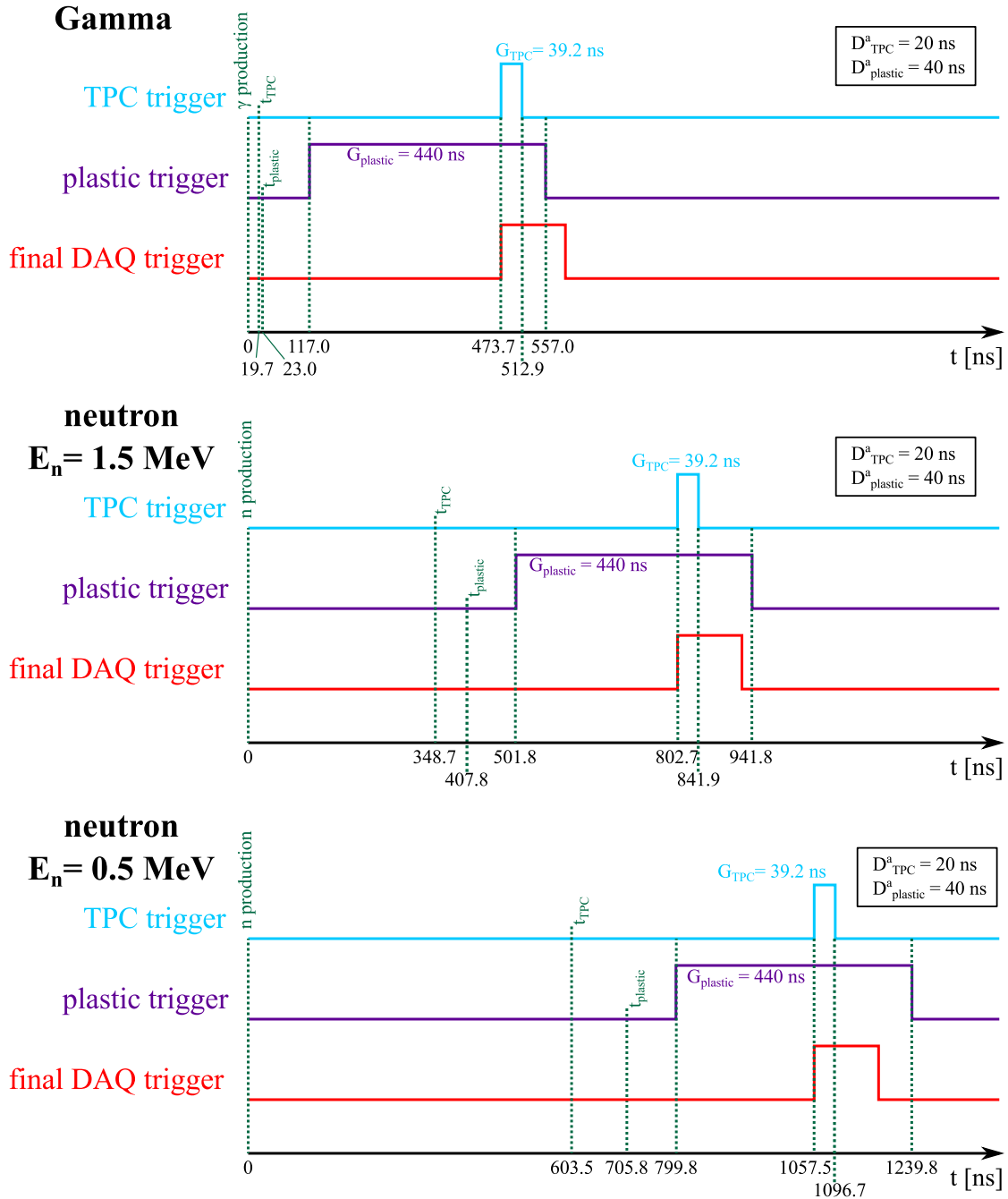


Figure 4.37. Trigger states for TPC trigger, plastic trigger and DAQ trigger for different scattered particles: Gammas, typical nELBE neutrons $E_n = 1.5 \text{ MeV}$ and slow nELBE neutrons $E_n = 0.5 \text{ MeV}$. The analog delays D_{TPC}^a and D_{plastic}^a have not been measured, but the difference of the two ΔD^a has been extracted from data to be 20 ns. In the drawing the analog delay of the TPC is assumed to originate from the length of the cables (5 m) only and a value of 20 ns is used. Neither the DAQ trigger hold-off during the TPC drift time and DAQ recording nor the veto by the ELBE accelerator clock is shown here.

For the fastest particles (gammas), the DAQ is triggered close to the end of the gate opened by the plastic scintillator, due to the long delay of the TPC trigger. For slower particles, the DAQ trigger is generated earlier in the plastic gate. But the gate is long enough to cover even very slow neutrons with $E_n > 10 \text{ keV}$.

4.7. THE NEUTRON SCATTERING EXPERIMENT

Of course, the probabilities for those kind of events cannot be easily estimated, one has to simulate the setup and experimental hall to obtain proper numbers. We will see in section 7.2 that there definitively is a non-negligible amount of different types of background events.

5. Raw Data Analysis - Framework and Algorithms

5.1. Data Format and Analysis Framework

5.1.1. Raw Data Format

The data format is following the class-structure of the analysis framework. In the following only a short description of the data format will be given. A more extensive description will be contained in [Sis17].

Each of the major classes has a header, containing general information. The headers representing hardware like (FADC) board, channel, sensor contain information about the hardware. Board headers for example contain the sampling frequency and resolution of the FADC and sensor header contains the sensor type (PMT, APD, ...), among other values. There are also headers for DAQ run, acquisition period, event, waveform and TDC data. The latter provide run and trigger related information, such as run start- and end-time, number of events.

The data is written to several files per run, where files exist in three hierarchies. The highest hierarchy holds one file, containing the run, FADC board, channel, TDC board, TDC channel and sensor headers. The next level contains one file per acquisition period. The DAQ software automatically stops the DAQ system if certain criteria are fulfilled, copies the data from the VME boards to the DAQ computer and restarts the VME boards. A time window, where the VME boards are active and acquire data, is called acquisition period. The file on the second level holds the acquisition period header, containing information on the current acquisition period, such as start and end time and the number of events in this acquisition period. On the third level there are two parallel files, one containing the FADC data including waveform headers and the waveform data, the second one containing the data from the TDC.

5.1.2. Analysis Framework

The analysis framework is built using the object oriented programming language C++. The framework itself is built in an object oriented way, reflecting objects existing in reality like FADC

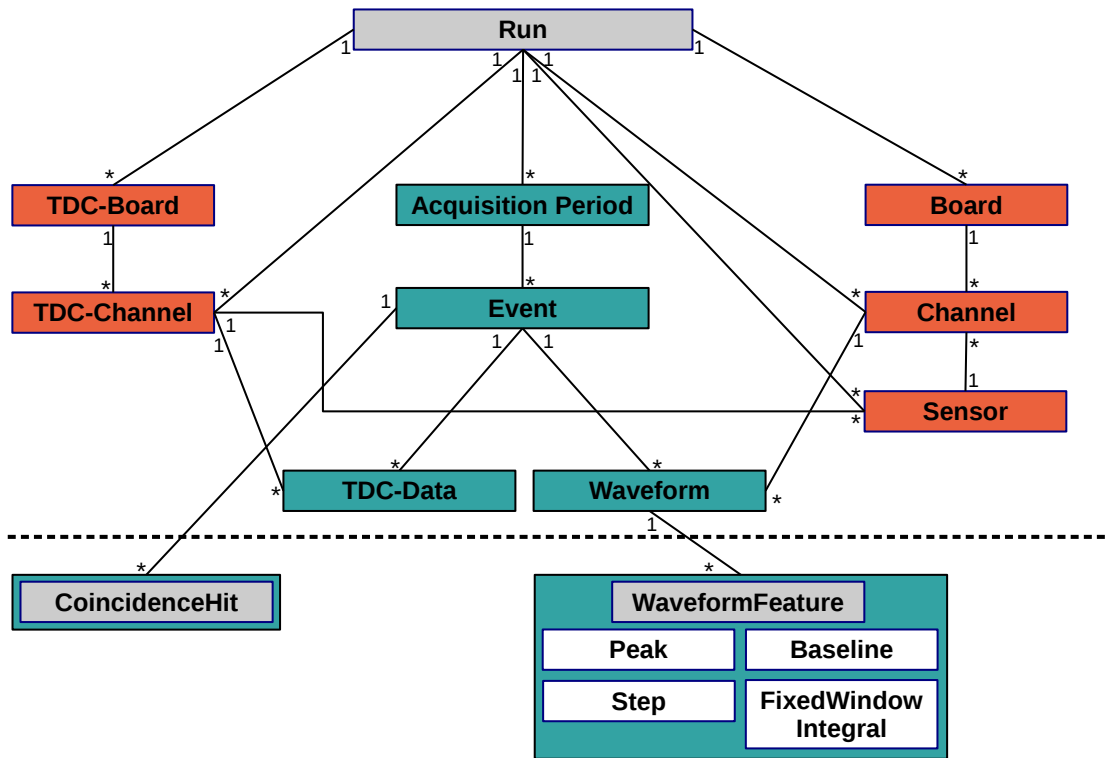


Figure 5.1. Simplified class diagram of the analysis framework. Red are classes that represent hardware, turquoise are classes that represent non-physical entities. The classes above the dashed line are filled by reading the raw data files, whereas the classes below the dashed line are used by analyzers to store analysis results. The meaning of the symbols on the connections like “1”, “*” and full/open arrows follow the definitions of UML.

boards and their channels and sensors. It is extended with virtual (=non physical) entities like Events, Waveforms and chunks of TDC data. Objects above the dashed line in the class diagram (figure 5.1) are objects that are generated and filled with information by reading the raw data files written by the DAQ software. Objects below the dotted line are generated and filled by the analysis routines.

In the class-diagram (figure 5.1) waveforms are represented in a simplified way. In reality, for the waveforms the so-called decorator pattern is used. The class *MainzWaveform*, is an abstract super class, with two classes inheriting from it: the class *RawDataWaveform* and the (again abstract) class *FilteredWaveform*. The data read from the raw data files is stored in *RawDataWaveform* entities, whereas *FilteredWaveforms* typically do not store any data, but provide a filtered view of the *RawDataWaveform*. Normally, *FilteredWaveforms* are computed on-the-fly when their data is accessed, but one can pre-compute the complete waveform, for efficiency reasons. Several implementations of the abstract class *FilteredWaveform* exist, those are described in section 5.2.

The analysis system is based on the visitor pattern, which will be explained in the next section. Different analyzer classes each with specific tasks inherit from the abstract class *Analyzer*. Each *Analyzer* can then visit objects of type *Run*, *Event*, *Waveform* etc. and go down in the hierarchy of these classes in a predefined way, executing a certain analysis step on each level before and/or after descending to the next level. This provides a flexible way of analyzing the raw data in different ways. Different analyzers are implemented, such as peak and step finders. The peaks and steps found can be stored in ROOT files [CER17] for further usage, this is done using another *Analyzer*.

The analysis framework in general and the different analyzers in particular, can be configured via a extended markup language (XML) configuration file. This configuration file is read by an entity of the class *MainzXMLConfig*, which is implemented as a singleton object (a class that can only be instantiated once) and provides the information from the file to other objects (e.g. *analyzers*). To parse the XML file, the library *libxml++* is used. An example of such an XML configuration file including explanatory comments can be found in the appendix C.

To keep the output generated by the analysis routines together with the results of the analysis, another class called *AnalysisLogger* is implemented, making use of *Tee* and *Stream* from the boost-libraries. This class is again implemented as singleton. It copies all output sent by any class of the framework to standard output (i.e. *cout*) of the operating system into a text file.

The analysis framework also contains a class called *DataViewer*, which is meant to display the recorded waveforms. The *DataViewer* can also run the Analyzers used for peak finding, step finding and step fitting and display the peaks and steps found and the filtered waveforms used by the algorithm.

Currently, the analysis in the framework is primarily used for peak finding, step finding and fitting of the FADC waveforms, and to find *CoincidenceHits* (see section 5.7) on the data recorded by the TDC. The found *Peaks*, *Steps* and *CoincidenceHits* are then stored in ROOT trees. Higher level analysis is done using ROOT-based scripts.

5.1.2.1. Visitor pattern: Analyzer

Using the visitor pattern, allows to use different analysis routines and combinations of those on different levels. In the following, the principle is explicitly explained using a generalized example: Let's assume we want to analyze a whole dataset using the exemplary analyzer *AnalyzerPeakFinder*. The Code snippet in figure 5.2 shows, how one would read a set of data files into the framework, using the member function *Run::readFile(std::string PathToFile)* and running an analyzer named *AnalyzerPeakFinder* on the dataset.

```

1  std::string allFiles[nFiles]; //we create an array containing the path of all files that belong
   to the dataset
2  readFileNames(allFiles); //somehow get the path of all files into the array...
3  Run * currentRun = new Run(); // we create an empty object of class Run called currentRun
4
5  //we read all files
6  for(int i=0; i< nFiles; i++)
7  {
8      currentRun->readFile(allFiles[i]);
9  }
10
11 AnalyzerPeakFinder *myPF = new AnalyzerPeakFinder(); //create the Analyzer
12 currentRun->analyzeViaAqPeriod(myPF); //we call the member-function analyzeViaAqPeriod of the
   class "Run" and supply as argument our analyzer

```

Figure 5.2. Example for a simple main program, i.e. a `int main(int argc, char **argv)` function. This example illustrates how to read data files into the framework and start an analysis using an exemplary analyzer of type `AnalyzerPeakFinder`.

In 5.3 an expanded version (pseudo-code) is illustrating, what the call to the function `Run::analyzeViaAqPeriod(Analyzer *an)` does in the background. The call leads to a descent through the hierarchy of the run through all levels down to Peaks and Steps. On each level, three functions are called:

- `Analyzer::analyzePre(currentObject)`
- `currentObject::analyze(Analyzer *)`
- `Analyzer::analyzePost(currentObject)`

Here `currentObject` is a replacement for objects of different types (from the classes is the framework). Notice the overloaded functions `AnalyzerPeakFinder::analyzePre(Object *)` and `AnalyzerPeakFinder::analyzePost(Object *)`. Of course, these functions can be empty, i.e. doing nothing. For each level the call to `currentObject->analyze(Analyzer *an)` is the one that implements the loop over all elements of the next lower level. To get an idea, what `AnalyzerPeakFinder` could do at the different stages, figure 5.4 shows an exemplary pseudo-code implementation of the analyzer.

The visitor pattern allows a flexible way of writing common analyzers and using them to analyze the data. It also allows combining analyzers. A good example of how to combine Analyzers using the visitor pattern is a step finding analyzer for the APD waveforms, (let's call this analyzer `AnalyzerAPDStepFinder`). This `Analyzer` (which does not exist yet) could for example check in the function `AnalyzerAPDStepFinder::analyzePre(Event *evt)`, if a peak finder has already found peaks on the PMT waveforms. If not it could generate an entity of type `AnalyzerPeakFinder` and run this on the PMT waveforms. The analyzer now can use the position of the S2 peaks, to search for steps on the individual APD waveforms in its `analyzePre(Waveform *wf)` method.

```

1 //Using pseudo-code here:
2 myPF->analyzePre(currentRun); //doing what should be done before analyzing a "Run"
3 for(i=0; i<nAcquisitionPeriods; i++) //loop over all acquisitionPeriods of the run-object
4 {
5     myPF->analyzePre(currentAqPeriod); //doing what should be done before analyzing an
6     AcquisitionPeriod
7     for(int j=0; j<nEvents; j++) //loop over all events of the current AcquisitionPeriod-object
8     {
9         myPF->analyzePre(currentEvent); //doing what should be done before analyzing an Event
10        for(k=0; k<nWaveforms; k++) //loop over all waveforms of that event
11        {
12            myPF->analyzePre(currentWaveform);
13            for(l=0; l<nPeaks; l++)
14            {
15                > currentPeak->analyze(myPF); //we cannot descend any further, so we call the
16                member-function "analyse(Analyzer *)" of the deepest element; In the higher
17                levels, the loops for the next lower levels are implemented in the function
18                "analyse"; e.g. event->analyse(Analyzer *an) loops over all waveforms of the
19                event...
20            }
21            myPF->analyzePost(currentWaveform);
22        }
23        myPF->analyzePost(currentEvent); //doing what should be done after analyzing a
24        waveform
25    }
26    myPF->analyzePost(currentAqPeriod); //doing what should be done after analyzing an AqPeriod
27 }
28 myPF->analyzePost(currentRun); //doing what should be done after analyzing a Run

```

Figure 5.3. Illustration of the descent into the class hierarchy and the different calls to member functions on the different levels generated by a single call of *Run::analyzeViaAqPeriod(Analyzer *an)*.

5.2. Class: MainzWaveform and inheriting classes

As already mentioned before, the classes for waveforms and the filtered waveforms are implemented using the decorator pattern. This means, there is an abstract class, called *MainzWaveform*, the so-called component. This class defines the interface for the inheriting classes. The concrete component, i.e. the implementation of the real waveform containing the data is the *RawDataWaveform*. The decorator is the class *FilteredWaveform*, which again is abstract. The concrete implementations of the decorator are the different types of filters. Several decorators can be put behind each other, therefore allowing several filters being used in a defined sequence. Currently there are five different implementations of *FilteredWaveform*:

- MovingWindowFilteredWaveform
- MedianFilteredWaveform
- LinearFilteredWaveform
- FFTFilteredWaveform
- PatternFilteredWaveform

In general, entities of *FilteredWaveform* do not calculate the filtered data in advance, but do so on-the-fly for single requested data points. This is not efficient for all applications and for

```

1 AnalyzerPeakFinder::analyzePre(Run * cRun)
2 {
3     cout << "Hello! I am now starting to analyse the Run!" << endl;
4 }
5 AnalyzerPeakFinder::analyzePre(Waveform *cWf)
6 {
7     if(cWf->getNPeaks() == 1) //check if there are already peaks for this waveform (e.g. found by
8         another PeakFinder)
9     {
10        cout << "Already Peaks existing! Will add newly found peaks!" << endl;
11    }
12    findPeaks(); //we find peaks on the Waveform
13 }
14 AnalyzerPeakFinder::analyzePost(Waveform *cWf)
15 {
16     savePeaks(cWf); //we store the peaks that have been found in the RawWaveform
17 }
18 AnalyzerPeakFinder::analyzePost(AcquisitionPeriod *cAqP)
19 {
20     savePeaksToRoot(); //we save the peaks in a root file
21 }

```

Figure 5.4. Exemplary implementation of AnalyzerPeakFinder as an illustration what an analyzer could do at the different levels. Of course additional or less member-functions *analyzePre()* and *analyzePost()* for different levels can be implemented.

FFTFilteredWaveform the complete filtered waveform has to be calculated at once. All types of filtered waveforms therefore allow to pre-calculate the filtered data.

5.2.1. MovingWindowFilteredWaveform

The *MovingWindowFilteredWaveform* is used by many analyzers, such as peak finders and step finders. It applies a moving weighted average window to the waveform, reducing the length of the waveform by the length of the filter. The moving window consists of a set of weights. The number of weights defines the width of the moving average window. The filter and coefficients are set when calling the class' constructor. Different methods for the construction are available. Two of those (raised cosine and derivative) are taken from XeRawDP, the Xenon100 analysis framework. [Pla12], [Ae12]

manual: The coefficients can be defined manually. The sum of all coefficients is undefined. This is currently not used anywhere in the framework.

raised cosine: The coefficients are calculated by Fourier transformation of a raised cosine (described below) in frequency space. The sum of all coefficients is one.

CFD-like: The moving window consists of $N_{avWidth}$ identical negative coefficients followed by $N_{centerWidth}$ zeros and then followed by $N_{avWidth}$ identical positive coefficients. The sum of all coefficients is zero, i.e. the absolute value of the negative and the positive coefficients is the same. This reproduces the way the SIS3316 uses to generate a trigger internally, which was originally used for the Compton setup.

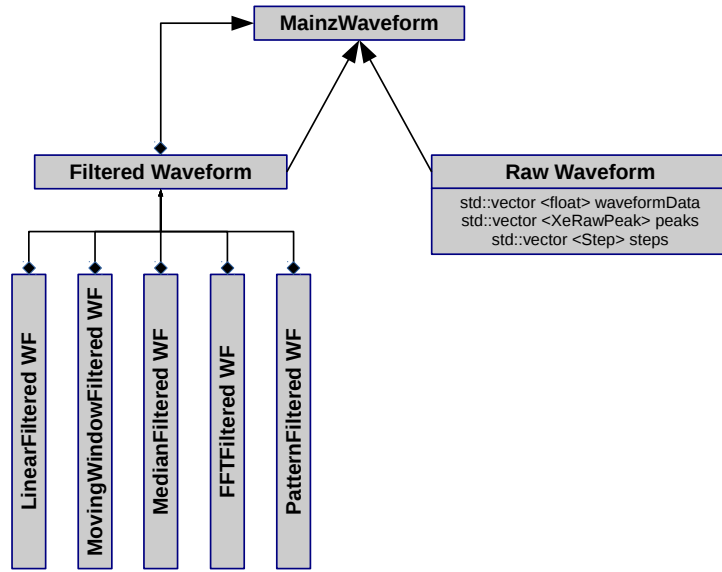


Figure 5.5. Class diagram of MainzWaveform, RawWaveform and FilteredWaveform to illustrate the decorator pattern. Again, the symbols on the connections like \blacklozenge and the fully colored arrow heads follow the definitions of UML.

derivative: A predefined filter of length nine to create the derivative from a waveform. The sum of all coefficients is zero. Currently not used, but could be used for step finding algorithms.

5.2.1.1. Raised cosine filter

$$H(f) = \begin{cases} 1 & |f| \leq (1 - \beta) \cdot l \\ 0.5 \cdot \left(1 + \cos \left[\frac{\pi}{2l\beta} \cdot (f - l(1 - \beta)) \right] \right) & (1 - \beta) \cdot l < |f| \leq (1 + \beta) \cdot l \\ 0 & \text{else} \end{cases} \quad (5.1)$$

A raised cosine filter can best be visualized in frequency space. A raised cosine filter normally is a low pass filter as shown in equation 5.1 and visualized figure D.1 in the appendix and in figure 5.7 in this chapter. The transfer function is constant up to a certain frequency and drops then using a cosine shape. The transfer function is 0.5 at the limit frequency f^{limit} , which is

$$f^{\text{limit}} = 2 \cdot l \cdot F$$

with F , the sampling frequency of the digitizer. The steepness of the cosine shape is defined by the so-called roll-off factor β . $\beta = 0$ means a rectangular step and $\beta = 1$ meaning that the width of

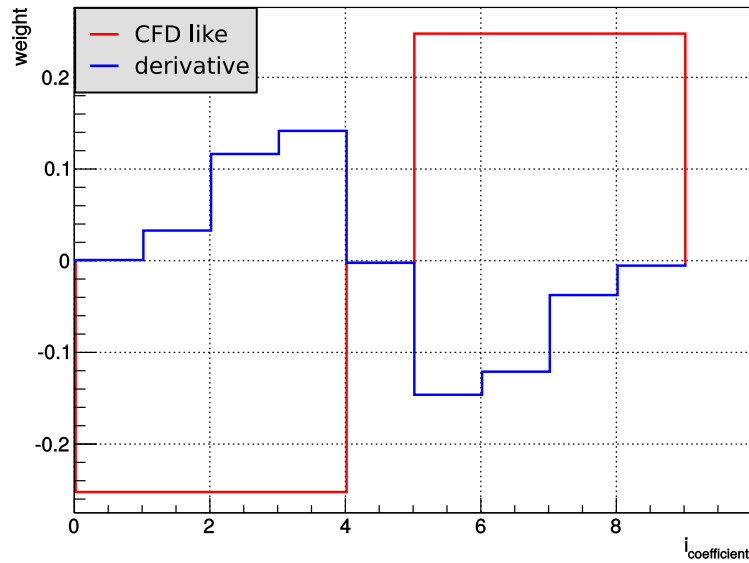


Figure 5.6. Moving weighted average windows (MAW) created by different methods of constructing the filtered waveform. The MAW used for derivative (blue) and a CFD-like MAW (red) with a length of nine ($N_{\text{centerWidth}} = 1$, $N_{\text{avWidth}} = 4$) are shown.

the decreasing part of the transfer function is twice the limit frequency. In figure 5.7 the transfer function used for S1 and S2 peak finding (on both FADCs) is shown, together with the MAW used. As in the transfer function the x-axis is in units of the sampling frequency F of the FADC, the limit frequency for the SIS3305 is:

$$f_{3305}^{\text{limit}} = 0.06 \cdot 5 \text{ GS/s} = 300 \text{ MHz}$$

and, although the transfer function looks identical, for the SIS3316:

$$f_{3316}^{\text{limit}} = 0.06 \cdot 125 \text{ MS/s} = 7.5 \text{ MHz}$$

The transfer function is discretized in the code in 1024 equally wide samples for the whole transfer function from $f = 0$ to $f = F$. After the Fourier transformation the program uses only the central samples of the result as MAW for the filter. The number of samples is defined in the XML configuration with the variable *length* and the selected MAW is then normalized. This restriction to the innermost samples, if chosen too narrow, can change the effect of the filter such that it does not reflect the expected response of the frequency space transfer function any more. This happened for our choice of the S1 peak finder on SIS3316, where only the innermost five samples are used (compare figure 5.7). In appendix D transfer functions for different choices of the limit frequency and the roll-off factor are shown, together with the corresponding MAW. Additionally, the raised cosine can also be used as a high-pass filter. The formula used for the transfer function as well as some examples are given in appendix D too.

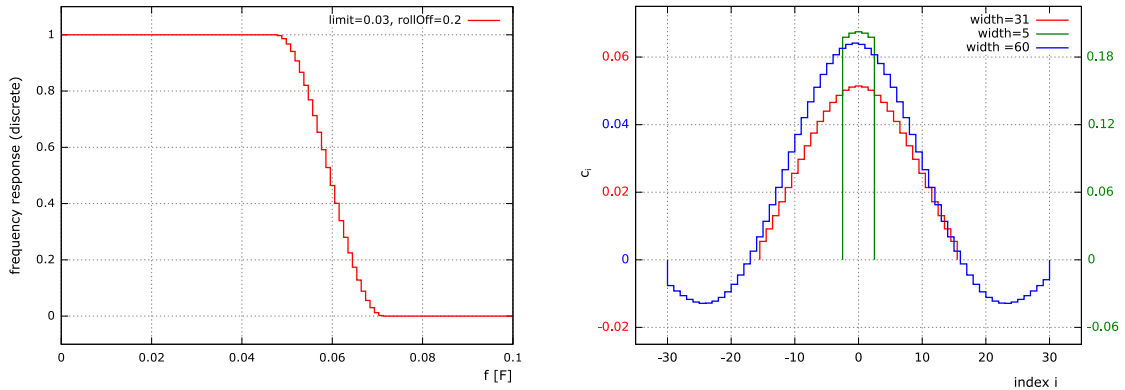


Figure 5.7. On the left a raised cosine transfer function (as used for peak finding on both FADCs and for S1 and S2 signals) is shown. It is shown here discretized in f like it is done in the code. On the right, the MAWs for peak finding of S1 and S2, that are obtained from this transfer function are shown in blue (SIS3305 - S1), in red (SIS3316 - S2) and in green (SIS3315 - S1). Looking at the latter, it is clear that the choice of parameters is not the best, although the peak finding works properly. By limiting to an only five sample wide MAW, the frequency response is much different from what one would expect from the transfer function, in this case, higher frequencies are less suppressed than the transfer function suggests.

In the constructor four arguments are required:

bool lowPass: True if the raised cosine filter should be implemented as low-pass filter, which is typically the case. Otherwise the raised cosine is generated as high-pass filter.

float limit l : The parameter defines the limit frequency of the filter. The value is given as fraction of two times the sampling frequency. This means, that a given value for $limit$ has a different meaning for the SIS3305 and SIS3316. For peak finding with the *AnalyzerXeRawPeakFinder* we currently use $l=0.03$ for searching S1- and S2-peaks on both FADCs. On the SIS3316 this corresponds to a limit frequency of $f_{3316}^{limit} = 7.5$ MHz, whereas the same limit value for SIS3305-waveforms means $f_{3305}^{limit} = 300$ MHz.

float rollOff β : As stated before, the roll-off value defines the steepness of the cosine in the transfer function. The value has to be larger than 0 and should not be larger than 1, although it may be larger than one, but one should think about the meaning by visualizing the transfer function before. In general, the larger β the flatter the transfer function. Again, the value chosen in the XML configuration file, has different meaning for different sampling frequencies.

int length: This value states the width of the MAW in samples. Only the central $length$ samples of the MAW are used. The right side of figure 5.6 illustrates this. Restricting the window to a narrow window (like done for the S1-peak finding on SIS3316 waveforms) means of course, that the real transfer function will be different than what one would expect from the raised cosine transfer function. Higher frequencies will be less suppressed in this case.

Of course, one can generate a band-pass filter using two raised cosine filters in sequence, one high-pass and one low-pass.

5.2.2. MedianFilteredWaveform

The *MedianFilteredWaveform* does, as the name suggests, a median filtering. Two parameters can be defined: the length of the window preceding the current sample, and the length of the window following the current sample. A *MedianFilteredWaveform* has the same length as the original waveform, as each sample is replaced with the median of the samples in the window. That means, that the first N_{pre} and the last N_{post} samples of the waveform are not filtered properly, but for a median filter the effect should not be that bad.

5.2.3. LinearFilteredWaveform

A *LinearFilteredWaveform*, is a waveform where a constant value (offset) is subtracted from the value of each sample, the resulting value is then multiplied by a scaling factor, i.e., a linear function is applied to each sample. This does not change the length of the waveform, it has the same length as the unfiltered version. This filter is used to subtract the baseline and change the amplitude from binary ADC value to a value in volts. For this purpose, a constructor reading the voltage range and the resolution of the FADC automatically from the singleton object: `MainzXmlConfig` and calculating the baseline of the waveform automatically exists. In addition to this specific constructor a more general version is available, where offset value and scaling factor have to be given manually.

This decorator is used in almost every analyzer, as in most cases we are interested in baseline-subtracted waveforms converted to volts.

5.2.4. FFTFilteredWaveform

The so-called *FFTFilteredWaveform*, is a waveform where the waveform is transformed into frequency space. `GNUScientificLibrary` is used to perform the **F**ast **F**ourier **T**ransformation and re-transformation after applying some filters. The waveform in frequency space can be obtained, or one can apply frequency filters, before re-transforming the waveform. Although a *MovingWindowFilteredWaveform* using a raised cosine to generate the MAW can be used as a low-pass or high-pass filter, the *FFTFilteredWaveform* is more versatile, as one or several frequency-bands can be suppressed, in addition to simple high- and low-pass filtering. As one can obtain the waveform in frequency-space (which is not possible using the raised cosine MAW), the *FFTFilteredWaveform* also allows frequency analysis of the waveforms. Frequency analysis in combination with suppression of frequency-bands can be used to suppress (low-frequency)

noise. This waveform-type is implemented with the forward and backward transformation, but no frequency filters are currently included. It is also not used yet.

5.2.5. PatternFilteredWaveform

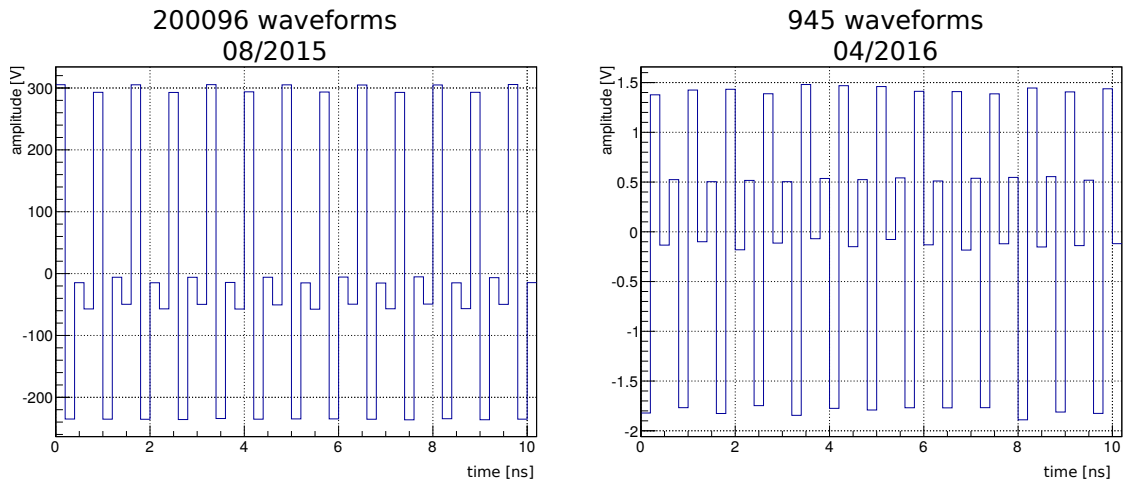


Figure 5.8. Sum of waveforms recorded with the first channel of SIS3305 in 5 GS/s mode without any sensor connected, the system has been triggered with an external pulser in both cases. On the left, $V_{pp}/N = 2.75$ mV, on the right: $V_{pp}/N = 3.62$ mV.

The *PatternFilteredWaveform* is subtracting a fixed, repetitive pattern from the Waveform. The use of this filter is very limited. Originally it was created to filter the waveforms of SIS3305 when used in the 2.5 GS/s or 5 GS/s modes, which was always the case. If one does not connect any input (or the connected sensor shows no signal) and one adds up many waveforms one can see a repetitive pattern in the summed waveform. This is probably due to the way, the 5 GS/s-sampling rate is achieved by multiplexing between four different ADCs. A very slight constant DC-offset between those four ADCs, would generate this pattern, if the sampling after a trigger starts always with the same ADC. As the offset is less than one ADC-count and therefore smaller than the electronic noise, one cannot see it on a single waveform, but adding up many waveforms, the electronic noise is averaged whereas the systematic pattern sums up and gets visible. This effect for example occurs when doing PMT calibration measurements, where signals occur only in a short window of the waveform. Unfortunately it turned out, that the offsets one would infer from the summed waveform vary slightly from DAQ run to DAQ run. To use this filter one should first systematically study the behavior of the offsets and find a way to retrieve the pattern, also from real data. For this thesis, this kind of filtering is not used.

5.3. Waveform Features

The purpose of analyzing the raw data is, to find the interesting features and quantify their properties. In this chapter, the different “features” are described, with a focus on the properties that are written into ROOT files for further analysis, neglecting member functions. In the description, the variable names as used in the framework and written to the ROOT files are used.

5.3.1. XeRawPeak

XeRawPeak is a class taken from *XeRawDP*. It can hold the information on peaks found on waveforms by *XeRawPeakFinder*. A peak is the typical shape of the signal of PMTs. The class *XeRawPeak* can of course hold information on peak-shaped signals, independent of the sensor that generated the signal. If, for example, signals from SiPMs are recorded with the DAQ and the data should be processed with this framework, there is no need of adding a further class. Depending on the search algorithm, the values stored in the different variables might have a slightly different meaning. The description here is for the *XeRawPeakFinder*. The “i” or “f” in the variable name indicates if it’s an integer or a float.

m_iPosition: The position of the peak in samples.

m_iLeftEdge: The sample number of the left edge of the peak.

m_iRightEdge: The sample of the right edge of the peak.

m_fAmpltd: The amplitude of the filtered peak in volts.

m_fWidth: Full width at half maximum of the filtered peak in samples.

m_fLowWidth: Full width at 10% of the maximum of the filtered peak in samples.

m_fIntegral: The integral of the filtered peak within full width at 10% in $V \cdot$ samples.

m_iPositionRaw: The position of the peak in the unfiltered waveform in samples.

m_fAmpltdRaw: The amplitude of the unfiltered waveform in volts.

m_fIntegralRaw: The Integral of the unfiltered waveform in $V \cdot$ samples.

peakType: The type of the Peak. *XeRawPeakFinder* either sets this to S1 or S2. if other peak finder algorithms are implemented using the same class to store the results, more types can and should be added, especially as values stored in the variables might not have the exactly identical meaning. *PeakType* is implemented as an *enum class* in the analysis framework.

5.3.2. Step

APDs and the germanium detector use a charge-sensitive preamplifier to amplify the signal. A CSP translates a charge into a voltage pulse, with an amplitude proportional to the charge. The output signal of a CSP has a long decay constant compared to a relatively fast rise. For our CSPs the decay constant is longer than the window recorded by the FADC, therefore the baseline is not restored within this window. To store the properties of the steps found the class `step` was implemented with the following properties:

position: The position of the maximum of the step in samples.

amplitude: The amplitude of the raw waveform at *position* in volts.

peakAmplitude: The amplitude of the filtered waveform.

decayConstant: The decay constant of the step.

stepType: The type of step. Again implemented as *enum class*. Currently there are two step types: *simple* and *stepFitter*. *Simple* is used by *AnalyzerOneStepFinder* and *stepFitter* is used by *AnalyzerStepFitter*. The two *Analyzers* are described later in section 5.6.

t_high: The position where the decay of the step starts. Similar to *position*, but not used by *AnalyzerOneStepFinder* just by *AnalyzerStepFitter*.

t_rise: Rise time of the step.

chi2: The χ^2 -value of fitted steps. Not used by *AnalyzerOneStepFinder*.

5.3.3. Format of the ROOT file: WaveformFeaturesToRoot

Writing peaks and steps that have been found into a root file for further processing can be done using the class *AnalyzerWffToRoot*. This will generate a ROOT file with the filename in the format *YYYYMMDDTHHMMWffToRoot.root*. *YYYYMMDD* and *HHMM* reflect the start date and start time of the DAQ run in GMT. The ROOT file contains two trees per channel activated in the DAQ. The tree containing the *XeRawPeaks* is called *peaksChX*, the tree containing the steps is called *stepsChX*. *X* stands for the Id of the channel. In addition to the information on the peaks and steps, the *eventId* and *triggerTime* are contained in the trees. Furthermore there is a tree, with a branch for each channel, containing information on the baseline of each event. The representation of the trees in the *TBrowser* of root is shown in figure 5.9. It shows, that S1-peaks and S2-peaks are separated already. *nPeaksS1* and *nPeaksS2* can be different, depending on how many S1 and S2 peaks have been found.

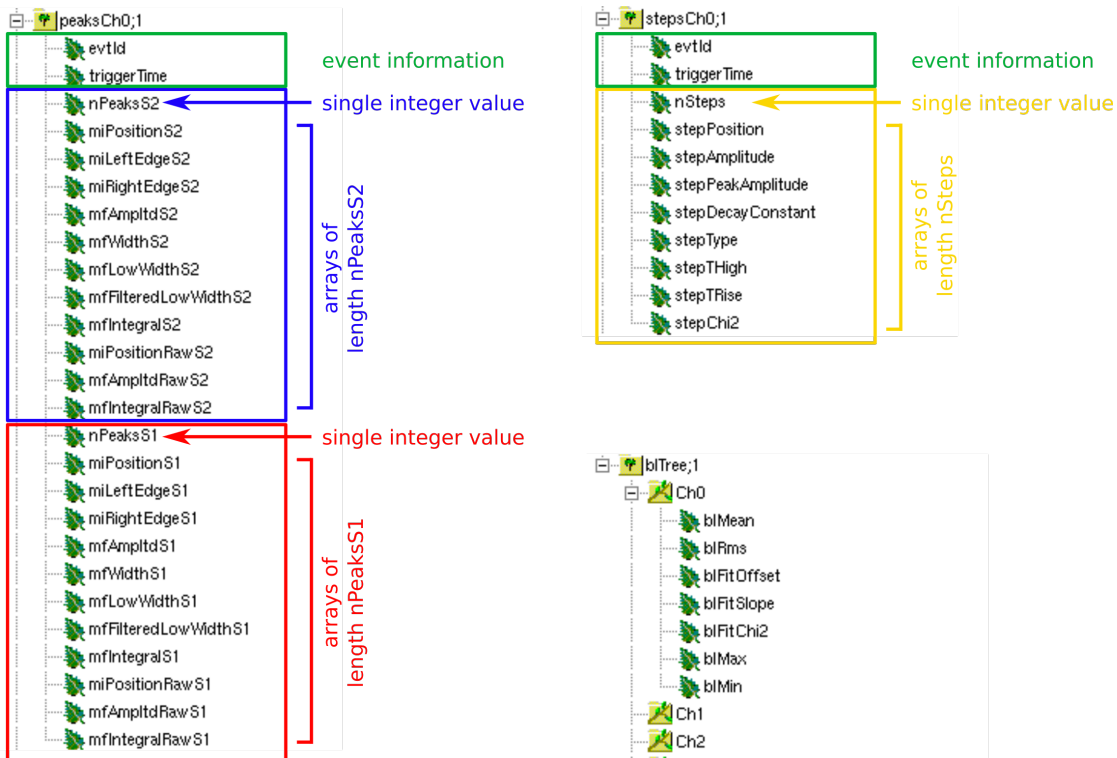


Figure 5.9. Screenshot of the TBrowser representation of the file containing *XeRawPeaks* and *Steps* found by the analyzers.

5.3.4. FWIntegral

To analyze PMT-calibration data, one does not want to rely on the peak-finding algorithms for three reasons (compare chapter 6):

- One would bias the result by the efficiency of the algorithm.
- One already knows where the signal is expected.
- Not every trigger includes a signal, most waveforms are empty.

One wants to integrate a fixed window for every waveform in this case. To store the properties of this fixed window, the class *FWIntegral* (= **F**ixed **W**indow **I**ntegral) has been implemented. The properties of this class are:

preBIMean: The mean value of N_{pre} samples before the window.

preBIMse: Mean squared error of *preBIMean*.

preBISamples: Number of samples (N_{pre}) used to calculate *preBIMean*.

postBIMean: The mean value of N_{post} samples after the window.

postBIMse: Mean squared error of *postBlMean*.

postBISamples: Number of samples (N_{post}) used to calculate *postBlMean*.

windowIntegral: The integral of the waveform in the window in $V \cdot \text{samples}$.

maxPosition: The sample with the highest amplitude in the integration window.

maxVal: The maximum amplitude in the integration window in volts.

realBlMean: The mean value of the baseline as measured at the beginning of the waveform

realBlRms: Root-Mean-Square of the baseline measured at the beginning of the waveform

type: The type of the FWIntegral. Implemented as a string in this case.

5.3.5. Format of the ROOT file: FWIntegralToRoot

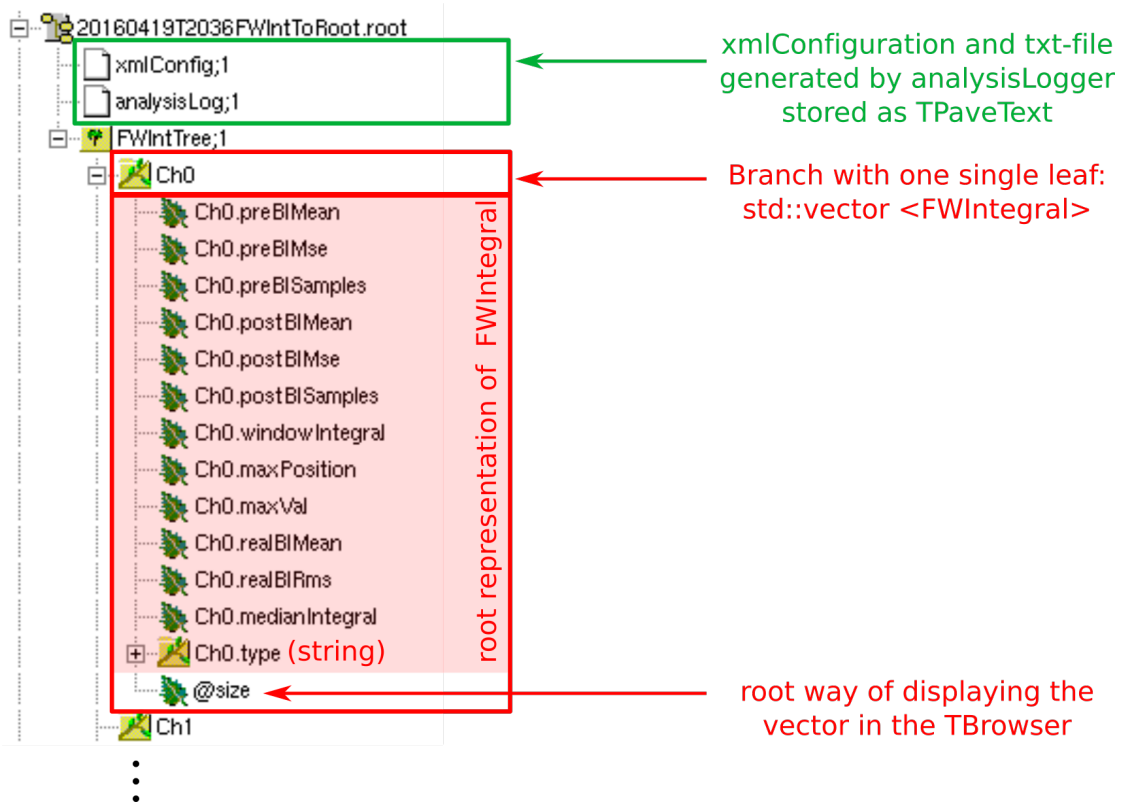


Figure 5.10. Screenshot of the TBrowser representation of the ROOT file generated for PMT-SPE-analysis.

Writing *FWIntegrals* into a root file is done by generating one single tree with a branch for each FADC-channel. The branches have one single leaf, containing a `std::vector<FWIntegral>`. To access the information, one has to compile the class *FWIntegral* as shared object and load it in root. The format of the file name follows the same scheme as for *WaveformFeaturesToRoot*, with the

difference that date and time of the DAQ run are followed by FWIntegralToRoot.root. The XML configuration file used for the analysis and the log-file of the analysisLogger generated during the raw-data processing is stored in the ROOT file as TPaveText objects. The representation of the `std::vector<FWIntegral>` and the format of the trees and branches is visualized in figure 5.10.

5.4. TDCFeatures

The data recorded by the TDC is less complex than the waveforms recorded by the FADCs. In principle, if triggered, the TDC stores all so-called hits on all channels in a defined window before and after the trigger. A hit is just one single time stamp, stating when a digital signal from a CFD arrived at the TDC on a certain channel. Of course, more than one hit can be recorded per channel. In this thesis, terms hit and time stamp are partially used equivalently. The term hit is used to describe what the TDC recorded and the term time stamp is used, when the focus is on the time rather than the technical hit.

5.4.1. CoincidenceHit

Of more interest are so called *CoincidenceHits*. A *CoincidenceHit* is a combination of two hits occurring on two different sensors of one detector within a certain time window. For the TDC each sensor is connected to one channel of the TDC, except the APDs, which are not recorded on the TDC. Examples for sensors are therefore the topPMT or the bottomPMT of the MainzTPC, or the single PMTs mounted on each end of the plastic scintillators. The term *CoincidenceHit* in this thesis is **not** used for a coincidence between two detectors, a *CoincidenceHit* always belongs to only **one** detector, like the MainzTPC or one of the plastic scintillators.

A *CoincidenceHit* has the following properties, some directly taken from the hits that make up the *CoincidenceHit*, some calculated from the combination of the two hits:

detectorId: The identification number (ID) of the detector it belongs to. Id=0 is the MainzTPC, Id=1...10 are the plastic scintillators that are currently connected.

topChannelId: The ID of the TDC-channel, where the topPMT of the detector is connected.

bottomChannelId: The ID of the TDC-channel, where the bottomPMT of the detector is connected.

timestampTop: The time stamp/hit of the topPMT hit that makes up the *CoincidenceHit* together with a hit on the bottomPMT of the same detector. Units are the units of the TDC: 25 ps.

timestampBot: The corresponding time stamp/hit of the bottomPMT hit.

z-position: The z-position of the interaction location in the detector. This value is calculated by the *AnalyzerCoincidenceHitFinder* using *timestampTop*, *timestampBot* and the effective velocity of photons in the detector, as described in section 5.7

distance: The distance of the interaction location to the center of the MainzTPC. Calculated by *AnalyzerCoincidenceHitFinder*.

timestampRealhit: This is the actual interaction time in the detector. Calculated from *z-position* and *timestampTop*. It is in the same units as the original hits and only to be used relative to another hit or *CoincidenceHit* to achieve the full 25 ps resolution. *timestampRealHit* is used for all analysis based on *CoincidenceHits*, i.e. almost everything in this thesis.

5.4.2. Format of the ROOT file: TDCToRoot

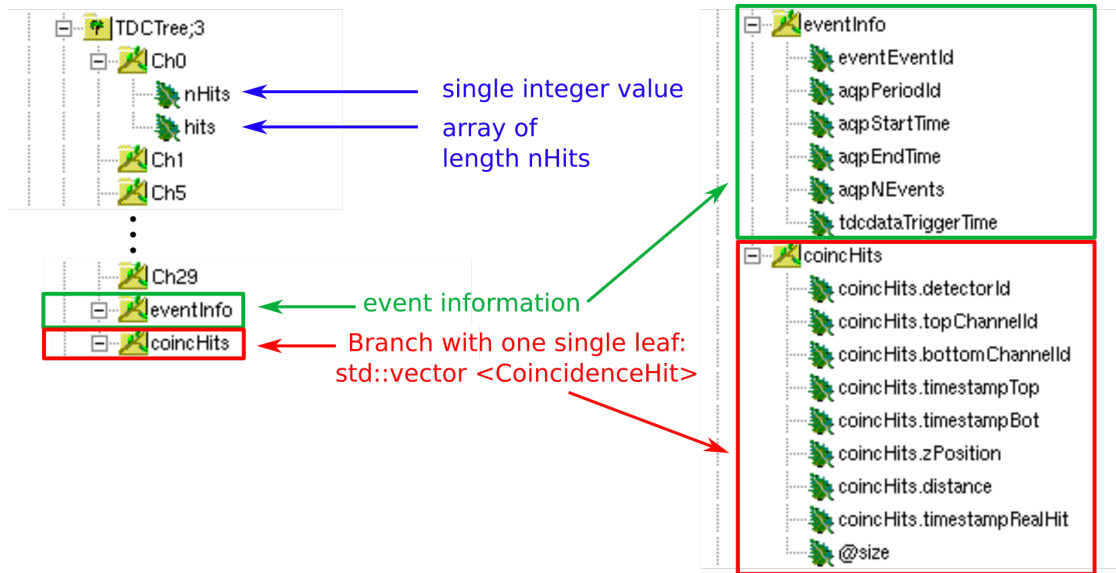


Figure 5.11. Screenshot of the TBrowser representation of the File containing the hits recorded by the TDC and the *CoincidenceHits* found by *AnalyzerCoincidenceHitFinder*.

Different than for the FADCs, the complete recorded information of the TDC is written to the ROOT file by *AnalyzerTDCToRoot*. This is possible because the amount of data is comparably small, as each hit only consists of one 64bit integer, as compared to a waveform. The ROOT file generated again follows the same naming convention as for *WaveformFeaturesToRoot* and *FWIntegralToRoot*. Here date and time are followed by “TDCToRoot.root”. The structure of the ROOT file is similar to the one from *FWIntegralToRoot*, with just one single tree and a branch per TDC channel. The channel branches hold an array of hits (long integers) and one single integer called *nHits* stating the length of the array, as shown in figure 5.11. In addition to the channel branches, the *TDCtree* contains one branch with information on the event, such as event

Id and trigger time and one branch holding **all** *CoincidenceHits* found. *CoincidenceHits* are, as *FWIntegrals*, stored as an `std::vector` of *CoincidenceHits*, therefore to be accessed in ROOT, one needs to load the according “shared object” before. To generate a shared object see the comments in the file *CoincidenceHit.h*. As for *FWIntegrals*, the XML configuration file and the log file are stored in the ROOT file too.

5.5. PeakFinder

5.5.1. Algorithm

To search for peaks on the recorded PMT waveforms, the peak finding algorithm used by XENON100 and described in [Pla12], [Ae12] has been adapted to be used in an analyzer called *AnalyzerXeRawPeakFinder*. The algorithm first searches for S2 peaks on the waveform. To do so, the waveform is filtered by a MAW, as described in section 5.2.1 of this chapter. Starting from the first sample, the algorithm checks for each sample if it is above the threshold defined in the XML configuration-file. The sample position where the filtered waveform rises above threshold is defined as left edge of a peak, the sample where the waveform drops below threshold again is defined as right edge of the peak. If the number of consecutive samples that are above threshold is larger than a predefined value (via xml), it is tagged as an S2 peak and FWHM and the width of the peak at 10% are calculated. The baseline before and after the peak are calculated, too. If FWHM and the baselines before and after the peak match the definition of an S2 peak (as defined in XML config), the integral of the peak is calculated and the peak is stored.

In the original algorithm of *XeRawDP* the S2 search is followed by a *tinyS2-search*. This step is currently skipped in the implemented algorithm, but can of course be added if need arises later. *AnalyzerXeRawPeakFinder* proceeds with the search for S1 peaks, directly after the search of S2 peaks. The search for S1 peaks is only done in regions that are not tagged as S2 peak. S1 search follows a similar algorithm as S2 search: as the filtered waveform (now using a different MAW), exceeds the S1-threshold a peak starts and it ends where the waveform drops below the threshold. To be tagged as an S1-peak the peak has to fulfill the conditions defined in the XML file, regarding the width and the baseline before and after the peak. Additionally, the lowest (negative) value in a certain window around the maximum of the peak must be absolutely smaller than the maximum peak. This suppresses bipolar noise to be tagged as S1.

5.6. StepFinding and StepFitting

To find steps and define their properties, two algorithms are implemented. The first is really an algorithm to find steps. The second part uses steps that have previously been found and fits the

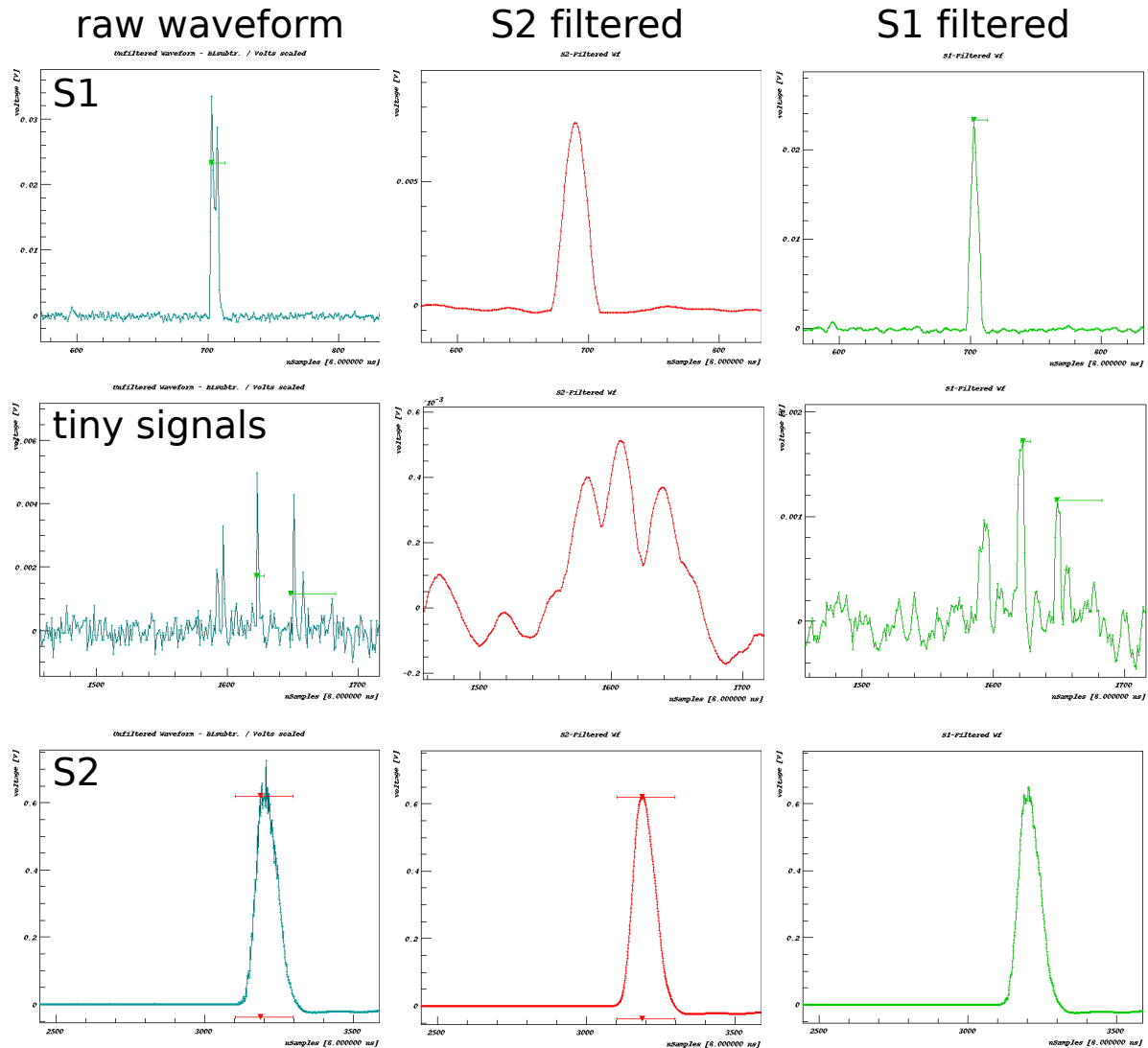


Figure 5.12. Illustration of the effect of the raised cosine filters applied to the raw waveform (left column) for the SIS3316 digitizer (topPMT). The event chosen here exemplary originates from a Compton scattering dataset. The first line shows the region of the trigger (S1-signal), the second show some tiny signals somewhere between the identified S1- and S2-signal and the last line shows the region of the S2-signal. The central column shows the waveform after applying the S2-filter from figure 5.6 and the right one the effect of the S1-filter. Detected S1- and S2-peaks and their width are marked with green and red symbols.

Applying the S2-filter to an S1-signal broadens the shape and decreases its amplitude (here: from 30 mV to 8 mV), whereas the S1-filter preserves shape and amplitude better. The tiny signals are suppressed below threshold (1 mV) with the S2-filter, but the two larger peaks would still be detected as S2-signals. If the S2-filter from figure 5.6 is applied to an S2-signal, its shape and amplitude are well preserved. Fast fluctuations of the shape are better preserved by the S1-filter, but that is not wanted for the wider S2-signals.

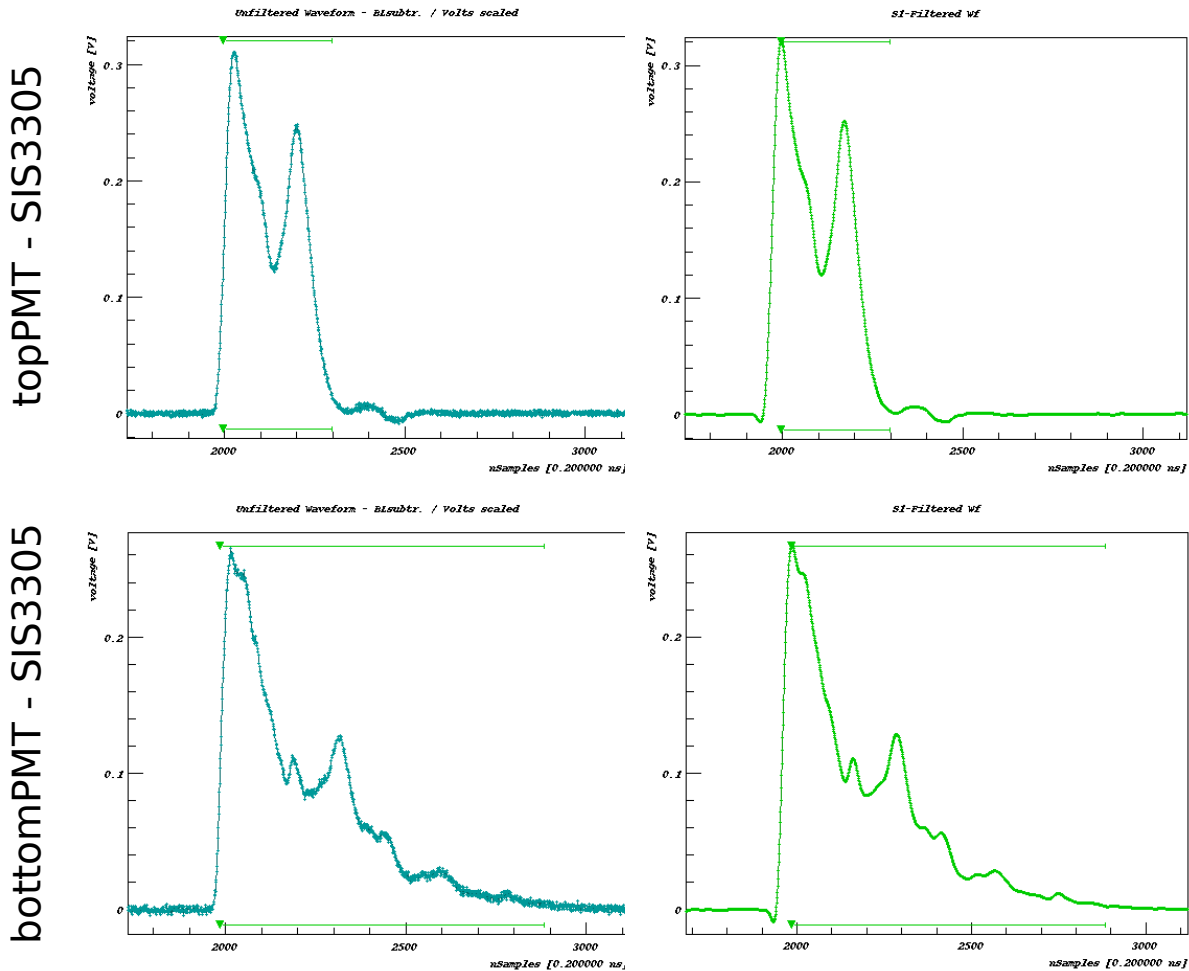


Figure 5.13. The S1-signal recorded with the fast FADC with the two PMTs. The effect of the moving average filter (raised cosine as in figure 5.6) for the SIS3305 is shown on the right. The substructures are not identified as individual peaks, instead the whole signal is treated as one S1 signal as intended. Of course, the peak finding on the SIS3305 is done independently from the results on the SIS3316 waveforms. One can see, that signal shape and amplitude are very well preserved here. The double peak structure of photons on the topPMT is kept even after applying the filter and the shape of the structures is significantly better resolved in time compared to the recorded waveform on SIS3316 (figure 5.12) where the double peak structure is visible in the raw waveform, but smoothed out by the S1-filter.

5.6. STEPFINDING AND STEPFITTING

waveform with a function. The function consists of a linear baseline and step-shaped function, which consists of a linear rise and an exponential decay. The advantage of the fit is that it uses all information contained in the waveform, and therefore should provide a better resolution.

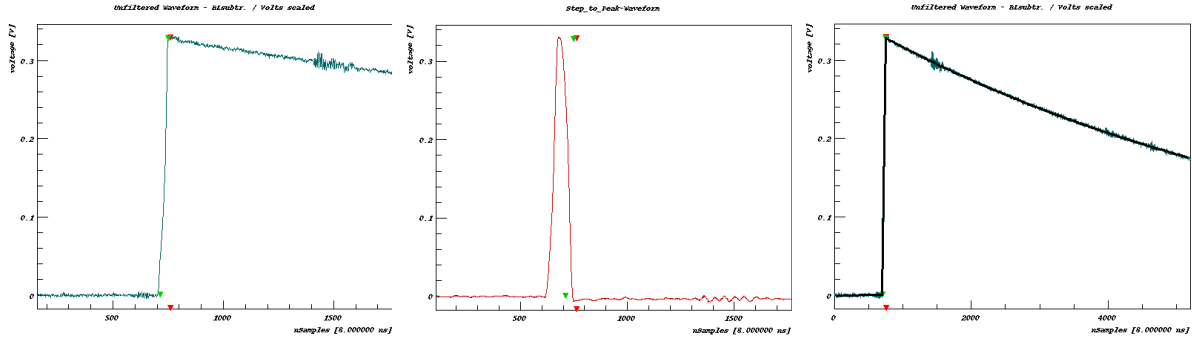


Figure 5.14. On the left the waveform of the germanium detector is shown before applying any filters. In the center, the effect of a CFD-like moving average window ($N_{\text{centerWidth}} = 20$, $N_{\text{avWidth}} = 20$) as used by the step finding algorithm. The resulting waveform now shows a peak as a feature instead of a step and can be found by peak-finding algorithms. As the CFD-like MAW is normalized the amplitude of the step represents the amplitude of the step rather well, as can be seen by the marker for the peak (red). The found step can also be fitted by the step-fitting algorithm. On the right the complete waveform is shown, together with the applied fit. The green marker shows the transition from rise to decay as found by the fitting routine.

5.6.1. StepFinding algorithm

To find steps, the waveform is first filtered using a CFD-like MAW. This transforms the step of the waveform into a peak-like structure. The peak can now easily be found using a peak-finding algorithm or just searching for the maximum of the filtered waveform. As the step-shaped waveforms originate from CSPs, one is not interested in the integral of the step, but on the amplitude. This is equal to the amplitude of the filtered waveform, as the CFD-like MAW is normalized and the width of the MAW is small compared to the rise of the decay time constant of the step. *StepAmplitude* and *StepPeakAmplitude* for steps found by this algorithm are therefore identical. The decay time constant of the step cannot be inferred by the waveform transformed into a peak. The value calculated for the decay time constant should not be taken too serious, as it is calculated by using only a few individual samples distributed between the position of the maximum of the step and the end of the waveform. Therefore it will definitely not be a good estimate if the waveform contains several steps.

5.6.2. StepFitting algorithm

For an improved characterization of the shape of the found steps, an additional analyzer (*AnalyzerStepFitter*) has been created. The algorithm relies on steps found previously, and uses their positions and amplitudes as start parameters for the fit function. The fit function itself is generated by using a linear function to reflect the baseline, and then recursively adds section-wise defined functions consisting of a linear rise and an exponential decay. If the baseline should be prefit (or assumed to be flat and zero) can be defined via XML configuration, as well as the range in which the fit parameters can be varied or if they should be fixed. The decay constant could for example be a parameter that one wants to fix, as it is primarily given by the circuit of the CSP and can therefore be measured in advance using test pulses. In figure 5.15 the function that is used to fit a single step is shown, and the parameters that are used to fit the function are given in red. Parameters shown in green can be used for an alternative representation of the ones in red, to make equations more readable.

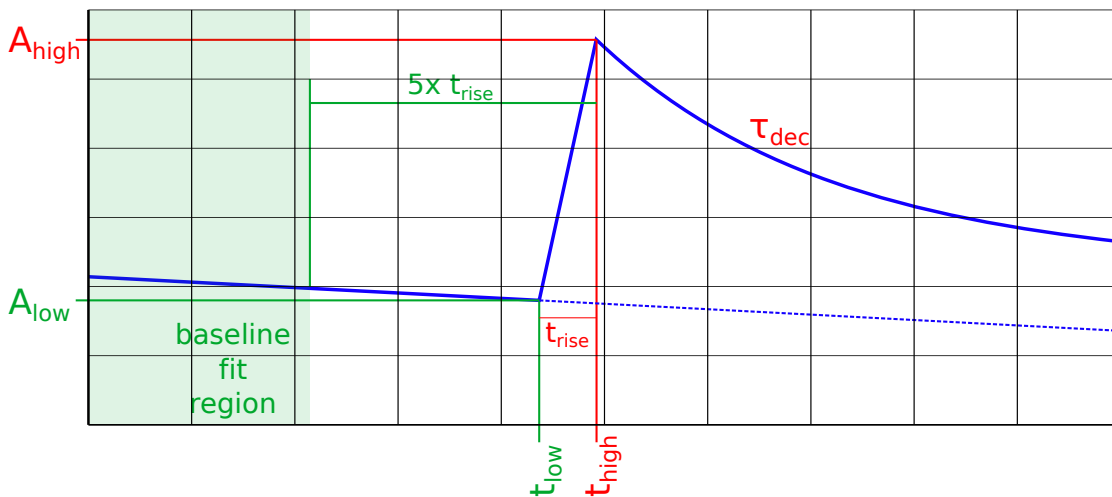


Figure 5.15. Function used to fit a waveform with a step. The free fit parameters are shown in red, quantities shown in green are inserted to make explanations simpler.

The fit function can be written as a sum of the linear baseline and the step-shaped function:

$$f_{\text{fit}}(t) = f_{\text{BL}}(t) + f_{\text{step}}(t)$$

The baseline function is a simple linear function, written as:

$$f_{\text{BL}}(t) = s_{\text{BL}} \cdot t + O_{\text{BL}}$$

The slope (s_{BL}) and offset (O_{BL}) can either be fixed to zero by XML configuration or be fitted in advance to fitting the whole waveform. In this case, a linear fit is done starting at the first sample and ending five-times the rise time before t_{high} , as illustrated in figure 5.15. The linear function is

extended to the whole waveform after fitting it before the first step and the slope and offset are fixed. On top of this linear function, for each step a section-wise defined function is added, with the following properties:

$$f_{\text{step}}(t) = \begin{cases} \left(\frac{A_{\text{high}} - A_{\text{low}}}{t_{\text{rise}}} - s_{\text{BL}} \right) \cdot (t - t_{\text{low}}), & \text{if } t_{\text{low}} < t < t_{\text{high}} \\ (A_{\text{high}} - f_{\text{BL}}(t_{\text{high}})) \cdot \exp\left(-\frac{t - t_{\text{high}}}{\tau_{\text{decay}}}\right), & \text{if } t \geq t_{\text{high}} \end{cases}$$

For the rise of the step one has to take into account the slope of the baseline function, that is why it is subtracted in the equation. As the fit parameter is not the slope but t_{rise} and the amplitudes, this is automatically done by the fitting routine in reality.

5.7. Coincidence Hit Finder

5.7.1. CoincidenceHit finding algorithm

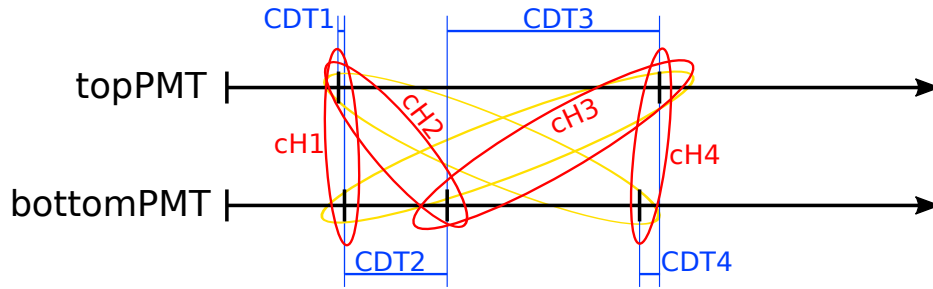


Figure 5.16. This illustrates the different combinations of CoincidenceHits that result from three hits for topPMT and bottomPMT. The red ellipses mark combinations with short enough coincidence time differences to be kept as CoincidenceHit, the yellow ellipses show the combinations that could be rejected.

As previously described in section 5.4, the term *CoincidenceHit* in this thesis defines a hit on one single detector (like the MainzTPC or one of the plastic scintillators) that is seen on both PMTs of this detector. The search algorithm is simple. We call the hits on the topPMT h_i^{top} and the hits on the bottomPMT h_j^{bottom} . Now we create all combinations $(h_i^{\text{top}}, h_j^{\text{bottom}})$. After that, the routine checks if the coincidence time difference (CTD) value fulfills the coincidence criterion:

$$|\text{CTD}| = |h_i^{\text{top}} - h_j^{\text{bottom}}| \leq t_{\text{coinc}}$$

If the absolute CTD value of the combination is smaller than the coincidence time window defined via xml-configuration this combination is a *CoincidenceHit* and the additional quantities (timestampRealHit, z-position and path-of-flight-2) of this *CoincidenceHit* are calculated.

5.7.2. Interaction time

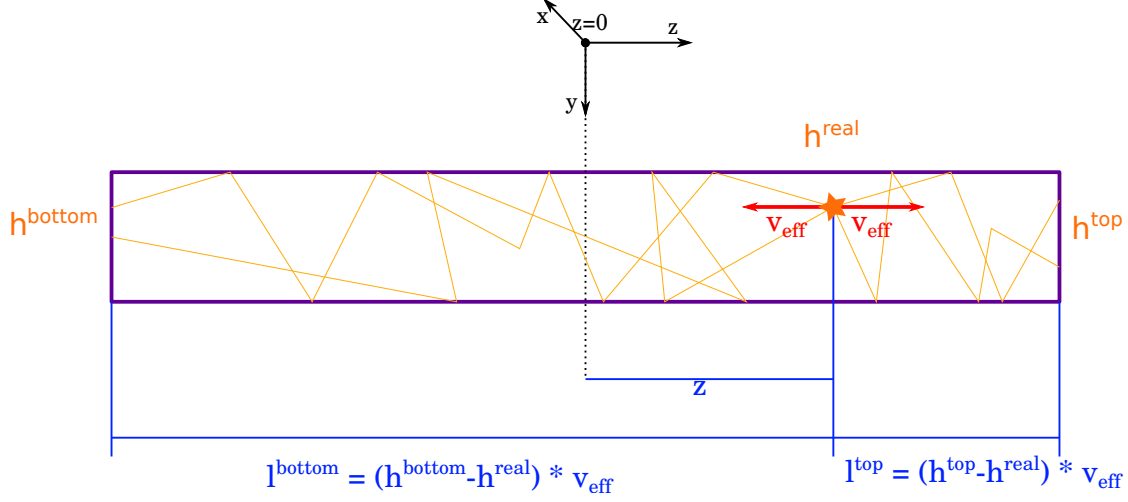


Figure 5.17. The interaction in a detector (here: plastic scintillator panel) always happens before the time the single hits on topPMT and bottomPMT of the detector suggest. Using both values and knowing the effective velocity of light in z-direction in the panel, one can calculate the time of the interaction.

The hits (h_i^{top} and h_j^{bottom}) do not represent the time of the interaction in the detector, but the time when the analog signal of the PMT passed the threshold, or more precisely, the CFD signal has its zero-passing. The interaction time of a particle is always before both hits that make up the CoincidenceHit, due to the finite effective velocity of the photons in the detector and the distance the photons have to travel before reaching the PMT. At this point, we have to distinguish CoincidenceHits of the MainzTPC and of the plastic scintillators. In the MainzTPC, the two PMTs are very close, but as we're interested in small energy deposits, the scintillation pulse shape rather than the distance and the finite velocity of the photons defines the time between interaction and passing the thresholds of the CFDs. Therefore, the timestampRealHit, which represents the time of interaction in the detector, is set to the value of the first of the two hits:

$$h_{\text{TPC}}^{\text{real}} = \min(h^{\text{top}}, h^{\text{bottom}}) \quad (5.2)$$

For the plastic scintillators the case is different. The effective velocity of the photons is about 15 cm/ns as measured previously at HZDR [BGH⁺07], [Bey14]. This means, that after an interaction at the center of the plastic scintillator, it takes about 3.33 ns to reach the PMTs. For the plastic scintillators one can calculate the time of the interaction as:

$$h_{\text{plastic}}^{\text{real}} = 0.5 \cdot \left[(h^{\text{top}} + h^{\text{bottom}}) - \frac{l_{\text{tot}}}{v_{\text{eff}}} \right] \quad (5.3)$$

This follows from solving the following set of equations:

$$h^{\text{top}} = h^{\text{real}} + \frac{l^{\text{top}}}{v_{\text{eff}}} = h^{\text{real}} + t^{\text{top}} \quad (5.4)$$

$$h^{\text{bottom}} = h^{\text{real}} + \frac{l^{\text{bottom}}}{v_{\text{eff}}} = h^{\text{real}} + t^{\text{bottom}} \quad (5.5)$$

$$t^{\text{top}} + t^{\text{bottom}} = t_{\text{tot}} = \frac{l_{\text{tot}}}{v_{\text{eff}}} \quad (5.6)$$

The symbols used in equations 5.4 - 5.6 are defined in the sketch in figure 5.17. t^{tot} is the time scintillation photons need to travel from one end of the scintillator panel to the other end. t^{top} and t^{bottom} are the times that scintillation photons need for the distances l^{top} and l^{bottom} respectively, with the effective photon velocity v_{eff} in the scintillator panel (in z-direction).

5.7.3. z-position and path-of-flight-2

The z-position in the plastic scintillator is of relevance, as it is used to calculate the path-of-flight-2, i.e. the path from the center of the MainzTPC to the interaction position at the plastic scintillator, and/or the scattering angle for each event. Therefore again z-position and distance are only calculated for the plastic scintillators. For the TPC, both values are set to zero. For the plastic scintillators we have (compare figure 5.17):

$$z = \frac{l_{\text{tot}}}{2} - l_{\text{top}}$$

Combining this with equation 5.1 we get:

$$z = \frac{l_{\text{tot}}}{2} - t^{\text{top}} \cdot v_{\text{eff}} = \frac{l_{\text{tot}}}{2} - (h^{\text{top}} - h^{\text{real}}) \cdot v_{\text{eff}}$$

Knowing the z-position of the interaction and the distance from center of the TPC to the center of the plastic scintillator, one can calculate the path-of-flight-2 using Pythagorean theorem.

6. Photomultiplier Calibration

To translate measured light signals (S1 and S2) into a number of detected photons, the absolute gain of the PMTs has to be measured. This can be accomplished by determining the charge generated by one single photon detected by the photo cathode of the PMT, using the same bias voltage and amplifiers as in the experiments. Additionally the dependency of the gain from bias voltage can be measured with stronger light signals (relative gain), which allows extrapolating the absolute gain to bias voltages, where the SPE charge is not well separated from the electronic noise. For pulse shape analysis, it is helpful to know not only the charge of SPEs, but also to know the shape of the SPE response.

6.1. Measurement of the absolute gain

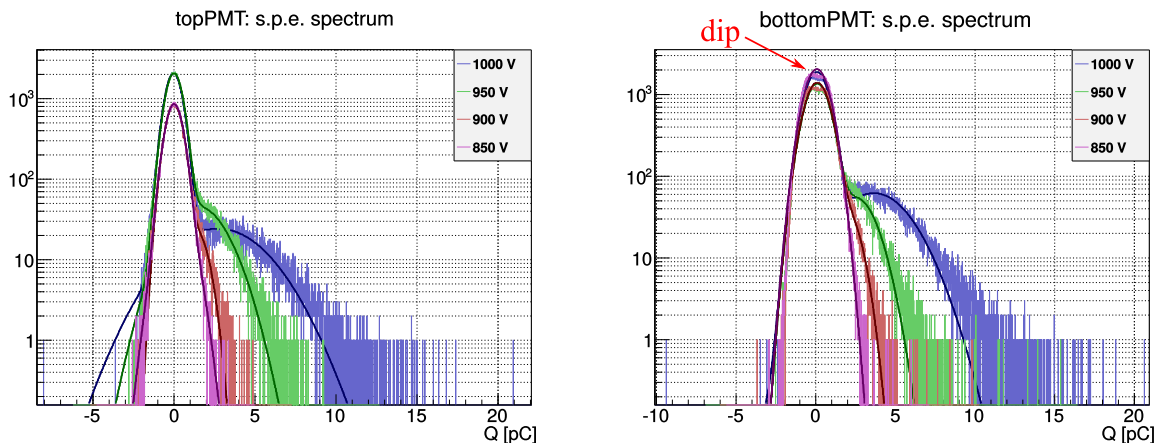


Figure 6.1. Single photo-electron spectra of top and bottom PMT, measured with the DetectorLab amplifier at different bias voltages using the SIS3316-ADC.

The absolute gain of a PMT is defined as the number of electrons measured at the anode of the PMT per photon detected by the PMT's photo cathode. Hamamatsu states a gain of 1×10^6 electrons per photon for the R6041s at a bias voltage of 900 V. The gain does not only depend on the bias voltage, but also on the distribution of the voltage between photo cathode and the dynodes. The distribution suggested in the data-sheet is: 2-2-2-1-1-1-1-1-1-1-1-1.2 (appendix A.1). After some tests and contact with Hamamatsu engineers, we ended up using higher voltage

PMT: bias voltage	pedestal		s.p.e.-peak	
	σ [pC]	mean [pC]	σ [pC]	mean [pC]
top: 1000 V	0.4627 ± 0.0008	-0.02147 ± 0.00099	2.52 ± 0.02	2.735 ± 0.032
top: 950 V	0.4605 ± 0.0009	0.00708 ± 0.00004	1.499 ± 0.011	1.444 ± 0.021
top: 900 V	0.4681 ± 0.0014	0.01287 ± 0.00009	0.5843 ± 0.0248	1.469 ± 0.032
top: 850 V	0.455 ± 0.000	0.01518 ± 0.00020	0.7919 ± 0.0166	0.137 ± 0.015
bottom: 1000 V	0.6573 ± 0.0007	0.069 ± 0.000	1.955 ± 0.014	3.659 ± 0.018
bottom: 950 V	0.6812 ± 0.0009	0.09515 ± 0.0004	1.078 ± 0.018	2.53 ± 0.02
bottom: 900 V	0.6837 ± 0.0009	0.1025 ± 0.0001	0.6951 ± 0.0027	2.063 ± 0.019
bottom: 850 V	0.6639 ± 0.0007	0.07489 ± 0.00009	0.6676 ± 0.0025	0.8302 ± 0.0481

Table 6.1. Fit parameters to pedestals and single photo-electron peak as shown in figure 6.1

drops between the photo cathode and the first dynodes (3-3-3-1-1-1-1-1-1-1-1.2), to improve separation between SPE peak and pedestal in the charge spectrum.

To measure the gain, we use a blue LED driven by a voltage pulse from a pulse generator. The amplitude of the voltage pulse is chosen such that one finds a peak in only about 5% of the recorded waveforms. This adjustment is done by eye using an oscilloscope. Using binomial statistics, one can show that the amount of pulses where two or more photons contribute to the signal is negligible in this case. After adjusting the setting, we recorded 10^5 waveforms with our DAQ, triggered for every pulse of the pulser. This means that we have 95,000 “empty” waveforms (= waveforms that only contain electronic noise) and 5,000 waveforms with a SPE response.

This measurement has been done for different settings of the bias voltage, ranging from 850 V up to the maximum recommended bias voltage of 1000 V, once with the DetectorLab amplifier and once with the KPH amplifier. We changed the connection scheme (compare figure 4.25) for this measurement, as we do not need the CFDs for this measurement. Instead of connecting the second output of the PMT amplifier to the CFD we connected it to another channel of the slower digitizer. This way we recorded the amplified signal both, with the fast digitizer SIS3305 and with the slower high-resolution digitizer SIS3316. Additionally, the unamplified signal from the passive split has been recorded by SIS3316, as in the scattering experiments.

Figure 6.1 shows the spectra of the amplified signals recorded by the SIS3316 and a fit with the sum of two Gaussians, reflecting the pedestal and the SPE-peak. One can see that for lower bias voltages, the SPE peak merges with the pedestal and determining the gain is therefore not possible. To determine the gain of the PMTs at lower bias voltages, one has either to improve the measurement and analysis or to extrapolate the gain from 1000 V bias to the lower values, by measuring the relative gain. This has been done and is described later.

Improving the measurement technique should contain reduction of noise, maybe by measuring the PMTs outside the TPC setup and by an improved grounding scheme. To improve the measurement one could:

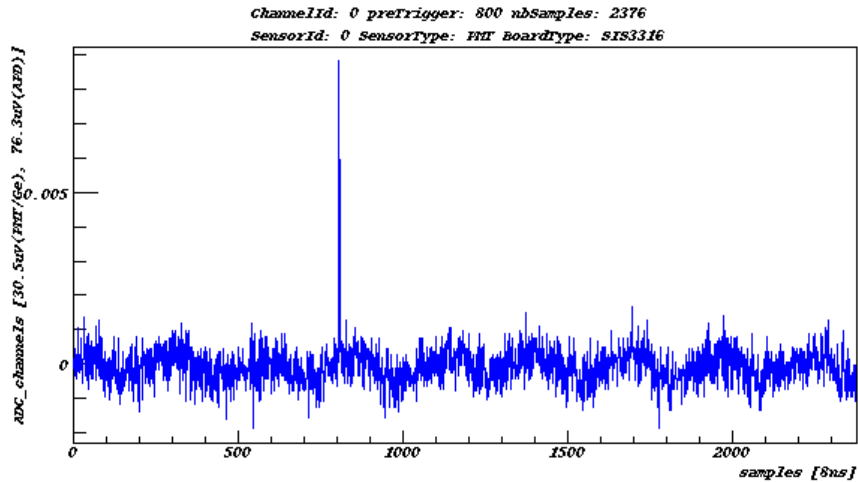


Figure 6.2. Single photo-electron waveform of bottomPMT using the DetectorLab amplifier and recorded by SIS3316. The baseline is not flat but oscillates with a frequency of about 473 kHz (9 oscillations within 19008 ns).

- a) Use a light source with a significantly better timing (for example a pico-second laser) as compared to the LED, which was driven with a voltage pulse of 20 ns. This would allow to better define the integration window and therefore one would integrate less baseline together with the signal.
- b) Illuminate only a certain spot of the photo cathode instead of having photons that randomly hit the photo cathode on any point. Scanning the surface would help understand if the broad distribution of the single photon peak is due to such inhomogeneities.

In figure 6.1 one realizes that the pedestal of the bottomPMT shows a dip instead of being pure Gaussian. After some investigation, it turned out that this is due to an oscillating baseline, with a frequency of about 473 kHz (figure 6.2). Depending on the phase of this oscillation with respect to the trigger, the integration of the fixed window integrates the high or low part of one oscillation. As the frequency of the oscillation seems to be well defined one could use a band suppression filter to get rid of this effect. Applying a band suppression is foreseen using the `FFTFiltedWaveform` in the analysis framework, but not yet done.

Further improvement on the data already taken could also be achieved by modifying the way the fixed window is defined and integrated. Currently it is just integrating a fixed number of samples before and after the trigger time. This integration window is relatively large, as it spans not only the length of a single photo-electron but also the length of the time-window where the LED can generate photons, i.e. the length of the LED-driving voltage pulse (20 ns). Instead of integrating the long window, one could search for the maximum in an extended window around the trigger, and integrate a shorter window around the maximum. Still this technique (implemented by `AnalyzerFixedWindowIntegrator`) will bias the pedestal to positive values. Much better would

be the use of a faster light source, such as a pulsed laser, which is currently done in the course of a bachelor thesis.

6.2. Measurement of the relative gain

As the gain of the PMTs could not be properly measured for lower bias voltages, we also measured the relative gain, i.e. the change of the gain when changing the bias voltage. For this measurement we used the blue LED again with the driving pulse generator set to an amplitude such that each trigger of the pulser leads to a visible signal on the PMT, i.e., the PMT detects several photons per LED pulse. We repeated the measurement with three different settings of the driving pulse. This allows us to see if PMT, amplifier or digitizer saturate. In the three settings of the pulse generator, the pulse duration (20 ns) and frequency (500 Hz) remained unchanged. The amplitude of the driving pulse was changed with an attenuator from 0.8-fold to 0.9-fold and 1.0-fold. Using the attenuator guaranteed reproducibility of the setting. The light emission of the LED does not change linearly with the amplitude of the driving pulse. Table 6.2 summarizes the number of photons on top and bottom PMT corresponding to the LED settings.

LED setting	attenuator	topPMT	bottomPMT
LED 1	0.8-fold	34	30
LED 2	0.9-fold	516	188
LED 3	1.0-fold	1234	396

Table 6.2. Average number of photons detected by the PMTs at the three different settings of the driving pulser. Calculated from mean of the absolute gain calibration at 1000 V.

For each setting, each PMT and each amplifier 50,000 waveforms have been recorded. A fixed window around the trigger position has been integrated to generate the spectra in figure 6.3. Looking at the spectra, especially of the weakest setting of the LED (LED 1, corresponding to the attenuator set to 0.8-fold), one realizes that the recorded spectrum is not Gaussian, as one would expect, but narrower on the left side, compared to the right. This is exemplary shown in figure 6.4 for the top PMT at 1000 V with the weakest setting of the LED. To visualize the asymmetry, the residuals of a pure Gaussian are plotted as well as the residuals fitting with an asymmetric Gaussian, defined as:

$$f(Q) = \begin{cases} A \cdot e^{-0.5 \left(\frac{Q-Q_0}{\sigma_{\text{left}}} \right)^2} & \text{if } Q \leq Q_0 \\ A \cdot e^{-0.5 \left(\frac{Q-Q_0}{\sigma_{\text{right}}} \right)^2} & \text{if } Q > Q_0 \end{cases} \quad (6.1)$$

This asymmetric Gaussian has four free parameters (A , Q_0 , σ_{left} and σ_{right}), one more than a symmetric Gaussian, where $\sigma_{\text{left}} = \sigma_{\text{right}}$. Due to the asymmetric shape of this function, the value of Q_0 moves to the left, compared to the mean of the Gaussian. In figure 6.4 the values of Q_0 are marked with a dashed line in the residual plot.

6.2. MEASUREMENT OF THE RELATIVE GAIN

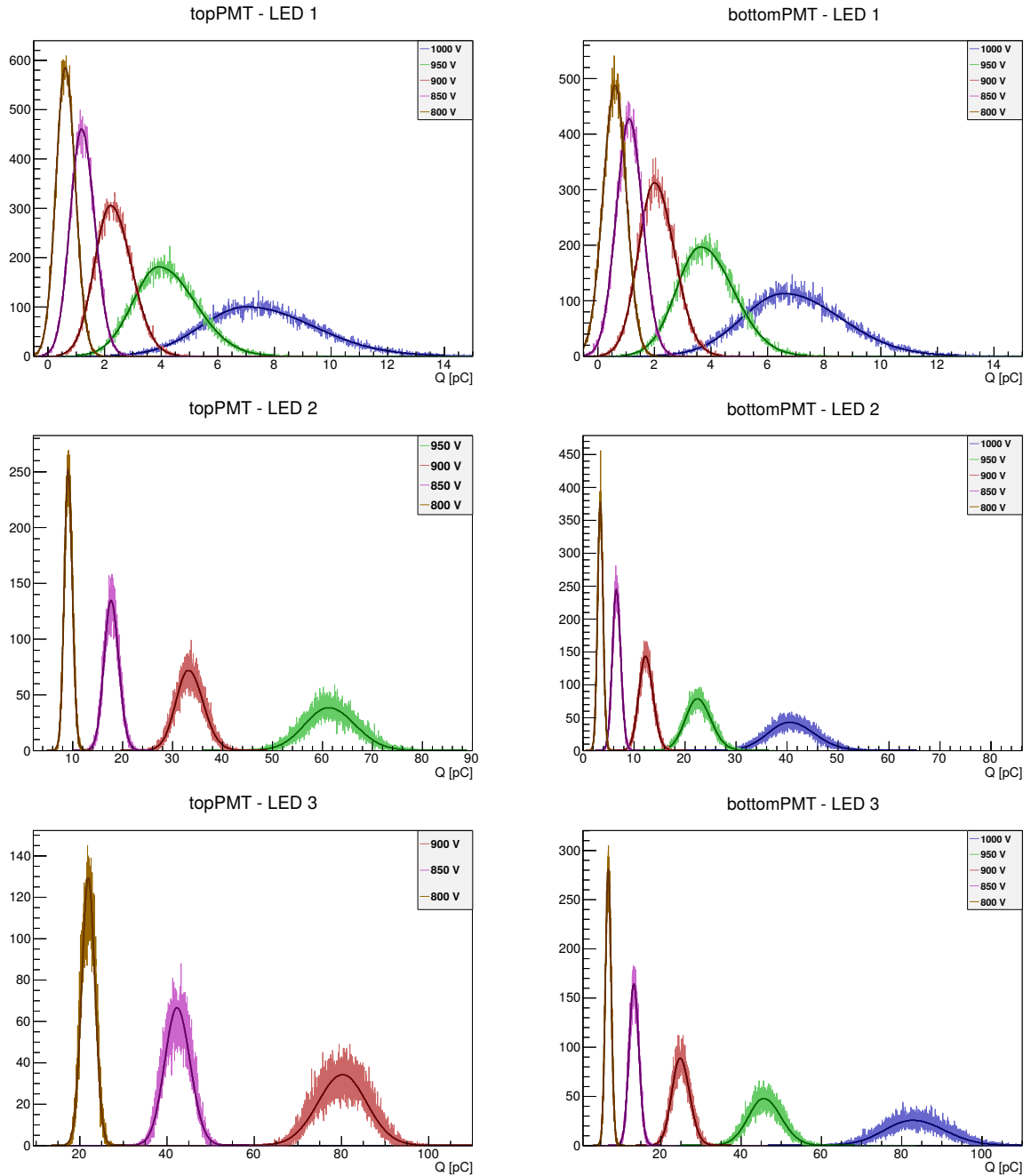


Figure 6.3. Spectra of the Waveform Integrals for top and bottom PMT at different strength of the illumination and different bias voltage. The unamplified signal after the passive split is used here, as recorded by SIS3316. A table with all fit parameters can be found in the appendix in table E.1

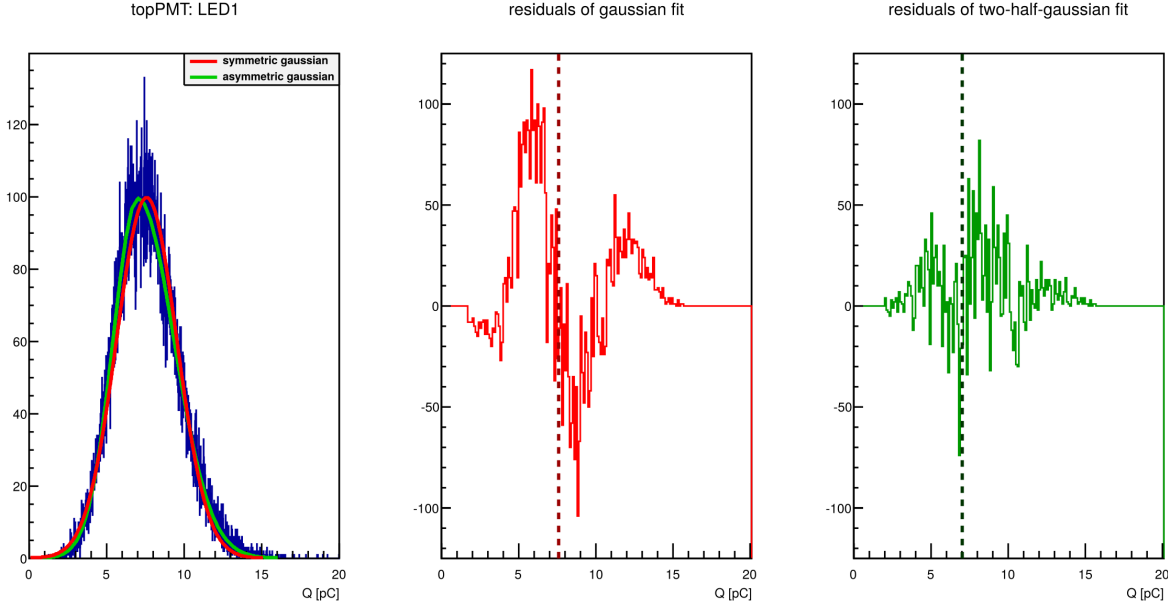


Figure 6.4. On the left the spectrum for the lowest setting of the LED is shown together with a fit of a Gaussian (red) and of an asymmetric Gaussian (green) following equation 6.1. In the center the residual of the Gaussian fit is shown, clearly illustrating the asymmetry around the mean of the Gaussian. On the right for comparison the residual of the asymmetric Gaussian. The dashed lines in the residual plots mark the position of Q_0 of the fit.

The reason for the asymmetric shape might be, that the average amount of photons hitting the PMT for the lowest settings of the LED is small enough to see the binomial nature of the quantum efficiency and collection efficiency of the photo cathode and first dynode(s) of the PMT. For the weakest setting of the LED, the topPMT has detected 34 photons in average and the bottomPMT 30 photons.

LED	topPMT		bottomPMT	
	o	s	o	s
Setting 1	-10.01 ± 0.02574	$0.01197 \pm 2.784e-5$	-9.954 ± 0.02829	$0.01183 \pm 3.026e-5$
Setting 2	-7.929 ± 0.008381	$0.01269 \pm 9.585e-6$	-8.628 ± 0.009076	$0.01234 \pm 9.981e-6$
Setting 3	-7.2701 ± 0.01256	$0.01295 \pm 1.483e-5$	-7.975 ± 0.007001	$0.01241 \pm 7.786e-6$
$\bar{g}(1000 \text{ V})$	$-1.253 \pm 1.742e-2$	$0.01253 \pm 1.742e-5$	$-1.219 \pm 1.601e-2$	$0.01219 \pm 1.601e-5$

Table 6.3. Fit parameters of relative gain. Last line is the average of all LED settings of one PMT, scaled to be 1 at 1000 V.

To get the relative gain, one can fit the measured values of Q_0 for each LED setting with an exponential function:

$$g(U) = o \cdot \exp(s \cdot U)$$

The measured mean values and the fits are shown in the upper part of figure 6.5. The resulting

6.2. MEASUREMENT OF THE RELATIVE GAIN

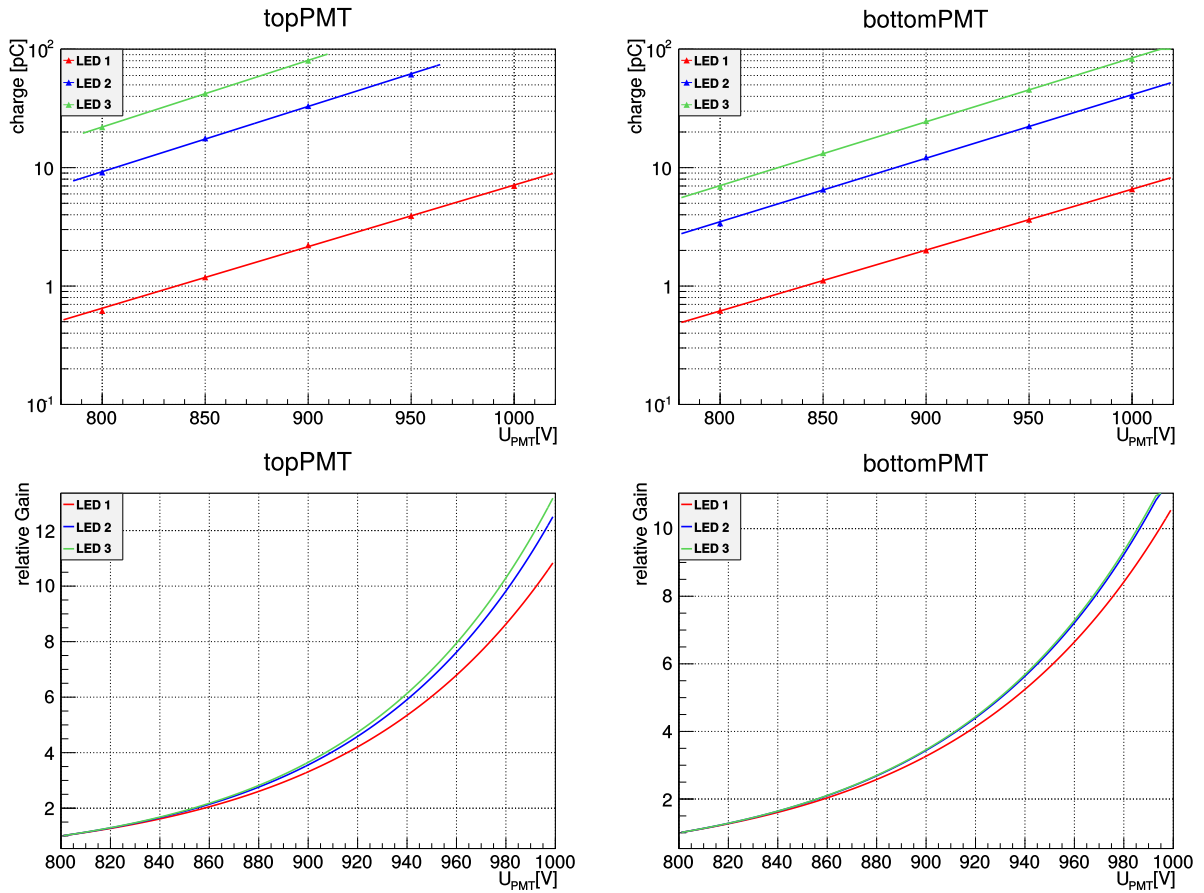


Figure 6.5. Gain curves: top: charge in pC, bottom: relative gain, normalized to 1 at 800 V.

curves can than be normalized to 1 at 800 V as shown in the lower half of the figure. This way of showing the measurements would allow to see saturation of the amplifier, FADC or the last dynodes of the PMT if the curves would flatten for higher bias voltages. Additionally one would realize a saturation of the photo cathode, if the slopes of the fits get steeper with decreasing amount of photons (i.e. LED 1 would have a steeper slope than LED 2 and/or LED 3). Non of those effects can be seen. Instead, one realizes that the weakest LED has the least steep slope. That is due to the fact, that for the low number of photons, the asymmetric Gaussian still does not reflect the shape of the single photo-electron peak. It might be better to fit with a generalized Poissonian, to reflect the statistical nature of photon-detection. Using these fit functions allows to extrapolate the single photon response measured at 1000 V to lower bias voltages.

6.3. Single photo-electron response

6.3.1. Model of the shape

One of the main goals of the MainzTPC is the measurement of the scintillation pulse shape. Hence, it is very important to understand the characteristic response of the sensor (PMT) and the readout chain. For this thesis, the characteristics are obtained from fitting a model to single photo-electron signals. The model contains three characteristic time-constants:

- τ_{anode} , the width of the charge-pulse at the PMT anode
- τ_{RC} , describing the shaping introduced by the RC-elements on the PMT-base (voltage divider and signal decoupling)
- σ , describing the bandwidth of the amplifier

The model follows the description of a PMT signal as given in [Leo94], which assumes only an RC-element and a scintillation light signal as input. In our case, we have a single photon, which corresponds to a perfect δ -pulse. This single photon produces one photo-electron, which produces an avalanche of electrons reaching the anode of the PMT. We expect this charge-pulse to be very sharp and δ -like. To describe this δ -like pulse we can use an exponential decay with a short decay time constant here. That means, that the model for the signal shape given in [Leo94] is still valid, keeping in mind the different meaning of the time constants. The scintillation time constant (τ_S) in [Leo94] means the width of the charge-pulse here. The time constant is renamed here from τ to τ_{RC} to be more descriptive. The model, which does not yet include the amplifier response, can accordingly be written as:

$$S_{PMT}(t) = \frac{A_0}{\tau_{RC} - \tau_{anode}} \left[\exp\left(-\frac{t - t_0}{\tau_{RC}}\right) - \exp\left(-\frac{t - t_0}{\tau_{anode}}\right) \right] \quad (6.2)$$

To include the bandwidth of the amplifier, the model (equation 6.2) can be convoluted analytically with a Gaussian ($g(\sigma, t)$), with σ describing the bandwidth of the amplifier. The result contains the error function and is quite lengthy and therefore not given here. The full model formula is given in the appendix F. To this model, one can add a linear slope s_{BL} and constant offset o_{BL} , to reflect low frequency noise on the measured signals.

$$S_{spe}(t) = [S_{PMT}(t) \otimes g(\sigma, t)] + o_{BL} + t \cdot s_{BL} \quad (6.3)$$

After obtaining the values for τ_{RC} and σ from single-photo electron signals, they can be fixed when fitting real scintillation signals, as both characterize sensor and readout properties and therefore do not depend on the origin of the signal, reducing the number of free parameters

6.3. SINGLE PHOTO-ELECTRON RESPONSE

for those fits. To find the typical single photo-electron signal shape, we decided to use a set of waveforms that contain a signal, from the dataset used to determine the absolute gain of the PMT. As the dataset taken for absolute gain measurement mainly contains “empty” waveforms, one had to select the ones containing a signal first. This has been done based on two criteria:

- charge of the signal as obtained by integration of a fixed window around the trigger of the SIS3305 waveform (1.4 pC - 2.6 pC)
- maximum amplitude of the signal (8 mV - 12 mV)

The spectra of all waveforms for maximum amplitude and charge measured, together with the selected range, is shown in figure 6.6.

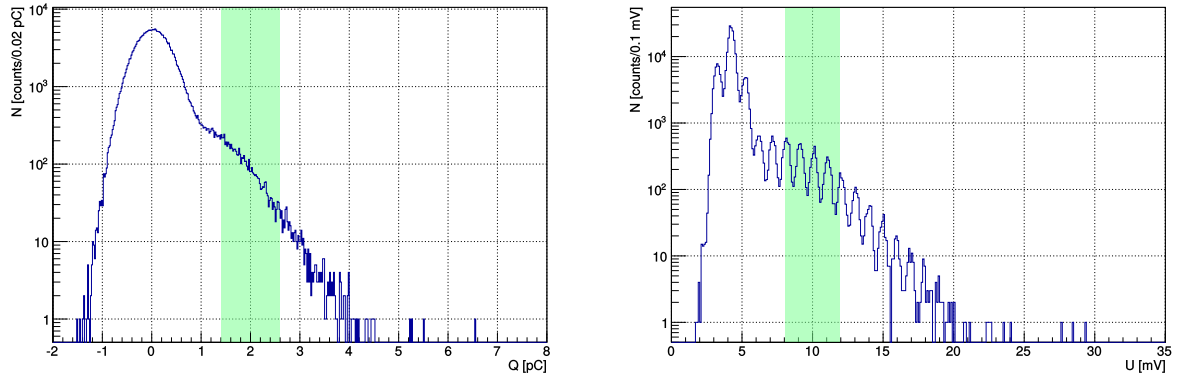


Figure 6.6. Single photo electron spectra of bottomPMT recorded with the fast digitizer SIS3305 using the KPH amplifier. At the top, the charge spectrum is shown, on the right the amplitude spectrum. The fingered structure in the amplitude spectrum reflects the lower resolution of only 10 bit, the width of the fingers is defined by variations of the baseline. The green areas mark the selection that has been used to find the shape of typical single photo-electron signal.

Using this set of waveforms containing a signal, one has different options to find the model parameters: one can produce an overlay of all (normalized) waveforms and fit the model to this 2D-representation, one can add up all (normalized) waveforms and fit the model to this superposition or one can fit the signal to the individual waveforms and look at the distribution of the fit parameters. As the time (relative to the trigger) when the single photo-electron signal appears is not identical for this measurement with an LED, the waveforms have to be shifted in time to compensate for this jitter when superimposing or overlaying multiple signals. This can either be done by using the position of the maximum amplitude of the signal or by using the parameter t_0 of fits to the individual waveforms. When using the position of the maximum to shift the signals in time, the DC-offset pattern of the SIS3305 gets visible (compare section 5.2.5 and figure 5.8), as one favors the bins with tendentious higher values for the adjustment in time. Therefore, the waveforms have been re-binned by factor four before being adjusted in time, reducing the time-resolution of the

signal from 0.2 ns to 0.8 ns. Table 6.4 shows the results obtained using the following different methods:

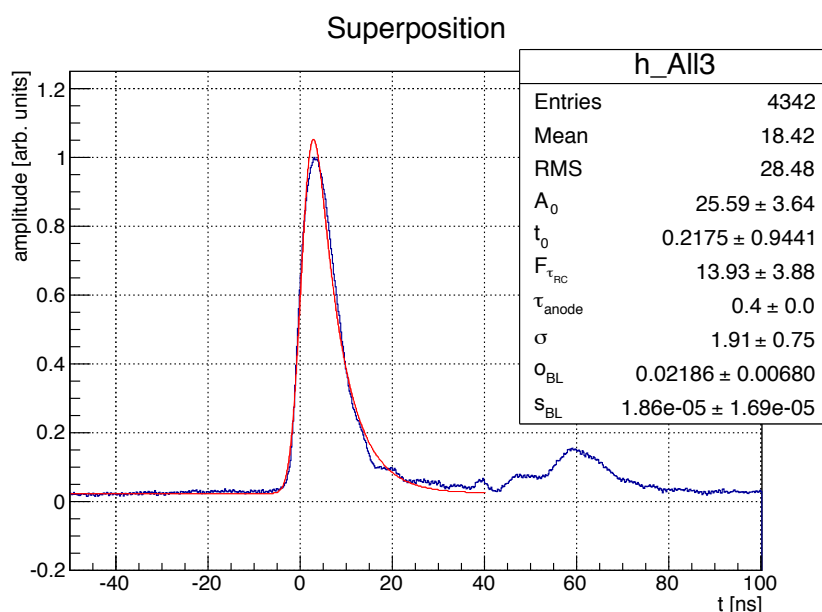


Figure 6.7. Superposition of waveforms following method 3. The parameter τ_{RC} is written as $F_{\tau_{RC}} \cdot \tau_{anode}$ in the fit function, to allow fixing the size order of the two time constants. After the main signal (around $t = 0$ ns one can see a second bump at about $t = 60$ ns, which is likely due to some kind of electronic reflection.

1. Superposition position of maximum of waveform
 - a) without re-binning
 - b) re-binning by 4
2. Overlay by position of maximum of waveform
 - a) without re-binning
 - b) re-binning by 4
3. Overlay by t_0 of fit to individual waveform
4. Superposition by t_0 of fit to individual waveform
5. Fit parameters of fits to individual waveforms

For all fits, the parameter τ_{anode} has been fixed to 0.4 ns, as it should reflect the δ -like charge pulse. The linear part, i.e. O_{BL} and S_{BL} has been fitted on the waveform before the signal in the time range -600 ns to -100 ns and has been fixed when fitting the signal shape in the range -100 ns to 40 ns.

Figure 6.7 shows the superposition of all waveforms according to method 4 (blue) and the model fit (red). One can see a second bump at about 60 ns. The origin of this bump is discussed later in this chapter. Because of this bump, the signal shape is only fitted up to $t = 40$ ns. In figure 6.8 the overlay method (method 3) is illustrated: On top the 2-dimensional overlay of the waveforms containing an SPE signal is shown. The waveforms are normalized to the maximum amplitude and shifted in time by the parameter t_0 of fits to the individual waveforms. Taking the mean value and the root mean square of each 0.2 ns time-slice of this 2D-histogram allows to create the plot on the bottom of figure 6.8, where the darker blue line depicts the mean values, and the lighter blue area reflects the root mean square values. When fitting the model (red), the root mean square values are used as errors in this case. The superposition and overlay plots for methods 1 to 4 are shown in appendix E, as well as exemplary fits to single waveforms and the histograms illustrating the distribution of the fit parameters to individual waveforms.

method	description	τ_{RC} [ns]	σ [ns]
1.a)	Superposition maximum (no re-binning)	2.686 ± 1.661	2.408 ± 0.8630
1.b)	Superposition maximum (re-binned)	5.544 ± 3.196	2.268 ± 1.484
2.a)	Overlay maximum (no re-binning)	5.120 ± 0.8764	2.410 ± 0.4126
2.b)	Overlay maximum (re-binned)	5.168 ± 1.805	2.402 ± 0.8437
3)	Superposition t_0	5.572 ± 1.520	1.910 ± 0.7500
4)	Overlay t_0	5.216 ± 0.840	2.193 ± 0.3646
5)	Individual waveform fits	5.83 ± 1.42	2.124 ± 0.3922

Table 6.4. Different methods to get the typical single photo electron response, described by equation 6.3. The quantities of interest are τ_{RC} and σ . The former describing the response of the RC-circuit and the latter describing the bandwidth of the amplifier used. The errors given are the fit errors, except for the distribution of fit parameters (method 5), where it is the RMS of the parameter. Parameters that do not describe the spe response (A_0 , t_0 , s_{baseline} and σ_{baseline}) can be found in the plots in figures 6.7 and 6.8 and in appendix E.

Using method 1.a one derives a significantly shorter τ_{RC} than for any other method. This is due to a fit that obviously does not reflect the decay properly because of the pattern effect of the SIS3305. All other methods are compatible with each other within the errors.

We see, that both time constants involved here are as large ($\sigma \approx 2$ ns) or larger ($\tau_{RC} > 5$ ns) than the decay time of the faster singlet-state scintillation (2 ns, compare chapter 3) as measured previously by other groups. That means, that it will be difficult in our measurements to resolve the fast decay time constant involved in the scintillation process, and, that it will be especially important to include the obtained values when fitting scintillation signals later in section 7.4. It also means, that it will be of high interest to improve the readout chain towards higher bandwidth for future measurements. Additionally, a better method to determine the response of the amplifier and the RC-elements should be established. Currently, the first step towards deeper understanding and improvements is done in a bachelor thesis, measuring the response of the readout using a pico-second laser instead of an LED, and measuring the response of the amplifier independently from the PMT.

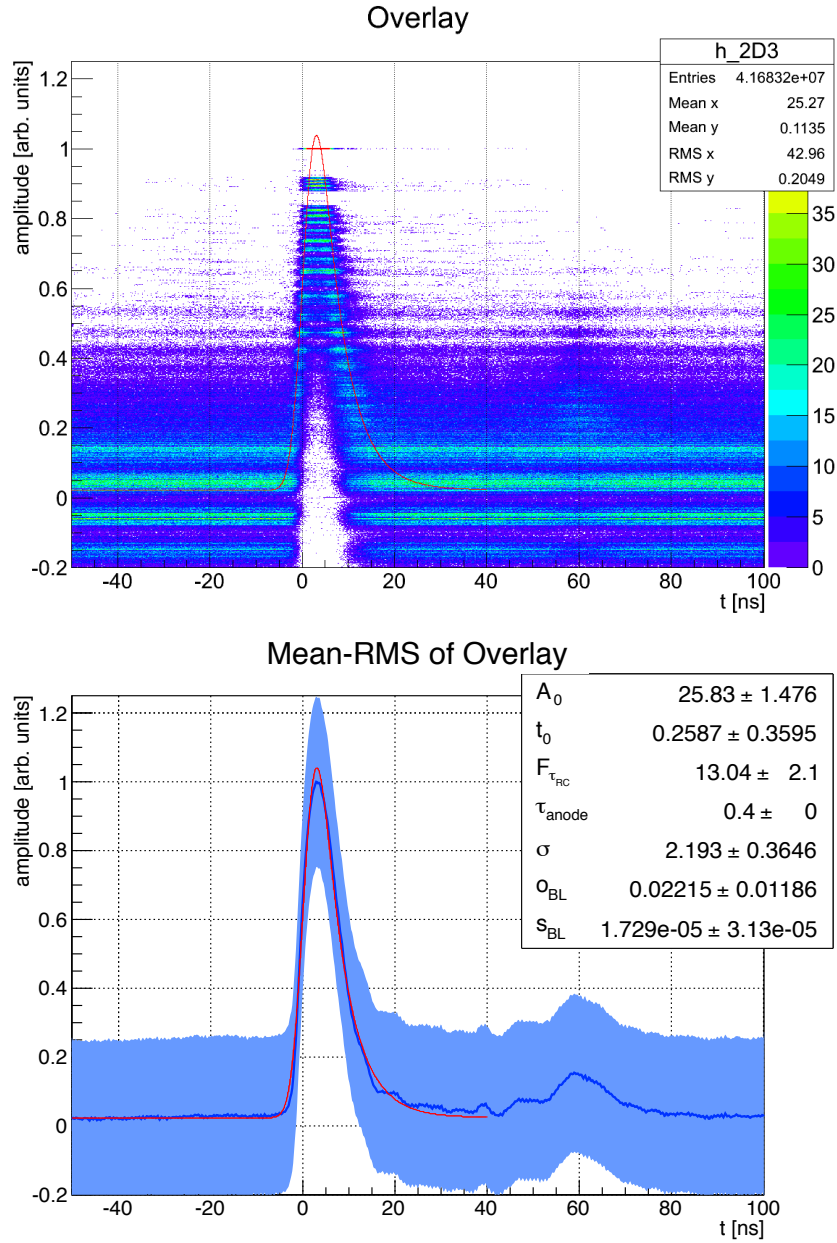


Figure 6.8. The upper image shows an overlay of the waveforms following method 4 (i.e. using the parameter t_0 of fits to the individual waveforms for adjustment in time). The red line is the fit to the mean and RMS values of each time-slice (0.2 ns) as shown in the lower graph.

6.3.2. Investigation of the second bump

As previously mentioned, there is a second bump after the signal peak (figure 6.7). Two explanations for this bump exist: either it originates from a reflection in the electronics due to an impedance mismatch, or it is a time window of after-pulses of the PMTs. Looking into individual waveforms of the absolute gain calibration data could help understanding this effect:

If it is due to an reflection, it should be visible on every waveform at the same position. The amplitude ratio of signal to reflection should be always the same as in the averaged waveform. Of course, as single photo-electron response is only about 10 mV and the amplitude of the second peak about 10% of the first, this will hardly be above noise.

If it is after-pulsing, it should only occur in some waveforms. The second peak could than vary a bit in position, depending on where between cathode and dynode the rest gas atom in the PMT was ionized. The amplitude of the second pulse, should in this case be in the same order of magnitude as the single photo electron response. The amplitude ratio in the averaged waveform would therefore reflect the ratio of signals without after-pulse to signals with after-pulse.

Out of the first 100 waveforms used to create figure 6.7 no waveform has shown an after-pulse at 60 ns, but almost all show an slight extend. This gets more distinct when applying the raised cosine filter used for S1-peak-finding on the waveforms of the fast digitizer (figure 6.9). Therefore it is more likely a reflection than an after-pulse.

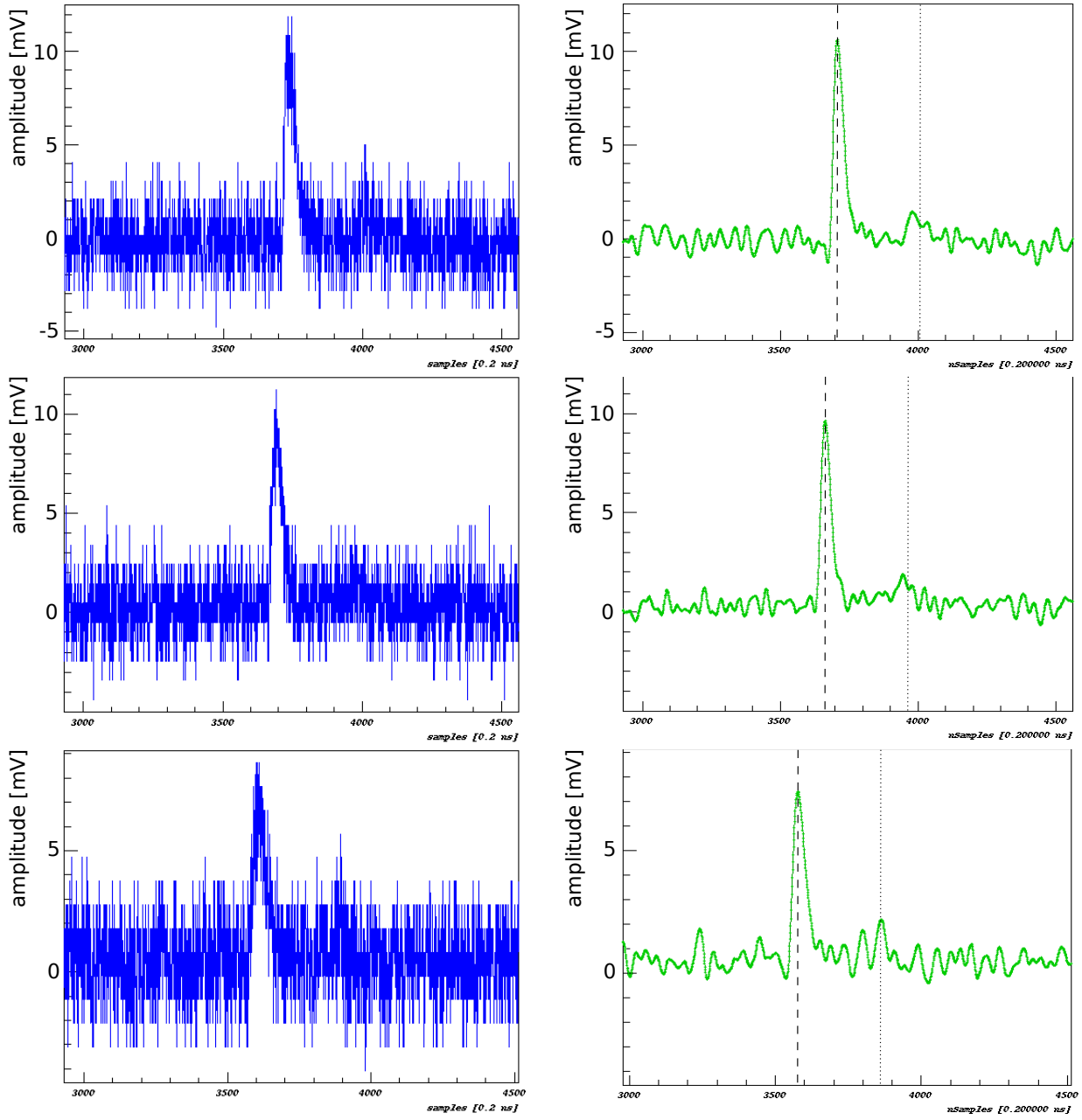


Figure 6.9. Some example waveforms of single photo-electrons. On the right, the raised cosine filter for S1 peak finding on the fast digitizer is applied to the raw waveforms (left). The dashes and dotted lines mark the peak position and 60 ns after the peak respectively.

7. Data Analysis

Raw data analysis is only the very first step of the analysis chain required to extract physics results from the data taken. This chapter describes the steps following the raw data analysis for the data taken at the nELBE neutron source. In this thesis, the analysis is using the data taken by the TDC to reject bad events and classify events into different categories after selecting *CoincidenceHits* for the MainzTPC and the plastic scintillators for each event. This chapter describes the criteria and reasons for rejecting events, explains how the *CoincidenceHits* to be used for later analysis are selected and how the resulting selections are used to classify events into different categories.

After event categorization, the analysis in this thesis focusses on achieving first results on the scintillation pulse shape and its difference for the different event types. The technique used to find the pulse shape is described and ideas for future improvements are given. Additionally the influence of different drift fields to the pulse shape is investigated.

7.1. Selections

7.1.1. Event Selection

As already described in the previous chapter, one has to apply selections on event level to the processed data. For the analysis described here, the following selections have been done:

- exactly one hit on the accelerator clock channel
- on exactly one plastic scintillator coincidenceHits have been found (compare 5.7)

The first selection assures that the accelerator clock is available as a reliable mark to calculate the absolute time values. This selection typically does not exclude events, as normally there is exactly one hit on the accelerator clock TDC-channel. The second selection (criteria described in section 7.1.2) makes sure the plastic that detected the scattered particle is clearly defined. This selection does cut out events, and might be too strict, as the coincidenceHit search is done allowing a very large time difference (± 100 ns) between the hits of topPMT and the bottomPMT that make up a *CoincidenceHit*. *CoincidenceHits* with time differences between the hits of topPMT and the bottomPMT significantly larger than 6.66 ns cannot originate from one interaction in the plastic

scintillator, because the effective velocity of light in the plastic scintillators is about 15 cm/ns and their length is 1 m. However, the cut does not remove a large amount of events. In case of dataset 20160322T0515 it removes 5.8% of the events.

Dataset 20160322T0515 is used in this chapter to illustrate the selection of events and *CoincidenceHits*, if not stated otherwise. In this dataset, the trigger was set to topPMT&bottomPMT in the TPC and requiring a coincidence with a plastic scintillator, too. The cathode and anode voltage of the TPC were set to 0 V, so no drift and extraction fields have applied for this dataset.

7.1.2. CoincidenceHit Selections

Events that pass the event selection often show more than one *CoincidenceHit* in the TPC and typically several *CoincidenceHits* on the plastic scintillator found by the raw data analysis routine. Now one has to select **one** *CoincidenceHit* in the TPC and **one** *CoincidenceHit* in the plastic. For the combination of the two coincidenceHits, one can state the time-of-flights and therefore the energy of the incoming neutron (E_n) and the scattered neutron (E'_n).

7.1.2.1. CoincidenceHit selection: TPC

To find the *CoincidenceHit* in the TPC, three selection criteria are applied:

responsible for trigger: Only *CoincidenceHits* that generated the trigger are kept

coincidence time difference: The coincidence time difference must be in a certain range

first: Only the first *CoincidenceHit* that fulfills the previous selection criteria will be used

For this work, the selection windows chosen are very restrictive. This is probably not always the best choice, but it helps for a first analysis to reduce the background, and can be improved after thorough investigation in future analysis.

Selection: responsible for trigger

As described previously in section 4.7.6, the trigger is always generated by a signal in the TPC. Therefore, it is possible to restrict the *CoincidenceHits*' timestamp to a narrow window, with a width given by the jitter of the TDC of 25 ns. The TDC has, as mentioned previously, a precision of 25 ps (compare section 4.5.3.4), but to make use of this, one always has to relate the hit of one channel to the hit of another channel. Without subtracting two timestamps, the TDC is only precise within 25 ns. For high precision time-of-flight the accelerator clock hit is used as reference. However for the selection of the *CoincidenceHit* that led to the trigger, this procedure cannot be used and we have to rely on the less precise raw timestamp of the *CoincidenceHit*.

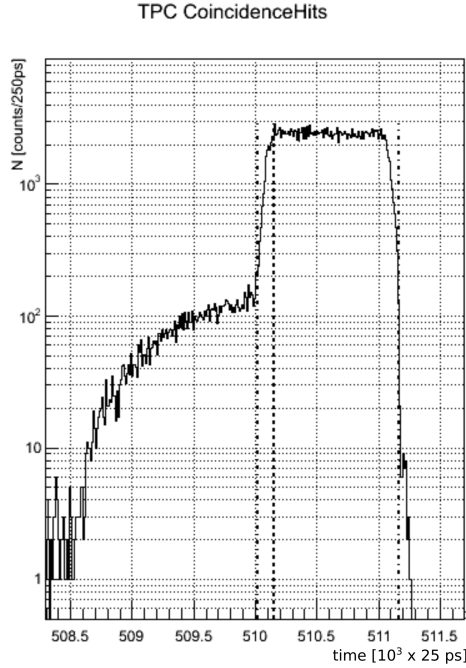


Figure 7.1. Selecting *CoincidenceHits* in the TPC (at this point ignoring the hits in the plastic scintillators) that lead to the trigger. The vertical dotted lines mark the selected region (left line and right line) and the maximum (central line) of the histogram. This selection could be improved by selecting on $h_{\text{coincidenceHit}} - h_{\text{TPCtrigger}} = 0$ instead of using the window on the raw timestamps shown here.

The distribution of TPC *CoincidenceHits* in the TPC, independent of the hits and *CoincidenceHits* (and their timestamps) in the plastic scintillators, is shown in figure 7.1. We select only those, which fall within a 10%-region around the maximum in the histogram, as indicated by the dotted lines. The shoulder to the left belongs to events that have not been triggered by the TPC but by the plastics. This can happen for some special cases as described in chapter 4.7.6. The width of this shoulder is given by the width of the gate opened by the TPCtrigger (39.2 ns).

This selection could be improved, by using relative timestamps. As subtracting the accelerator clock timestamp from the *CoincidenceHits*' timestamps does not help here, one could subtract the timestamp of the TPC-trigger, which was also recorded on the TDC. *CoincidenceHits* that generated the trigger will fulfill the following criterion: $h_{\text{coincidenceHit}} - h_{\text{TPCtrigger}} = 0$. This is exact selection of the hits that generate the trigger, but it wasn't applied in this thesis.

Selection: coincidence time difference

After selecting only *CoincidenceHits* that generated the trigger, there might still remain more than one per event. To further narrow down the selection, *CoincidenceHits* are rejected if the CTD is

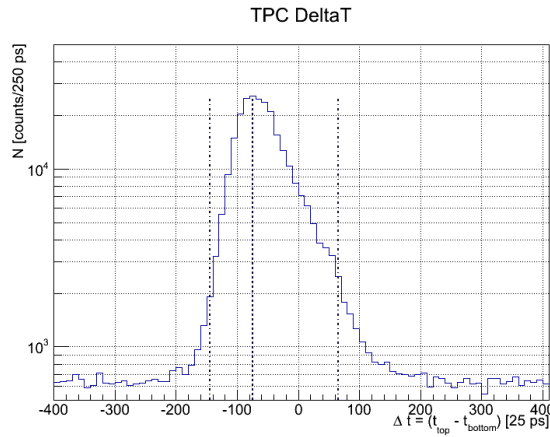


Figure 7.2. Histogram of $CDT = \Delta t = h_{top} - h_{bot}$ for the TPC. The vertical lines mark the region and the maximum of the histogram, used for selecting the coincidence hit in the TPC. The asymmetry could be caused by the higher probability for the bottomPMT to detect the first photon.

outside a certain window. For this work, the window is defined to be within full-width at 10% of the maximum in the histogram showing the CTD-values of all coincidenceHits (figure 7.2).

This selection is definitively too narrow to include all good events, especially the ones with low energy deposits, as the time constants involved in the scintillation process are longer than the width of the selected window. Therefore, in events where just a few photons are generated, no *CoincidenceHit* might fulfill this criterion, or not the right one, which leads to a worse measurement of TOF-1, the TOF from the liquid lead circuit to the TPC.

Selection: first

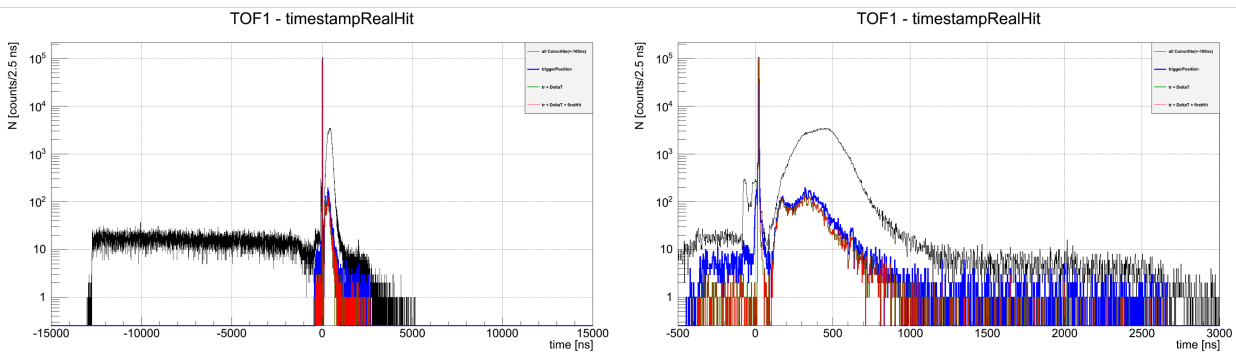


Figure 7.3. Time-Of-Flight from source to TPC for the coincidence hits found and the different selections. Right side shows a zoomed view of the full spectrum(left).

If there are events, where more than one *CoincidenceHit* passes the *responsible-for-trigger-* and the *CTD-selection*, only the first of the remaining *CoincidenceHits* is kept, making sure a maximum of one *CoincidenceHit* survives the selection. It is of course possible, that no *CoincidenceHit* passes

7.1. SELECTIONS

the selection. In the example dataset 8.5% of the events do not have a *CoincidenceHit* that passes the selections, probably due to the too restrictive selection on CTD.

Figure 7.3 shows the TOF-1 for the example dataset for all *CoincidenceHits*, and what is left after applying the various selection criteria. It is evident, that the strongest cut is the one selecting the coincidenceHits in the trigger region. The other selection criteria do not cut out many more additional coincidence hits, at least, if the selections are done in the order used here.

7.1.2.2. CoincidenceHit selection: Plastics

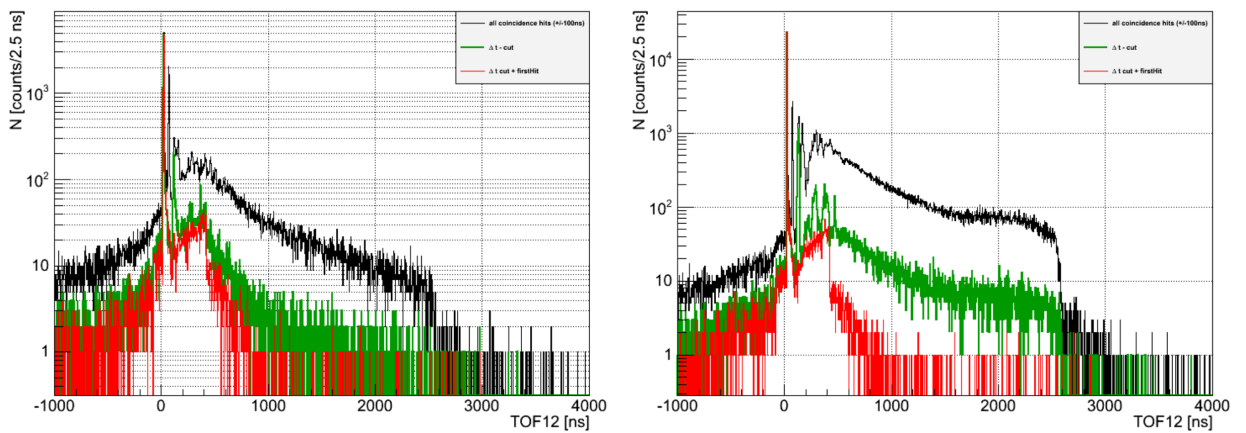


Figure 7.4. Time-Of-Flight-12 from source two exemplaric plastic scintillators for the *CoincidenceHits* found and the different selections applied. Left: plastic 7 (forward at $+16^\circ$), Right: plastic 3 (backward at $+144^\circ$). Even in the final selection the spectrum does not show a similar distribution for the neutrons as for TOF-1. The reason is, that more 6.3 times more triggers have been generated by a combination of a gamma in the TPC and a neutron in the plastic scintillator, than by neutrons scattered in the TPC and detected in the plastic scintillator.

In general, the coincidenceHit selection for the plastic scintillators is done similar to the selection in the TPC, except that the first selection criterion – the coincidence hit being the one that led to a trigger – cannot be applied as easily. One would have to subtract the hit of the plastic trigger from the CoincidenceHit and choose the one that would have opened the gate. Although for the plastic scintillators there is no explicit selection of the *CoincidenceHits* that opened the window for the trigger-generation, this is implicitly done, by selecting the first of the *CoincidenceHits*. The first *CoincidenceHit* (with a CTD-value in the suitable range) will have opened the trigger-gate. This is not necessarily always the case, as the selection on CTD applied is narrower than the coincidence window realized in hardware (± 40 ns). It is worth mentioning that the selection of *CoincidenceHits* on the plastic scintillators is completely independent from the selection of *CoincidenceHits* in the MainzTPC. In particular there is no selection criterion requiring the *CoincidenceHit* in the plastic to come after the *CoincidenceHit* in the TPC. As a

consequence, there can be negative values for TOF-2, if the plastic scintillator is hit by a different particle than the TPC.

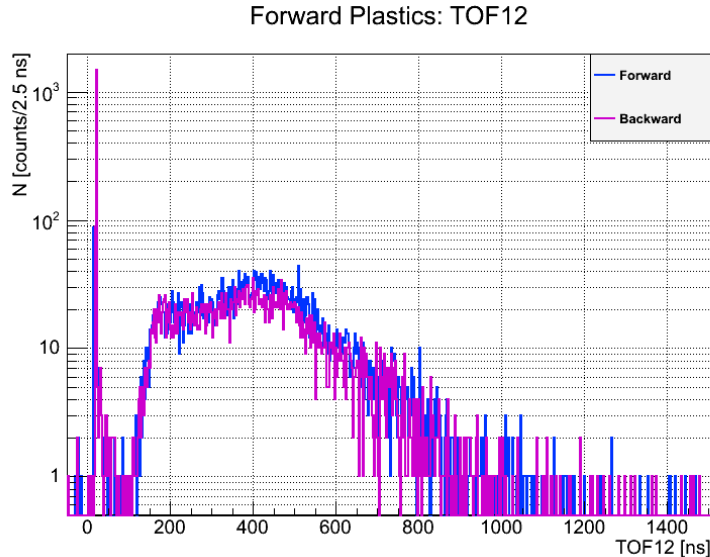


Figure 7.5. Time-Of-Flight-12 from source to plastics for events where the trigger was generated by a neutron in the TPC. One realizes a gamma flash, although only neutron interactions in the MainzTPC contribute to this plot. Therefore the gamma flash originates from random coincidences between a neutron interacting in liquid xenon and a gamma interacting in the plastic scintillator.

The TOF-12-spectra (from source to plastics) shown in figure 7.4 do not show the expected features as nicely as the TOF-1 spectrum. The gamma flash is clearly visible, but the neutron TOF distribution is not. The reason is, that the trigger setup allowed triggering on gammas in the MainzTPC with a neutron in the plastic scintillator from the same accelerator bunch. Triggering on gamma(TPC) - neutron(Plastic) (or Population Y, as defined in section 7.2) happened 6.3 times more often than triggering on a neutron in the TPC in total in the example dataset. Therefore these events dominate the TOF-12 distribution. The sharp edge at 420 ns is defined by the length of the gate opened by the plastic scintillators. After the edge, the distribution of neutron(TPC)-neutron(plastic)-events is visible. Before selecting just the first hit, one can also see several peaks after the gamma flash and in the range of TOFs, that would fit to neutrons (> 100 ns). This is due to afterpulses of the PMTs of the plastics.

To make sure the selection criteria are chosen well, one can plot the TOF-12 for events, where a neutron interaction in the MainzTPC generated the trigger. The selection of these events, is based on the requirement of TOF-1 exceeding at least 70 ns to remove the gamma flash, using the selected *CoincidenceHit* in the TPC. In this TOF-12 spectrum of neutrons (figure 7.5) one can see, that the distribution is similar to the TOF-1 distribution, which is expected as the energy-loss by elastic scattering in liquid xenon is negligible compared to the start energy of the neutrons ($< 0.3\%$ for forward plastics and $< 3\%$ for backward plastics). This means that the change of the

TOF-1 spectrum to the TOF-12 spectrum (for the neutrons) should primarily originate from the additional 1 m flight path. In the TOF-12 spectrum shown in figure 7.5 one realizes the existence of a gamma flash. This can only originate from random coincidences between a gamma in the plastic scintillator and a neutron interacting in the MainzTPC, which is not suppressed by the trigger system, as described in chapter 4.7.6.

7.2. Event Classification and Identification

7.2.1. TOF1 vs TOF2

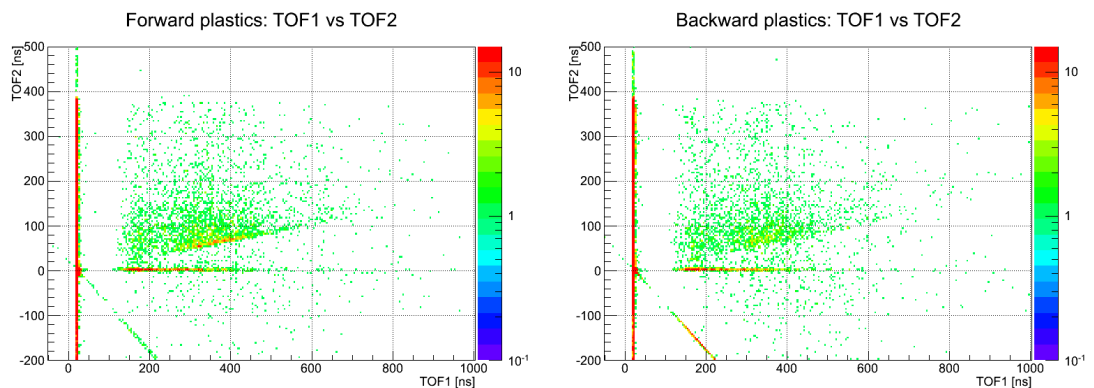


Figure 7.6. TOF1 vs TOF2: Comparing the TOF1 vs. TOF2 2d-colorscale spectra of events triggered by the forward directed plastics and the backward directed plastics, shows the wider distribution in TOF2 for the backwards plastics, due to the higher energy loss.

After having selected one single *CoincidenceHit* for the MainzTPC and one single *CoincidenceHit* for the plastic scintillator, one can calculate TOF-2. As the flight path from MainzTPC to plastic scintillator differs, depending on where (z-position) the scattered particle hit the plastic, one can normalize TOF-2 to the shortest possible flight path-2, which is 1 m. After doing this, one can plot a 2D histogram TOF-1 versus TOF-2. Figure 7.6 shows the 2D histograms for the forward plastics (left) and backwards plastics (right) for the example dataset.

7.2.2. Event Classification

In the 2D histograms (TOF-1 vs. TOF-2) one can see different clusters of events. In figure 7.7 the principal clusters are shown and named. The events in the different clusters are of different types. For some the origin is obvious, for others the origin is less clear and will be discussed in the following. The expected populations are gammas, scattered in the TPC and then detected in the plastic scintillators and of course neutrons, elastically scattered in the TPC and detected in the plastic. Additionally there are background events, where two independent particles, both

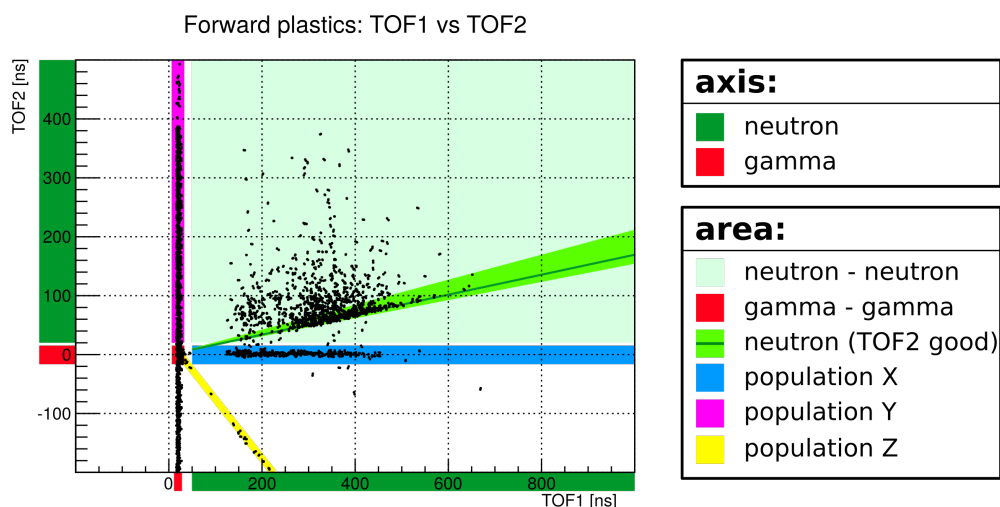


Figure 7.7. TOF1 vs TOF2: Scatter plot using the forward plastics only. At the axis green and red areas mark time-of-flight intervals matching gammas or neutrons respectively. Various populations of interest are marked in the plot.

produced by the same beam bunch at the target, interact in the TPC and the plastic scintillator respectively.

gamma-gamma: Events, where the trigger is generated by a gamma interacting in the MainzTPC and a gamma in a plastic scintillator. The population contains events where the gamma from the TPC is scattered towards the plastic scintillator and detected there and also contain events originating from two independent gamma particles of the same beam bunch, as those cannot be distinguished by our setup.

neutron-neutron: Events, where TOF-1 and TOF-2 are long enough to constitute a neutron. These could be from one single neutron scattered in the TPC or from two independent neutrons of the same beam bunch. Especially events where the particle would have to move faster from TPC to plastic scintillator than from source to TPC i.e.

$$\frac{\text{path-of-flight-2}}{\text{TOF-2}} < \frac{\text{path-of-flight-1}}{\text{TOF-1}}$$

likely originate from two independent neutrons.

neutron (TOF-2 good): From kinematics for elastic scattering, we expect the neutrons to lose only small amounts of their original energy ($< 3\%$). Therefore, the velocity of neutrons before and after scattering should be roughly identical. Events, where TOF-2 matches the expectation from TOF-1 assuming zero energy loss in the MainzTPC within an uncertainty of $\pm 25\%$ are tagged as neutrons with “TOF-2 good”. The darker green line marks exactly zero energy loss.

Inelastic neutron scatter: If the neutron interacts inelastically in liquid xenon, the energy deposit is at least the energy required to excite the xenon nucleus. Excited states of the different isotopes exist at different energies up to several hundreds of keV. Therefore the neutrons can lose a large fraction of their primary energies and have significantly larger TOF-2 than the ones marked as “TOF-2 good”.

population X: Events, where TOF-1 identifies the particle triggering the DAQ as neutron, but the *CoincidenceHit* in the plastic is too short after. This can occur for inelastic neutron interactions in the MainzTPC, where the promptly emitted gamma from the excited xenon nucleus is detected by the plastic scintillator.

population Y: Events, that are triggered by a gamma interacting in the MainzTPC and a neutron interacting in the plastic scintillator. These events might still be used for future analysis of the relative scintillation efficiency, as it is likely that the neutron interacted in the TPC after the gamma and is scattered towards the plastic scintillator. It will require a sophisticated way of finding the *CoincidenceHit* in the TPC that belongs to the neutron. Additionally the S1-signal of the neutron will only be recorded on the slower FADC and without additional amplification.

population Z: Events, with a gamma interacting in the plastic scintillator and neutron interacting in the MainzTPC. In theory, the trigger system should not allow triggering on this type of events, except for neutrons with very high energies ($\text{TOF-1} < 100 \text{ ns}$). One needs to check for those events, if the selection of the *CoincidenceHits* did not work as intended.

7.3. S1 vs. Energy Deposit

As the MainzTPC was not only build to improve understanding of the scintillation pulse shape, but also to measure the scintillation efficiency of liquid xenon, we tried to find a correlation between energy deposit in the TPC and the amount of primary scintillation light (S1) we detected. As it turned out that a double time-of-flight measurement would not provide a good energy resolution we focused on using time-of-flight to determine the primary neutron energy, and the scattering angle to determine the energy deposit in liquid xenon.

The energy transfer for elastic neutron scattering off xenon nuclei is described by the formula:

$$\Delta E = E_{\text{TPC}} = E_n^0 \frac{2 \cdot m_n \cdot m_{Xe}}{(m_n + m_{Xe})^2} (1 - \cos \Theta)$$

with an energy transfer $\Delta E = E_{\text{TPC}}$ to the xenon nucleus, E_n^0 the energy of the primary neutron, m_n and m_{Xe} the mass of neutron and xenon atom and Θ the scattering angle.

For the scintillator panels mounted in backwards direction, the scattering angle Θ in the laboratory system is large, i.e. the variations on one panel due to different z-positions on the scintillator panel do not lead to strong changes of $\cos \Theta$. That is also shown in table 4.2. As a consequence, for neutrons of one certain energy, the energy deposit in the MainzTPC does not vary much within one of the backwards directed plastic scintillators. Even the variation between different scintillator panels is small, compared to the variations due to different primary neutron energies E_n^0 .

The current strict selections and event classification result in a small number of neutron interactions remaining in the data sample. Therefore we focus here on the results of a combination of all backwards directed plastic scintillators for the dataset 20160322T0515, where no drift field was applied. The events classified as neutrons with good TOF-2 have been grouped into five classes by the primary neutron energy, each group spanning 500 keV. This means that the variation of the energy deposit within one group is mainly determined by the variation of the primary neutron energy and not by the interaction position in the TPC or the precise scattering angle. Hence, neither the position on the plastic, nor the fact which of the backwards plastics was hit by the scattered neutron should have a strong effect (compare table 4.2).

Figure 7.8 shows the full range of S1-spectra obtained for various primary neutron energies and figure 7.9 presents a detailed view up to 1000 photo electrons. One would expect to see a broad peak in each of the spectra, which is centered at higher amounts of S1-photons for higher primary neutron energies. This cannot be found in the spectra shown here. Instead, one finds very broad distributions, and many events with very small S1-signals (less than 100 photo electrons). A small peak can be found for all primary neutron energies at about 240 photo electrons, but the position does not vary with the E_n^0 by a factor of about five as one would expect.

7.3. S1 VS. ENERGY DEPOSIT

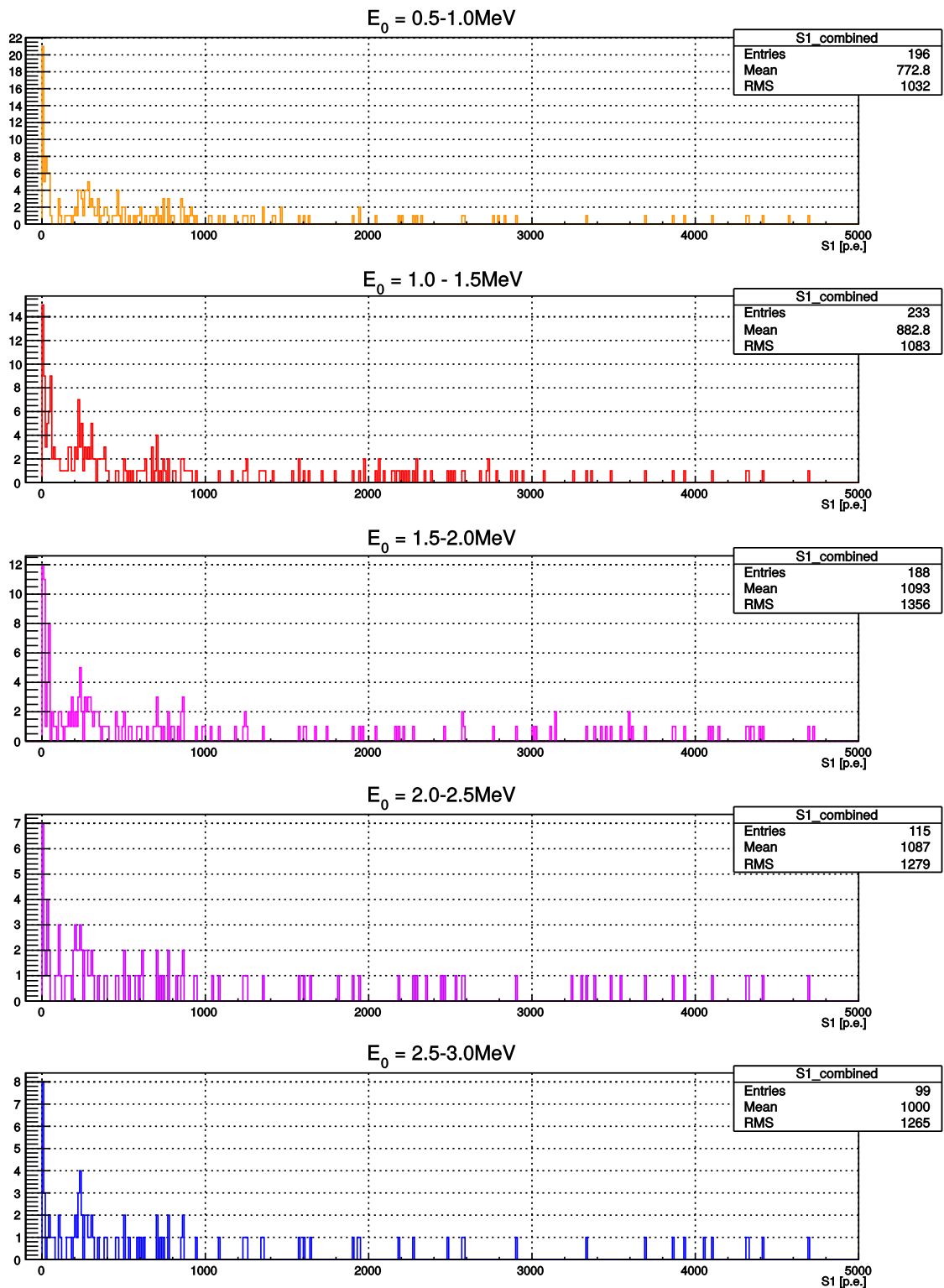


Figure 7.8. S1 spectra of events flagged as neutron with “TOF-2 good“ for all backwards-directed plastics, separated into 5 ranges of primary neutron energies E_n^0 . S1 is shown in photo electrons as a combination of top and bottomPMT using the gain calibration from chapter 6. The spectra do not show the expected behaviour: a clear peak that moves to higher amount of detected photo-electrons for higher primary neutron energies. Data is taken without drift field.

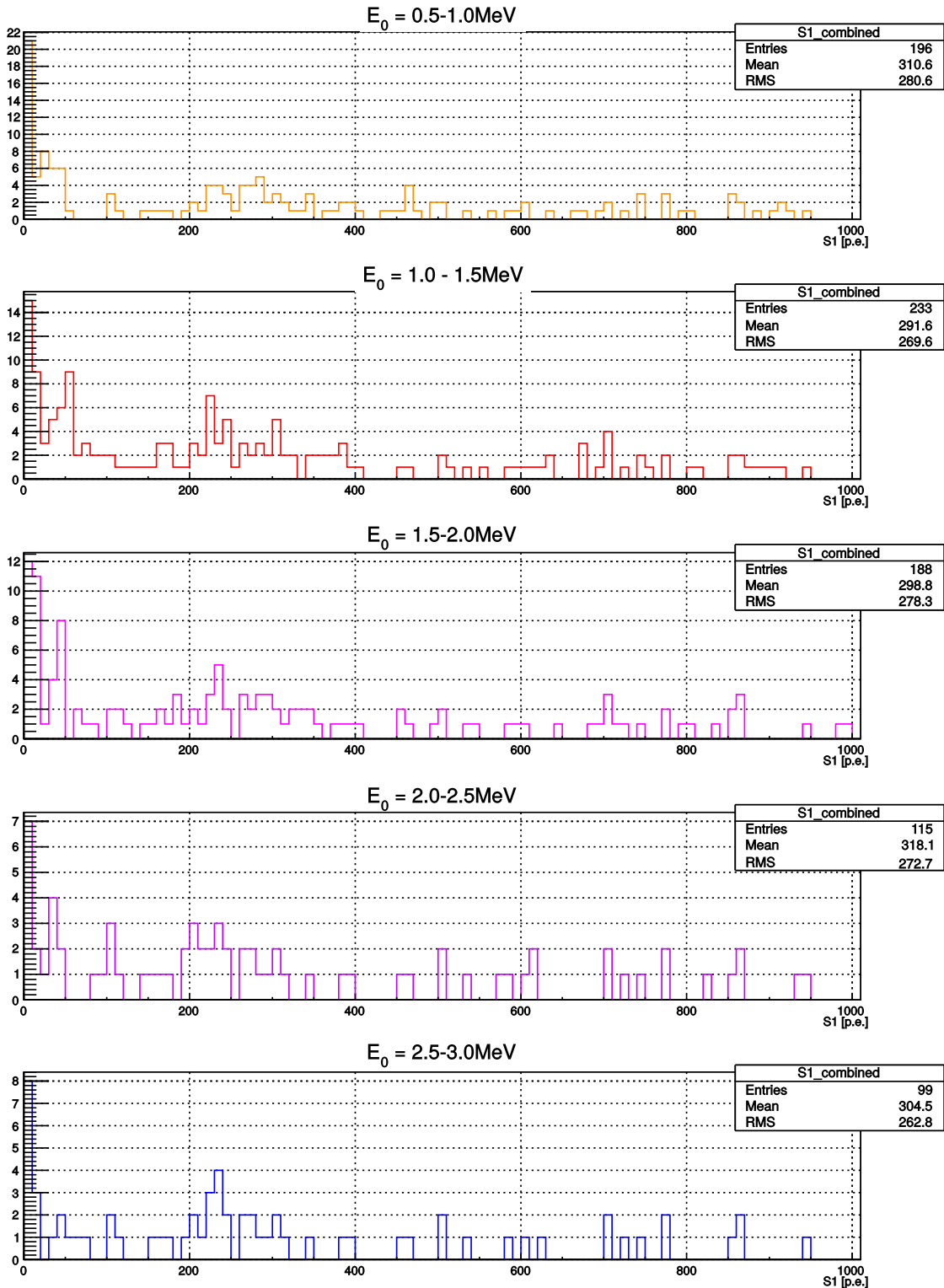


Figure 7.9. Detailed view on the first 1000 photo electrons of the histogram of figure 7.8.

Either the analysis technique (defining the S1-peak) does not work as intended or it is due to a physics reason. Problems with the definition of the S1-peak and the measured amount of photons are rather unlikely, as it works well for data taken in the Compton scattering setup, which will be shown in [Sis17]. Still it could happen that photons are not accounted for if they come well separated from the main S1 signal, due to relatively late recombination of electron-ion pairs.

Due to inhomogeneities in the light collection efficiency of the TPC, and the fact that currently no position resolution and therefore no position dependent correction of the measured signals is applied, the resolution of the S1-signals is worse than what could be reached with the TPC. Including this, will also help improving the spectra.

From the physics side, it could be that the spectra contain events from inelastic neutron scattering, where the promptly emitted gamma also deposits some energy in the TPC. Multiple scattering of the primary neutron or background events where the interaction in the TPC and in the plastic scintillator originate from different primary neutrons might also be contained in the data-sample. More thorough investigation of the interactions will be necessary. This will include checking for multiple S2 signals and discrimination of events where scattering angle and primary neutron energy do not match.

7.4. Pulse shape analysis

Pulse shape discrimination in general requires a figure of merit (M), which is used to distinguish the two interaction types. A simple method is, to use the ratio of early to late part of the signal $S(t)$:

$$M = \frac{\int_0^{t_1} S(t) dt}{\int_{t_1}^{\infty} S(t) dt} = \frac{Q_{\text{early}}}{Q_{\text{late}}}$$

Of course it is also possible to use the ratio early to total or late to total. The best choice of the definition of M and the time t_1 depends on the experiment and setup. Once M and t_1 are defined, discrimination can be done by comparing the measured value M of an event, with the expected value for each recoil type.

A more complex method for pulse shape discrimination consists of understanding and modeling the complete scintillation process and the resulting signals. From measurements, one has to learn the model parameters for electronic and nuclear recoils. For liquid noble gases these are rise and decay time constants of the excimer states and their ratio, as well as the recombination time. If the parameters are measured one can realize pulse-shape discrimination (PSD) by fitting waveforms of individual events with the models, keeping as free parameters only the position in time and the amplitude. The respective quality of fits of the models for electronic and nuclear recoils then provides the figure-of-merit for pulse shape discrimination.

Even if future large scale xenon detectors would use a simpler technique for PSD, we want to

understand the scintillation process as this is required to study PSD abilities for the larger scale detectors by simulations.

Obtaining the model requires a function describing the signal shape, ideally based on a microscopic model of the scintillation process. The parameters for the electronic recoil and nuclear recoil models then have to be obtained from measured data. This can be done in three ways:

- a) Averaged waveform fit. The model parameters are obtained from a fit to a waveform, averaged over many normalized waveforms of different events.
- b) Individual waveform fit. The model parameters are obtained from a fit to each individual waveform. This allows statistical treatment of the fit results. In general this is the preferred technique, though it is the most challenging because fitting individual waveforms may be influenced by event-to-event fluctuations in the signal shape due to noise and the statistical fluctuations in the emission of photons. The latter being of importance especially if only several tens or hundreds of photons are emitted in the whole scintillation process.
- c) Using a very strong signal containing several thousands of photons, assuming that this signal reflects the typical shape, as statistical fluctuations and noise are small compared to the signal. The disadvantage of this technique is, that it assumes the pulse shape to be independent of the energy deposit. This is definitively not correct in the general case: The scintillation process itself will be different because the ionization density will differ with energy deposit. Hence, recombination will be different and the amount of bi-excitonic quenching will change for different energy deposits too. Additionally the photo-detector and electronics might saturate for too high light intensities.
- d) Use **one** model fit on many waveforms simultaneously. Parameters of shape may be universal or a parameter of energy, but amplitudes are individual.

7.4.1. Fit functions

Fitting individual waveforms requires a priori an assumption on the signal shape. The signal shape is given by a combination of the interaction, recombination, the scintillation process and the response of the readout chain: PMTs, amplifier, cables and FADC. The response of the readout chain could be measured using a pico-second laser, which is planned but not yet done. The scintillation process is relatively complex (compare chapter 3). To describe it properly, one has to model the generation of the xenon excimers and the decay of the excimers. The latter of course can be assumed to follow an exponential law, whereas the generation of excimers includes the stopping process of electrons and ions in the scintillator and the resulting excitation and recombination. To understand this one would have to simulate the interactions on a microscopic level. As this simulation is rather difficult, two simple approaches have been chosen in this thesis:

Fermi-Dirac threshold: Using a Fermi-Dirac threshold together with two exponential decays provides a simple analytical formula and seems to describe the signal shape we measured. The disadvantage is a discontinuity at t_0 and that the rise does not follow any microscopic model.

Modell in analogy to radioactive decay chains: This model is more complex, especially when trying to include the response of the readout by a convolution. The advantage is that it does follow from a simple model describing the microscopic processes of the scintillation.

7.4.1.1. Fermi-Dirac Threshold with Exponential Decays

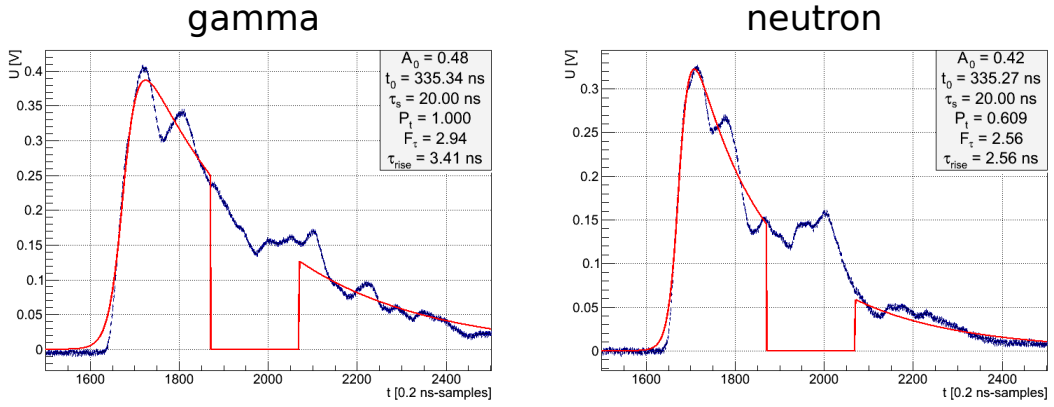


Figure 7.10. Example of S1-signal from a gamma (left) and a neutron (right) at zero drift field. Fitted by the Fermi-Dirac threshold multiplied by two exponential decays.

The first approach uses a Fermi-Dirac threshold together with two exponential decays. The Fermi-Dirac threshold describes the signal rise, including the formation of excimers and the response of the readout chain. The two exponential decay functions reflect the decay of the two excimer states: singlet and triplet. The resulting function can be written as:

$$\tilde{S}(t) = A \cdot S_{FD}(t) \cdot S_{2Exp}(t) \quad (7.1)$$

with the scaling factor A , to adapt the amplitude of the function to the amplitude of the signal, $S_{FD}(t)$ the Fermi-Dirac rise and $S_{2Exp}(t)$ the two decays, normalized to amplitude 1 at $t = t_0$.

$$S_{FD}(t) = \left[\exp\left(-\frac{t-t_0}{\tau_{rise}}\right) + 1 \right]^{-1}$$

$$S_{2Exp}(t) = A_s \cdot e^{-\frac{t-t_0}{\tau_s}} + A_t \cdot e^{-\frac{t-t_0}{\tau_t}}$$

with

$$A_s, A_t \in [0, 1] \text{ and } A_s + A_t = 1$$

The time t_0 is the same for both parts of the exponential decay and the Fermi-Dirac rise. To limit the parameters of the fits, it is advantageous to rewrite $S_{2Exp}(t)$ using $A_s = 1 - A_t$ and $\tau_t = \tau_s \cdot F$ with $F > 1$. A provides the total normalization ($S_{FD}(T_0) = 0.5$), whereas A_s, A_t provide the fractions of singlet and triplet states. The decay time τ_t of the slower triplet state is expressed as multiples of τ_s .

$$S_{2Exp}(t) = \begin{cases} (1 - A_t) \cdot e^{-\frac{t-t_0}{\tau_s}} + A_t \cdot e^{-\frac{t-t_0}{\tau_s \cdot F}} & t > t_0 \\ 1 & t \leq t_0 \end{cases} \quad (7.2)$$

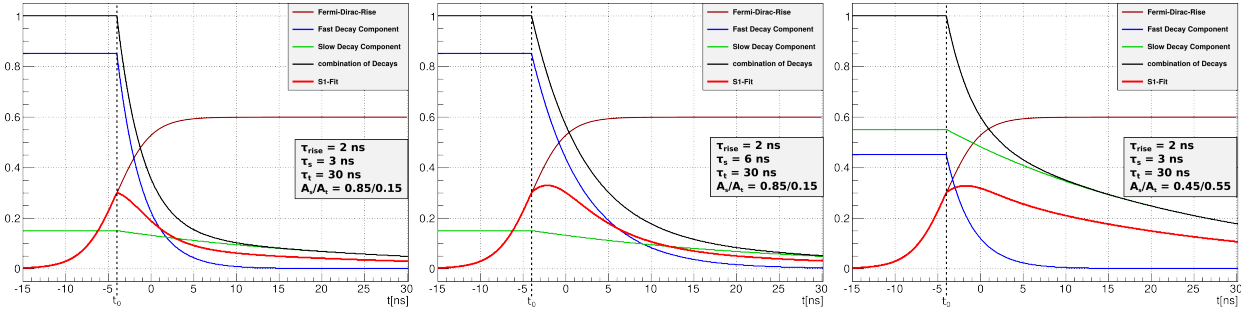


Figure 7.11. Using the Fermi-Dirac rise function, leads to a strong deviation from the typical shape of S1-signals at $t = t_0$ if the fast decay contributes strongly and its decay time constant τ_s is similar to the rise time constant τ_{rise} . On the left, the edge at $t = t_0$ is clearly visible. It gets less prominent when doubling the decay time of the fast component (center) or when the slower component gets more prominent.

At first sight, the shape of this function reflects quite well the shape of signals (figure 7.10) but more sorrow examination reveals a bias towards long decay time constants and/or a strong contribution of the slow component. The reason for this effect is that $\tilde{S}(t)$ is non-differentiable at t_0 , as the two exponential functions. For strong contributions of a fast decay, the difference of the slopes for $t = t_0 + \epsilon$ and $t = t_0 - \epsilon$ with $\epsilon \rightarrow 0$ gets larger, and the shape of the function does not reflect the shape of the measured S1-signals any more, as shown in figure 7.11. Note, that the amount of triplet excimers N_t and singlet excimers N_s generated in the whole process are proportional to the product of amplitudes and decay constants:

$$N_s \propto A_s \cdot \tau_s$$

$$N_t \propto A_t \cdot \tau_t$$

Hence, that even in the example chosen in figure 7.11 on the left the amount of singlet and triplet excimers are at the same order of magnitude:

$$N_s/N_t = \frac{A_s \cdot \tau_s}{A_t \cdot \tau_t} = \frac{0.85 \cdot 3 \text{ ns}}{0.15 \cdot 30 \text{ ns}} = 0.566$$

Despite this unwanted effect, this fit function can still be used for a more accurate timing of the S1-signals (compared to PeakFinder positions) when overlaying and averaging multiple waveforms.

7.4.1.2. Model-based fit function

Scintillation process

To model the scintillation process as described in more detail in chapter 3, we first assume an energy deposit E in the TPC and an average energy W required to create one excimer. This means, we will create $N_{\text{tot}} = E/W$ excimers, each emitting one scintillation photon. As described earlier, two states of excimers exists – singlet and triplet. The probability to create a triplet-state-excimer is P_t , the probability to create a singlet-state excimer is P_s , i.e. the deposit of an energy E will produce $N_t = N_{\text{tot}} \cdot P_t$ triplet-state-excimers and $N_s = N_{\text{tot}} \cdot P_s$ singlet-state-excimers, with $P_s + P_t = 1$. We apply in this section the following convention: time dependent quantities, such as the signal shape S are explicitly written with the time dependency (i.e. $S(t)$), whereas quantities such as N_t , N_s and N_{tot} are constant in time.

The scintillation pulse shape is given by the sum of the (time dependent) decay rates of the two excimer states. As both parts are independent and can be treated analogously, the index i is used for singlet- and triplet-state in the following equations.

The process for one of the two components can now be described as follows: ground state xenon atoms are excited with a probability per unit time p and combine with a neutral xenon atom to an excimer. Note that $p_{i=s,t} = P_i/T$ with T the typical time for excimers to form after the initial interaction. Subsequently, the excimers decay to ground-state xenon atoms, with a time constant τ_i . We distinguish here between the ground-state atoms that will be excited and haven't been yet $N_{i=s,t}^g(t)$ and the ones that have been excited and the excimer has already decayed $N_{i=s,t}^0(t)$. Of course, an atom could be re-excited within the same event, but that is equal to any other atom again and it would have to be counted twice in the number of excimers $N_{i=s,t}^x$, as long as the number density of excited atoms is small compared to the one of ground-state atoms. The following differential equations describe the formation of excimers, the change in number of existing excimers and the decay of excimers to ground-state.

$$\frac{d}{dt}N_{i=s,t}^g(t) = -p \cdot N_i^g(t) \quad (7.3)$$

$$\frac{d}{dt}N_{i=s,t}^x(t) = p \cdot N_i^g(t) - \frac{1}{\tau}N_i^x(t) \quad (7.4)$$

$$\frac{d}{dt}N_{i=s,t}^0(t) = \frac{1}{\tau_i}N_i^x(t) \quad (7.5)$$

The part that describes the scintillation pulse shape, is the last of the three equations, as only when an excimer decays, a scintillation photon is generated. Solving these equations is analogous to radioactive decay chains and detailed solutions can be found in many textbooks [Dem10]. As

solutions we get:

$$N_{i=s,t}^g(t) = N_i \cdot e^{-p_i t} \quad (7.6)$$

Using the initial conditions $N_{i=s,t}^x(0) = 0$ one obtains:

$$N_{i=s,t}^x(t) = \frac{p_i \cdot N_i}{\frac{1}{\tau_i} - p_i} \left(\exp(-p_i t) - \exp\left(-\frac{t}{\tau_i}\right) \right) \quad (7.7)$$

Plugging this expression for the number of existing excimers into equation 7.5 one gets the following formulas for one of the components:

$$S_{i=s,t}(t) = \frac{dN_i^0(t)}{dt} = \frac{1}{\tau_i} N_i^x(t) = N_i \frac{\frac{p_i}{\tau_i}}{\frac{1}{\tau_i} - p_i} \left(e^{-p_i t} - e^{-\frac{t}{\tau_i}} \right) \quad (7.8)$$

Note that for $\tau_i = p_i$ the equation diverges, due to a division by zero. For this special case, the equation can be written as:

$$S_{i=s,t}(t) = -N_i \cdot t \cdot e^{-p_i t} \quad (7.9)$$

Using $N_{i=s,t} = P_i \cdot N_{\text{tot}} = p_i \cdot T \cdot N_{\text{tot}}$ the total scintillation process is given by:

$$S(t) = N_{\text{tot}} \cdot T \cdot \left[p_s \frac{\frac{p_s}{\tau_s}}{\frac{1}{\tau_s} - p_s} \left(e^{-p_s t} - e^{-\frac{t}{\tau_s}} \right) + p_t \frac{\frac{p_t}{\tau_t}}{\frac{1}{\tau_t} - p_t} \left(e^{-p_t t} - e^{-\frac{t}{\tau_t}} \right) \right] \quad (7.10)$$

Describing the scintillation process with this model means having not only different decay constants for the two excimer states, but also two different rise times for their creation. p_s and p_t have the meaning of an inverse time-constant $\tau_i^{-1} = p_i$. The ratio of the rise-times of the two components, is defined by the ratio of their probabilities to create the two states:

$$\frac{P_s}{P_t} = \frac{p_s}{p_t} = \frac{\tau_t^{\text{rise}}}{\tau_s^{\text{rise}}}$$

To reduce the number of paramters in the equation, we replace p_i by P_i/T and eliminate P_s by replacing it with $1 - P_t$. As we know that $\tau_s < \tau_t$, we introduce $F = \tau_t/\tau_s$. This allows to replace τ_t by $\tau_s \cdot F$ and fix the size-order of the two decay constants, by forcing F to be larger than 1.

$$S(t) = N_{\text{tot}} \cdot T \cdot \left[\frac{(1 - P_t)^2}{T - \tau_s(1 - P_t)} \left(e^{-\frac{1-P_t}{T}t} - e^{-\frac{t}{\tau_s}} \right) + \frac{P_t^2}{T - \tau_s \cdot F \cdot P_t} \left(e^{-\frac{P_t}{T}t} - e^{-\frac{t}{\tau_s \cdot F}} \right) \right] \quad (7.11)$$

Improvements of the model

The model for the scintillation process described above assumes a fixed probability per unit time to form an excimer. This is a simplification and especially the recombination of xenon ions in case of zero or only weak applied fields is not reflected well. Previous descriptions (compare chapter 3)

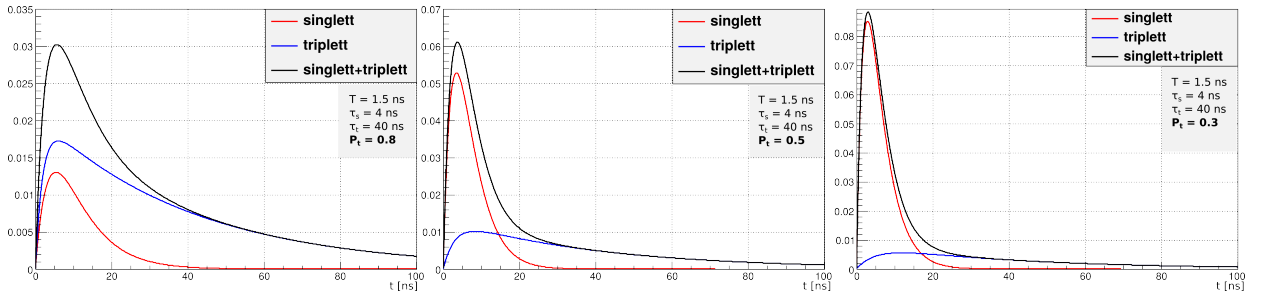


Figure 7.12. Examples for the shape that results from equation 7.10 for different values of P_t , the relative amount of the slower triplet component (left: $P_t = 0.3$, center: $P_t = 0.5$, right: $P_t = 0.8$). Note that the relative amount means the integral, not the amplitude. For all examples the typical excitation-time T and the two decay constants are the same: $\tau_s = 4$ ns and $\tau_t = 40$ ns. For better visualization $T = 1.5$ ns is much longer than the excitation time is in reality.

have the same downside. The rather slow recombination time is then expressed by an increase of the decay times measured for the singlet and triplet excimer states. Introducing a mathematical description of the recombination would definitively improve the model and make its parameters more meaningful, as they would not represent a combination of several quantities.

Additionally, the probability to create an excimer per unit time p_i is assumed to be constant. This is an approximation, too. To improve the model, one would have to describe the thermalization of the electron (electronic recoil) or xenon ion (nuclear recoil) created by the primary interaction. Still this approximation is not likely to influence the conclusions drawn from measurements much, as this would require the ability to have photo detectors and signal sampling that allows to resolve the involved time-scales, which are in the sub-ns regime.

Modeling the response of the electronics and photo multiplier tube

Equation 7.11 describes the production of scintillation photons. It starts immediately at $t = 0$ with a steep rise. The readout chain has limited bandwidth, and therefore will not show the sharp edge of the rise. To get the shape of the measured signal $\tilde{S}(t)$ one has to convolute $S(t)$ with the response of the readout chain $R(t)$:

$$\tilde{S}(t) = S(t) \otimes R(t)$$

The response of the readout chain is the pulse shape of single photo-electrons. If we instead model the readout response by a Gaussian, it is possible to do the convolution analytically. The result contains the inverse error-function $erfc$, which is numerically implemented in ROOT and can therefore be directly used in the fitting routine. Convolution of a Gaussian with an exponential

decay yields:

$$\int_0^{\infty} \exp\left(-\frac{t'}{\tau}\right) \cdot \exp\left(-\frac{1}{2} \frac{(t-t')^2}{\sigma^2}\right) dt' = \frac{1}{2} \exp\left(-\frac{t}{\tau}\right) \cdot \exp\left(\frac{\sigma^2}{2\tau^2}\right) \cdot \operatorname{erfc}\left(\frac{\sigma}{\sqrt{2}\tau} - \frac{t}{\sqrt{2}\sigma}\right) \quad (7.12)$$

The formula for the complete convoluted model with both decay components is quite lengthy and can be found in the appendix F.

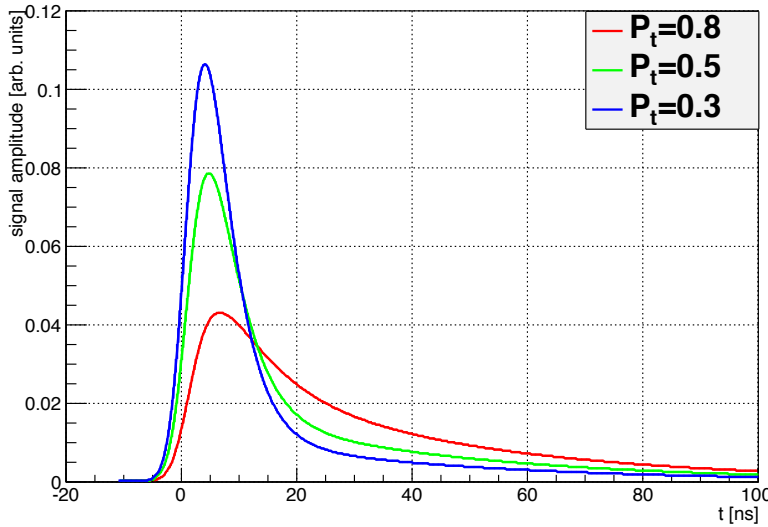


Figure 7.13. Examples for the shape resulting from equation F.1. The contribution of the triplet component is varied (30%, 50% and 80%). The decay and rise time constants are fixed: $\tau_{\text{rise}} = 1.5$ ns, $\tau_s = 4.0$ ns and $\tau_t = 40$ ns. The electronics response of the Gaussian is represented by $\sigma = 2.2$ ns.

7.4.2. Waveform overlaying and averaging

As mentioned previously one way of obtaining a model is to create an averaged waveform. This is done by selecting a set of waveforms that fulfill certain criteria, i.e. have a maximum amplitude in a certain range. Those waveforms are normalized and shifted in time. Overlaying several hundred waveforms of one interaction type in a 2-dimensional histogram allows visualizing the shape. Data used in this thesis result from neutrons and gammas generated by nELBE, not from the Compton scattering experiment. Waveforms have been selected according to TOF-1 and TOF-2 as described previously (section 7.1). Here, we only use the waveforms from the bottomPMT as it was equipped with the faster KPH amplifier and usually sees more of the S1 photons. For future experiments, the readout should be optimized to have fast light detectors and readout for top and bottom. This would allow combining the signals also for pulse shape analysis.

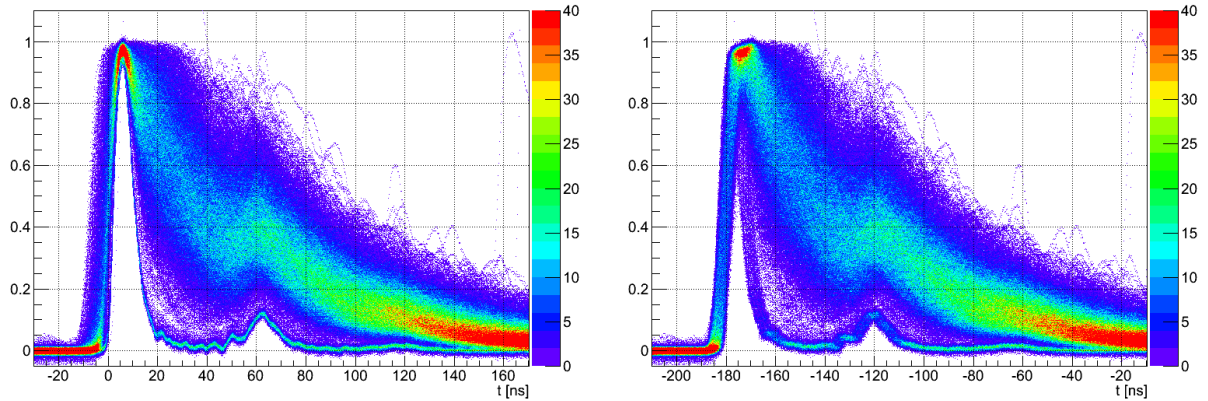


Figure 7.14. Overlay of 4238 waveforms from gammas with amplitudes between 200 mV and 500 mV at zero drift field. On the left the time of the waveforms is adjusted using the position found by the peak-finding algorithm, on the right, by using the TDC hit. Using the peak-finder timing, leads to a broad distribution of the signal rises, whereas the TDC timing improves on the rising edge, but the population of fast decaying signals is not well overlaid. In both cases clearly visible is a bump about 60 ns after the main peak, which probably originates from electronics.

Several options have been tried to find the best way of shifting the waveform in time and normalizing them. The following methods are illustrated using electronic recoils from gammas with a total amplitude of 200-500 mV (zero drift field) on the bottomPMT:

- The position of the peak as found by the PeakFinder algorithm. The amplitude of the peak was used as normalization factor.
- The TDC hit of the bottomPMT relative to the hit recorded for triggering the DAQ. Normalization is based on the amplitude of the peak as found by the peak finder.
- The parameter t_0 when fitting the Fermi-Dirac threshold function to the waveform. In this case, the amplitude of the fit was used for normalization.

The overlay of the waveforms using the peak position as shown in figure 7.14 (left) is not very satisfactory. The width of the rising edge of the signal is distributed over 10 ns, which reflects in part the expected jitter from threshold-based timing for pulses of varying amplitudes. One also realizes a number of very similar waveforms with a faster decay than most waveforms. Although the color code creates the impression that this is a significant fraction of all waveforms, this is not the case. Only about 5% of the waveforms that contribute to the plot are of this fast-decaying shape. The reason why they are so prominent in color is the fact that random fluctuations on these waveforms are small. It is not yet understood what these waveforms are but as they are so similar, they also provide a good way to test the accuracy of the timing of the overlay. Using the triggering TDC hits to overlay waveforms (figure 7.14 (right)), one realizes that the rising edge of the signals indeed gets narrower, as expected for timing based on constant fraction discrimination,

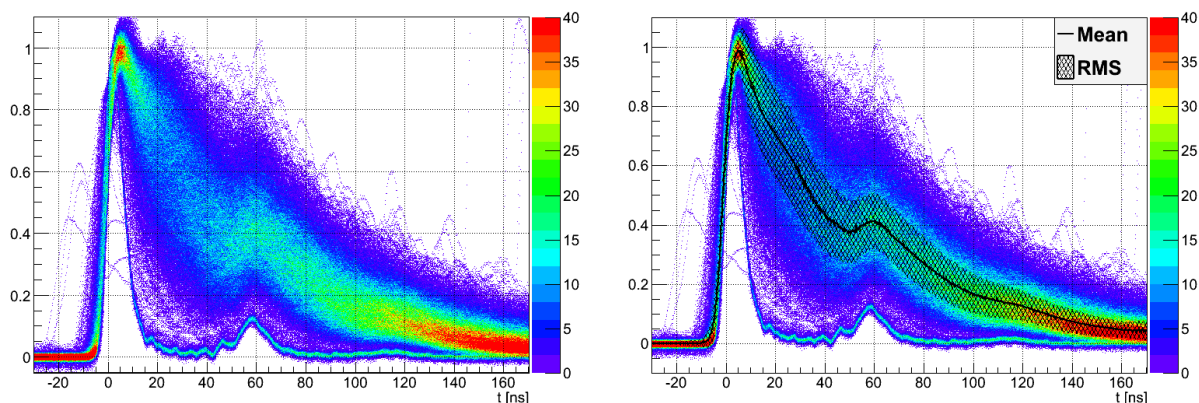


Figure 7.15. Overlay of the waveforms using the timing from a fit with a Fermi-Dirac threshold-Function (equation 7.1). On the right additionally the mean value and $1\text{-}\sigma$ -region of Gaussian fits to 0.2 ns slices is shown. This is used for further analysis.

but still the width is several nano-seconds. The color plot also gives the impression, that this width does not originate from fluctuations in the shape, but rather from bad timing. This is even clearer when looking at the fast-decaying signals, which now also have a wider distribution. It is not clear, why this is the case. It may hint to a time resolution of several nano-seconds for the time-of-flight measurements. However, considering that the rise time distribution became sharper for the bulk of waveforms but apparently broader for the fast decaying waveforms, suggests that the delay in the CFDs was optimized for the shape of the general waveforms but is not ideal for the fast decaying ones.

To extract a model from this overlay and compare it with a similar overlay from nuclear recoil waveforms, from each 0.2 ns time-slice the mean value m and the RMS-value r are extracted and the slice is fitted with a Gaussian. The restriction of the fit range to $m \pm 3 \cdot r$ makes sure that the fast decaying signals do not contribute to the resulting decay up to 140 ns . Although this does not help in the range above 140 ns and for the rise, those signals do not contribute very much, as there are 19-times more “real” signals than fast-decaying ones. The mean of the Gaussian fit and the 1-sigma -region are shown exemplarily together with the 2-D-histogram of the waveforms in figure 7.15 (right) for the set of electronic recoils at zero drift field.

The most prominent feature that can be seen in the curve of Gaussian mean-values is a bump at 60 ns which is visible also for the fast-decaying signals. That is the same feature as already discussed in chapter 6.3. Especially the fact that it is visible identically on all of the fast-decaying signals, and all of those show this second bump, confirms the assumption that it is due to electronic reflection of the signal, as already shown for the PMT calibration (chapter 6). Independent of its origin, this bump introduces an additional difficulty to the pulse-shape analysis. It has to be understood and should be removed for future measurements. If it is due to an

impedance mismatch, it should be straight forward to do so. If it is afterpulsing, one has to think about a different set of light detectors. An option would be to replace the topPMT and the APD-array with an array of SiPMs. Ideally one would have much more than the eight channels of the APDs for the SiPM array, allowing counting of individual photons and measurement of their detection time. This would help in disentangling the pulse shape from the photo-detector response.

7.4.2.1. Pulse shapes

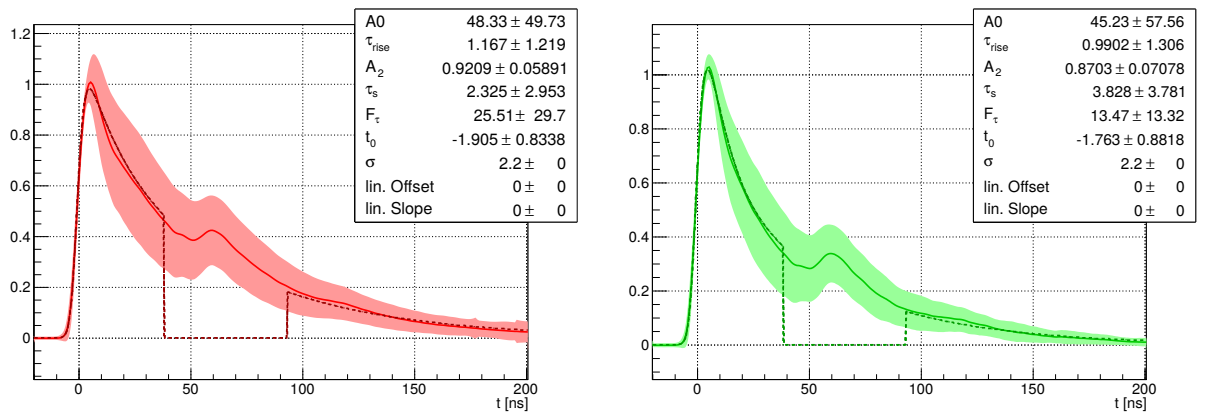


Figure 7.16. The graph of Gaussian mean and sigma values as obtained from the overlaid waveforms. The fit of the model according to equation F.1 is also shown. For the fit, the region of the reflection/afterpulse between 40 ns and 95 ns is ignored. The plots for gammas (left) and neutrons (right) are from dataset 20160322T0515, without drift field and amplitudes of the signal between 200 mV and 500 mV. Plots for datasets with field and different amplitudes can be found in the appendix.

To fit the overlay of waveforms, each time-slice of 0.2 ns is transformed into an histogram and fitted with a gaussian. A graph from the Gaussian mean values, using the Gaussian σ as error is created created, as shown in figure 7.15. We fit this graph with the model convoluted with the electronics response (equation F.1). For the fit, the region of the bump from 40-95 ns after the peak was ignored, that is why the fit-curves in figure 7.16 are zero in this range. The results are used to compare nuclear recoils with electronic recoils and the influence of an applied drift field and of the energy deposit. For this study, we used two datasets recorded at the neutron beam at HZDR. One of the datasets with zero drift field (dataset: 20160322T0515) and one with a drift field of 600V/cm (dataset: 20160321T2303). For each of the datasets, neutrons (TOF-2 good) and gammas have been selected based on TOF-1 and TOF-2 and classified into three groups based on the signal amplitude: 0mV to 200mV, 200mV to 500mV and 500mV to 800mV. Signals with larger amplitudes have been rejected to make sure the fast FADC did not saturate. Table 7.1 summarizes the results. We discuss the main results here and refer for a complete set of plots to appendix H.

dataset	E [V/cm]	particles	\hat{U} [mV]	$N_{\text{waveforms}}$	fit parameters			
					τ_s [ns]	τ_t [ns]	P_t	τ_{rise} [ns]
20160321T2303	600	gamma	500 - 800	35015	6.6	50.7	0.80	1.1
20160321T2303	600	neutron	500 - 800	82	4.4	47.0	0.82	1.3
20160321T2303	600	gamma	200 - 500	46838	6.9	51.4	0.81	1.1
20160321T2303	600	neutron	200 - 500	250	4.9	48.0	0.82	1.2
20160321T2303	600	gamma	0 - 200	15436	3.9	54.7	0.77	2.1
20160321T2303	600	neutron	0 - 200	186	3.2	51.5	0.75	2.0
20160322T0515	0	gamma	500 - 800	5325	2.2	60.0	0.965	2.1
20160322T0515	0	neutron	500 - 800	129	2.6	57.4	0.896	1.8
20160322T0515	0	gamma	200 - 500	4233	2.3	59.3	0.921	1.2
20160322T0515	0	neutron	200 - 500	227	3.8	51.6	0.870	1.0
20160322T0515	0	gamma	0 - 200	5325	1.1	55.1	0.792	1.1
20160322T0515	0	neutron	0 - 200	637	1.2	48.6	0.749	1.6

Table 7.1. Fit results for the curve of mean values from the overlaid waveforms for a drift field of 600 V/cm and zero drift field. The mean and sigma plots with the fits can be found in appendix H.

Studying the fit results presented in table 7.1 one can come to the following statements:

1. Nuclear recoils have slightly shorter τ_t than electronic recoils with and without drift field.
2. Nuclear recoils have smaller τ_s if a field is applied, and larger τ_s without field.
3. With applied field, the fraction of the triplet component is similar for nuclear recoils and electronic recoils.
4. Without drift field, the fraction of the triplet component is smaller for nuclear recoils than for electronic recoils.
5. With applied field, the fraction of triplet component is reduced, independent of interacting particle, except for neutrons with low energy deposits (0 mV - 200 mV).
6. With applied field, the measured decay constant of the singlet state is longer.
7. With applied field, the measured decay constant of the triplet state is longer for electronic recoils and shorter for nuclear recoils.

Overall, we find a clear difference of the shape of nuclear recoils and electronic recoils if no field is applied. In the fit the difference appears as a longer triplet state decay constant and almost no contribution by the faster component for electronic recoils compared to nuclear recoils. The difference is strongest for signals with amplitudes of 200 mV to 500 mV, but also visible for other amplitudes. In figure 7.17 this is shown.

With an applied field, the difference is less clear and only reflected in the fit, the mean curves look very similar for nuclear recoils and electronic recoils, as shown in figure 7.18. The fits show similar value for the contribution of the triplet component. The decay times τ_s and τ_t obtained

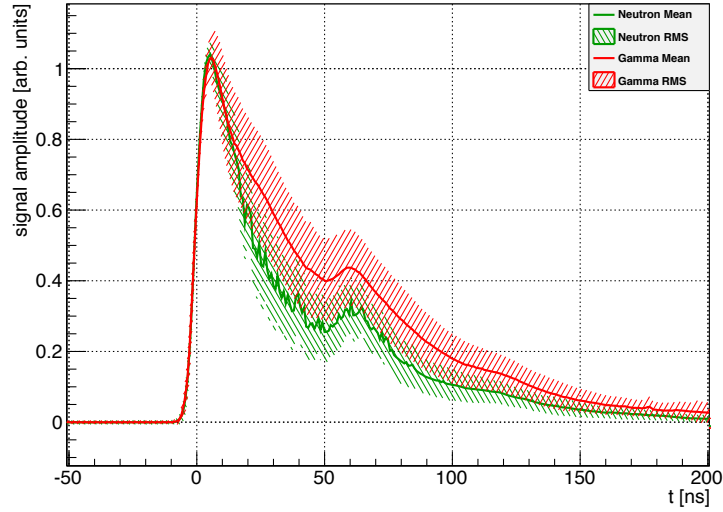


Figure 7.17. Comparison of the averaged pulse shape of electronic recoils with nuclear recoils at zero field. Only signals with amplitudes of 200mV - 500mV contributed here. A difference in the shape of the two interaction types is obvious.

from the fit are shorter for nuclear recoils.

As measured by [HTF⁺83], we see a difference between electronic recoils and nuclear recoils at zero field. We also find that for electronic recoils (zero field) the decay of the signal is mainly given by one component, though we measure two components for the electronic recoils too, as opposed to the previous measurement. Additionally the slow component we measure is significantly larger than the 45 ns stated. The decay time constants and ratios we measure for nuclear recoils from neutrons is also different than the one stated for alpha particles or fission fragments. Of course, especially for our measurement of nuclear recoils using neutrons the process might not be perfectly comparable to the one from alpha-particles or fission fragments. Even for gammas scattering off a shell electron, the microscopic process might be different than for electrons as primary particles stopped in the liquid. Additionally, the reflection (and a reflection of the reflection at around 120 ns) in our setup, not accounted for in the fit, may lead to longer decay constants of the fit. When looking at the values for τ_s we obtained, one should keep in mind the decay time for the single photo-electron response we measured in chapter 6.3 ($\tau_{spe} = 4.9$ ns). Many of the τ_s -values we got are shorter.

Overall the recombination seems to strongly influence the obtained values for the decay time constants. Disentangling the recombination from the decay of the excimers is not possible this way. A good way to do this would be to measure the time constants of singlet and triplet states with complete suppression of the recombination (i.e. at high fields) for electronic recoils. Then one can fix these constants and include the recombination to the model and investigate low field data.

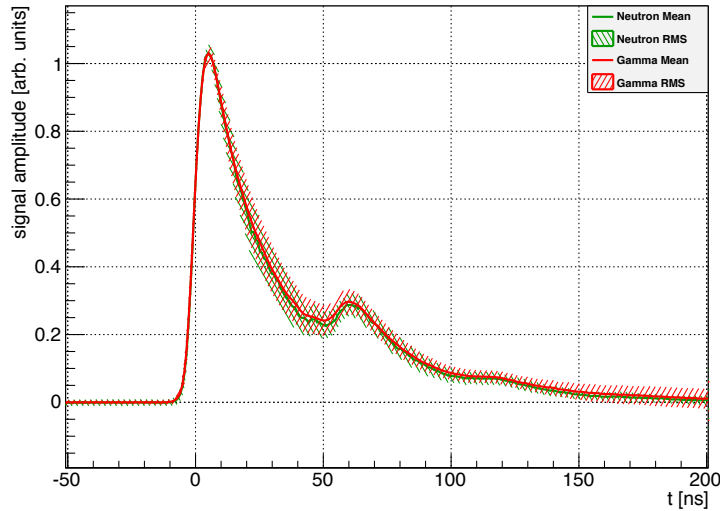


Figure 7.18. Comparison of the averaged pulse shapes of electronic recoils with nuclear recoils at a drift field of 600V/cm. Only signals of 200mV- 500mV contributed here. The difference which was clearly visible without field in figure 7.17 is suppressed by the field and features a suppression of the triplet (long decay) component even exceeding the one from nuclear recoils.

With the data investigated in this thesis and the current state of analysis, further interpretation of the results and improved understanding of the scintillation process is difficult. Studies of the complete data taken at the nELBE neutron facility will help to see the change of the fit parameters with increasing field. Still, the current event- and hit-selection techniques lead to low statistics especially for neutrons. This might be improved by improving the selection algorithms, but still the datasets will be dominated by unwanted events (gammas, inelastic scattering of neutrons (Population X) and events originating from two independent particles (Population Y and Population Z)).

The results shown here will still be helpful when improving the experiment for future measurements. Especially the following technical improvements of the detector will help:

- using a fast amplifier for both PMTs, as this would enable us to retrieve the signal shape from a combination of both PMTs, reducing the fluctuations from photon statistics and allowing to study lower energy deposits.
- Improving the shape of the single-photo electron response of the PMTs. As currently the measured decay time is longer than the singlet-state decay time stated in [HTF⁺83], the values obtained here might well be doubted to reflect the molecular decay time constants. A strong influence of those parameters by the large τ_{RC} derived for the spe-response in section 6.3 can be assumed. This should be better understood and improved. Investigations with a pico-second laser are currently ongoing.

- getting rid of the reflection in the electronics will definitively make fitting the signal shape easier and more reliable.

Population X: Inelastically scattered neutrons

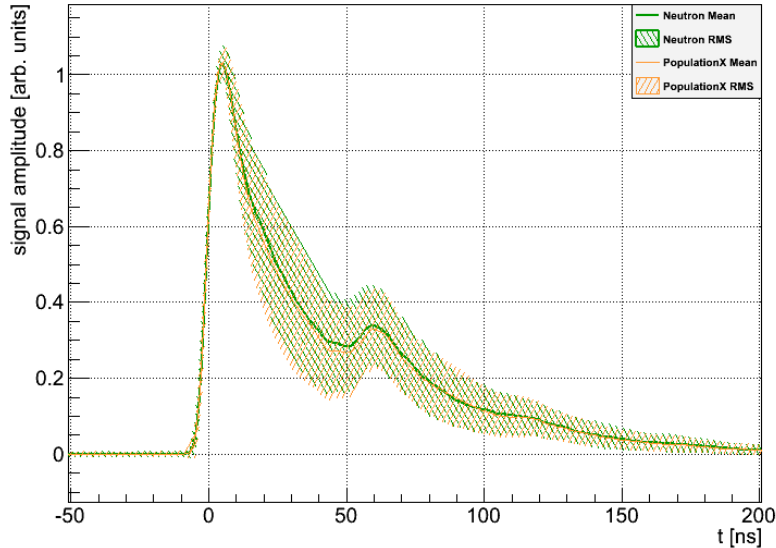


Figure 7.19. Comparing the average waveform of PopulationX-Events with the one from neutrons at zero drift field. Only signals with amplitudes between 200 mV and 500 mV contribute here.

In chapter 7.2 some events were marked as Population X in figure 7.7. Those events have a TOF-1 corresponding to neutrons, but the time-of-flight to the plastic-scintillators corresponds to a photon. This can be explained, if the events are inelastically scattered neutrons, where the excited xenon-atom decays promptly emitting a gamma. The gamma is then detected by the plastic scintillator. To confirm this, the averaged signal shape of those events can be compared to the ones of gammas and neutrons (with expected TOF-2). Figure 7.19 shows that the signal shape of the events in Population X show the same shape as the one originating from neutrons with TOF-2 corresponding to elastic scattering - another confirmation that Population X are indeed inelastically scattered neutrons.

7.4.3. Fitting individual waveforms

A more sophisticated and more complex method to derive the model parameters from data taken for nuclear and electronic recoils is to fit all recorded signals. This allows statistical treatment to find the right model parameters. As already shown in figure 7.13, the individual waveforms are not as smooth as the averaged one. Fitting the individual waveforms therefore turned out to be difficult.

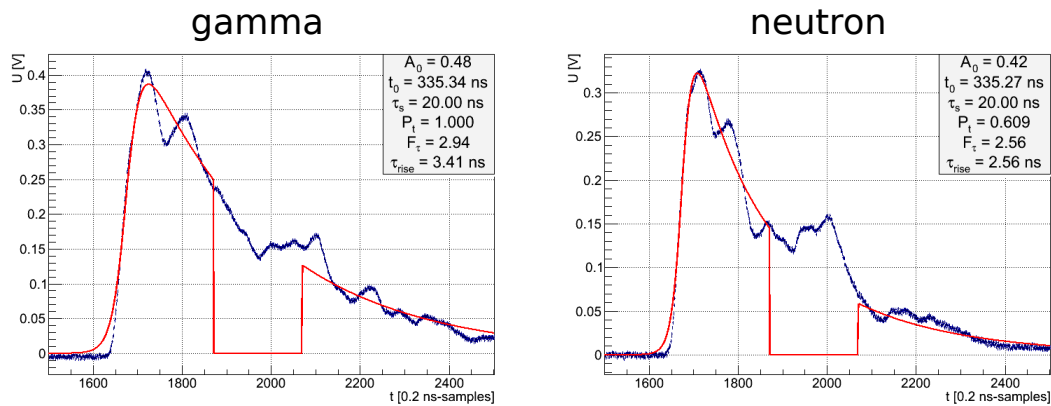


Figure 7.20. Examples for fits of the model to individual waveforms. A gamma interaction is shown on the left, and a neutron interaction on the right. In both cases, no drift field has been applied. In figure 7.10 the same waveforms are fitted with the Fermi-Dirac threshold for comparison. Further example waveforms and fits can be found in the appendix.

If the parameters were restricted to be close to the values obtained from the averaged waveform, they often hit the boundaries. Even if they are left relatively free (variations of $\pm 100\%$ around the values from the averaged waveform) this happens for a relatively large amount of signals. In figure 7.20 fits to a gamma interaction (left) and a neutron interaction (right) are shown. For fitting individual waveforms, the start values of the parameters have been chosen according to the values obtained from the averaged waveform. The boundaries of the parameters have been set to $\pm 100\%$. The value of σ describing the electronic response has been fixed to the value obtained from a fit to the single photo-electron response (method 1.b) from table 6.4). The start parameter for A_0 was obtained from the maximum value of the waveform and allowed to fluctuate by 50%.

When fitting many waveforms and looking at the distribution of the fit parameters, an additional difficulty occurs: the fit parameters are not independent, in the sense that for example the slower decay constant τ_t is written as $\tau_s \cdot F_t$, and if P_t is close to 100% the value of τ_s has no meaning except that it defines the value of τ_t together with the parameter F_t . In figures 7.21 and 7.22 the distribution of parameters for gammas and neutrons with amplitudes of 200 mV to 500 mV at zero drift field are shown, together with the values obtained from fitting the averaged signal shape.

The distribution of the values spans a wide range and determining a model parameter from the distribution seems difficult. For photons one would infer a larger contribution of the triplet component than from the fit to the averaged waveform, and shorter singlet decay time, although one would have to investigate the correlation of the signals with $\tau_s = 5\text{ns}$ with the other parameters (especially P_t). For P_t one would assume a slightly larger value using the distribution of fit parameters, but the value of τ_t will not deviate much between the two techniques. For the rise time it is unclear which value to pick from the wide distribution.

For neutrons, obtaining a model from the distribution of fit parameters would most likely lead to

7.4. PULSE SHAPE ANALYSIS

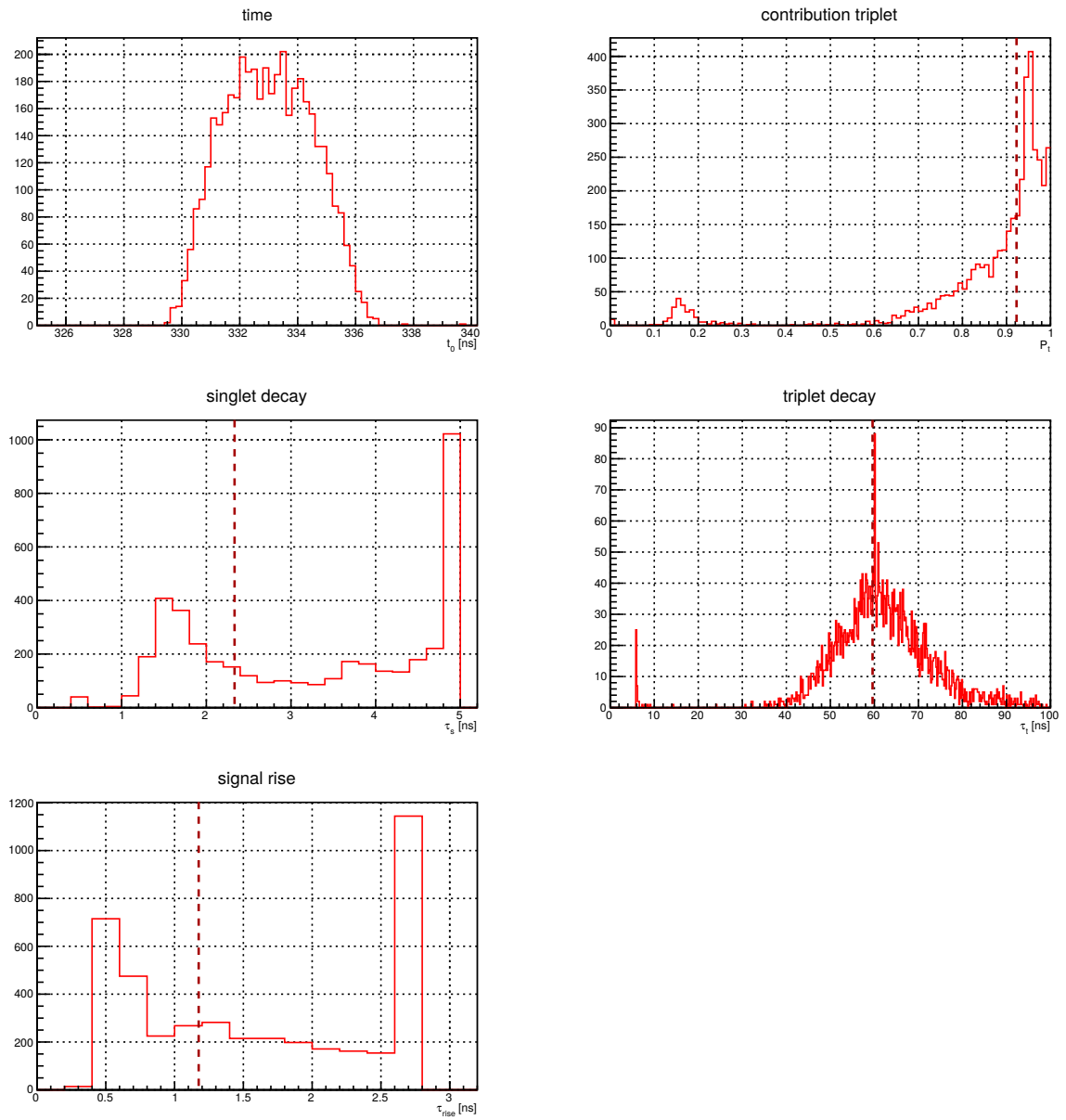


Figure 7.21. Fit parameters of fits to individual waveforms from gamma interactions at zero drift field. The dashed lines mark the values obtained from fitting the averaged waveform.

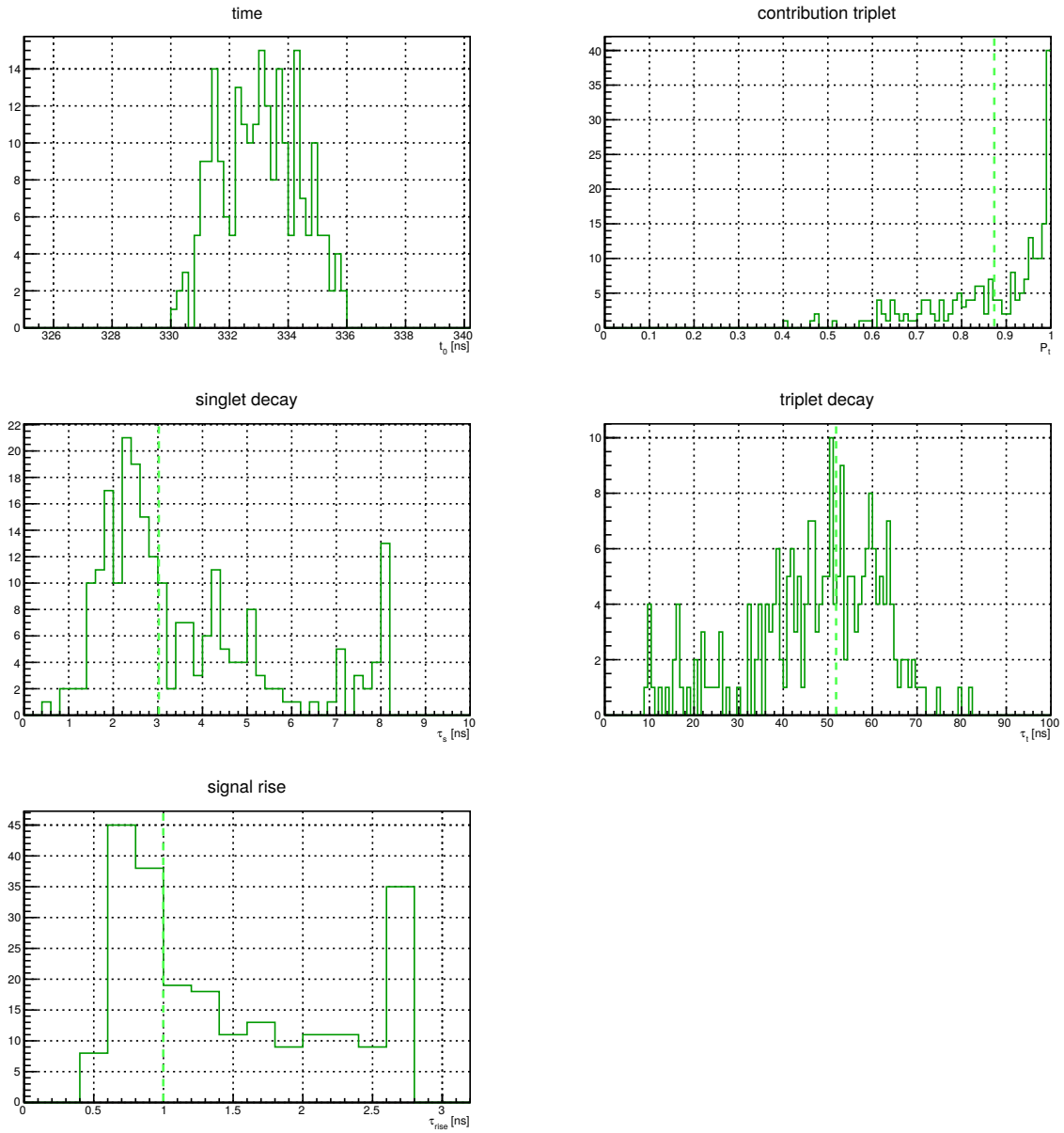


Figure 7.22. Fit parameters of fits to individual waveforms from neutron interactions (TOF-2 good) at zero drift field. The dashed lines mark the values obtained from fitting the averaged waveform.

having no singlet component. This is interesting, as for the averaged waveform fit, the contribution of triplet is smaller than for gammas. The distribution of the parameters would lead to a result opposing the one from the averaged waveform. This has to be kept in mind when looking at the distribution for τ_s . For τ_t the individual waveform fits match well with the value obtained from the averaged waveform.

Fitting individual waveforms currently does not appear to help understanding the scintillation process or allow obtaining model parameters that could be used for pulse-shape discrimination. It might still be a good option if more parameters could be fixed using a priori knowledge for example on the signal rise.

7.5. Simulating the scintillation signal shape

7.5.1. Simulation approach

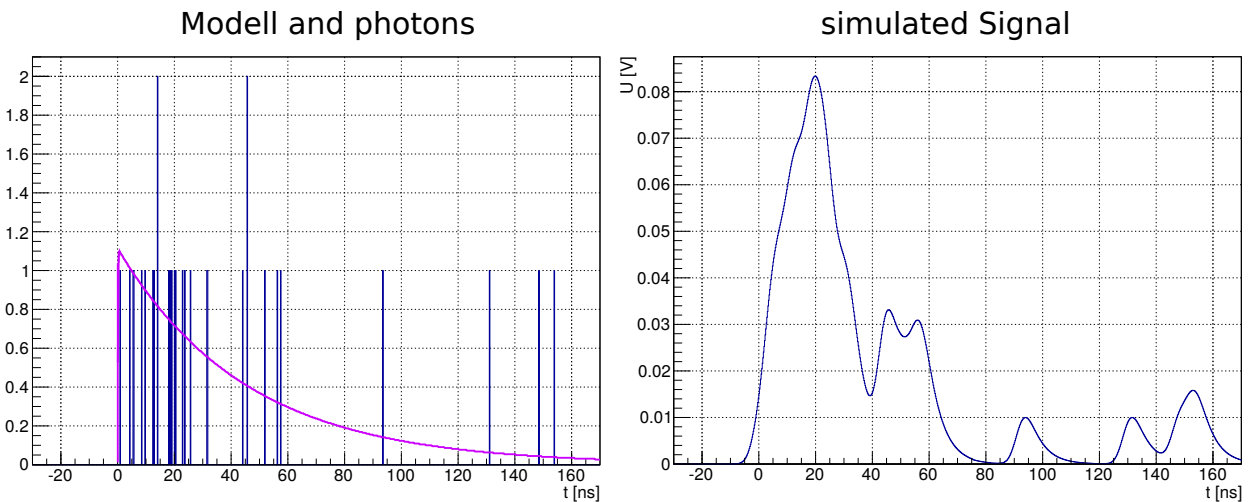


Figure 7.23. Simulation of the pulse shape. The left plot shows the model function (purple) with only one decay component ($\tau = 45\text{ns}$) as measured for electronic recoils at zero drift field in [HTF⁺83], the rise time has been set to $\tau_{\text{rise}} = 0.1\text{ns}$. 30 photon generation times are picked randomly from the model (blue underlying histogram). On the right, one can see the signal resulting from adding up the single photon response for each time value. The shape of the single photo-electron response follows the shape found in chapter 6.3, the amplitude has been set to 10 mV. In the example shown here, at 94 ns a photon is far enough from other photons to see the simulated spe-shape.

As the fitting of single waveforms turned out to be difficult, due to the randomly distributed small bumps on the decay, as shown in the examples in the previous section, we attempted to simulate an expected scintillation signal to compare it with the measured ones. To do so we used the model function (equation 7.11) and used as parameters the values previously measured in [HTF⁺83]. Following this model, we randomly picked the times of photon generation. For each photon generation time we added the shape of a single photo-electron as shown in chapter 6.3, with an amplitude fixed to 10 mV. In an improved simulation, the amplitude, and maybe other parameters for the spe-modell should be randomly chosen within the fluctuations of the measured spe-response. In figure 7.23 on the left the model and 30 randomly generated photons are shown and on the right, the resulting signal shape. This procedure has been done for several photon numbers and for the model settings of electrons and alpha-particles at zero field from [HTF⁺83]. The signal shapes simulated this way do neither include the afterpulse/reflection discussed in the previous section, nor any fluctuations in the shape and amplitude of single photo-electrons. Electronic noise is also not included. Despite these simplifications, the simulated signals should provide a good impression of the expected shapes.

7.5.2. Simulated signals

Figure 7.24 shows three simulated waveforms per number of photons (30, 100, 500 and 2500) as expected for electronic recoils. Obviously the underlying statistics of the photon creation times dominates the shape of the signals for 30 and 100 photons. This is the case not only for the decay of the signal, but also the shape of the rise shows strong variations. For signals containing 500 photons, the decay still shows wiggles due to fluctuations of the photon generation time, but the rise is already well defined. For 2500 photons, the decay of the individual signals follows relatively well the input model. The individual waveforms shown are not normalized as opposed to the ones in the overlay. One can therefore see that electronic recoils with 100 photons will typically produce signals with an amplitude just above 200 mV. Electronic recoils resulting in a total of 500 produced photons already yield amplitudes above 900 mV, and would not have been used in the analysis of the previous chapter, because they would be close to saturating the 1 V range of the FADC. Comparing the overlay of 1000 simulated signals of 100 photons (figure 7.24) with the overlay of measured electronic recoils from gammas with total amplitudes of 200-500 mV (appendix H), one can conclude that the overlays look relatively similar. The overlay of measured data seem to show stronger fluctuations, which might be due to fluctuations in the shape and amplitude of single photo-electrons. Also, the overall different distribution we measured compared to the model used here will influence the overlay.

For alpha particles, the additional fast component leads to a well defined rise already for signals containing 100 photons in total (figure 7.25). The wiggles on the decay seem smaller, but indeed they are of similar absolute size. The maximum amplitude of signals from nuclear recoils (alpha particles) is about a factor of two higher compared to electronic recoils (electrons) with the same total number of photons generated. This is the reason, why the overlays, which are normalized by the amplitude, look sharper for simulated alpha particles in figure 7.25. As for electronic recoils, the signal shape follows well the input model for 2500 generated photons, and only some wiggles occur on the tail for 500 simulated photons.

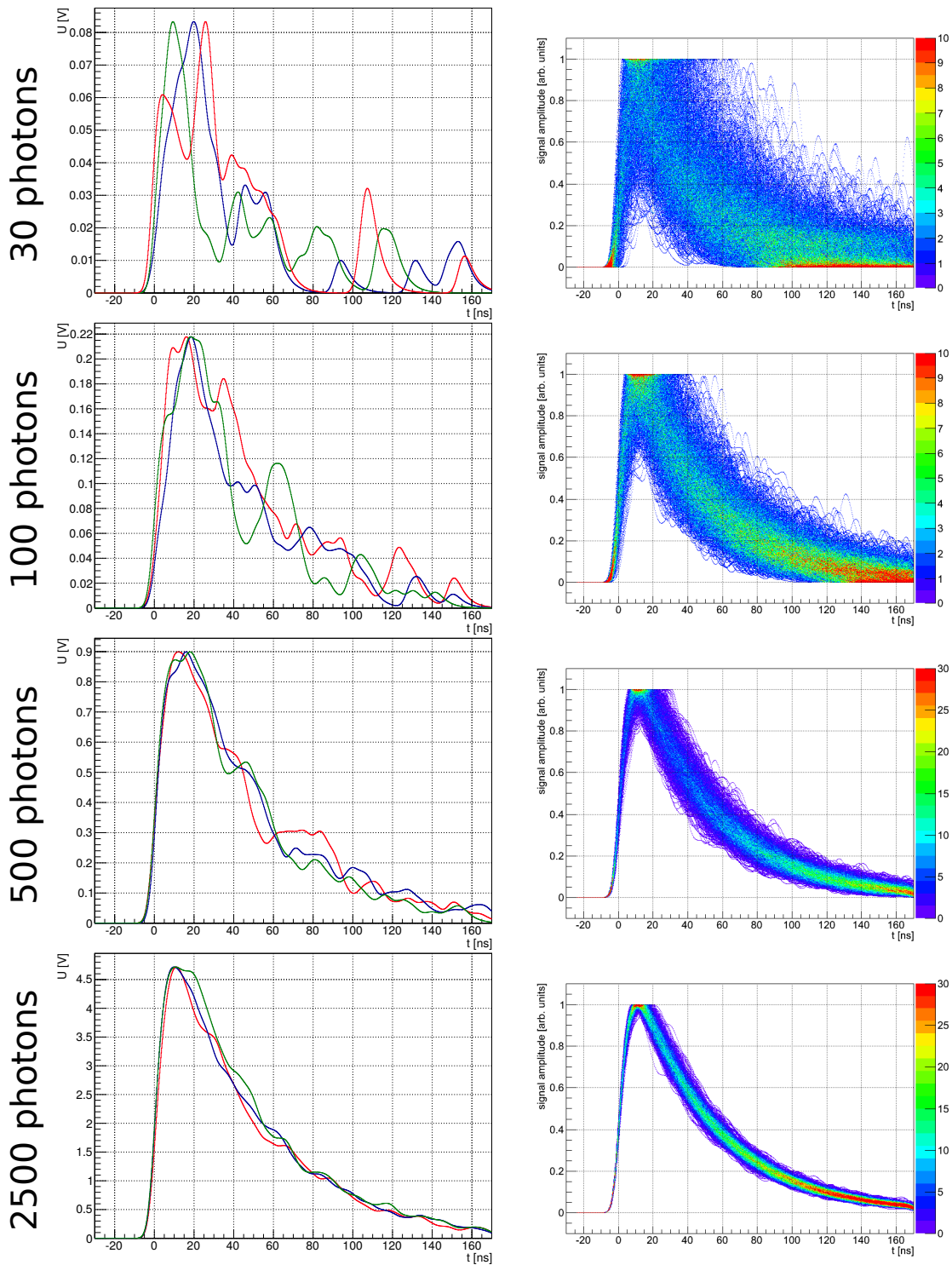


Figure 7.24. Electrons ($\tau = 45$ ns from [HTF+83]) without drift field. The amplitudes of the example waveforms (left) containing 30, 100, 500 and 2500 photons in total are not normalized and therefore reflect real expected signal amplitudes. To generate the overlays of 1000 simulated signals no time-shifting has been done.

7.5. SIMULATING THE SCINTILLATION SIGNAL SHAPE

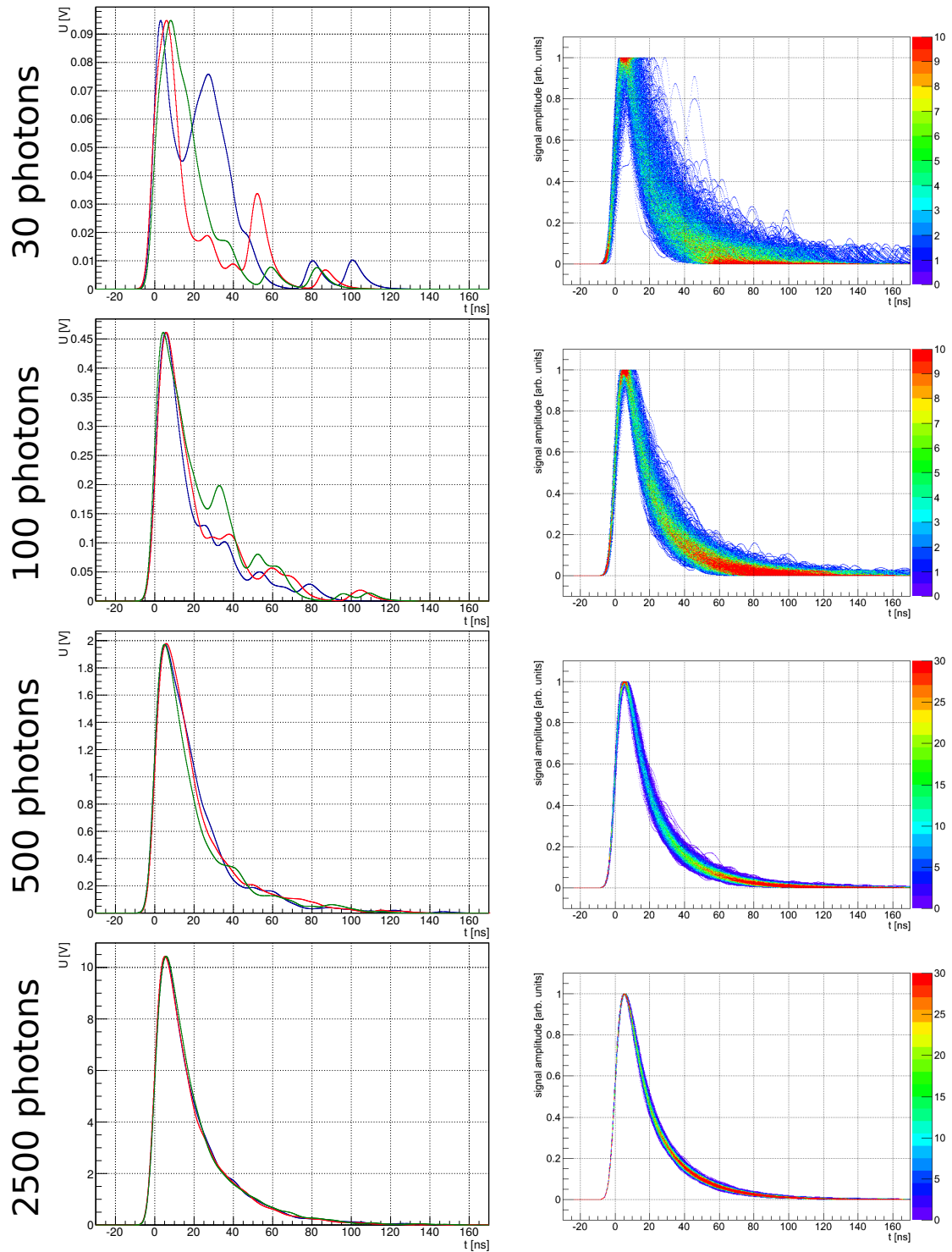


Figure 7.25. Alpha particles ($\tau_s = 4.2$ ns, $\tau_t = 22$ ns, $I_s/I_t = 0.43$ from [HTF⁺83]) without drift field. The amplitudes of the example waveforms (left) containing 30, 100, 500 and 2500 photons in total are not normalized and therefore reflect real expected signal amplitudes. To generate the overlays of 1000 simulated signals no time-shifting has been done.

8. Summary and perspectives

8.1. Summary

A small dual-phase xenon TPC, the MainzTPC, has been designed and built. The design of the detector was led by the optimization for a Compton scattering experiment, still allowing to carry out neutron scattering experiments to study nuclear recoils, since the purpose of the MainzTPC is to study both, electronic recoils and nuclear recoils with one single detector. An improvement compared to previous experiments is the ability to read charge and light simultaneously and to achieve 3D position resolution.

The design and construction of the detector is accompanied by the construction of the required infrastructure: the gas system for purification of the xenon and storage of the gas while the detector is not operated, the cooling and liquefaction system as well as the cryostats for the TPC and the cooling chamber and a slow-control system, monitoring the state of the detector through multiple sensors. A data acquisition system has been set up, including in particular a fast FADC to provide the required time resolution to study the scintillation pulse shape.

This thesis included the development of an analysis framework and of the tools to investigate the scintillation pulse shape, by overlaying many different signals. A simple model containing the decay of two scintillation components is described. The model is convoluted with a Gaussian to reflect the response of the electronics. The analysis framework also contains a routine that allows fitting individual waveforms by the model.

First measurements have been performed, including calibration sources and Compton scattering from gammas emitted by a Cs-137 source, where the energy deposit is measured using a germanium detector. These measurements are currently studied as part of another doctoral thesis [Sis17]. In this thesis, we showed first results from two datasets of nuclear and electronic recoils measured at the neutron source nELBE at HZDR. The focus was on a first study of the scintillation pulse shape and the influence of an applied drift field and the type of interaction. Our results at zero drift field qualitatively show the same behavior as in [HTF⁺83], although the time constants and the ratio of the two components differ from what was formerly obtained. With an applied drift field, the difference between the two interaction types was suppressed in our measurements. The analysis delivered first insights in the scintillation pulse shape and helped understand which changes to the

experiment and the analysis are required to achieve improved and more systematic studies of the pulse shape.

8.2. Future perspectives

The results in this thesis are promising and motivate further detailed studies of the scintillation process in liquid xenon. The work and first analysis presented here show that several changes to the detector will be required to fully realize the goals for which the MainzTPC has been built. Although not an issue for the analysis presented here, one aspect which has definitely to be improved is the liquid level issue. Without a reliable and stable liquid level the use of the charge readout is hampered due to the reduction of charge resolution. Of course, it still allows discrimination of multi-scattering and 3D-position reconstruction of interactions and with the state we could achieve in several measurement runs. But the charge and energy resolution one can achieve with using the S2-signal will suffer from the current conditions. A minor issue is the fact that we could not reach the design value of the drift field. Improving the connections to prevent sparking will be necessary for final studies of scintillation and charge yield in a wide range of fields. This will also be important to find and understand a model of the scintillation process, including the recombination of electron-ions pairs and the suppression of the recombination due to the applied field. Understanding the scintillation pulse shape will also have to include a better inclusion of the response of the electronics, as compared to the simple Gaussian used here. To achieve more reliable results it will be helpful to remove the reflection (or afterpulse) on the PMT signals. Besides this technical changes to the detector and the setup, this will allow further improved measurements, it will be important to deepen the understanding of the current state of the detector by analyzing the data from the Compton scattering experiment and the remaining data from neutron scattering. Especially making use of the APD signals to achieve the 3D position resolution will help improving all analyses significantly, by applying position dependent corrections to the signal. Including the charge signal will further improve event selections.

Regarding the response of the PMTs a measurement is currently planned using a pico-second laser to understand the time response of the PMT alone without the amplifier and also to study the difference between the single photo-electron response and signals of higher amplitudes. This measurement will also lead to an improved understanding of the gain of the PMTs. These measurements might lead to modifications of the voltage divider circuit used currently for the PMTs or to upgrades of the amplifiers. Ideally one would find a solution where the signal decay from a pico-second light pulse would be shorter than the 2 ns time constant measured for the scintillation process.

A further change of the MainzTPC currently under consideration is the exchange of the topPMT and the APDs by an array of SiPMs. As this would mean, to have many light detectors with fast signals, one would at least for small signals get the detection time of individual photons,

rather than one combined signal. The advantage is obvious: One does not have the difficulty of disentangling the response to a single photon from the complete scintillation signal. SiPMs for this purpose need to be sensitive to the VUV wavelength of the xenon scintillation light with a good photon-detection efficiency. Possible candidates from KETEK are currently under investigation for their usability in liquid xenon. Alternatively, Hamamatsu provides SiPMs that work for xenon scintillation light as they are specifically developed for the upgrade of the MEG-experiment, which also uses xenon as detector material.

With these improvements, it will be possible to extend the studies of the pulse shape. Further data taking at a different neutron source might be helpful. The neutron source should ideally not produce gammas together with the neutrons and have an energy spectrum that does not extend above 500 keV, to reduce inelastic scattering as far as possible. With these measurements using, developing a detailed model of the scintillation process and the feasibility of pulse-shape discrimination in large scale xenon detectors will be possible.

A. Datasheets and Schematics

HAMAMATSU PRELIMINARY DATA SHEET Aug.2011	PHOTOMULTIPLIER TUBE R6041-406
--	--

**For Low Temperature Operation especialy for Liq.Xe application,
 Bialkali Photocathode Low profile
 57mm(2Inch)Diameter,12stage,Head-on Type, Synthetic Silica**

General

Parameter	Description	Unit
Spectral response range	160 to 650	nm
Window material	Synthetic silica glass	-
Photocathode	Material	Bialkali
	Minimum Effective Area	45 mm dia
Dynode structure	Metal channel Dynode	-
Number of stages	12	-
Weight	Approx 110	g
Operating Ambient Temperature	-110 to +50	deg C
Storage Temperature	-110 to +50	deg C

Maximum Ratings (Absolute Maximum Values)

Parameter	Value	Unit
Supply voltage Between Anode and Cathode	1000	V dc
Average anode current	0.1	mA

Characteristics at 25 deg C

Parameter	Min.	Typ.	Max.	Unit
Cathode Sensitivity	Luminous (2856K)	-	100	uA/lm
	QE at 175 nm	20	30	%
Anode Sensitivity	Luminous (2856K)	-	100	A/lm
	Gain (Current Amplification)	-	1x10 ⁶	-
Anode Dark Current (after 30min. storage in darkness)	-	5	50	nA
Time Response	Anode Pulse Rise Time	-	2.3	ns
	Electron Transit time	-	16	ns
	Transit Time Spread	-	0.75	ns
Pulse Linearity at ±2 % Deviation	-	40	-	mA

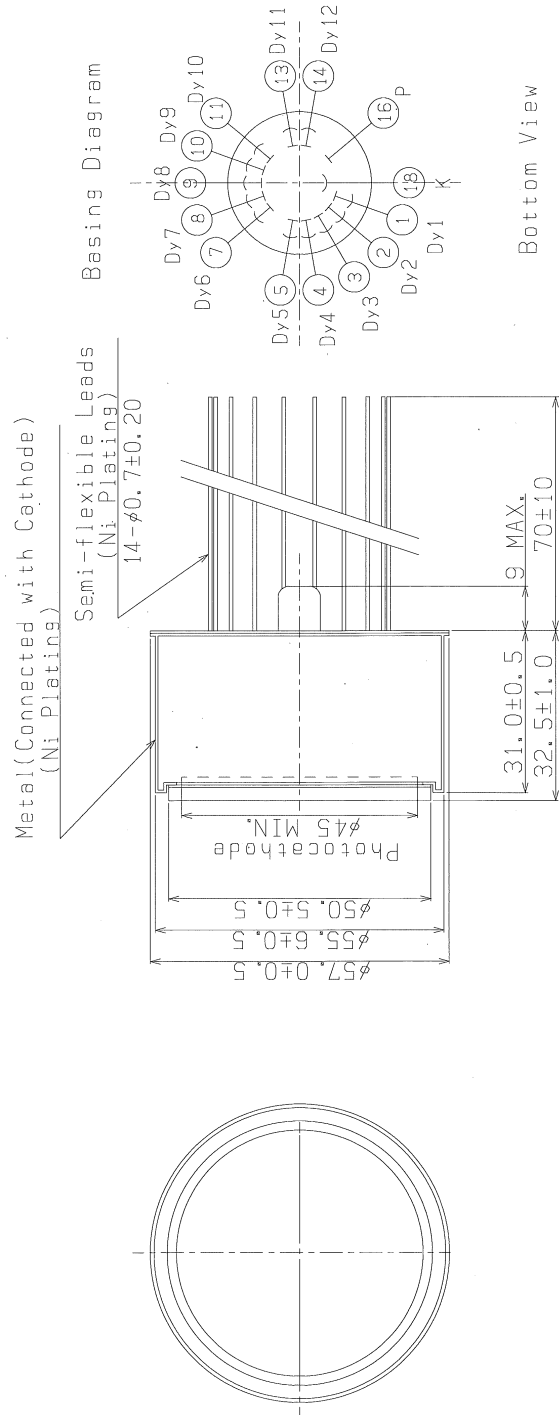
NOTE: Anode characteristics are measured with a voltage distribution ratio shown below

Voltage Distribution Ratio and Supply Voltage

K	Dy1	Dy2	Dy3	Dy4	Dy5	Dy6	Dy7	Dy8	Dy9	Dy10	Dy11	Dy12	P
2	2	2	1	1	1	1	1	1	1	1	1	1	1.2

Supply Voltage : 800 V K : Cathode Dy : Dynode P : Anode

Figure A.1. Datasheet of the PMTs Hamamatsu R6041



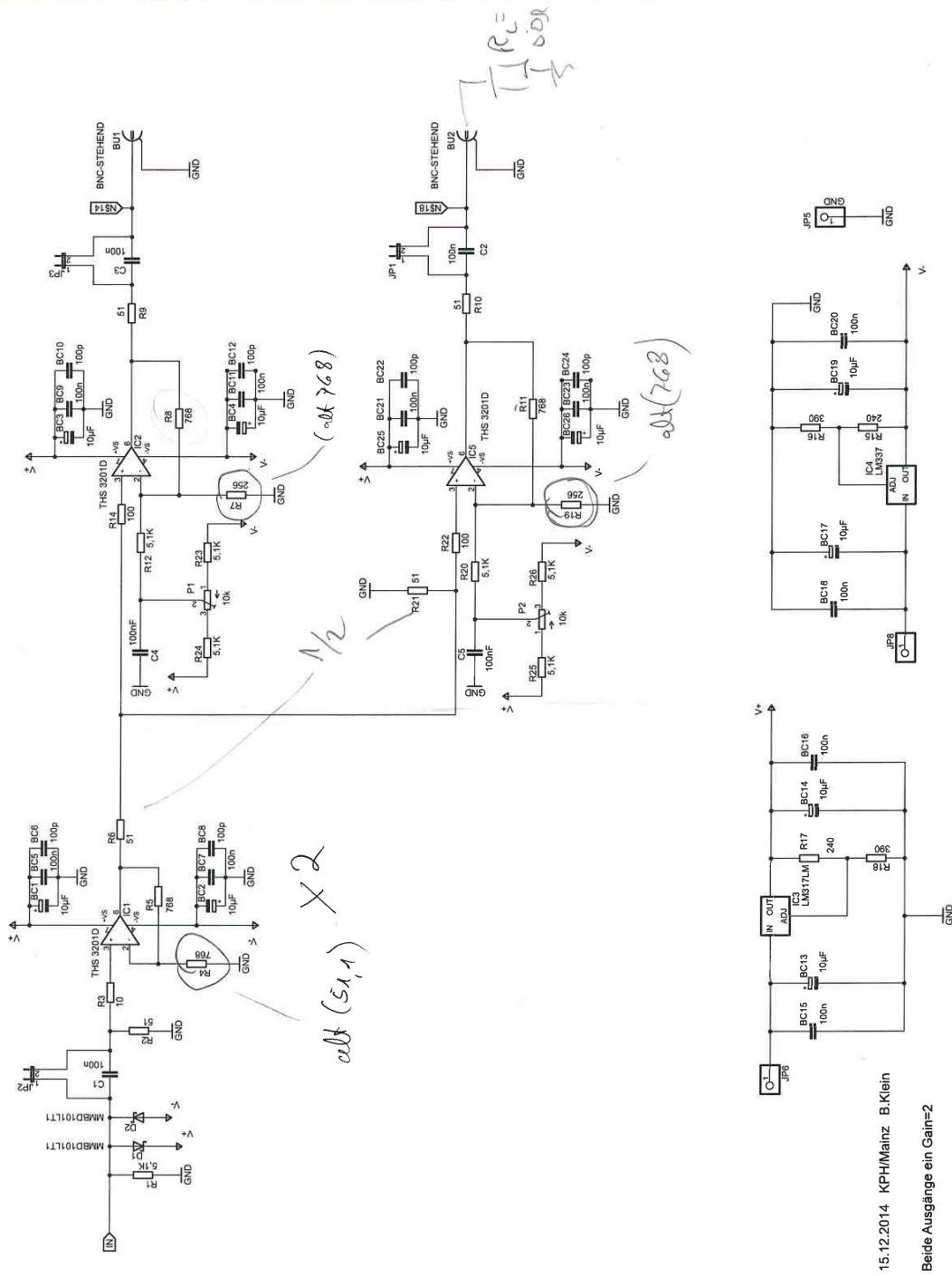
UNIT: mm

This information is furnished for your information only.
 No warranty, expressed or implied, is created by furnishing this information.

1/1

2011.08.24 R6041-406

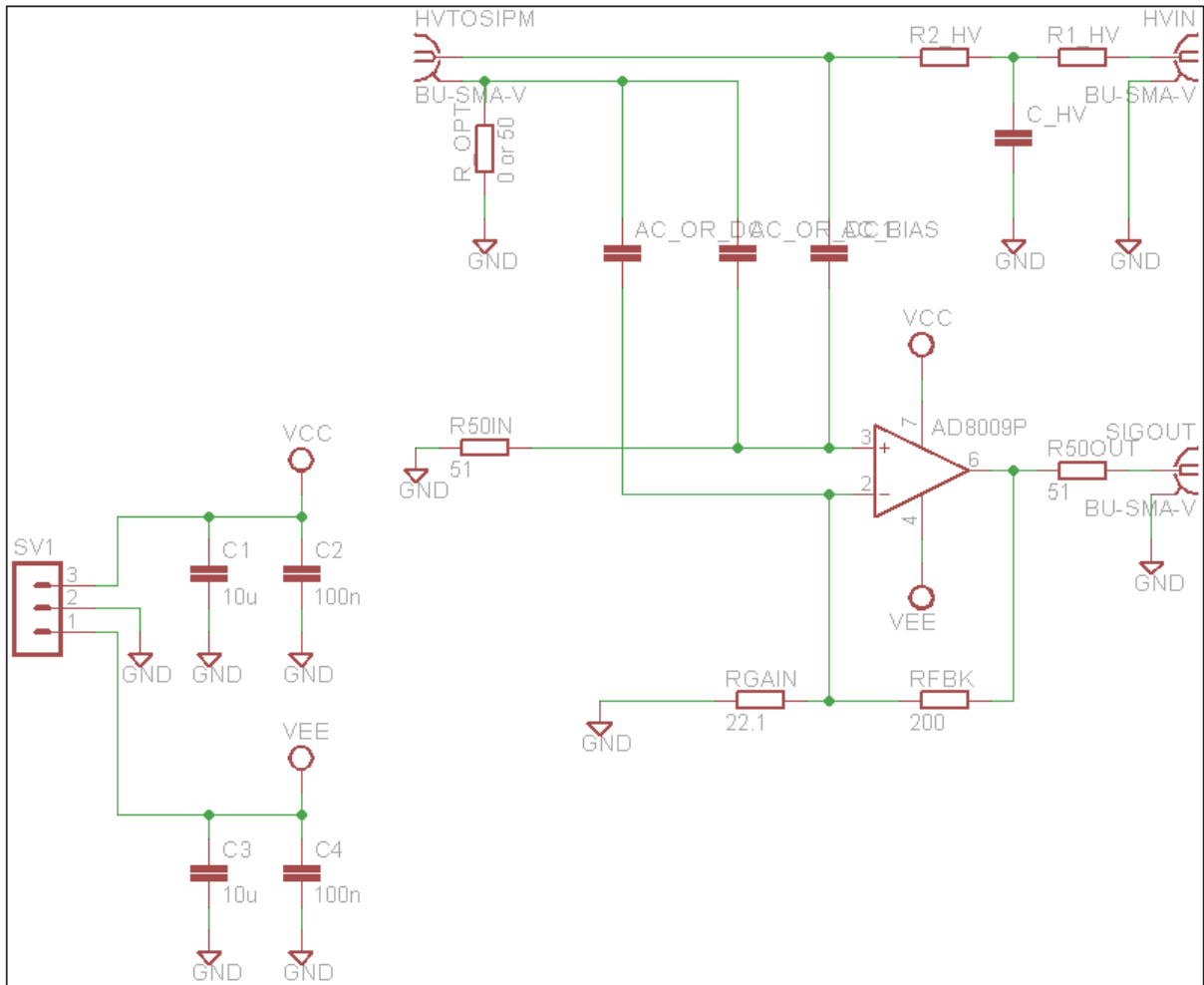
Figure A.2. Geometry of the PMTs. Pins have been shortened to about 3 cm.



18.12.2014 13:01:00 f=0.79 Z:\Projekte\A1-VV-PM\BASE-XP4222B\Base-XP4222B-V2_Ausgänge-Gain=2.sch (Sheet: 1/1)

Figure A.3. Schematic of the KPH amplifier

EAGLE Schematic



Sheet	Size	Description
Sheet 1	5.197 x 4.272 inch	

Figure A.4. Schematic of the detector lab amplifier

B. Trigger Setup: Tables

In section 4.7.6 the conditions to generate a trigger are described and illustrated. The trigger conditions for particles scattering in the MainzTPC first and interacting in one of the plastic scintillators after that are stated by equations 4.6 and 4.7. To check for possible background triggers originating from two independent particles, these equations can be solved to t_{TPC} :

$$t_{\text{TPC}} > t_{\text{plastic}} + \Delta D^a + D_{\text{plastic}} - D_{\text{TPC}} \quad (\text{B.1})$$

$$t_{\text{TPC}} > t_{\text{plastic}} + 20 \text{ ns} + 54 \text{ ns} - 434 \text{ ns} \quad (\text{B.2})$$

$$t_{\text{TPC}} > t_{\text{plastic}} - 360 \text{ ns} \quad (\text{B.3})$$

For equation 4.7 we get:

$$t_{\text{TPC}} < t_{\text{plastic}} + 80 \text{ ns} \quad (\text{B.4})$$

These forms of the conditions allow to define one particle that interacts in the plastic scintillator and find the minimum and maximum time of interaction in the TPC ($t_{\text{TPC}}^{\text{min}}$ and $t_{\text{TPC}}^{\text{max}}$) of a second particle to generate a trigger:

$$t_{\text{TPC}}^{\text{min}} = t_{\text{plastic}} - 360 \text{ ns} \quad (\text{B.5})$$

or, if we allow for trigger generation at the leading edge of the plastic gate instead of the TPC:

$$t_{\text{TPC}}^{\text{min}} = t_{\text{plastic}} - 360 \text{ ns} - 39.2 \text{ ns} \quad (\text{B.6})$$

For the maximum time we get:

$$t_{\text{TPC}}^{\text{max}} = t_{\text{plastic}} + 80 \text{ ns} \quad (\text{B.7})$$

From $t_{\text{TPC}}^{\text{min}}$ we can derive E_n^{max} , the maximum energy of a neutron to fulfill this condition and from $t_{\text{TPC}}^{\text{max}}$ we get E_n^{min} . For photons we can of course not derive the energy, as any photon moves with the speed of light, but we can anyway state if the condition would be fulfilled by a photon or not. For any combination of photon and neutron for the following calculation we use a flight path of 5.9 m from production site to the MainzTPC and 7.0 m from production to plastic scintillator. This is a bit longer than the direct path, but due to the collimation we assume that particles interacting in the plastic scintillator have scattered on passive material somewhere before.

In the table we also check if the conditions for $t_{\text{TPC}}^{\text{max}}$ and $t_{\text{TPC}}^{\text{min}}$ are fulfilled by backscattered gammas, for which we assume flight paths of 20 m to 30 m from the original production, corresponding to 66 ns to 100 ns. The difference of flight path between interaction in TPC or plastic is negligible, as we anyway do not know their exact trajectories.

The results for a defined particle in the plastic scintillators are shown in table B.1. Of course, one can turn around the argumentation. That means, defining a particle that interacts in the MainzTPC and check for the conditions a second particle interacting in one of the plastic scintillators must fulfill to generate a trigger. Equations 4.6 and 4.7 have to be written as follows to find the maximum interaction time in the plastic scintillator $t_{\text{plastic}}^{\text{max}}$:

$$t_{\text{plastic}}^{\text{max}} = t_{\text{TPC}} + 360 \text{ ns} \quad (\text{B.8})$$

or, if we allow for trigger generation at the leading edge of the plastic gate instead of the TPC:

$$t_{\text{plastic}}^{\text{max}} = t_{\text{TPC}} + 360 \text{ ns} + 39.2 \text{ ns} \quad (\text{B.9})$$

And for the lowest allowed interaction time $t_{\text{plastic}}^{\text{min1}}$:

$$t_{\text{plastic}}^{\text{min}} = t_{\text{TPC}} - 80 \text{ ns} \quad (\text{B.10})$$

Some exemplaric results are stated in table B.2.

particle in plastic scintillator	t_{plastic} [ns]	$t_{\text{TPC}}^{\text{min}}$ [ns] with/without G_{TPC}	E_n^{max} [MeV] with/without G_{TPC}	γ	γ_{back}	$t_{\text{TPC}}^{\text{max}}$ [ns]	E_n^{min} [MeV]	γ	γ_{back}
	γ	23.35	-346.65 / -385.85	∞ / ∞	\checkmark / \checkmark	\checkmark / \checkmark	103.35	17.51	\checkmark
neutron (5 MeV)	227.3	-132.7 / -171.9	∞ / ∞	\checkmark / \checkmark	\checkmark / \checkmark	307.3	1.93	\checkmark	\checkmark
neutron (1.5 MeV)	413.7	53.7 / 14.5	70.26 / ∞	- / \checkmark	\checkmark / \checkmark	493.7	0.747	\checkmark	\checkmark
neutron (0.5 MeV)	716.0	356.0 / 316.8	1.439 / 1.818	- / -	- / -	796.0	0.287	\checkmark	\checkmark
neutron (0.1 MeV)	1600.0	1240.0 / 1200.8	0.118 / 0.126	- / -	- / -	1680.0	0.064	\checkmark	\checkmark

Table B.1. The first column states a particle that interacts in one of the plastic scintillators, after scattering somewhere around the MainzTPC on passive material. The following columns show the minimal and maximal time (after particle production by the nELBE beam) when a second particle may interact in the MainzTPC and still generate a trigger. For neutrons the restrictions on kinetic energy is stated, for gammas and backscattered gammas it is just stated if they fulfill the time criterion, as this is energy independent.

particle in TPC	t_{TPC} [ns]	$t_{\text{plastic}}^{\text{max}}$ [ns] with/without G_{TPC}	E_n^{min} [MeV] with/without G_{TPC}	γ	γ_{back}	$t_{\text{plastic}}^{\text{min}}$ [ns]	E_n^{max} [MeV]	γ	γ_{back}
	γ	19.7	379.7 / 418.9	1.782 / 1.463	\checkmark / \checkmark	\checkmark / \checkmark	-60.3	∞	\checkmark
neutron (5 MeV)	191.5	515.5 / 590.7	0.965 / 0.735	\checkmark / \checkmark	\checkmark / \checkmark	111.5	21.31	-	-
neutron (1.5 MeV)	348.7	708.7 / 747.9	0.510 / 0.458	\checkmark / \checkmark	\checkmark / \checkmark	268.7	3.568	-	-
neutron (0.5 MeV)	603.5	963.5 / 1002.7	0.276 / 0.255	\checkmark / \checkmark	\checkmark / \checkmark	523.5	0.936	-	-
neutron (0.1 MeV)	1349.0	1709.0 / 1748.2	0.088 / 0.084	\checkmark / \checkmark	\checkmark / \checkmark	1269.0	0.159	-	-

Table B.2. As the table above, but the first particle is assumed to interact in the MainzTPC.

C. Example xml configuration file

```

1 <?xml version="1.0" ?>
2 <mainztpc> <!-- general bracket for the MainzTPC-->
3   <global> <!-- global settings -->
4     <verbosity>2</verbosity> <!-- currently unused-->
5     <processed_data_dir>/localscratch/OutputDirectory</processed_data_dir> <!--directory where
6     processed files will be stored: no "/" at the end! -->
7     <TdcChannelMask>0x0</TdcChannelMask> <!-- for older version of the DAQ program (Dec2015):
8     copy&paste from: DAQ-settings.xml <caen_vx1290><bd_set><enable_channel_mask>; newer version
9     set to 0x0-->
10  </global>
11  <Analyzers>
12    <!-- generally all analyzer configurations have the following settings , extended by
13    individual settings. Of course, one can specify several analyzers:-->
14    <analyzer id="11" type="ThisIsTheType" description="A random analyzer for illustration
15    purposes"> <!-- This is the scheme for ALL analyzer configuration, the combination of type
16    and id must be unique, the description is only used for displaying purposes. Available
17    AnalyzerTypes are specified in ./src/AnalyzerTypes.h-->
18      <channels>11,13</channels> <!-- restrict the analyzer to the channels stated
19      here.Can state several channels here separated by comma. Does not necessarily have
20      to be implemented, i.e. can be ignored by the Analyzer -->
21      <sensors>
22        <sensor>PMT</sensor> <!-- restrict the sensor types here, one line per
23        sensor type, sensortypes are defined in ./src/DataFormat/Types.h-->
24        <sensor>Ge</sensor> <!-- not necessarily implemented by the Analyzers, i.e.
25        can be ignored by the analyzer does not have to be in the xml-file in this
26        case-->
27      </sensors>
28      <verbosity>2</verbosity> <!-- overwrite the general verbosity setting for this
29      analyzer -->
30      <someMoreSpecificProperties></someMoreSpecificProperties> <!-- each analyzer can
31      have many specific additional properties -->
32    </analyzer>
33  </Analyzers>
34  <DataViewer><!--Configuration for the DataView-->
35    <XeRawPeakFinder> <!--This is a matrix for the DataView to know, which sensor should be
36    used with which analyzer of type XeRawPeakFinder -->
37    <channel channelId="0" XeRawPF_Id="99999"/> <!--for channel 0 the DataView will
38    use the AnalyzerXeRawPeakFinder with id=99999 when calling plotWaveforms; if no
39    analyzer is defined for the channel this will fail; otherwise filtered waveforms and
40    found peaks are displayed-->
41    <channel channelId="1" XeRawPF_Id="99999"/><!--several channels may use the same
42    PeakFinder-->
43    <channel channelId="14" XeRawPF_Id="2"/>
44  </XeRawPeakFinder>
45 </DataViewer>
46 </mainztpc>

```

Figure C.1. XML Config file for the analysis framework. This shows the structure of the file and general settings.


```

110 > >
111 > > <analyzer id="5" type="StepFitter" description="StepFitter for Ge"> <!--StepFitting only works if Steps have been found in
advance! Use OneStepFinder or implement a more sophisticated StepFinder for this; id=5 is used by the DataViewer
hardcoded-->
112 > > > <channels>15</channels> <!-- not used-->
113 > > > <sensors>
114 > > > > <sensor>Ge</sensor>
115 > > > > <sensor>APD</sensor>
116 > > > </sensors>
117 > > > <verbosity>2</verbosity>
118 > > > <decayConstant>6877</decayConstant><!-- in samples; start value for the fit -->
119 > > > <riseTime>45</riseTime> <!-- in samples; start value for the fit -->
120 > > > <baselinePrefit>1</baselinePrefit> <!-- 1:true; 0: false; select if you want to fit with a polynom-degree-1 before
the first step; this will be fitted before fitting the steps and the parameters are than fixed -->
121 > > > <fitEndSample>0</fitEndSample> <!--define a sample where the fit should end; if <=0 will fit the whole waveform-->
122 > > > <fitVariation> <!--parameter ranges for the fitparameters; set to 0.0 if you want to fixe a parameter-->
123 > > > > <decayConstant>0.1</decayConstant> <!-- 0.1 = 10% -->
124 > > > > <position>40</position> <!-- in samples -->
125 > > > > <amplitude>0.3</amplitude> <!-- 0.3 = 30% -->
126 > > > > <riseTime>0.9</riseTime> <!-- 0.3 = 30% -->
127 > > > </fitVariation>
128 > > > </analyzer>
129 > > > <analyzer id="5" type="OneStepFinder" description="Simple StepFinder for Ge"><!--finds one step on the waveform, by
applying a CFD-like MAW-filtering and searching for the maximum amplitude on the filtered waveform; id=5 is used by the
DataViewer hardcoded-->
130 > > > > <channels>15</channels>
131 > > > > <sensors>
132 > > > > > <sensor>Ge</sensor>
133 > > > > > <sensor>APD</sensor>
134 > > > > </sensors>
135 > > > > <verbosity>2</verbosity>
136 > > > > <filterWindow><!--definition of the CFD-like window-->
137 > > > > > <lengthAveraging>20</lengthAveraging><!-- number of samples for the averaging; faster signals need smaller
values-->
138 > > > > > <lengthCenter>20</lengthCenter><!--in samples; the gap between positive and negative averaging; should be
about the length of the signal rise -->
139 > > > > </filterWindow>
140 > > > </analyzer>

```

Figure C.4. XML Config section for AnalyzerOneStepFinder and AnalyzerStepFitter.

```

141 > >
142 > > <analyzer id="11" type="S1Fitter" description="S1Fitter for bottomPMT 3305"><!-- can be used to fit with Fermi-Dirac-
Threshold*2Exponentials or with a Modell-based-function; Modell-based function can be convoluted with a gaussian to reflect
electronics response; compare phdThesis Bastian Beskers-->
143 > > <channels>11</channels> <!-- only one channel -->
144 > > <sensors>
145 > > <sensor>PMT</sensor>
146 > > </sensors>
147 > > <verbosity>2</verbosity>
148 > > <keepWaveformHistos>1</keepWaveformHistos> <!-- bool; do not set to 1 if treating much data. Will otherwise produce
large root file-->
149 > > <t0>1670</t0><!-- in samples-->
150 > > <amplitude>0</amplitude><!-- in Volts; (default:) 0 means use maximumValue of waveform-->
151 > > <fastDecayTau>20</fastDecayTau><!-- in samples-->
152 > > <relAmplitudeSlowDec>0.87</relAmplitudeSlowDec> <!-- 1.0 = 100%, i.e. both exponentials have the same amplitude
(20160725:amplitude for FD; Intensity for ModellFunction)-->
153 > > <FTau>14</FTau><!-- the slow decay time constant is <fastDecayTau>*FTau; This allows to make sure that the slow
decay is always slower than the fast...-->
154 > > <TauRise>7</TauRise><!-- in samples-->
155 > > <sigma>1</sigma><!-- in samples--><!-- sigma>0: use ModellConvoluted with Gaus; sigma = 0: use Modell without
convolution; sigma<0: use Fermi-Dirac-Threshold+2Exp-->
156 > > <baselinePrefit>0</baselinePrefit> <!-- 1:true; 0: false; a polynomial of degree-1 can be fitted in advance of fitting
the signal, parameters will than be fixed-->
157 > > <fitEndSample>3400</fitEndSample> <!-- if <=0 will fit the whole waveform-->
158 > > <fitGapStart>1870</fitGapStart> <!-- in samples; to define a gap in the fit-function-->
159 > > <fitGapEnd>2070</fitGapEnd><!-- in samples; to define a gap in the fit-function-->
160 > > <prefitFast>0</prefitFast> <!--bool; can prefit the fast component and fix the decay constant before fitting the
slow component and the ratio of intensities; currently not tested with the ModellFunction-->
161 > > <prefitFastEndSample>1750</prefitFastEndSample>
162 > > <fitVariation>
163 > > <t0>50</t0><!-- in samples; 0=fixed-->
164 > > <amplitude>3.0</amplitude><!-- in %; 0.1 = 10%; 0.0=fixed-->
165 > > <fastDecayTau>1.0</fastDecayTau><!-- in %; 0.1 = 10%; 0.0=fixed-->
166 > > <relAmplitudeSlowDec>1.0</relAmplitudeSlowDec><!-- in %; 0.1 = 10%; 0.0=fixed-->
167 > > <FTau>0.5</FTau><!-- in %; 0.1 = 10%; 0.0=fixed-->
168 > > <TauRise>1.0</TauRise><!-- in %; 0.1 = 10%; 0.0=fixed-->
169 > > <sigma>0</sigma><!-- in %; 0.1 = 10%; 0.0=fixed-->
170 > > </fitVariation>
171 > > <evtListFile>/localscratch/ListFile.txt</evtListFile> <!--This analyzer reads a txt-file and only treats events in
the list; can be generated from TEventLists using macro: generateListSuperimposeWaveform()-->
172 > > </analyzer>
173 > >
174 > > <analyzer id="70" type="SuperimposeWaveforms" description="Analyzer to produce a superimposed waveform of all neutronEvents
3305, bottomPMT"><!--Generates a root file with an overlay of waveforms from events specified by a file -->
175 > > <channels>11</channels>
176 > > <sensors>
177 > > <sensor>PMT</sensor>
178 > > </sensors>
179 > > <verbosity>1</verbosity>
180 > > <evtListFile>/localscratch/ListFile.txt</evtListFile> <!--can be generated from TEventLists using macro:
generateListSuperimposeWaveform()-->
181 > > <outputFileName>NeutronsBottom3305</outputFileName> <!-- Outputfile; will be in the path: processed_data_dir,
beginning with the FileDateTTime and followed with .root-->
182 > > <acceptanceWindowStart>1600</acceptanceWindowStart><!--only peaks with a shifting time value(sample) or position of
the Peak taken from the txt-file are treated if they are in the window-->
183 > > <acceptanceWindowEnd>1800</acceptanceWindowEnd>
184 > > </analyzer>

```

Figure C.5. XML Config section for AnalyzerS1Fitter and AnalyzerSuperimposeWaveforms.

D. Raised Cosine

Low-pass filter

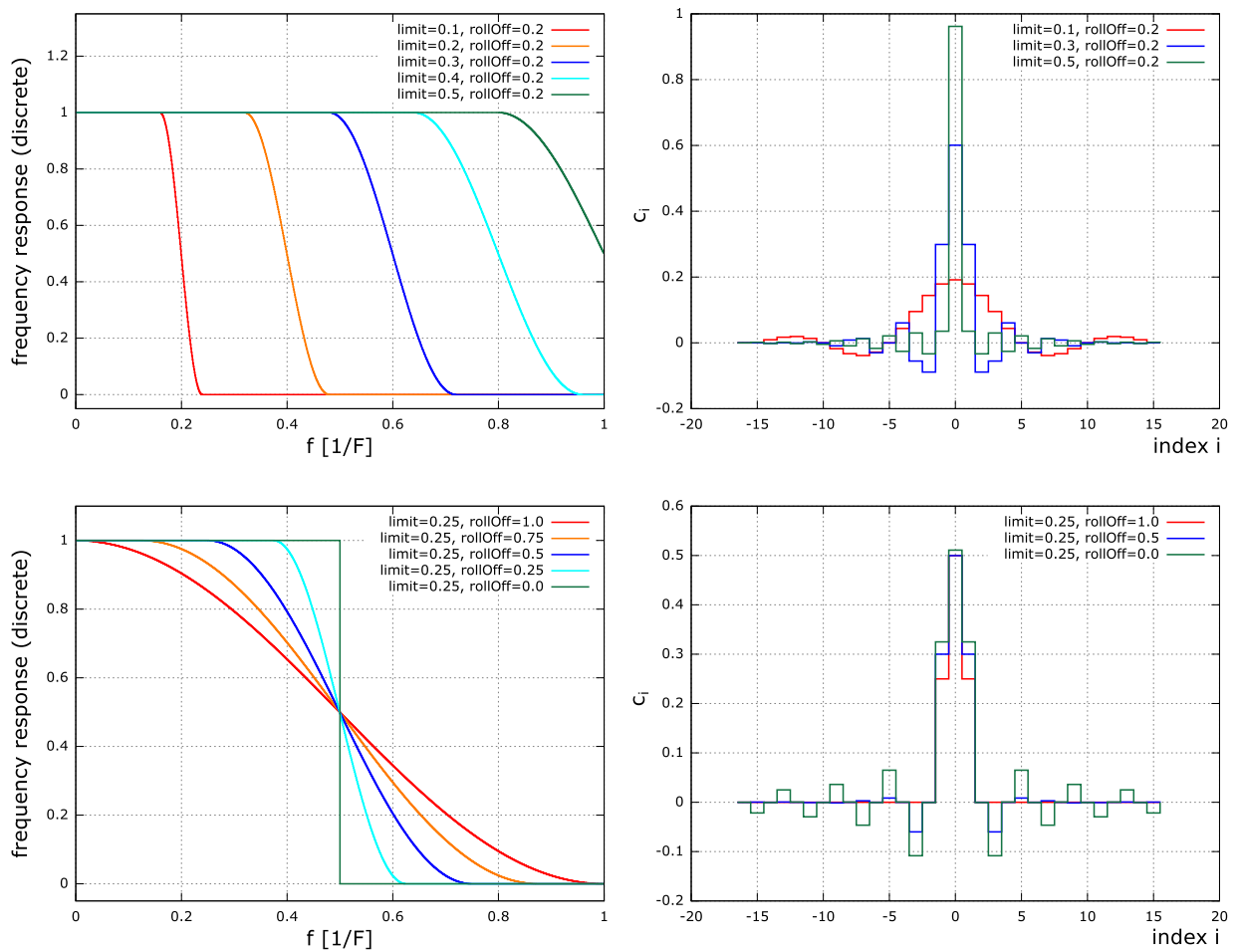


Figure D.1. Left: Transfer functions for different choices of the parameters *limit* (**top**) and *rollOff* (**bottom**).

Right: The corresponding moving average windows from some of those transfer functions. $length = 31$ was chosen here. One can see that lower values for *limit* lead to a broader MAW shape (**top**), whereas larger values for *rollOff* lead to less overshoot.

High-pass filter

A high-pass raised cosine filter has the transfer function:

$$H(f) = \begin{cases} 0 & |f| \leq (1 - \beta) \cdot l \\ 0.5 \cdot \left(1 - \cos \left[\frac{\pi}{2l\beta} \cdot (f - l(1 - \beta)) \right]\right) & (1 - \beta) \cdot l < |f| \leq (1 + \beta) \cdot l \\ 1 & \text{else} \end{cases} \quad (\text{D.1})$$

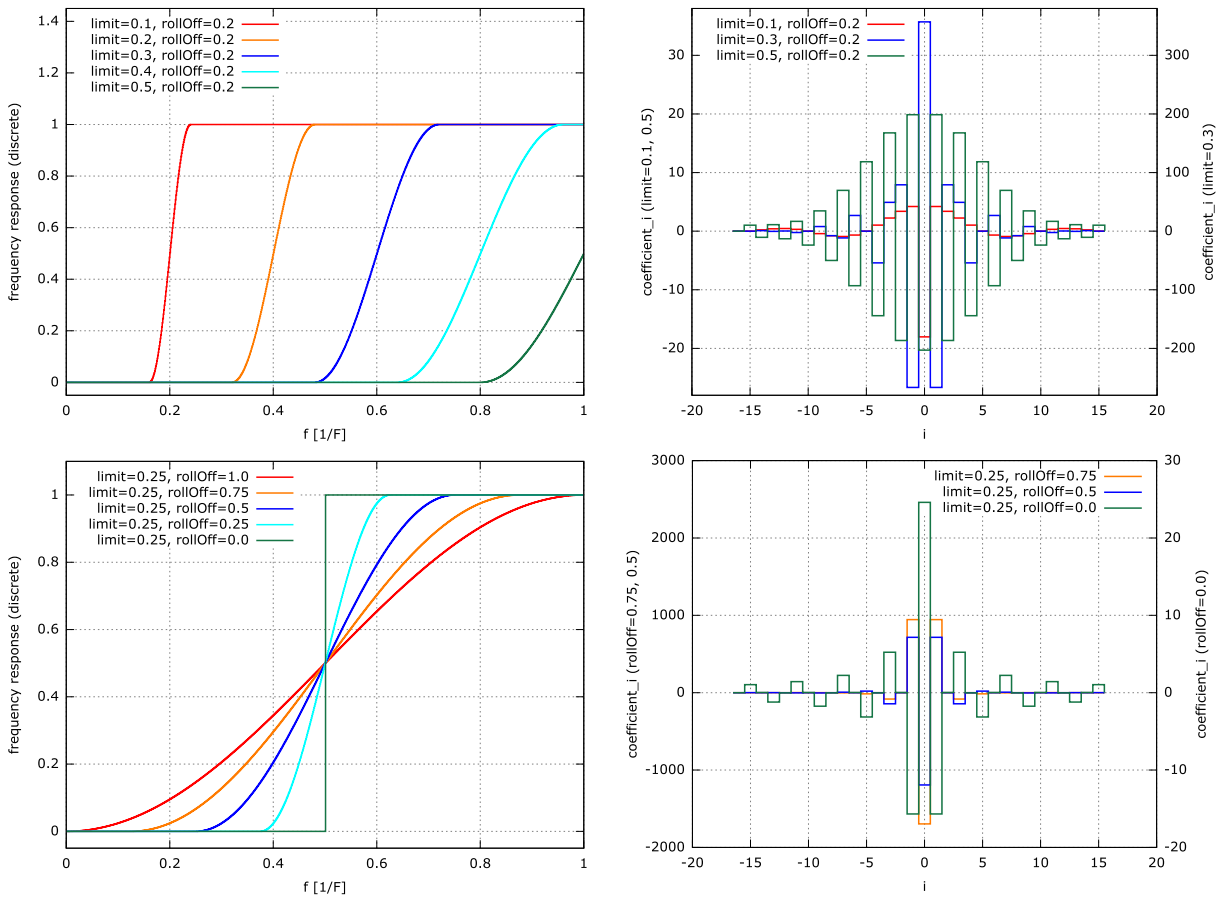


Figure D.2. As figure D.1 but for a high-pass raised cosine filter.

E. PMT calibration: Additional figures and tables

LEDDsetting - PMT	U_{bias} [V]	Q_0 [pC]	σ_{left} [pC]	σ_{right} [pC]	constant	χ^2	NDF
LED 1 - topPMT	1000	8.7324 ± 0.0104	1.8424 ± 0.0178	2.5431 ± 0.0191	87.2443 ± 0.4972	1381.11	1415
	950	4.8160 ± 0.0149	1.0350 ± 0.0091	1.3775 ± 0.0101	160.04 ± 0.8950	830.719	833
	900	2.6979 ± 0.0084	0.6290 ± 0.0052	0.7765 ± 0.0057	276.575 ± 1.5513	492.566	499
LED 2 - topPMT	850	1.4382 ± 0.0054	0.4223 ± 0.0033	0.4864 ± 0.0035	428.939 ± 2.3759	343.356	339
	800	0.7522 ± 0.0041	0.3393 ± 0.0026	0.3576 ± 0.0027	560.996 ± 3.1075	239.301	261
	950	74.0986 ± 0.0627	4.4067 ± 0.0425	4.7735 ± 0.0431	40.7492 ± 0.2386	2584.16	2723
LED 2 - bottomPMT	900	40.0855 ± 0.0318	2.3681 ± 0.0206	2.5734 ± 0.0211	77.1842 ± 0.4360	1564.06	1575
	850	21.2002 ± 0.0169	1.2712 ± 0.0107	1.3939 ± 0.0108	144.584 ± 0.8052	918.427	899
	800	10.8947 ± 0.0088	0.7017 ± 0.0056	0.7577 ± 0.0056	266.722 ± 1.4817	478.575	503
LED 3 - topPMT	900	99.303 ± 0.0520	3.7875 ± 0.0358	3.9981 ± 0.0354	48.2806 ± 0.2867	2178.35	2352
	850	52.3958 ± 0.0267	2.0184 ± 0.0173	2.1097 ± 0.0354	92.861 ± 0.5263	1275.94	1320
	800	26.9278 ± 0.0134	1.0546 ± 0.0085	1.1211 ± 0.0088	177.418 ± 0.9945	743.16	736
LED 1 - bottomPMT	1000	7.8762 ± 0.0238	1.6457 ± 0.0150	2.1324 ± 0.0162	101.365 ± 0.5738	1262.56	1249
	950	4.3387 ± 0.0134	0.9472 ± 0.0084	1.2265 ± 0.0089	178.163 ± 0.9950	774.626	756
	900	2.367 ± 0.0082	0.6097 ± 0.0052	0.7409 ± 0.0053	287.917 ± 1.5974	488.367	474
LED 2 - bottomPMT	850	1.3063 ± 0.0056	0.4752 ± 0.0036	0.4838 ± 0.0037	406.02 ± 2.2669	408.403	351
	800	0.6964 ± 0.0049	0.4255 ± 0.0032	0.3996 ± 0.0031	472.933 ± 2.6171	329.984	300
	1000	49.0631 ± 0.0610	4.2895 ± 0.0411	4.7320 ± 0.0416	41.3817 ± 0.2421	2670.96	2704
LED 3 - bottomPMT	950	27.0586 ± 0.0326	2.3975 ± 0.0212	2.6320 ± 0.0219	75.7651 ± 0.4344	1585.28	1589
	900	14.7200 ± 0.0175	1.3021 ± 0.0111	1.4756 ± 0.0114	138.564 ± 0.7707	989.004	950
	850	7.822 ± 0.0100	0.7738 ± 0.0063	0.8609 ± 0.0065	237.636 ± 1.3273	533.92	567
LED 1 - topPMT	800	4.0533 ± 0.0064	0.5267 ± 0.0041	0.5366 ± 0.0041	366.528 ± 2.0348	365.51	380
	1000	103.024 ± 0.0926	6.2754 ± 0.0648	6.8972 ± 0.0656	27.7918 ± 0.1670	3724.07	3772
	950	56.6683 ± 0.0478	3.500 ± 0.0319	3.7778 ± 0.0325	51.8721 ± 0.3006	2053.42	2238
LED 2 - topPMT	900	30.706 ± 0.0255	1.894 ± 0.0165	2.0720 ± 0.0169	96.6006 ± 0.5485	1264.49	1288
	850	16.3317 ± 0.0135	1.0683 ± 0.0087	1.1312 ± 0.0088	176.176 ± 0.9868	677.512	750
	800	8.4475 ± 0.0079	0.6425 ± 0.0050	0.6730 ± 0.0051	295.85 ± 1.6412	462.1	463

Table E.1. Parameters of the fits with an asymmetric gaussian to the relative gain data shown in figure 6.3

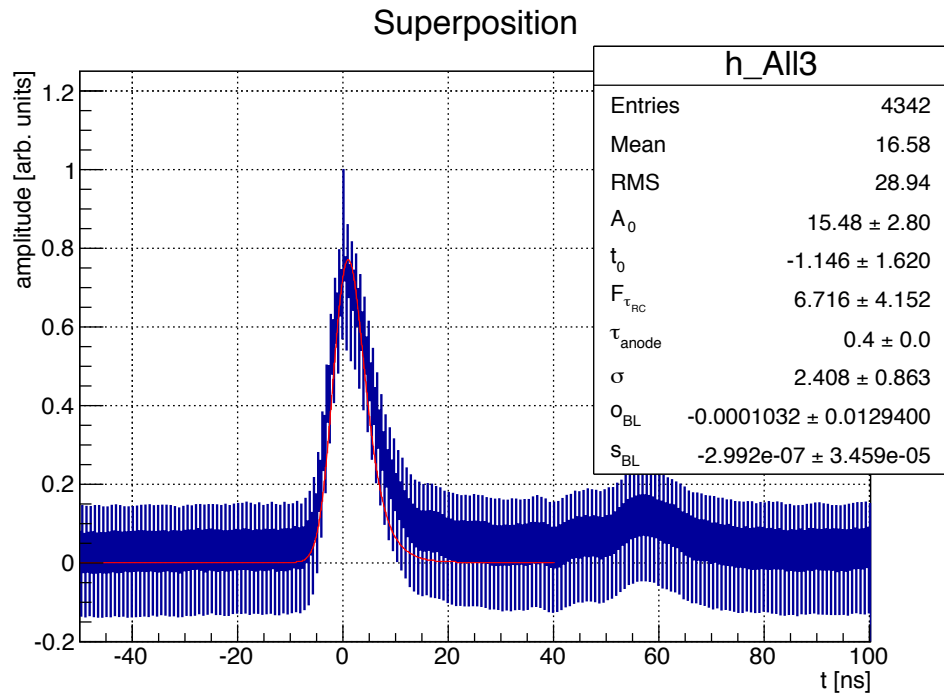


Figure E.1. As figure 6.7 but using the maximum of the waveform for time adjustment as described in section 6.3.

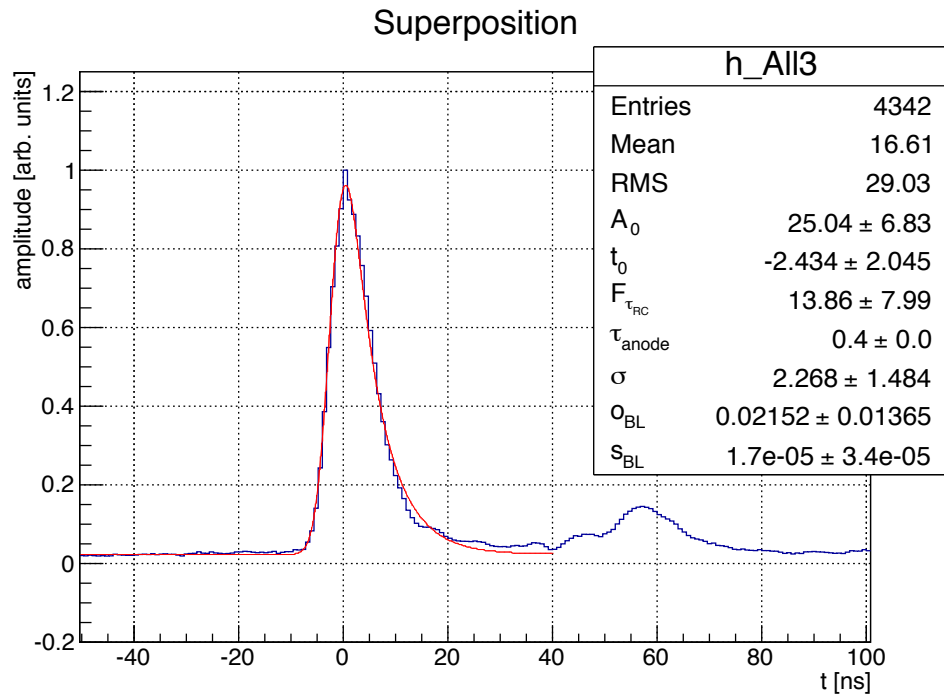


Figure E.2. As figure E.1 but rebinned by factor 4 to avoid the SIS3305 DC pattern.

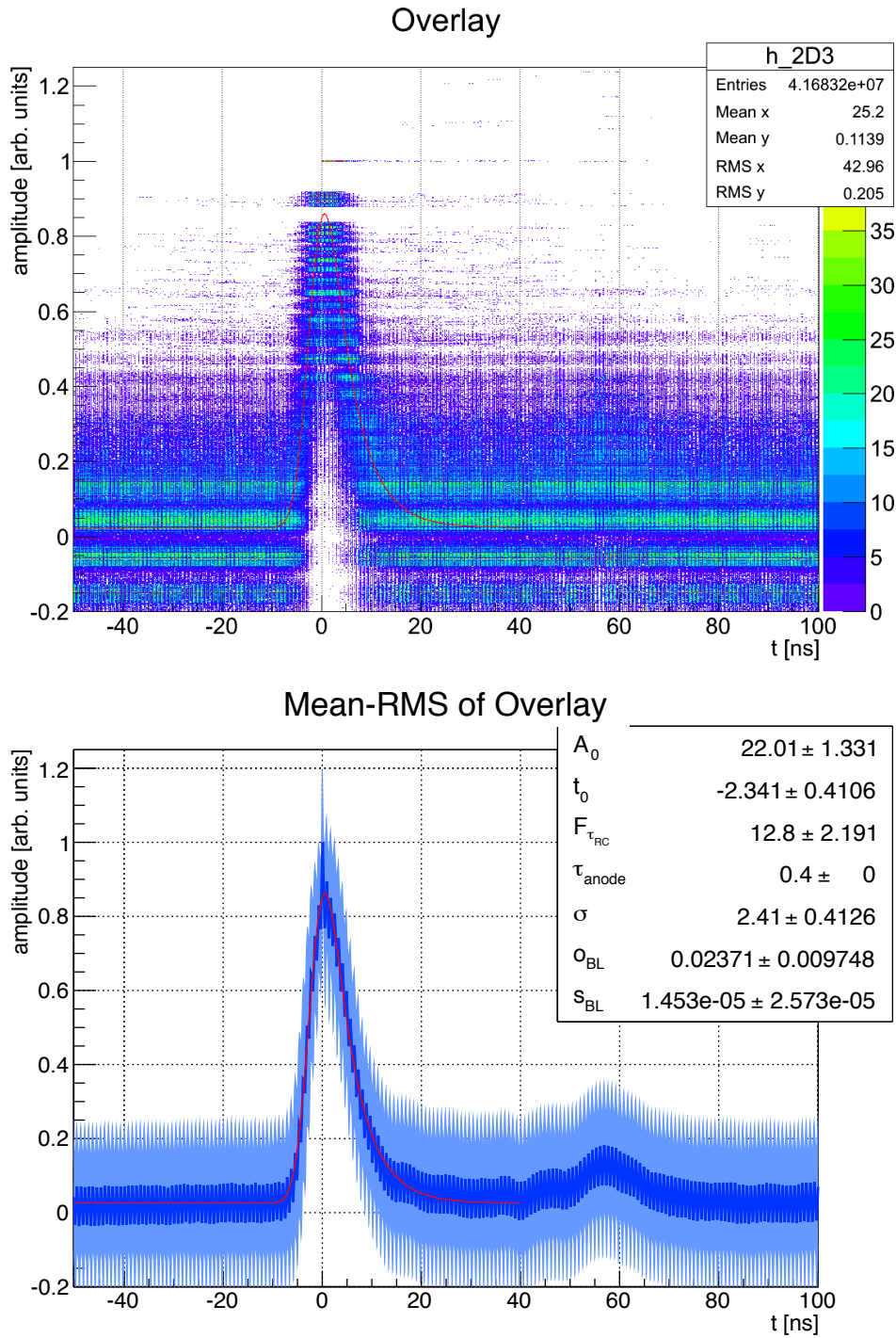


Figure E.3. As figure 6.8 but using the maximum of the waveform for time adjustment as described in section 6.3.

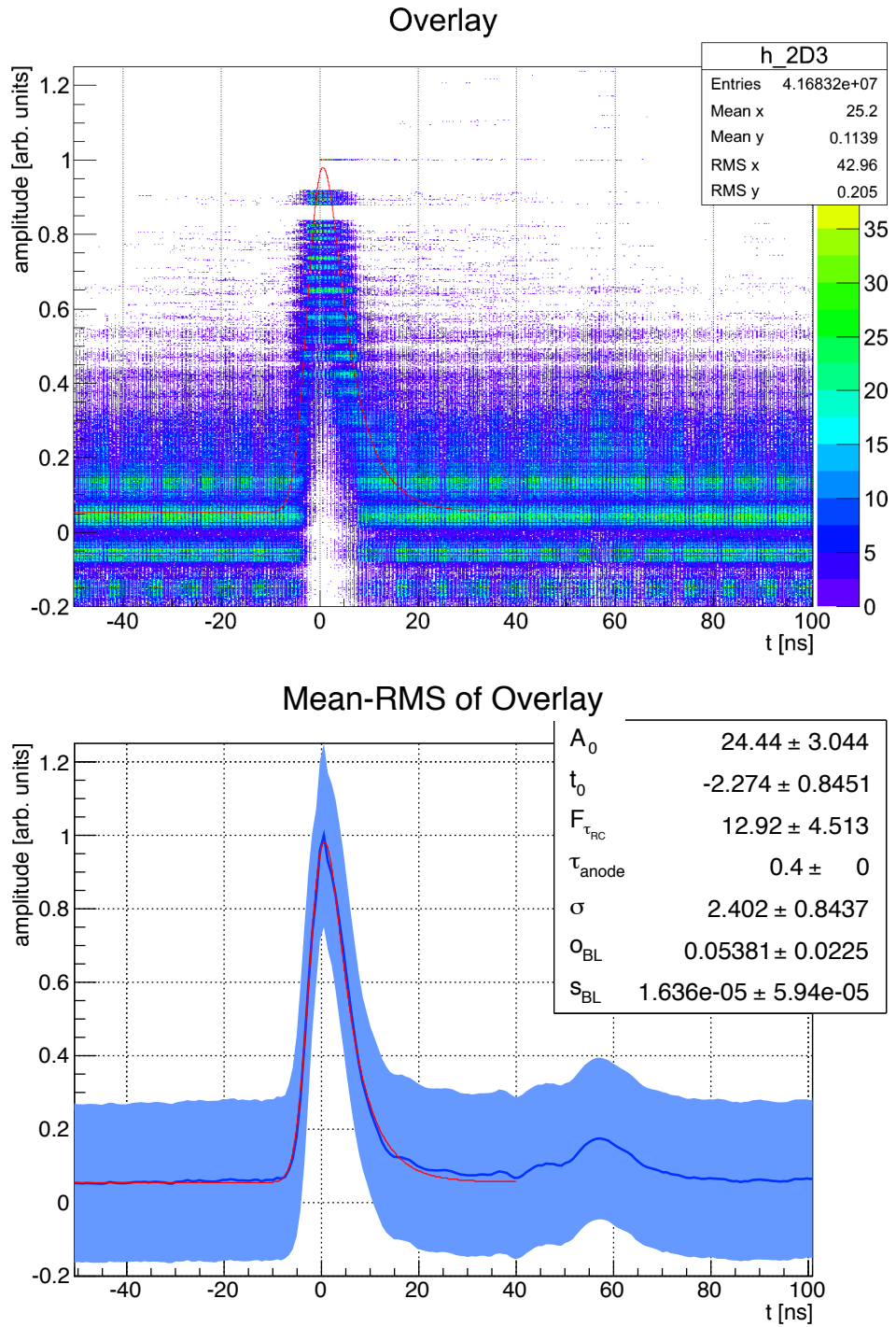


Figure E.4. As figure E.3 but rebinned by factor 4 to avoid the SIS3305 DC pattern.

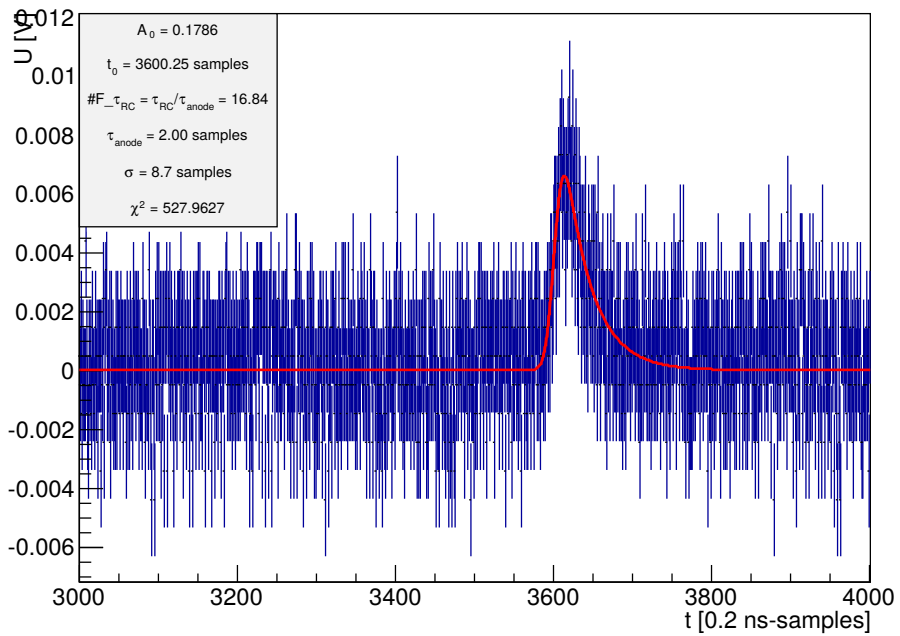
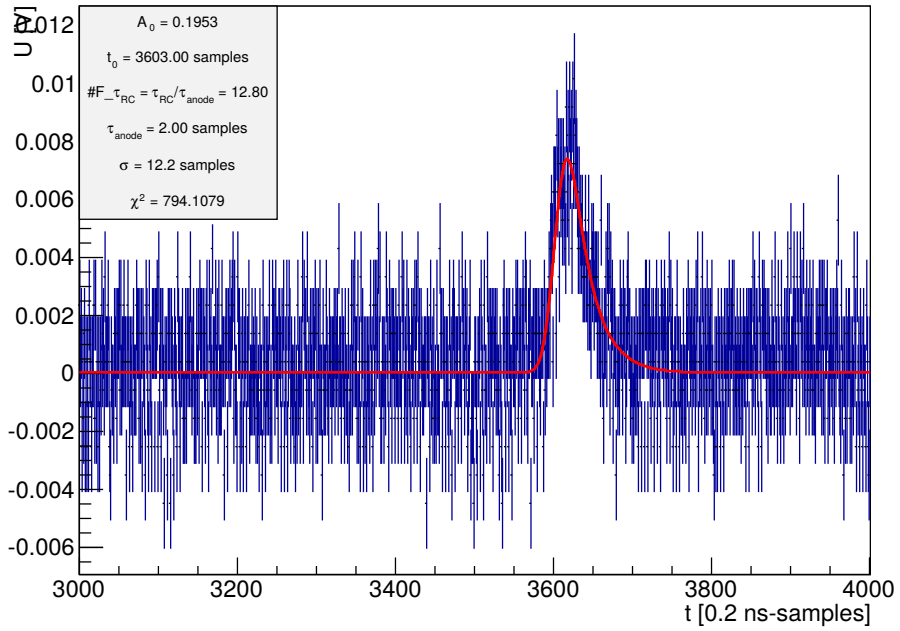


Figure E.5. Exemplaric fits to individual waveforms containing a spe signal.

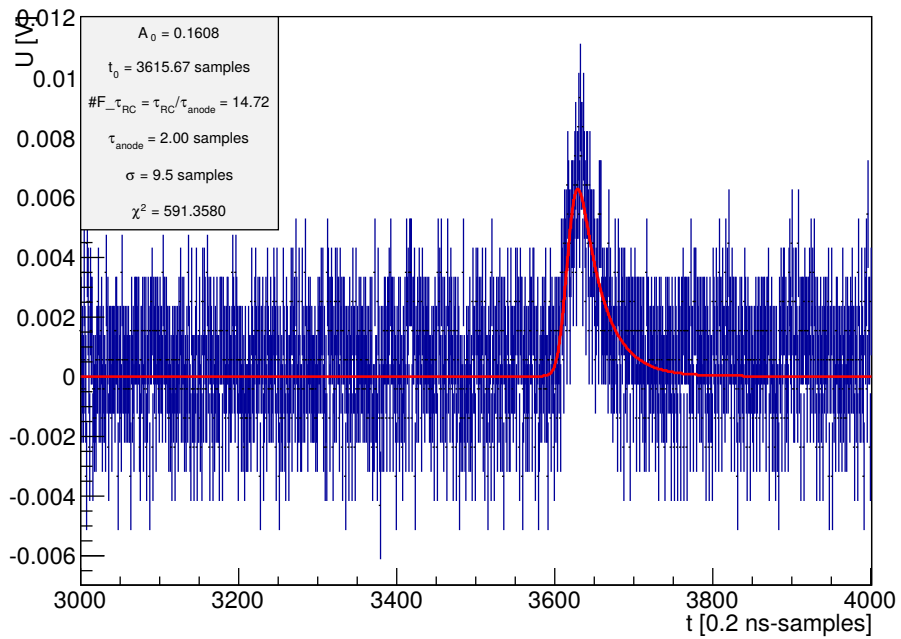
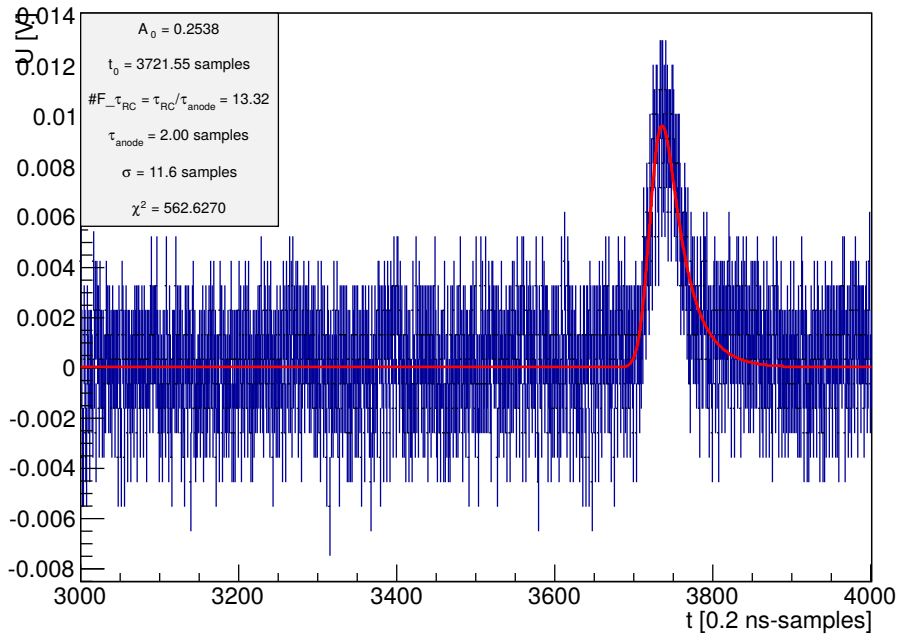


Figure E.6. Exemplaric fits to individual waveforms containing a spe signal.

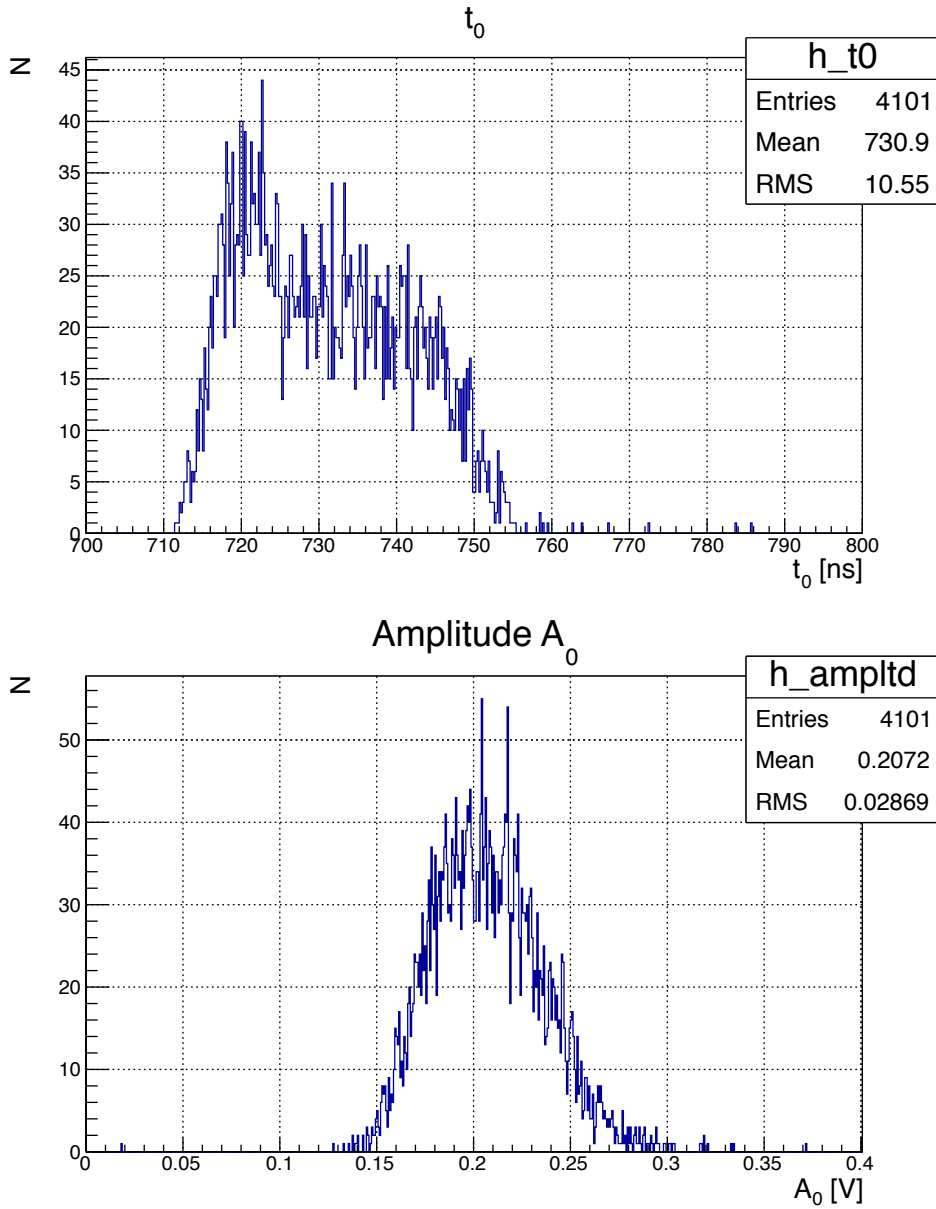


Figure E.7. Distribution of the fit parameters t_0 and A_0 when fitting individual spe signals. Compare section 6.3

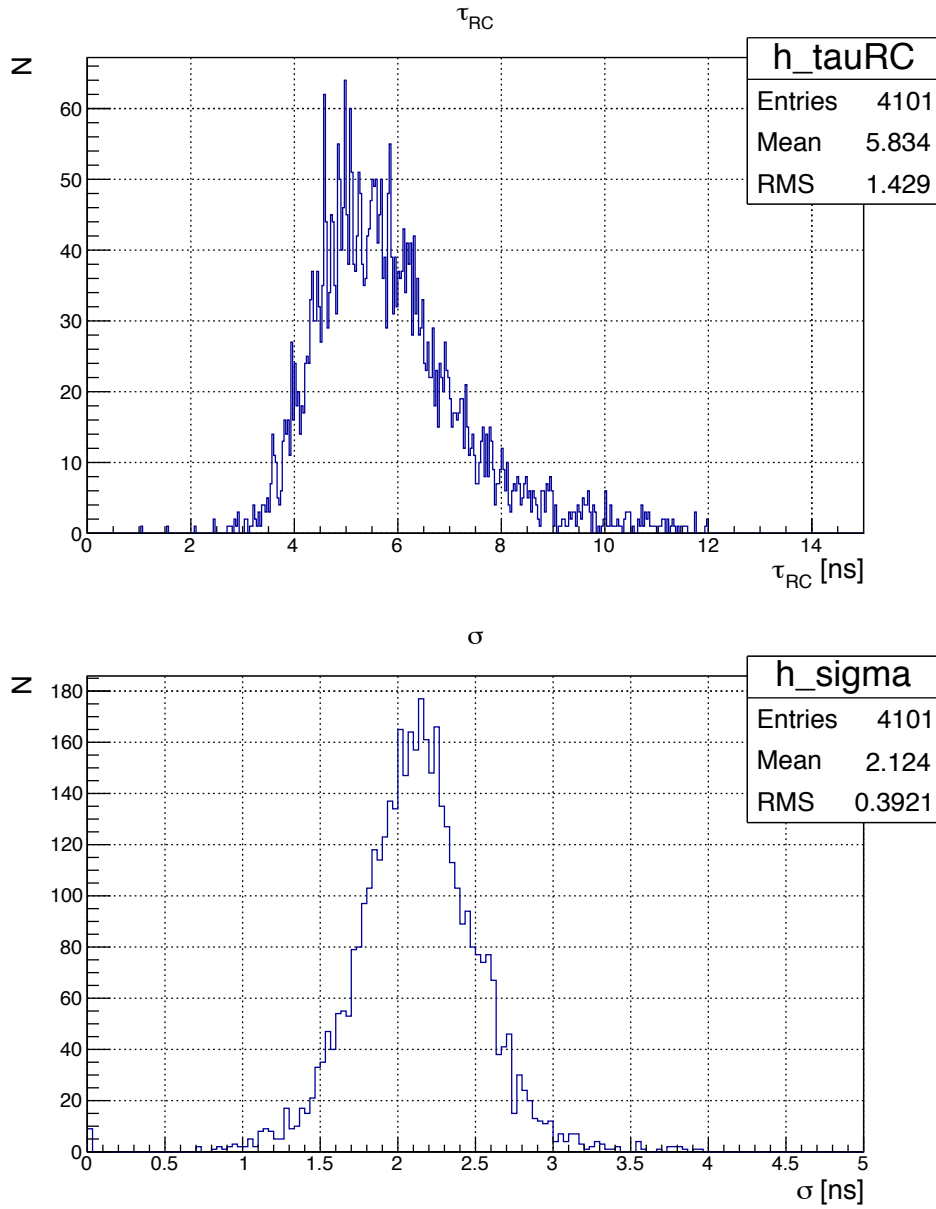


Figure E.8. Distribution of the fit parameters τ_{RC} and σ when fitting individual spe signals. Compare section 6.3

F. Pulse Shape: Model Function

We write the convoluted model as:

$$\tilde{S}(t) = N_{\text{tot}} \cdot T \cdot [\tilde{S}'_s(t) + \tilde{S}'_t(t)] \quad (\text{F.1})$$

Using equation 7.12 we get for the singlet component:

$$\tilde{S}'_s(t) = \frac{(1 - P_t)^2}{T - \tau_s \cdot (1 - P_t)} \cdot \left[K_s^r(t) \cdot \exp\left(- (t - t_0) \frac{1 - P_t}{T}\right) - K_s^d(t) \cdot \exp\left(- \frac{t - t_0}{\tau_s}\right) \right] \quad (\text{F.2})$$

$$K_s^r(t) = \frac{1}{2} \cdot \exp\left(\frac{\sigma^2}{2 \left(\frac{T}{1 - P_t}\right)^2}\right) \cdot \text{erfc}\left(\frac{\sigma}{\sqrt{2} \frac{T}{1 - P_t}} - \frac{t - t_0}{\sqrt{2}\sigma}\right) \quad (\text{F.3})$$

$$K_s^d(t) = \frac{1}{2} \cdot \exp\left(\frac{\sigma^2}{2 \cdot \tau_s^2}\right) \cdot \text{erfc}\left(\frac{\sigma}{\sqrt{2}\tau_s} - \frac{t - t_0}{\sqrt{2}\sigma}\right) \quad (\text{F.4})$$

and for the triplet component:

$$\tilde{S}'_t(t) = \frac{P_t}{T - \tau_s \cdot F \cdot P_t} \cdot \left[K_t^r(t) \cdot \exp\left(- (t - t_0) \frac{P_t}{T}\right) - K_t^d(t) \cdot \exp\left(- \frac{t - t_0}{F \cdot \tau_s}\right) \right] \quad (\text{F.5})$$

$$K_t^r(t) = \frac{1}{2} \cdot \exp\left(\frac{\sigma^2}{2 \left(\frac{T}{P_t}\right)^2}\right) \cdot \text{erfc}\left(\frac{\sigma}{\sqrt{2} \frac{T}{P_t}} - \frac{t - t_0}{F \cdot \tau_s}\right) \quad (\text{F.6})$$

$$K_t^d(t) = \frac{1}{2} \cdot \exp\left(\frac{\sigma^2}{2 \cdot (F \cdot \tau_s)^2}\right) \cdot \text{erfc}\left(\frac{\sigma}{\sqrt{2} F \cdot \tau_s} - \frac{t - t_0}{\sqrt{2}\sigma}\right) \quad (\text{F.7})$$

G. S1 vs. energy deposits: additional figures

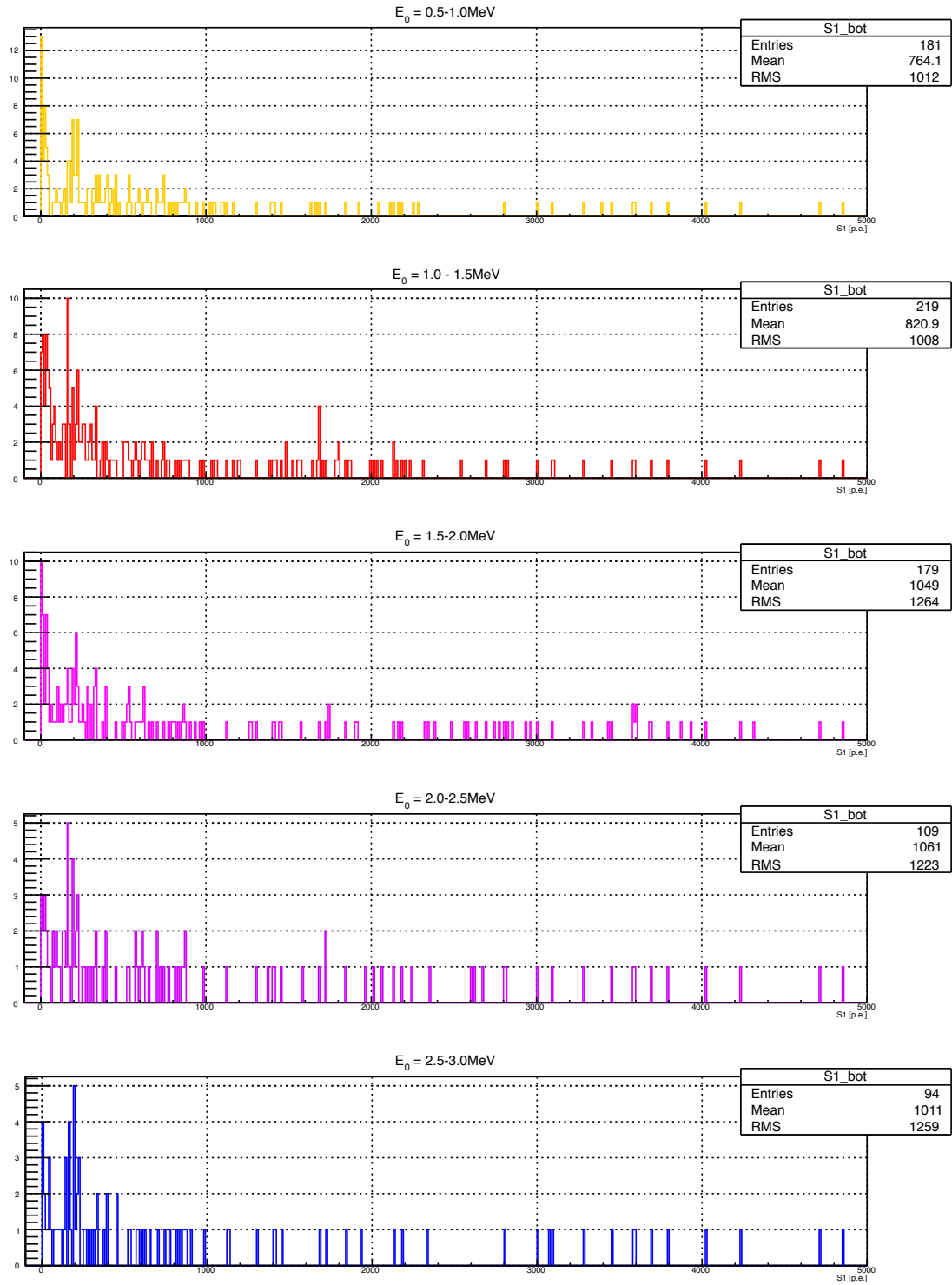


Figure G.1. S1 spectra of events flagged as neutron with “TOF-2 good“ for all backwards-directed plastics, separated into 5 ranges of primary neutron energies E_n^0 . S1 is shown in photo-electrons for the bottomPMT only. Data is taken without drift field.

APPENDIX G. S1 VS. ENERGY DEPOSITS: ADDITIONAL FIGURES

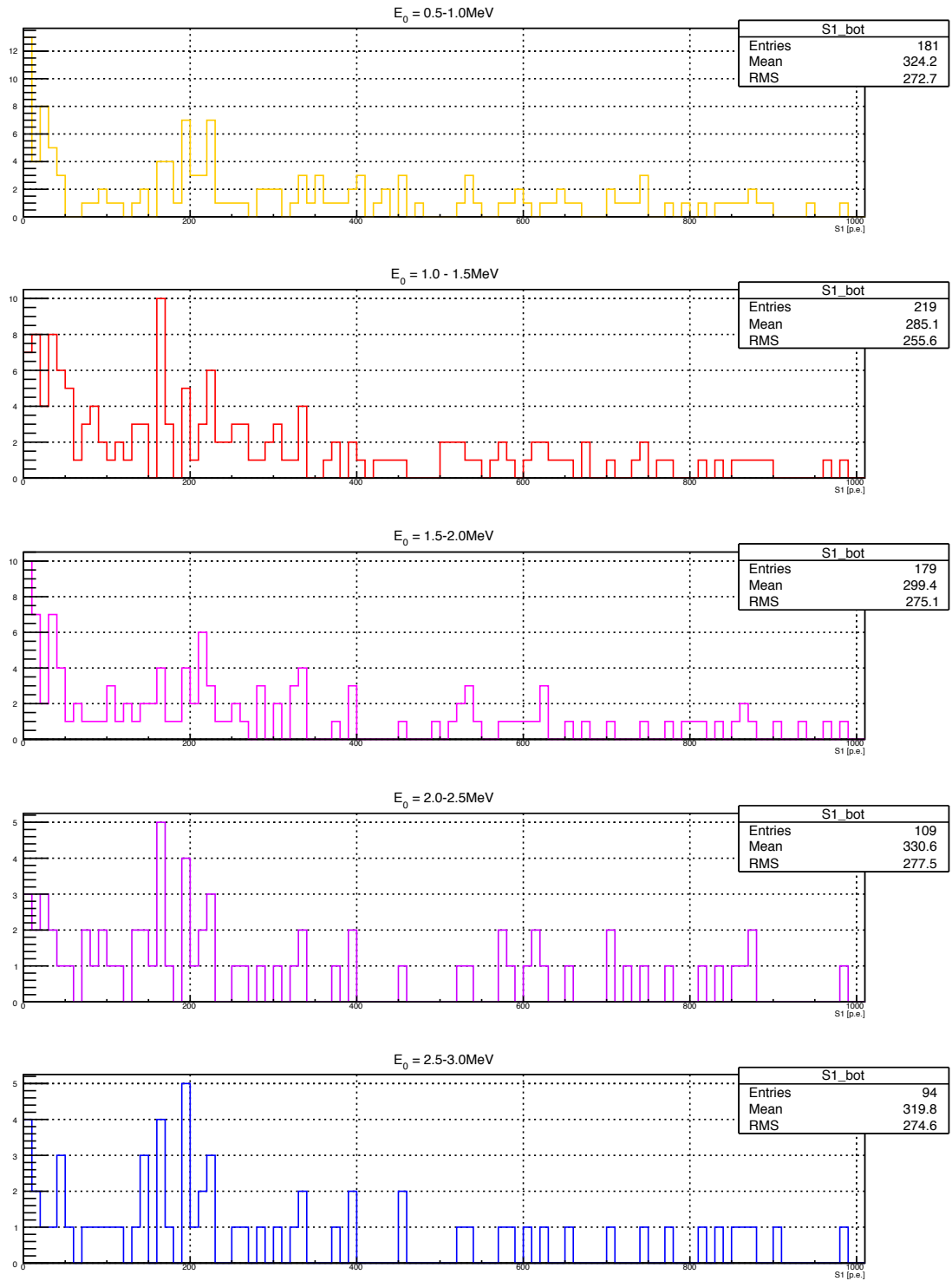


Figure G.2. Detailed view for lower amount of photons (bottomPMT only) of figure 7.8.

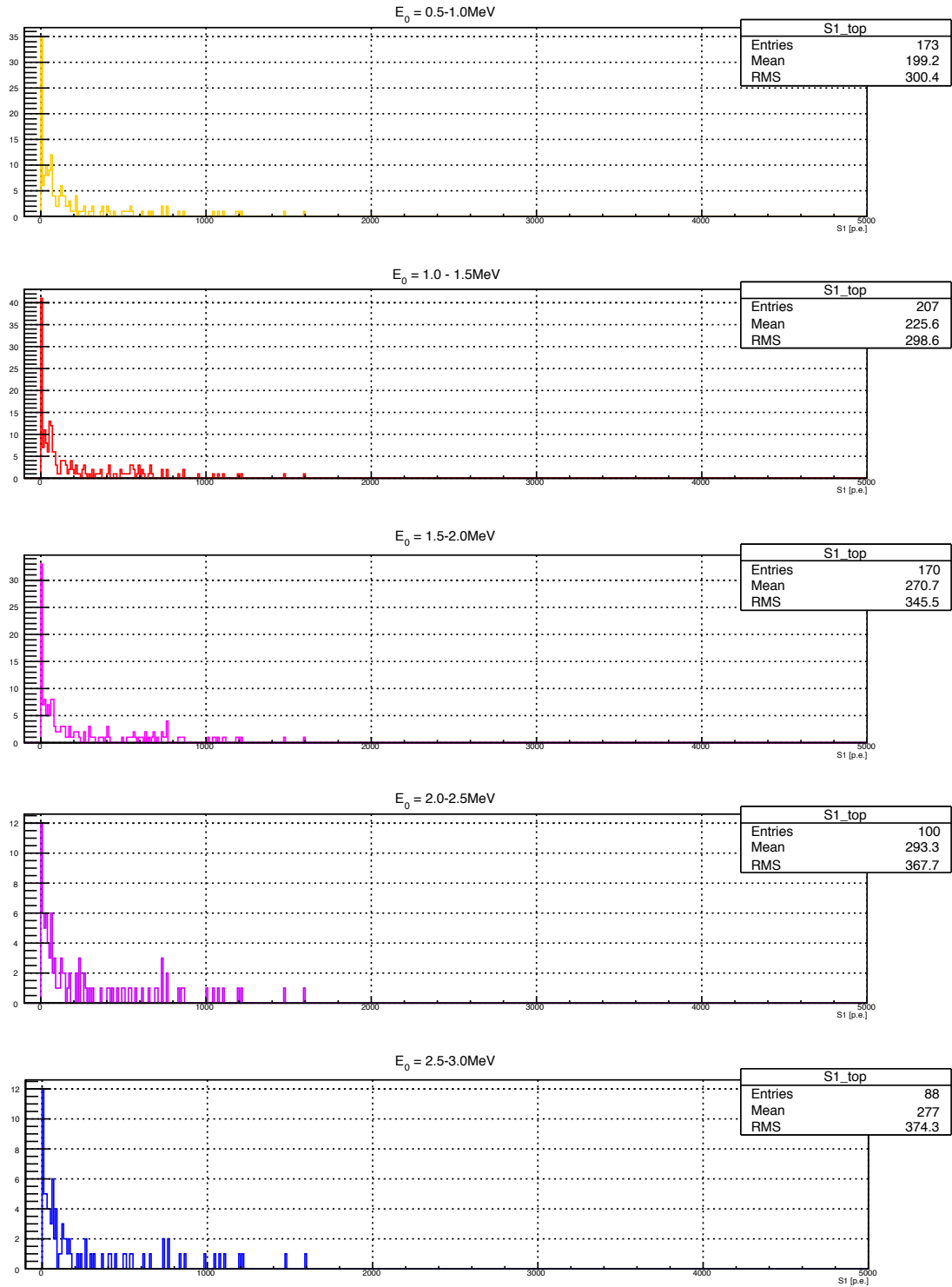


Figure G.3. S1 spectra of events flagged as neutron with “TOF-2 good“ for all backwards-directed plastics, separated into 5 ranges of primary neutron energies E_n^0 . S1 is shown in photo-electrons for the topPMT only. Data is taken without drift field.

APPENDIX G. $S1$ VS. ENERGY DEPOSITS: ADDITIONAL FIGURES

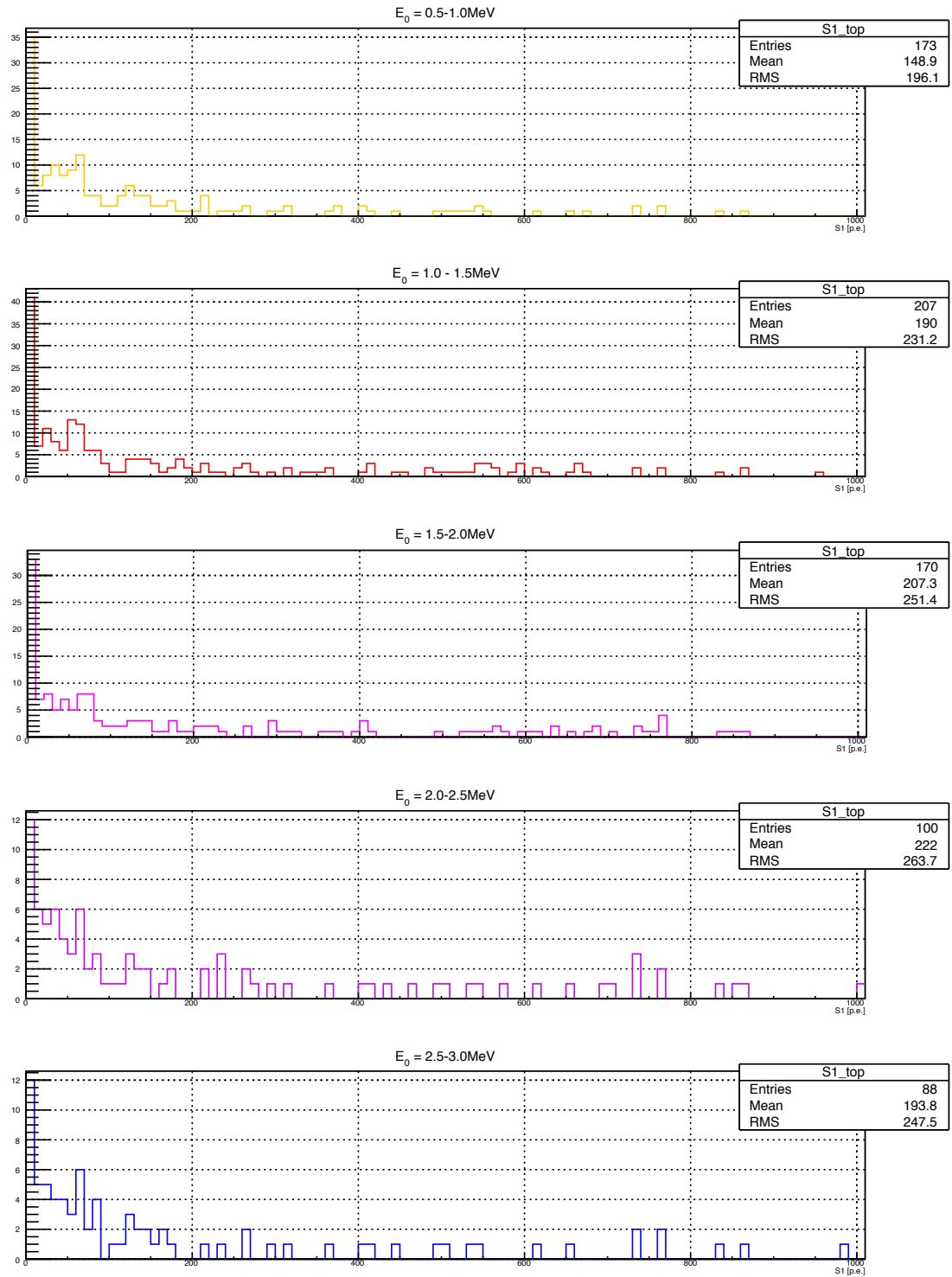


Figure G.4. Detailed view for lower amount of photons (topPMT only) of figure 7.8.

H. Pulse shape: additional figures

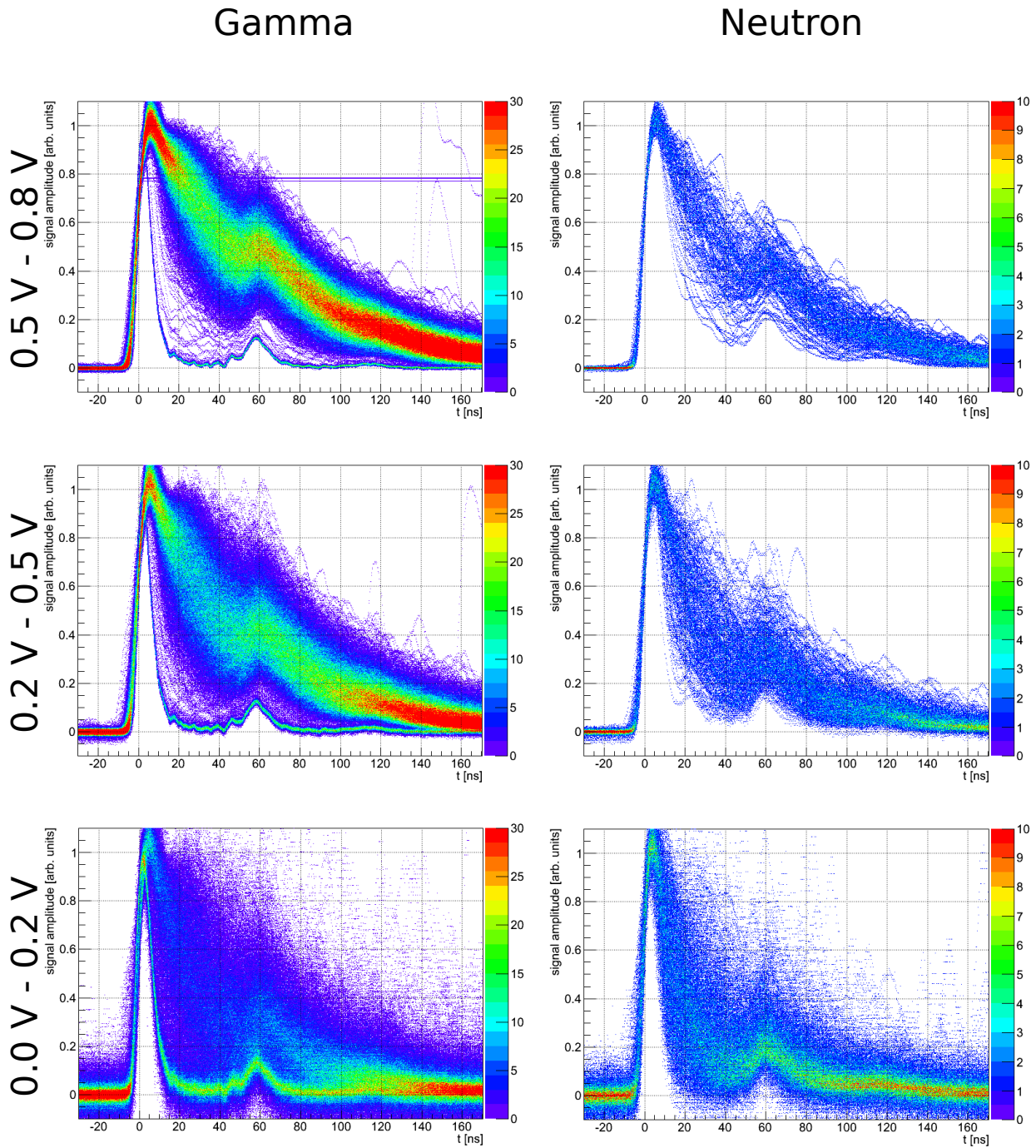


Figure H.1. No drift field. Overlay of gammas (left) and neutrons (right).

PopulationX

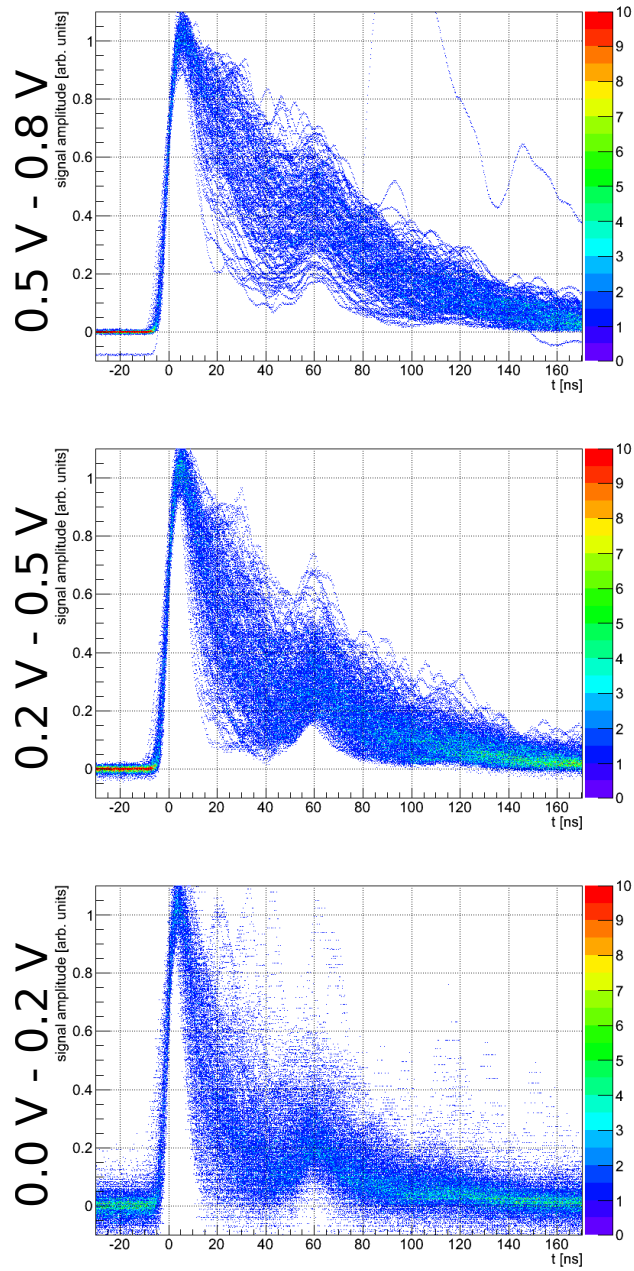


Figure H.2. No drift field. Overlay of events of PopulationX (inelastically scattered neutrons).

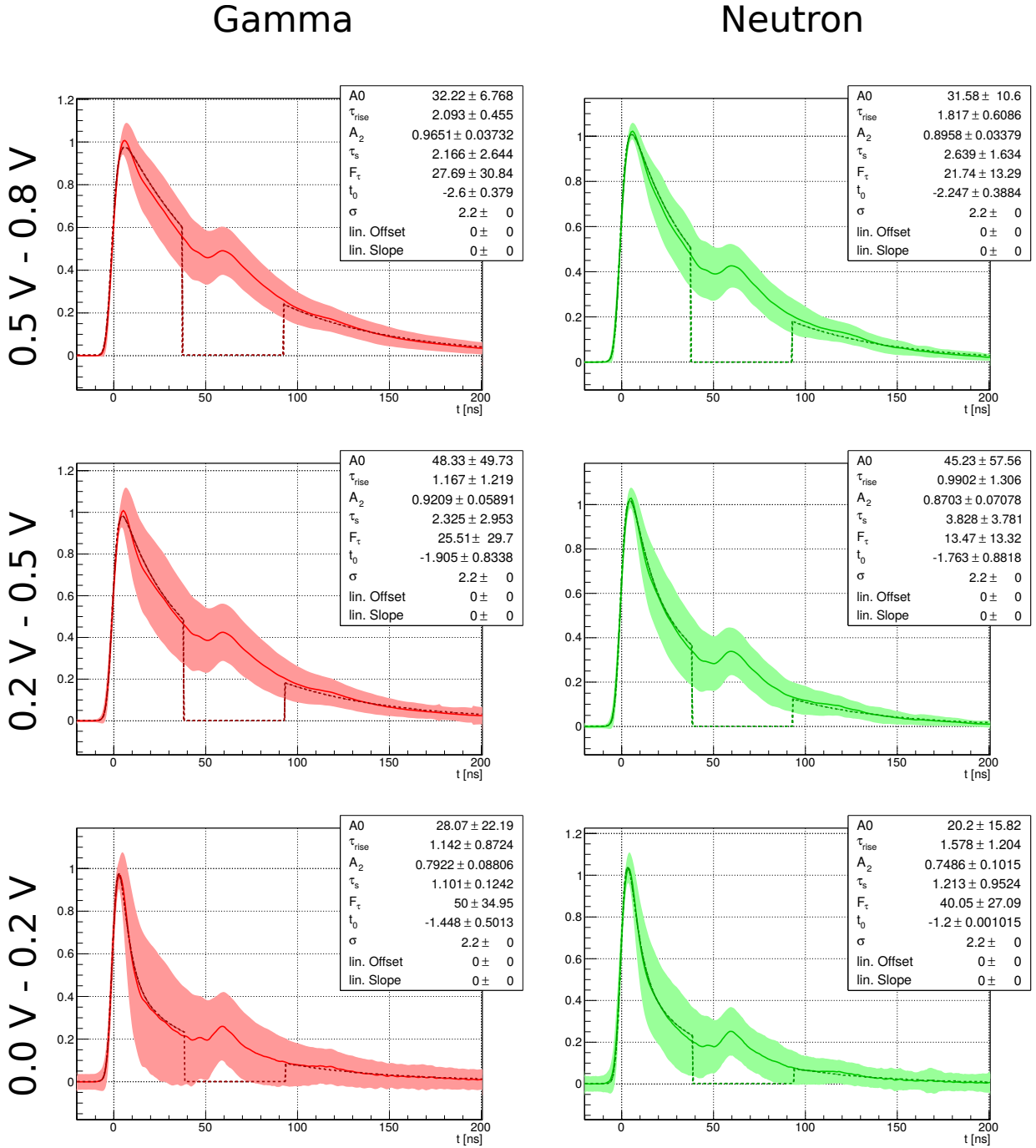


Figure H.3. No drift field. Fits to the curves of gaussian mean.

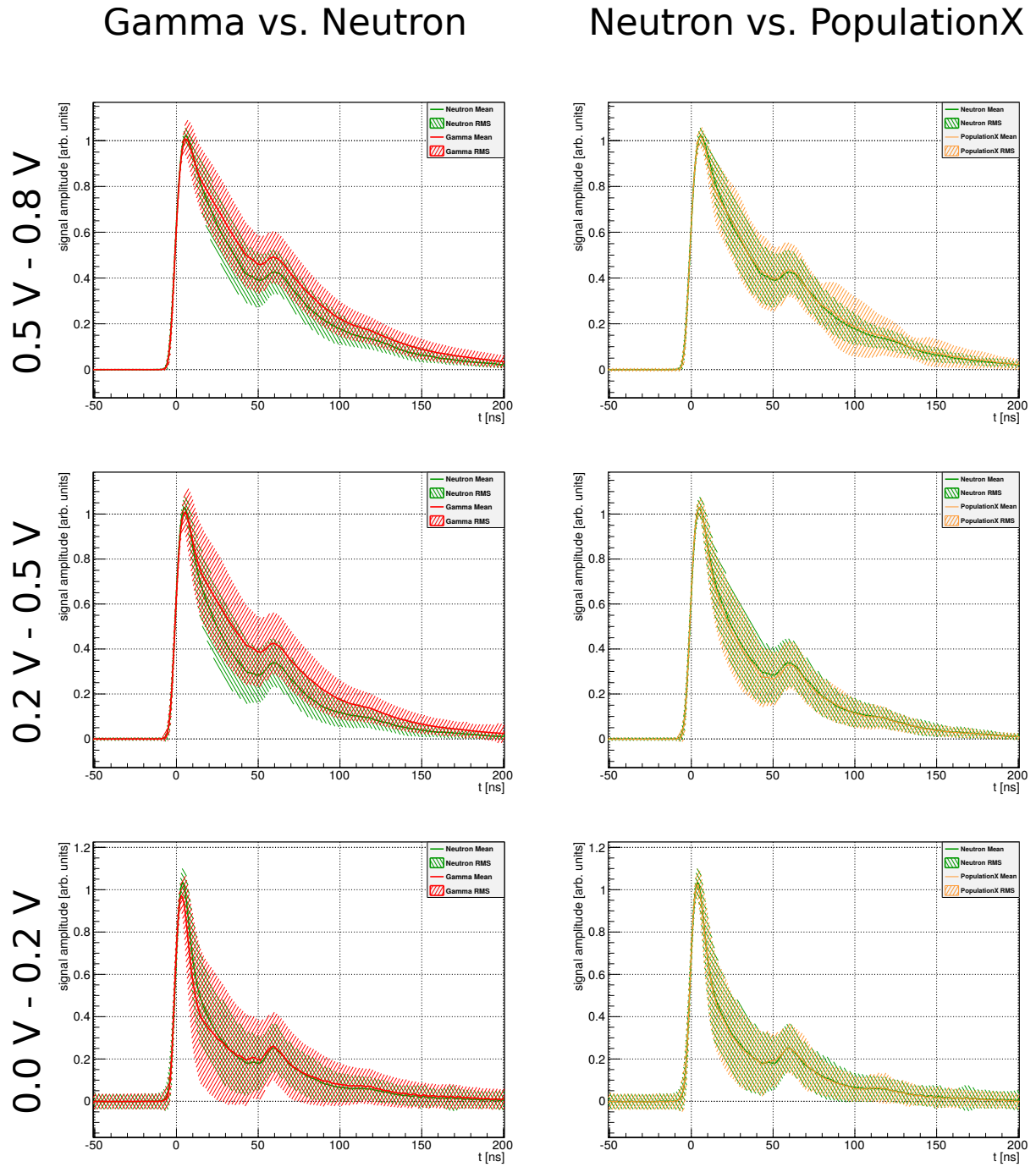


Figure H.4. Comparison of neutron events with “TOF-2 good” and PopulationX events (inelastic neutron scattering) for different signal amplitudes at zero drift field.

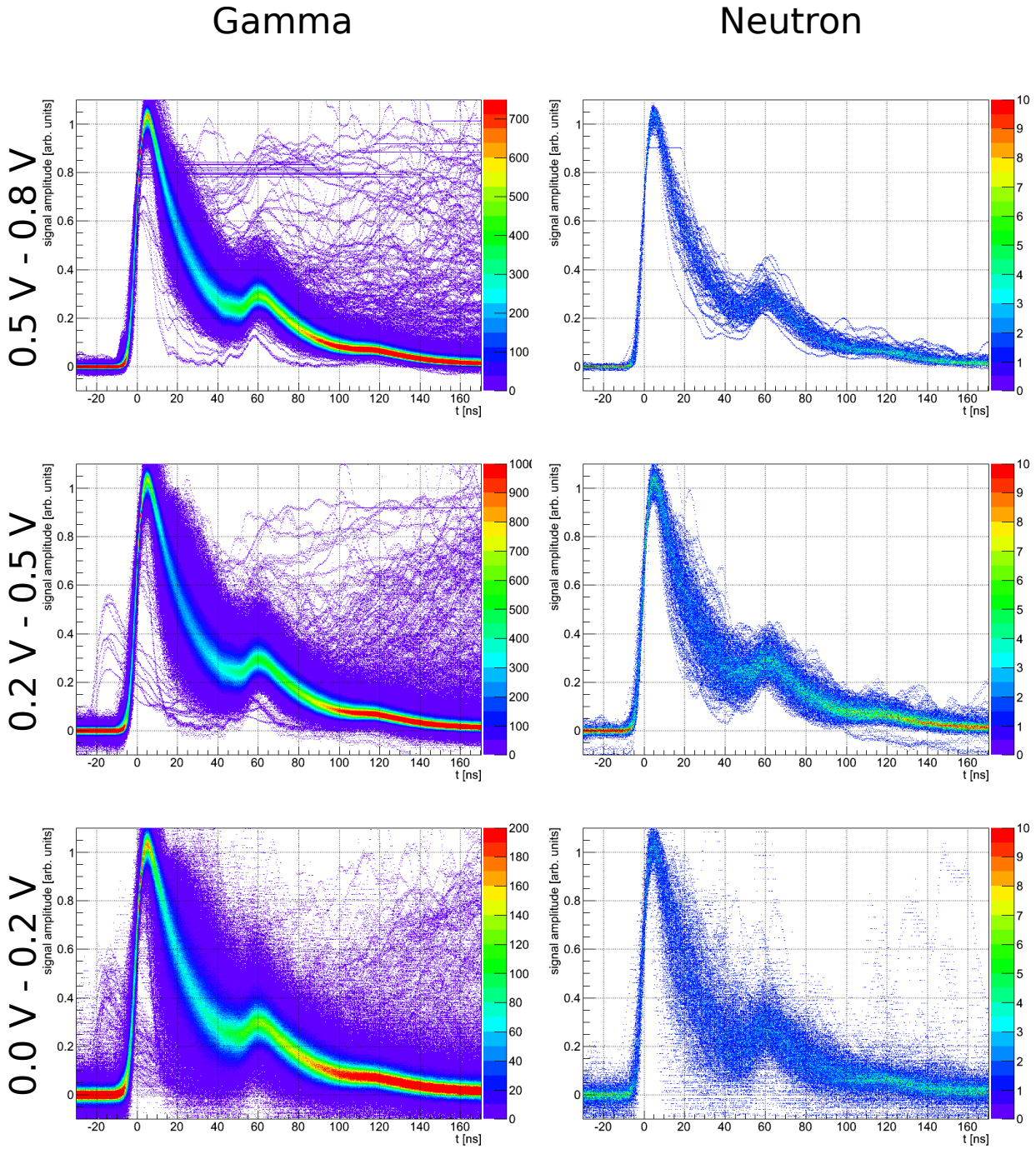


Figure H.5. Drift field of 600V/cm. Overlay of gammas (left) and neutrons (right).

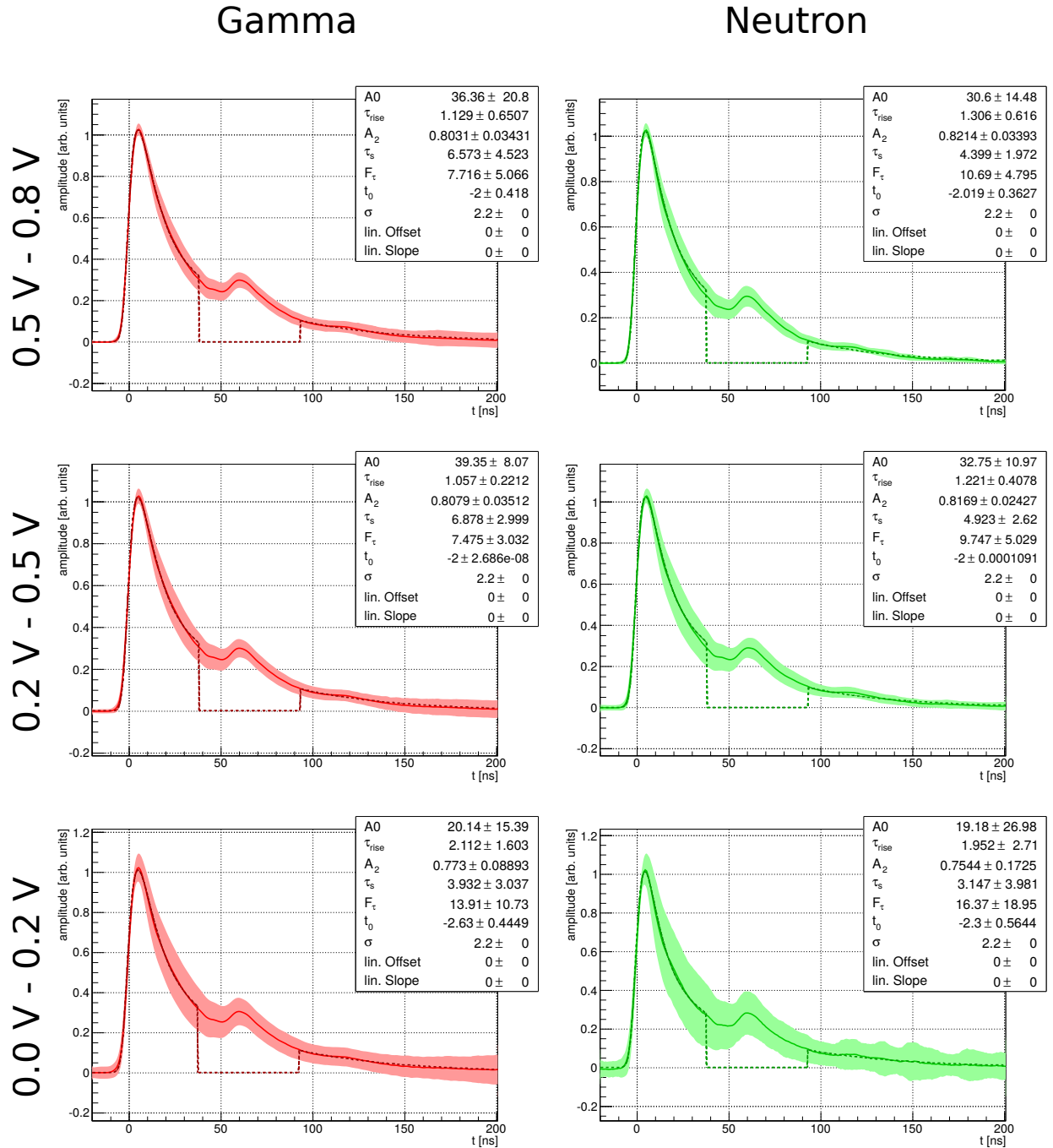


Figure H.6. Drift field of 600V/cm. Fits to the curves of gaussian mean.

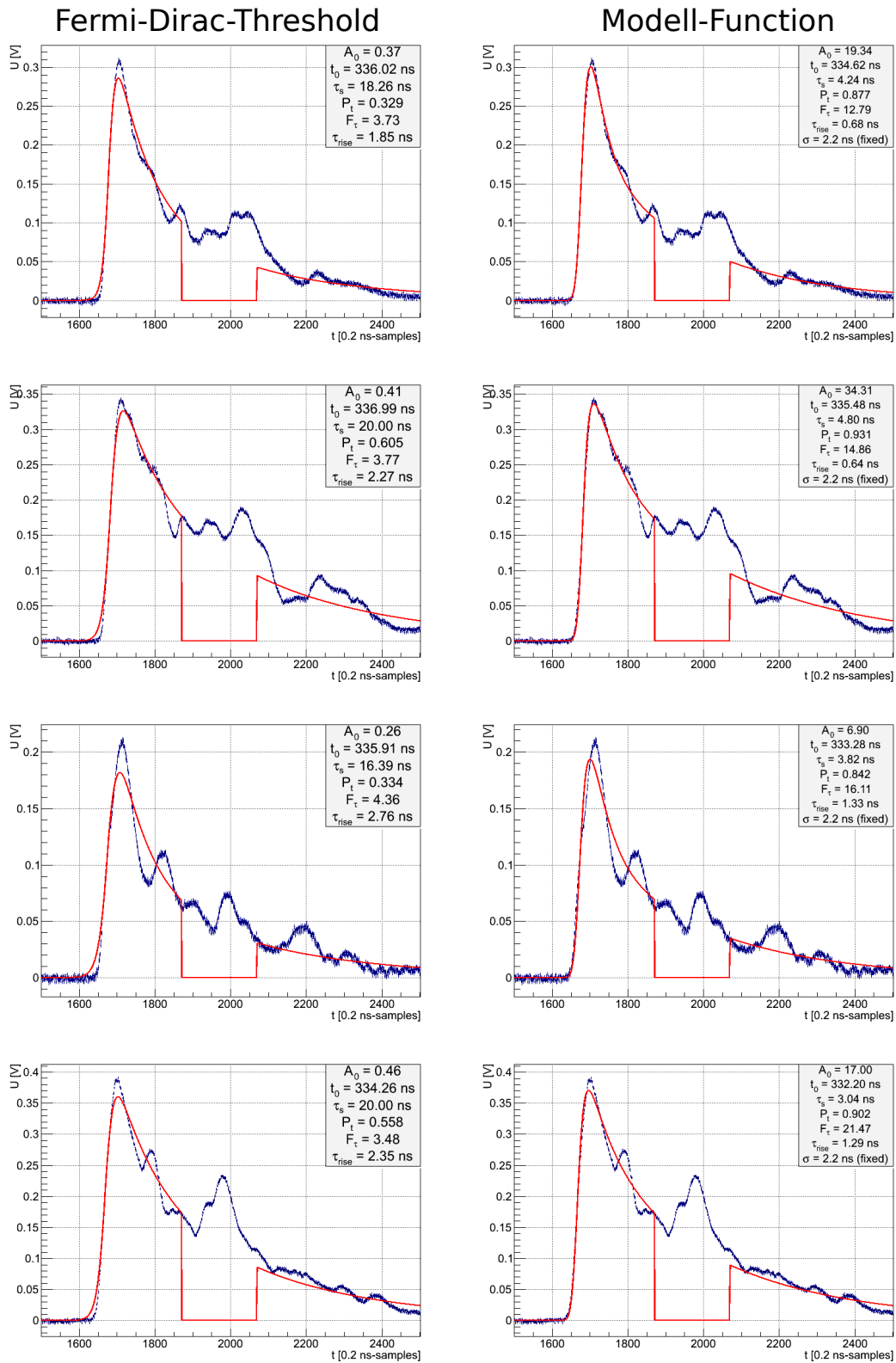


Figure H.7. Examples of gamma interactions (200 mV - 500 mV) at zero field. On the left the signals are fitted with the Fermi-Dirac function, on the right, the waveforms are fitted with the modell function.

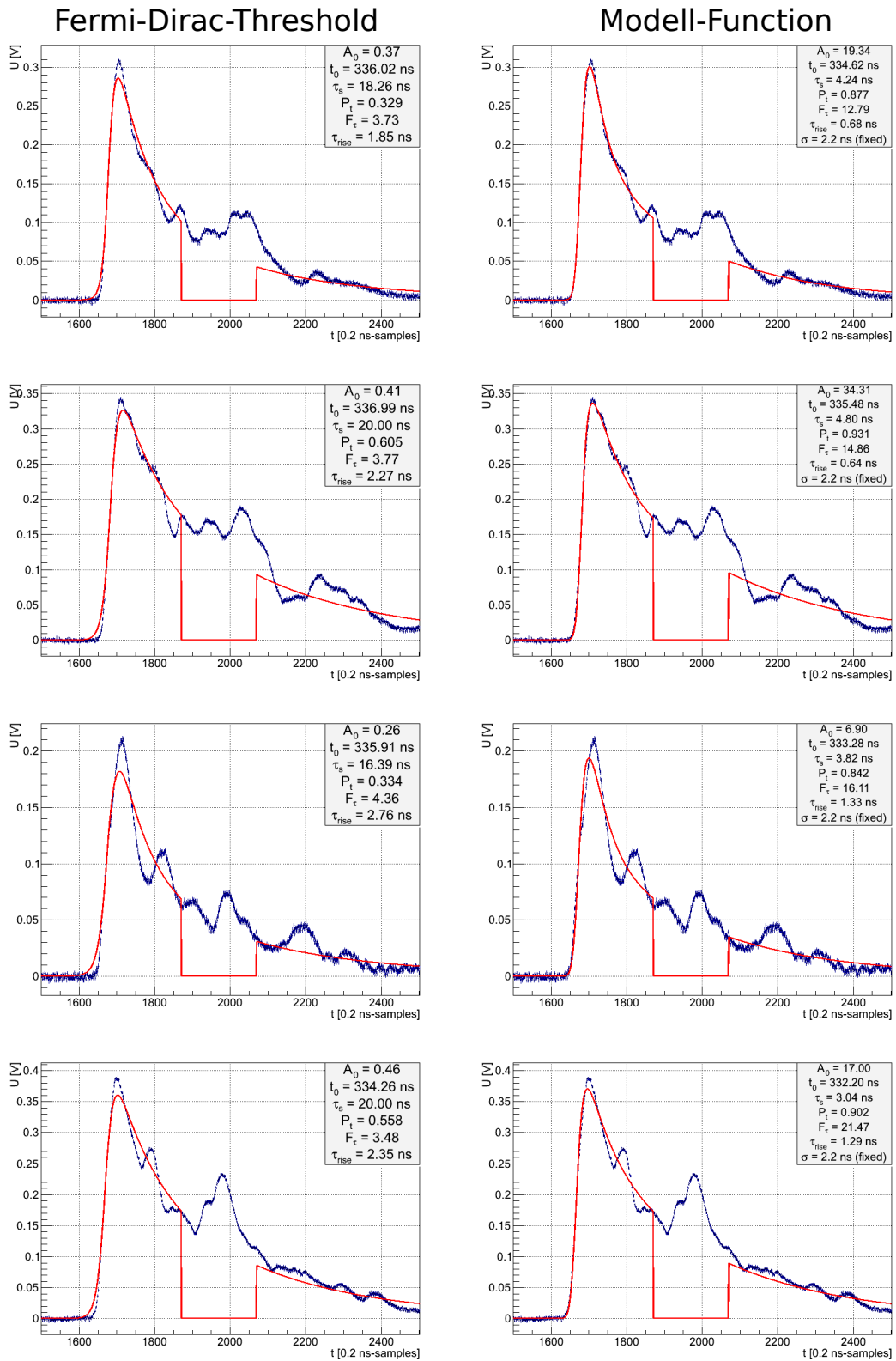


Figure H.8. Examples of gamma interactions (500 mV - 800 mV) at zero field. On the left the signals are fitted with the Fermi-Dirac function, on the right, the waveforms are fitted with the modell function.

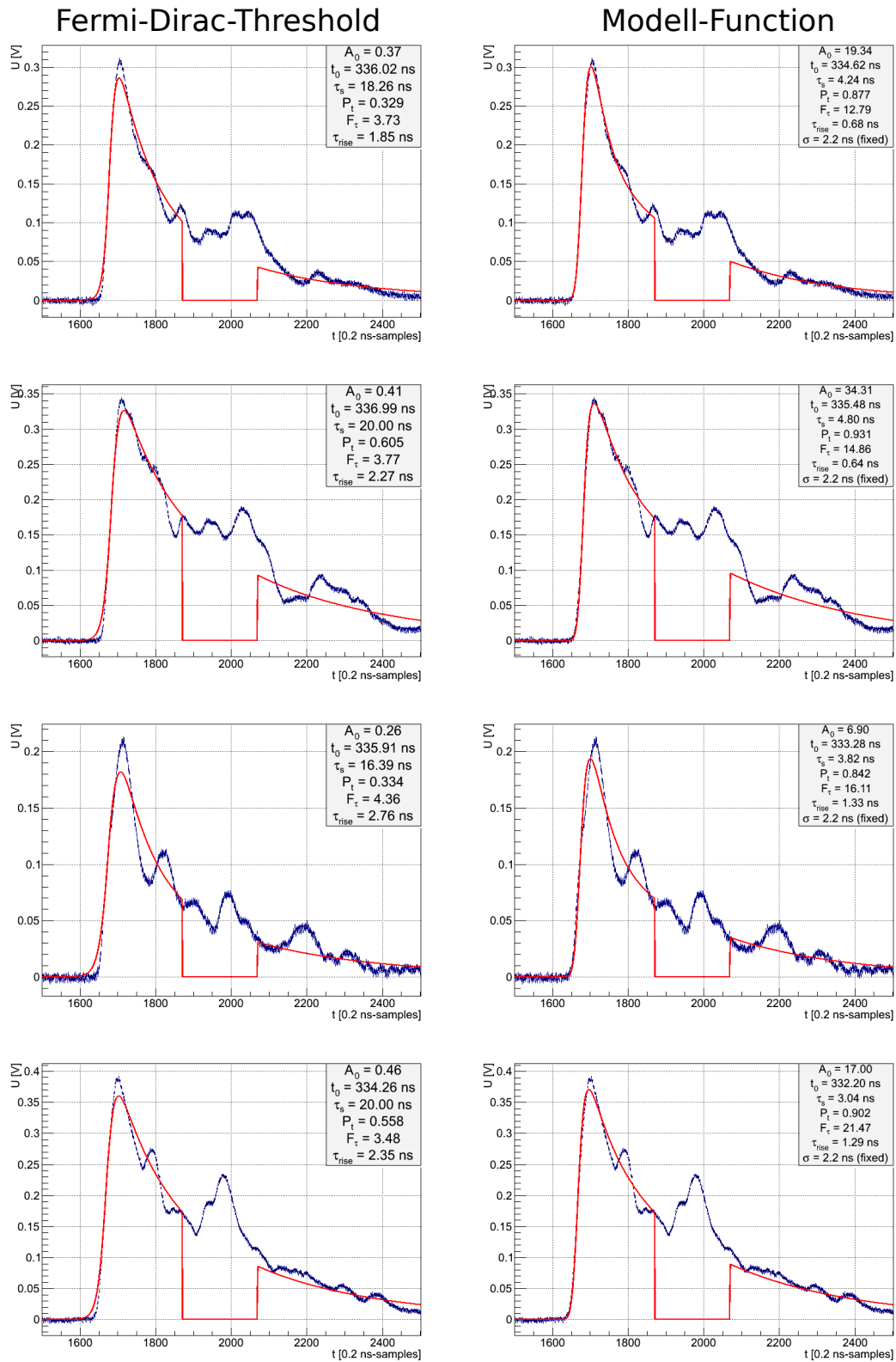


Figure H.9. Examples of neutron interactions (200 mV - 500 mV) at zero field. On the left the signals are fitted with the Fermi-Dirac function, on the right, the waveforms are fitted with the modell function.

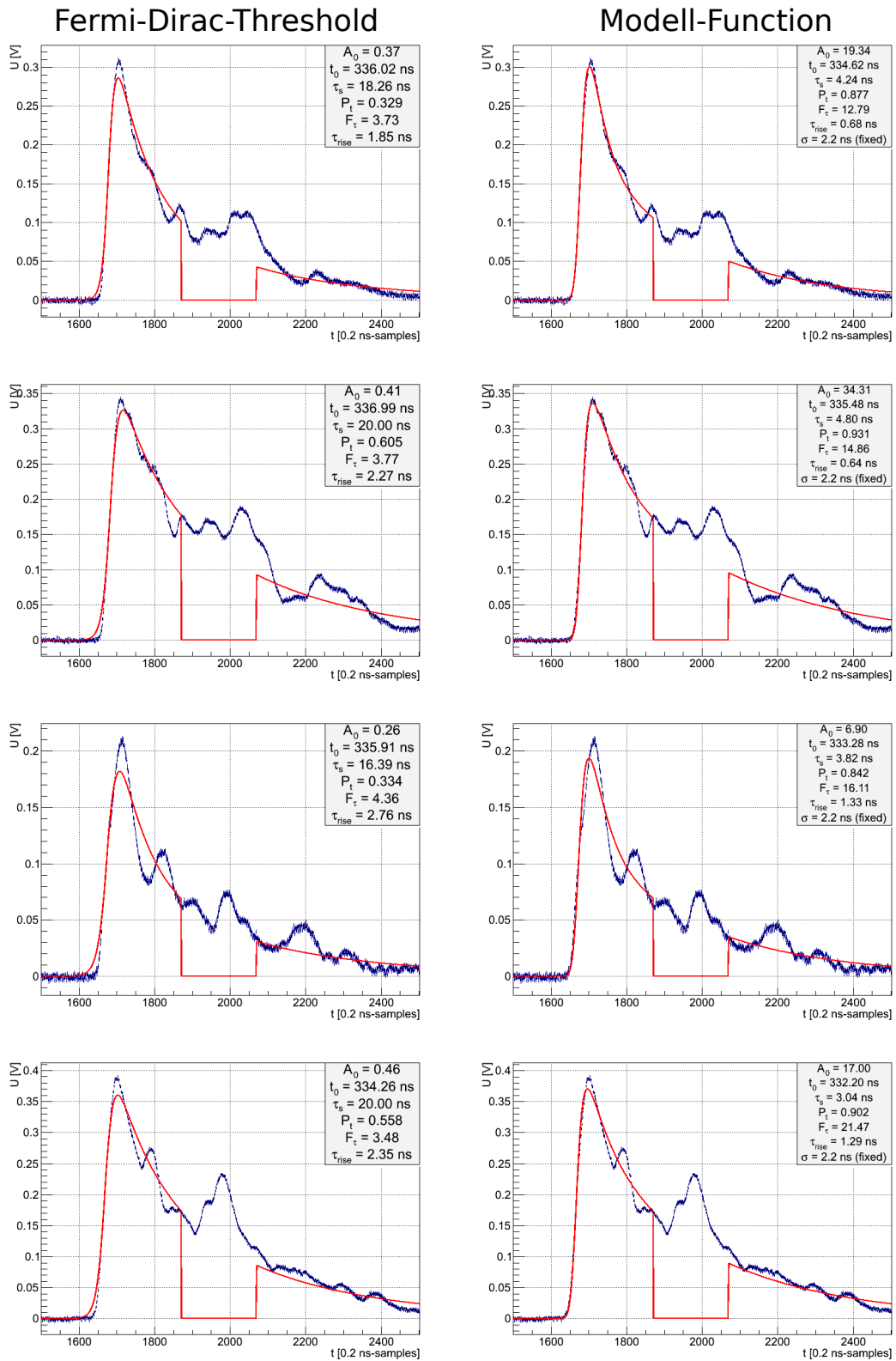


Figure H.10. Examples of neutron interactions (500 mV - 800 mV) at zero field. On the left the signals are fitted with the Fermi-Dirac function, on the right, the waveforms are fitted with the modell function.

Bibliography

- [Acc17] Accuglass Products. Website: HTL-133-1
<https://accuglassproducts.com/product.php?productid=16445&cat=459&page=1&variantid=641>, March 2017.
- [Ade14] P. A. R. et al. Ade. Planck 2013 results. XVI. Cosmological parameters. *Astron. Astrophys.*, 571:A16, 2014.
- [Ae10] Elena Aprile et al. (XENON Collaboration). First dark matter results from the XENON100 experiment. *Phys. Rev. Lett.*, 105:131302, Sep 2010.
- [Ae12] Elena Aprile et al. (XENON Collaboration). The XENON100 dark matter experiment. *Astroparticle Physics*, 35(9):573 – 590, 2012.
- [Ae13] Elena Aprile et al. (XENON Collaboration). Response of the XENON100 dark matter detector to nuclear recoils. *Phys. Rev. D*, 88:012006, Jul 2013.
- [Ae16] Elena Aprile et al. (XENON Collaboration). Physics reach of the XENON1T dark matter experiment. *Journal of Cosmology and Astroparticle Physics*, 2016(04):027, 2016.
- [Ae17] Elena Aprile et al. (XENON Collaboration). The XENON1T dark matter experiment. *to be published*, 2017.
- [Ake13] D. S. Akerib et al. (LUX Collaboration). The large underground xenon (lux) experiment. *Nuclear Instruments and Methods in Physics Research Section A: Accelerators, Spectrometers, Detectors and Associated Equipment*, 704:111 – 126, 2013.
- [Aki02] D. Akimov et al. Measurements of scintillation efficiency and pulse shape for low energy recoils in liquid xenon. *Physics Letters B*, 524(3&4):245 – 251, 2002.
- [Ana17] Analog Devices. Website
<http://www.analog.com/en/products/amplifiers/operational-amplifiers/current-feedback-amplifiers/ad8009.html>, March 2017.
- [BBB⁺01] J. Bonn, B. Bornschein, L. Bornschein, L. Fickinger, B. Flatt, O. Kazachenko, A. Kovalik, C. Kraus, E. W. Otten, J. P. Schall, H. Ulrich, and C. Weinheimer. The Mainz Neutrino Mass Experiment. *Nuclear Physics B Proceedings Supplements*, 91:273–279, 2001.

- [BBS91] K. G. Begeman, A. H. Broeils, and R. H. Sanders. Extended rotation curves of spiral galaxies: dark haloes and modified dynamics. *Monthly Notices of the Royal Astronomical Society*, 249(3):523–537, 1991.
- [Bey07] Roland Beyer. Aufbau und Entwicklung von Neutronen-Flugzeit-Detektoren für die Untersuchung astrophysikalisch relevanter (gamma,n)-Reaktionen. diploma thesis, Friedrich-Schiller-University Jena, 2007.
- [Bey14] Roland Beyer. *Inelastische Streuung schneller Neutronen an ^{56}Fe* . PhD thesis, Technische Universität Dresden, 2014.
- [BGH⁺07] R. Beyer, E. Grosse, K. Heidel, J. Hutsch, A.R. Junghans, J. Klug, D. Legrady, R. Nolte, S. Röttger, M. Sobiella, and A. Wagner. Proton-recoil detectors for time-of-flight measurements of neutrons with kinetic energies from some tens of keV to a few MeV. *Nuclear Instruments and Methods in Physics Research Section A: Accelerators, Spectrometers, Detectors and Associated Equipment*, 575(3):449 – 455, 2007.
- [Bro16] Brown University - Particle Astrophysics Group. DMTools <http://dmttools.brown.edu/>, June 2016.
- [CER17] CERN. Website: Root data analysis framework <https://root.cern.ch/>, March 2017.
- [Cha17] Chartindustries QDrive. Website <http://www.chartindustries.com/Industry/Industry-Products/Qdrive/Qdrive-Products/Pressure-Wave-Generators/Pressure-Wave-Generators-2S132W>, March 2017.
- [COM17] COMSOL Multipysics. Website <https://www.comsol.de/>, March 2017.
- [DDL⁺94] G.J. Davies, J.D. Davies, J.D. Lewin, P.F. Smith, and W.G. Jones. Liquid xenon as a dark matter detector. prospects for nuclear recoil discrimination by photon timing. *Physics Letters B*, 320(3):395 – 399, 1994.
- [Dem10] W. Demtröder. *Experimentalphysik 4*. Springer, 2010.
- [DHA⁺05] J.V. Dawson, A.S. Howard, D. Akimov, H. Araujo, A. Bewick, D.C.R. Davidge, W.G. Jones, M. Joshi, V.N. Lebedenko, I. Liubarsky, J.J. Quenby, G. Rochester, D. Shaul, T.J. Sumner, and R.J. Walker. A study of the scintillation induced by alpha particles and gamma rays in liquid xenon in an electric field. *Nuclear Instruments and Methods in Physics Research Section A: Accelerators, Spectrometers, Detectors and Associated Equipment*, 545(3):690 – 698, 2005.

- [DMS90] Tadayoshi Doke, Kimiaki Masuda, and Eido Shibamura. Estimation of absolute photon yields in liquid argon and xenon for relativistic (1 mev) electrons. *Nuclear Instruments and Methods in Physics Research Section A: Accelerators, Spectrometers, Detectors and Associated Equipment*, 291(3):617 – 620, 1990.
- [ESA17] ESA - European Space Agency. Website: European Space Agency <http://www.esa.int/>, March 2017.
- [GAC⁺11] K L Giboni, E Aprile, B Choi, T Haruyama, R F Lang, K E Lim, A J Melgarejo, and G Plante. Xenon recirculation-purification with a heat exchanger. *Journal of Instrumentation*, 6(03):P03002, 2011.
- [GEA17] GEA. Website: GEA (Kelvion) Plattenwärmetauscher <https://de.kelvion.com/de/produkte/plattenwaermetauscher/geloetete-plattenwaermetauscher-ecobraze/gbs-serie/>, March 2017.
- [Ger04] Christian Gerthsen. *Gerthsen Physik : mit 93 Tabellen, 105 durchgerechneten Beispielen und 1074 Aufgaben mit vollständigen Lösungen auf CD-ROM ; [die ganze Physik zum 21. Jahrhundert]*. Springer-Lehrbuch. Springer, Berlin [u.a.], 22., völlig neu bearb. Aufl. edition, 2004.
- [Gro17] MainzTPC Group. MainzTPC picture archive. 2017.
- [Hil14] Christopher Hils. Studie von internen Kalibrationsmethoden für Flüssig-Xenon-TPCs zur direkten Suche nach Dunkler Materie. diploma thesis, Johannes Gutenberg-University Mainz, January 2014.
- [Hit05] Akira Hitachi. Properties of liquid xenon scintillation for dark matter searches. *Astroparticle Physics*, 24(3):247 – 256, 2005.
- [HTF⁺83] Akira Hitachi, Tan Takahashi, Nobutaka Funayama, Kimiaki Masuda, Jun Kikuchi, and Tadayoshi Doke. Effect of ionization density on the time dependence of luminescence from liquid argon and xenon. *Phys. Rev. B*, 27:5279–5285, May 1983.
- [HTH⁺82] A. Hitachi, T. Takahashi, T. Hamada, E. Shibamura, N. Funayama, K. Masuda, J. Kikuchi, and T. Doke. Let dependence of the luminescence yield from liquid argon and xenon. *Nuclear Instruments and Methods in Physics Research*, 196(1):97 – 100, 1982.
- [HW55] M. L. Humason and H. D. Wahlquist. Solar motion with respect to the local group of nebulae. *Astronomical Journal*, 60:254, 1955.
- [HZD17] HZDR. Website: nELBE <https://www.hzdr.de/db/Cms?pNid=317>, March 2017.

- [IAE16] IAEA - International Atomic Energy Agency. Website: Evaluated nuclear data file(ENDF)
<https://www-nds.iaea.org/exfor/endl.htm>, March 2016.
- [Jen12] Thomas Jennewein. Charakterisierung von Photomultiplier Tubes hinsichtlich deren Verwendung in Flüssig-Xenon Zeitprojektionskammern. bachelor thesis, Johannes Gutenberg-University Mainz, April 2012.
- [JKG96] Gerard Jungman, Marc Kamionkowski, and Kim Griest. Supersymmetric dark matter. *Physics Reports*, 267(5):195 – 373, 1996.
- [KAB⁺07] J. Klug, E. Altstadt, C. Beckert, R. Beyer, H. Freiesleben, V. Galindo, E. Grosse, A.R. Junghans, D. Légrády, B. Naumann, K. Noack, G. Rusev, K.D. Schilling, R. Schlenk, S. Schneider, A. Wagner, and F.-P. Weiss. Development of a neutron time-of-flight source at the ELBE accelerator. *Nuclear Instruments and Methods in Physics Research Section A: Accelerators, Spectrometers, Detectors and Associated Equipment*, 577(3):641 – 653, 2007.
- [KBS⁺10] J. Kwong, P. Brusov, T. Shutt, C.E. Dahl, A.I. Bolozdynya, and A. Bradley. Scintillation pulse shape discrimination in a two-phase xenon time projection chamber. *Nuclear Instruments and Methods in Physics Research Section A: Accelerators, Spectrometers, Detectors and Associated Equipment*, 612(2):328 – 333, 2010.
- [KGS79] J. W. Keto, R. E. Gleason, and F. K. Soley. Exciton lifetimes in electron beam excited condensed phases of argon and xenon. *The Journal of Chemical Physics*, 71(6):2676–2681, 1979.
- [KHN78] Shinzou Kubota, Masahiko Hishida, and Akira Nohara. Variation of scintillation decay in liquid argon excited by electrons and alpha particles. *Nuclear Instruments and Methods*, 150(3):561 – 564, 1978.
- [KHR78] S Kubota, M Hishida, and J Raun. Evidence for a triplet state of the self-trapped exciton states in liquid argon, krypton and xenon. *Journal of Physics C: Solid State Physics*, 11(12):2645, 1978.
- [KHSR79] Shinzou Kubota, Masahiko Hishida, Masayo Suzuki, and Jian-zhi Ruan(Gen). Dynamical behavior of free electrons in the recombination process in liquid argon, krypton, and xenon. *Phys. Rev. B*, 20:3486–3496, Oct 1979.
- [KHSzR82] Shinzou Kubota, Masahiko Hishida, Masayo Suzuki, and Jian zhi Ruan. Liquid and solid argon, krypton and xenon scintillators. *Nuclear Instruments and Methods in Physics Research*, 196(1):101 – 105, 1982.

- [Kja12] Elvar Steinn Kjartansson. Realization of a system to control and monitor the operation of a liquid xenon time projection chamber. bachelor thesis, Johannes Gutenberg-University Mainz, SCS, slow control, May 2012.
- [KNF17] KNF. Website
<https://www.knf.com/products/process-pumps/product/products/diaphragm-gas-pumps-and-compressors/double-diaphragm-pumps/>, March 2017.
- [KNT⁺78] S. Kubota, A. Nakamoto, T. Takahashi, T. Hamada, E. Shibamura, M. Miyajima, K. Masuda, and T. Doke. Recombination luminescence in liquid argon and in liquid xenon. *Phys. Rev. B*, 17:2762–2765, Mar 1978.
- [KSR80] Shinzou Kubota, Masayo Suzuki, and Jian-zhi Ruan(Gen). Specific-ionization-density effect on the time dependence of luminescence in liquid xenon. *Phys. Rev. B*, 21:2632–2634, Mar 1980.
- [Leo94] William R. Leo. *Techniques for nuclear and particle physics experiments : a how-to approach*. Number 9783540572800. Springer, 1994.
- [M⁺94] John C. Mather et al. Measurement of the Cosmic Microwave Background spectrum by the COBE FIRAS instrument. *Astrophys. J.*, 420:439–444, 1994.
- [Mea17a] Measurement Computing. Website: USB-1608G
<http://www.mccdaq.com/usb-data-acquisition/USB-1608G-Series.aspx>, 03 2017.
- [Mea17b] Measurement Computing. Website: USBTemp
<http://www.mccdaq.com/usb-data-acquisition/USB-TEMP-Series.aspx>, 03 2017.
- [Mor12] Matthias Morbitzer. Aufbau einer Testkammer zur Charakterisierung von Avalanche-Photodioden für eine flüssig Xenon TPC. bachelor thesis, Johannes Gutenberg-University Mainz, October 2012.
- [NIS16] NIST - National Institute of Standards and technology. Webbook
<http://webbook.nist.gov/chemistry/fluid/>, March 2016.
- [O⁺14] K. A. Olive et al. Review of Particle Physics. *Chin. Phys.*, C38:090001, 2014.
- [Ort17] Ortec. Website: High purity germanium detectors
<http://www.ortec-online.com/products/radiation-detectors/germanium-hpge-radiation-detectors>, March 2017.
- [PAB⁺11] G. Plante, E. Aprile, R. Budnik, B. Choi, K.-L. Giboni, L. W. Goetzke, R. F. Lang, K. E. Lim, and A. J. Melgarejo Fernandez. New measurement of the scintillation efficiency of low-energy nuclear recoils in liquid xenon. *Phys. Rev. C*, 84:045805, Oct 2011.

- [Pla12] Guillaume Plante. *The XENON100 Dark Matter Experiment: Design, Construction, Calibration and 2010 Search Results with Improved Measurement of the Scintillation Response of Liquid Xenon to Low-Energy Nuclear Recoils*. PhD thesis, Columbia University, 2012.
- [PQ77] R. D. Peccei and Helen R. Quinn. CP Conservation in the Presence of Instantons. *Phys. Rev. Lett.*, 38:1440–1443, 1977.
- [Pre17] Precision Eforming LLC. Website
<http://www.precisioneforming.com/>, March 2017.
- [PRI17] PRISMA. Website: PRISMA cluster of excellence - detector laboratory
<http://www.precisioneforming.com/>, March 2017.
- [SAE17] SAES. Website: PS4
<http://www.saespuregas.com/Products/Gas-Purifier/PS4-MT315.html>, March 2017.
- [Sch13] Melanie Scheibelhut. Aufbau und Simulation eines Comptonstreuexperimentes mit einem Xenon- und einem Germaniumdetektor. diploma thesis, Johannes Gutenberg-University Mainz, December 2013.
- [Sch18] Melanie Scheibelhut. Phd thesis in preparation, Johannes Gutenberg-University Mainz, 2018.
- [SGO⁺09] P Shagin, R Gomez, U Oberlack, P Cushman, B Sherwood, M McClish, and R Farrell. Avalanche photodiode for liquid xenon scintillation: quantum efficiency and gain. *Journal of Instrumentation*, 4(01):P01005, 2009.
- [Sis12] Pierre Sissol. Monte-Carlo-Simulationen eines Compton-Streuexperimentes zur Messung der Szintillations- und Ionisationseigenschaften von flüssigem Xenon mit einer Zwei-Phasen-Xenon-Zeitprojektionskammer. diploma thesis, Johannes Gutenberg-University Mainz, June 2012.
- [Sis17] Pierre Sissol. Phd thesis in preparation, Johannes Gutenberg-University Mainz, 2017.
- [Sma17] Smartec. Website: UTI
<http://smartec-sensors.com/cms/pages/products/uti-interface.php>, March 2017.
- [Smi36] Sinclair Smith. The mass of the virgo cluster. *Astrophys. J.*, 83:23–30, 1936.
- [Sta17] Stanford Research Systems. Website: CTC100
<http://www.thinksrs.com/products/CTC100.htm>, March 2017.

- [Tel17a] Teledyne Hastings. Website: PowerPod
<http://www.tld-h.com/en/products/powerpod-series.htm>, March 2017.
- [Tel17b] Teledyne Hastings. Website:HFM-300
<http://www.teledyne-hi.com/products-services/thermal-mass-flow/hfm-300-hfc-302>, March 2017.
- [Tex17] Texas Instruments. Website
<http://www.ti.com/lit/ds/slos416c/slos416c.pdf>, March 2017.
- [Zwi33] F. Zwicky. Die Rotverschiebung von extragalaktischen Nebeln. *Helv. Phys. Acta*, 6:110–127, 1933.

Curriculum Vitae



Bastian Beskers

Domitianstr. 32
D-55126 Mainz
+49 176 23591027
bastian.beskers@web.de

16.07.1983
Karlsruhe
Single, no children
German

Work Experiences / Education

- July 2011 – July 2016 **Research associate/doctoral student** at Johannes Gutenberg-University Mainz, Institute of physics
Title of PhD thesis: „*Design, construction and commissioning of a dual-phase xenon time-projection chamber for improved understanding of scintillation properties and signal shape*“
- May 2012 – April 2016 **Elected member of the member-board** of Helmholtz Alliance for Astroparticle Physics
- 2010 – 2011 **Diploma student** at Karlsruhe Institute of Technology (KIT)
Title of diploma thesis: „*Measurement and optimization of properties of the monitor-detector for keV electrons in the cryogenic pumping section of the KATRIN experiment*“
Degree: Diploma in physics (equivalent to Master of Science)
grade: 1.7
- 2009 – 2010 **Student research assistant** at Forschungszentrum Karlsruhe: testing vacuum-pressure gauges in high magnetic fields
- 2003 – 2004 **Civil service** at ISB Karlsruhe (Individuelle Schwerstbehindertenbetreuung): individual care of a seriously disabled person
- 2000 – 2003 **Technical High School** (Albert-Einstein-Schule Ettlingen)
Degree: General qualification for university entrance (Abitur)
grade: 1.3
- 1994 – 2000 **High School** (Walahfrid-Strabo Gymnasium Rheinstetten)

Further Training/International Experience

- 2013 **Research visit** at Stanford University:
Test of a high-speed ring-sampler ASIC for suitability for the liquid xenon experiment
- 2012 **Workshop** at Laboratori Nazionali del Gran Sasso (LNGS) in Italy:
Xenon100 – Geant4 simulations
- 2012 **International School** on Trigger and Data Acquisition in Cracow (Poland)

Lebenslauf



Bastian Beskers

Domitianstr. 32
D-55126 Mainz
+49 176 23591027
bastian.beskers@web.de

16.07.1983
Karlsruhe
ledig, keine Kinder
deutsch

Berufliche Erfahrung / Ausbildung

Juli 2011 – Juli 2016	Wissenschaftlicher Mitarbeiter/Doktorand an der Johannes Gutenberg-Universität Mainz, Institut für Physik Thema der Doktorarbeit: <i>Entwurf, Aufbau und Inbetriebnahme eines Zweiphasen-Xenon-Detektors zur Untersuchung der Szintillationseigenschaften und der Szintillationslichtform von flüssigem Xenon</i>
Mai 2012 – April 2016	Gewähltes Mitglied des Member-Boards der Helmholtz-Allianz für Astroteilchenphysik
2010 – 2011	Diplomand am Karlsruher Institut für Technologie (KIT) Titel der Diplomarbeit: <i>Messung und Optimierung der Eigenschaften des Monitordetektors für keV-Elektronen in der kryogenen Pumpstrecke bei KATRIN</i> Abschluss: Diplom (Note: 1.7)
2009 – 2010	Hilfswissenschaftler am Forschungszentrum Karlsruhe (jetzt: KIT): Test von Vakuumdrucksensoren in starken Magnetfeldern
2003 – 2004	Zivildienst bei ISB Karlsruhe (Individuelle Schwerstbehindertenbetreuung): Individuelle Betreuung einer schwer an Multiple-Sklerose Erkrankten
2000 – 2003	Technisches Gymnasium (Albert-Einstein-Schule Ettlingen) Abschluss: Allgemeine Hochschulreife/Abitur Note: 1.3
1994 – 2000	Allgemeinbildendes Gymnasium (Walahfrid-Strabo Gymnasium Rheinstetten)

Weiterbildung/Auslandserfahrung

2013	Forschungsaufenthalt an der Stanford Universität (Kalifornien): Test eines Hochgeschwindigkeits-Ring-Sampler-ASICs hinsichtlich der Verwendbarkeit für ein Flüssigxenon-Experiment
2012	Workshop am Laboratori Nazionali del Gran Sasso (LNGS) in Italien: Xenon100 – Geant4 Simulationen
2012	International School on Trigger and Data Acquisition (ISOTDAQ) in Krakau (Polen)